Transitional Behaviour of Saturated and Unsaturated Tailings and Loess

A thesis submitted to the University College London for the degree of Doctor of Philosophy

By

Yahui WANG

Department of Civil, Environmental & Geomatic Engineering

University College London

August 2025

DECLARATION

I, Yahui WANG, confirm that the work presented in my thesis is my own. Where information has been derived from other sources, I confirm that this has been indicated in the thesis.

Yahui WANG

London, August 2025

ABSTRACT

This research investigates the transitional behaviour of soils under both saturated and unsaturated conditions through a comprehensive experimental programme. Transitional behaviour, characterised by non-unique Normal Compression Lines (NCLs) and Critical State Lines (CSLs), is a special case of the widely accepted Critical State Soil Mechanics (CSSM). Although this behaviour has been recognised in some soils under saturated conditions, its detailed characteristics and its persistence under partial saturation remain poorly understood.

Four types of reconstituted soils were examined, namely fine tailings, sandy tailings, silty loess, and a kaolin–sand mixture, selected for their differences in mineralogy, grading, and particle size distribution. The study first focused on saturated mechanical behaviour using oedometer and triaxial tests across a wide range of initial densities. All four materials exhibited transitional behaviour, with fine tailings displaying the most pronounced characteristics. Detailed investigations on fine tailings included quantification of NCL and CSL parameters, evaluation of small-strain stiffness, volumetric behaviour, and state boundary surface analysis.

The second part of the study explored the transitional behaviour under unsaturated conditions. An unsaturated triaxial system was developed using the axis translation technique. Filter paper tests were used to determine Soil Water Retention Curves in order to guide sample selection and sample preparation. Unsaturated triaxial tests were conducted on sandy tailings and silty loess under constant suction compression and constant water content shearing. Transitional behaviour was clearly observed in both soils, and suction was found to influence this behaviour.

IMPACT STATEMENT

This research provides new experimental evidence and interpretation of transitional soil behaviour in both saturated and unsaturated conditions. Transitional soils are a special case of the conventional critical state soil mechanics (CSSM) and are characterised by non-unique Normal Compression Lines (NCLs) and Critical State Lines (CSLs). These materials are increasingly relevant in modern geotechnical engineering, particularly in dealing with complex soils like tailings and problematic soils like loess. However, the transitional behaviour of these soils remains poorly understood, especially under unsaturated conditions.

The academic contribution of this research is the clear demonstration that transitional behaviour persists not only in saturated soils but also under unsaturated conditions. This transitional behaviour, found in reconstituted tailings and loess, provides valuable datasets and expands current understanding on transitional behaviour to unsaturated states. These findings contribute to the detailed characteristics of transitional behaviour, including the parameters of the NCLs and CSLs, state boundary surfaces, small-strain stiffness, and stress–dilatancy behaviour. These are of interest for theoretical and numerical modelling.

The research has important implications for engineering practice, particularly in the design and maintenance of tailings storage facilities. The presence of transitional behaviour in tailings challenges the CSSM, which is commonly used for construction design. In particular, the increasingly popular dry stacking method for tailings dams, which uses unsaturated tailings, is often assumed to offer safer and more stable performance than the conventional upstream method, which uses saturated tailings. However, the findings suggest that this assumption may not always be true due to the potential transitional behaviour. For both saturated and unsaturated conditions,

transitional behaviour affects the prediction of volume change, strength development, and liquefaction resistance. If the transitional behaviour of these soils is ignored, key behavioural features such as compressibility and critical states may be missed, leading to underestimated deformation and overestimated stability.

In summary, this thesis has generated fundamental insights and practical knowledge relevant to both the academic advancement and real-world application of soil mechanics. Its contributions are particularly significant for understanding and managing the behaviour of transitional soils in geotechnical engineering practice.

ACKNOWLEDGEMENT

I would like to express my deepest gratitude to my supervisor, Professor Matthew Coop. His support has been fundamental to every aspect of this work and at every stage of my PhD. I am truly thankful for his invaluable guidance and constant encouragement through many difficult moments, as well as for his patience and dedication throughout this journey. I am also thankful to Dr. Pedro Ferreira for his detailed and practical advice. His input was always thoughtful and precise. I sincerely thank Professor Béatrice Baudet for arranging opportunities to engage with the broader research community. These experiences helped me grow as a researcher, broaden my perspective, and share my work beyond the lab. Special thanks to Matt Wilkinson for his technical assistance in maintaining the equipment.

I would also like to thank all my colleagues and friends at UCL. It is impossible to name everyone, as each of them mattered to me in their own way. Their kind words, thoughtful advice, and the moments we shared together helped shape this journey and made it one I will always remember.

Finally, I am deeply grateful to my parents for their unconditional love, support, and understanding. Their patience, sacrifices, and unwavering encouragement have been my foundation throughout this journey. I am fortunate to carry their love with me, now and always.

CONTENTS

LIST OF SYMBOLS, ABBREVIATIONS, AND TESTING

Symbols	
A	Cross-sectional area
c'	Effective cohesion intercept in the equation $\tau = c' + (\sigma - u_a)\tan\varphi^a + (u_a - u_w)\tan\varphi^b$
C_c^*	Intrinsic compression index of ICL
D_{max}, D_{min}, D_{50}	Maximum, minimum and 50% percentage particle diameter
e, e_{100}^* and e_{1000}^*	Void ratio, void ratios on the ICL at 100 kPa and 1000 kPa effective stresses
G_s	Specific gravity
G, G_{hh}, G_{hv}	Tangent shear stiffness, shear stiffnesses in horizontal and vertical planes
h_n, h_t	Sample height for layer No.n from bottom, total sample height
I_v	Void index
k_0	Coefficient of earth pressure at rest
m	Parameter used for quantifying convergence of NCLs
m_d, m_w, m_n, m_t	Dry mass, wet mass, moist soil mass for No.n layer, total moist soil mass.
M, M_a, M_w,	Stress ratio at critical state, stress ratio for unsaturated soil and influence factor related to suction in equation $q = M_a(p - u_a) + M_w(u_a - u_w)$.
n, n_t	Sample layer number from bottom, total sample layer number
N, N^*	Intercept of NCL and intercept of ICL in the $v - lnp'$ plane
P	Parameter used for quantifying convergence of CSLs

p' , p'_{cs}, p^{χ}, p^{*}	Mean effective stress, p' normalised by an equivalent pressure taken on the CSL, effective stress with Khalili and Khabbaz's factor and Bishop stress for unsaturated soil.
q	Deviator stress
S_r	Degree of saturation
s, s_e	Matric suction ($s = u_a - u_w$), air entry value
u or u_w, u_a	Pore water pressure, pore air pressure
U, U_n	Under-compaction percentage, that for layer No.n
v, v_i, v_f, v_{20}, v_n	Specific volume, initial specific volume, final specific volume, specific volume at 20 kPa effective stress, normalized specific volume
V	Volume
w_i, w_f	Initial water content, final water content
γ_{bulk}, γ_d, γ_w	Bulk unit weight, dry unit weight, water unit weight
Γ or Γ^*, Γ_a, Γ_{aw}	Projected specific volume at 1 kPa on the CSL in the $lnv - lnp'$, that in the $v - lnp'$ plane, and that for unsaturated soil in equation $v = \Gamma_{aw} - \lambda_a \ln(p - u_a) - \lambda_w \ln(u_a - u_w)$ in the $v - lnp'$ plane.
Δ	Changed value
ε_a, ε_r, ε_s, ε_v	Axial strain, radial strain, shear strain, volumetric strain
λ, λ^*, λ_a, λ_w	Slope of NCL and slope of ICL in the $v - lnp'$ plan, slope of NCL for unsaturated soil and influence factor related to suction in equation $v = \Gamma_{aw} - \lambda_a \ln(p - u_a) - \lambda_w \ln(u_a - u_w)$.
π	Osmotic suction
σ, σ', σ'_v	Total stress, effective stress, effective vertical stress
τ	Shear strength

φ' or ϕ, φ^b	Friction angle in saturated conditions, friction angles related to matric suction in equation $\tau = c' + (\sigma - u_a)\tan\varphi' + (u_a - u_w)\tan\varphi^b$.
χ	Influence factor related to suction in equation of effective stress under unsaturated condition $\sigma' = (\sigma - u_a) + \chi(u_a - u_w)$
ψ	Total suction ($\psi = s + \pi$)

Abbreviations	
AEV	Air Entry Value
BBM	Barcelona Basic Model
CD	Consolidated Drained
CRSP	Constant Rate of Strain Pump
CSL(s), CSLi, CSLr	Critical State Line(s), CSL of the intact specimens, CSL of the reconstituted specimens.
CSSM	Critical State Soil Mechanics
CU	Consolidated Undrained
HAE	High Air Entry (porous stone)
LC	Loading-Collapse
ICL	Intrinsic Compression Line
LL	Liquid Limit
LVDT	Linear Variable Differential Transformer
MIP	Mercury Intrusion Porosimetry
NCL	Normal Compression Line
PEG	Polyethylene Glycol

PL	Plastic Limit
PSD	Particle Size Distribution or Pore Size Distribution (context dependent)
PTP	Phase Transformation Point
SEM	Scanning Electron Microscopy
SPF	Sand with Plastic Fines
SWRC	Soil Water Retention Curve
VG	Volume Gauge

Tests	
Summary of saturated tests	
Mixture of Leighton buzzard sand and kaolin	
85SK	Oedometer test on 85% sand and 15% kaolin
80SK	Oedometer test on 80% sand and 20% kaolin
75SK	Oedometer test on 75% sand and 25% kaolin
70SK	Oedometer test on 70% sand and 30% kaolin
65SK	Oedometer test on 65% sand and 35% kaolin
Mixture of 75% Leighton buzzard sand and 25% kaolin	
OM1	Oedometer test prepared by compaction method
OM2-OM12	Oedometer test prepared by slurry method
Silty loess	
OL1-OL4	Oedometer test prepared by slurry method
OL5-OL6	Oedometer test prepared by compaction method

TL1-TL3	Triaxial test prepared by compaction method
Sandy tailings	
OSTs1-OSTs4	Oedometer test prepared by slurry method
OSTc1-OSTc5	Oedometer test prepared by compaction method
KSTH, KSTL	Triaxial k_0 test prepared by compaction method
TST1-TST3	Triaxial test prepared by compaction method
Fine tailings	
O1-O4	Oedometer test prepared by slurry method
K1-K3	Triaxial k_0 test prepared by slurry method
T1CD100A-T16CU50A	Triaxial test prepared by slurry method; T for triaxial test; 1 for number; CD for drained shearing and CU for undrained shearing; 100 for consolidation pressure; A for density group.
Summary of filter paper tests	
Fine tailings	
FT1-FT2	Prepared by slurry method
Sandy tailings	
50ST	50% sand and 50% fine prepared by compaction method
60ST	60% sand and 40% fine prepared by compaction method
60ST1-60ST3	60ST samples in different initial specific void ratio
75ST	75% sand and 35% fine prepared by compaction method
Loess	
L1, L2	Prepared by slurry method and tested in different degree of saturation
L3-L5	Prepared by compaction method in different initial void ratio
Mixture of 75% Leighton buzzard sand and 25% kaolin	
KS1, KS2	Prepared by slurry method and tested in different degree of saturation

Summary of unsaturated triaxial tests	
Loess	
UL1-UL3	Prepared by compaction method in different initial void ratio
Sandy tailings	
UST1-UST3	Prepared by compaction method in different initial void ratio

CHAPTER 1 INTRODUCTION

1.1 Background

The mechanical behaviour of soils has been widely described using the Critical State Soil Mechanics (CSSM) framework. This framework assumes that soils exhibit unique Normal Compression Lines (NCLs) and Critical State Lines (CSLs), which are independent of the initial density or stress history. This means that, according to CSSM, soils with various initial densities and subjected to different stress conditions will converge to a unique volumetric state during monotonic loading. However, transitional soils have been found to deviate from this assumption, as transitional soils do not have unique NCLs and CSLs even at high stress levels. The locations of NCLs and CSLs are dependent on the initial specific volume or initial density. The presence of transitional behaviour complicates the fundamental soil parameters and characteristics of soil mechanical behaviour.

The non-convergent volumetric state in transitional soils indicates the presence of a stable or robust fabric that cannot be easily destructured through conventional loading. However, the nature of the robust fabric that causes transitional behaviour has not been clearly identified yet. This robust fabric likely originates from and varies with the initial density (Coop, 2015). Such robust fabrics have been found not necessarily to result from sample preparation and are distinct from natural structural elements.

Transitional behaviour has been observed in various soils, including gap-graded soils (Martins et al., 2001), reconstituted and natural well-graded clayey silts (Nocilla et al., 2006; Nocilla & Coop, 2008), well-graded sands (Altuhafi et al., 2010), well-graded coarse granular soils (Xiao et al., 2016) and decomposed volcanic rocks (Okewale & Coop, 2020). These soils are often characterised by mixed mineralogy and/or mixed

grading (Shipton & Coop, 2015). Particle breakage can occur in transitional soils, but it is not a necessary feature of their behaviour. Transitional behaviour has been found to be significantly influenced by the fines content, but grading alone is not a definitive indicator. Since there is no definitive indicator for predicting transitional behaviour, and small changes in soil components can change this behaviour, there is currently no simple method available to identify transitional soils. Therefore, each soil has to be tested individually to identify transitional behaviour (Shipton & Coop, 2015).

Most studies investigate soil behaviour using samples with a narrow range of initial densities, whereas transitional behaviour can only be identified when soils are tested across a sufficiently wide range of initial specific volumes. As a result, the frequency of transitional soils has likely been underestimated in the literature. This underestimation has important implications from an engineering perspective. For example, the stability analysis of tailings dams often relies on the accurate determination of CSLs to assess the soil potential for volumetric behaviour and liquefaction. If the soil exhibits transitional behaviour, the use of a single CSL may lead to incorrect estimations of liquefaction potential and stability. Similarly, in collapsible loess deposits, the prediction of settlement and collapse during wetting or loading requires reliable characteristics of the NCL and CSL. But these behaviours may not be estimated correctly using conventional CSSM when applied to transitional loess.

The behaviour of transitional soils under unsaturated conditions remains unexplored. Since suction influences effective stress and structure stability, it is expected to modify the mechanical response of soils. The effect of suction on transitional modes observed in saturated conditions has not yet been studied. Moreover, the experimental challenges in suction control and measurement as well as accurate volume change measurement in unsaturated soils have limited progress in this area.

Although the transitional behaviour has been recognised in several previous studies, its characteristics still remain limited. In addition, no published research to date has studied transitional behaviour under unsaturated conditions. Understanding whether transitional features persist in unsaturated states remains an open question. Microstructure studies may support the interpretation of the mechanisms responsible for non-convergent behaviour. Therefore, there is a need for a comprehensive study on transitional behaviour in both saturated and unsaturated conditions through a series of precise experimental tests.

1.2 Research objectives

This research aims to investigate the transitional behaviour of soils under both saturated and unsaturated conditions through a comprehensive series of laboratory experiments. Although transitional behaviour has been identified in various reconstituted and natural soils, its characteristics remain incomplete, particularly under partial saturation. The present study addresses this gap by focusing on the mechanical response of four types of soils with potential transitional features: fine tailings, sandy tailings, silty loess, and an artificial kaolin-sand mixture. These materials were selected to represent a range of particle sizes, mineralogies, and gradings that may influence transitional behaviour. The experimental work was carried out on reconstituted samples to control initial conditions and eliminate the effects of natural bonding or structure. Both slurry and static compaction methods were used to prepare samples with a wide range of initial specific volumes to assess the presence of transitional behaviour. This study mainly consists of two parts, addressing the mechanical behaviour in both the saturated and unsaturated states.

The first part investigates the mechanical behaviour of the four soil types under saturated conditions. One-dimensional oedometer tests were performed to establish compression paths and identify transitional behaviour through the observation of non-unique NCLs for each material. To evaluate the reliability of the oedometer compression results, triaxial k_0 compression tests were conducted because they have better saturation conditions and are free of the side-wall friction. Triaxial shearing tests were carried out to determine the non-unique CSLs to confirm the transitional behaviour during the shearing stage. The degrees of transitional behaviour were quantified using the m and P values defined by Ponzoni et al. (2014), enabling direct comparison between materials. These results were used to identify soils with pronounced transitional behaviour for further testing and to evaluate whether sample preparation methods influence the mechanical behaviour. The characteristics of transitional behaviour were identified by quantifying the parameters of the NCLs and CSLs, evaluating the small-strain stiffnesses using local LVDTs, studying the volumetric behaviours and interpreting the state boundary surfaces.

The second part of the research works on the unsaturated behaviour of selected soils, focusing on sandy tailings and silty loess. An unsaturated triaxial apparatus was developed using the axis translation technique, enabling constant suction and constant water content tests. The system was modified from a saturated triaxial setup, incorporating a pore air pressure system, a new pedestal, and a total volume measurement system. The pedestal was fitted with a 5 bar high air entry (HAE) porous stone, enabling suction control or measurement up to 500 kPa. The total volume measurement system used a combination of local LVDTs (two axial and two radial) and a cell volume gauge. Calibrations were performed for both compression and shearing stages, considering the effects of cell pressure, time, temperature, and axial

displacement on the volume gauge, and sample geometry on the local LVDT measurements of sample volume. Leakage was a major challenge during setup and was resolved through repeated and detailed inspections.

For the unsaturated triaxial tests, both constant suction compression and constant water content shearing were adopted. The objective was to determine whether the transitional behaviour identified under saturated states persists under partial saturation and the effect of suction on this behaviour. The constant suction compression tests were conducted to define the NCL for a given suction, for example, 100 kPa in this study. The constant water content shearing tests performed to define the CSL corresponding to the suction attained at the end of each test, allowing comparison with drained saturated triaxial tests conducted along the same stress paths. The Soil Water Retention Curves (SWRCs) for the soils studied were determined before the unsaturated triaxial tests to select the suitable soil materials and sample preparation methods. The SWRCs were also used to define the water content corresponding to the desired suction for the unsaturated triaxial tests. Filter paper tests were used for the SWRC measurement. A tensiometer was adopted to set up a system for SWRC measurements and incorporated into an oedometer for unsaturated compression tests. However, these tests were discontinued due to the tensiometer's failure.

To support the interpretation of mechanical responses, selected saturated and unsaturated samples were preserved after testing and examined using Mercury Intrusion Porosimetry (MIP) and Scanning Electron Microscopy (SEM) tests. These analyses provided insights into pore structure and particle arrangement before and after loading. These microstructural observations provided supporting evidence for the persistence of fabric, as a possible explanation for transitional behaviour.

1.3 Thesis outline

This thesis consists of seven chapters presenting the experimental investigations on soil transitional behaviour under both saturated and unsaturated conditions.

Chapter 2 provides a literature review for this study. The concept of transitional behaviour and key findings from previous studies are summarised, especially for the materials used in this research. Key principles of unsaturated soil mechanics are introduced, along with suction control and measurement methods. The influence of microstructure on mechanical behaviour is briefly discussed, and the research gap is highlighted at the end of this chapter.

Chapter 3 describes the materials used in the study, including fine and sandy tailings, a silty loess, and a kaolin-sand mixture. It outlines the sample preparation procedures and presents the detailed test equipment and test procedures used for saturated oedometer and triaxial tests. The procedures used for microstructural tests, MIP and SEM tests, are also explained.

Chapter 4 describes the unsaturated test programme and procedures. The use of filter paper tests and tensiometer measurements for determining SWRCs is introduced. The development and calibration of the unsaturated triaxial apparatus are described in detail, along with test procedures.

Chapter 5 presents the results of the saturated mechanical tests conducted on fine tailings, sandy tailings, loess, and a kaolin-sand mixture. Oedometer tests and triaxial tests were used to assess the transitional behaviour, which was observed in all four materials. Fine tailings were selected for further detailed investigation, including a detailed study of the NCLs and CSLs, small strain stiffnesses, volumetric behaviours, and the state boundary surfaces.

Chapter 6 presents the results of the unsaturated tests. SWRCs results from filter paper tests were used to select the suitable soils for the unsaturated triaxial tests, leading to the selection of sandy tailings and silty loess. Tests were conducted under constant suction compression and constant water content shearing to evaluate transitional behaviour in unsaturated states. Clear transitional behaviour was identified in both soils and the influences of suction and initial density were discussed.

Chapter 7 summarises the main works carried out in this study and the research contributions based on the research findings and engineering implications. The study limitations and recommendations for future research are then discussed.

CHAPTER 2 LITERATURE REVIEW

2.1 Introduction

This chapter provides a literature review for the study. Section 2.2 explains the background of transitional behaviour, including key features, previous findings and potential reasons. Three materials used in this study are introduced in Section 2.3, with previous research on the soil characteristics and transitional behaviour of these soils. Section 2.4 provides background information on unsaturated soil concepts and unsaturated soil mechanical frameworks, which are essential for the data analysis from the unsaturated tests conducted in this study. Section 2.5 presents the information for unsaturated tests, detailing the methods used in this study as well as other common methods. As the potential reason for the transitional behaviour, microstructure is introduced in Section 2.6, including the definition, data analysis and experimental tests. Section 2.7 introduces a case study of transitional behaviour on saturated loess from Xu and Coop (2017). Section 2.8 presents the current research gaps and outlines the research objectives of this study.

2.2 Transitional behaviour

2.2.1 Definition

The mechanical behaviour of most soils is typically described within the critical state framework, where volumes during compression and shearing converge to a unique Normal Compression Line (NCL) and Critical State Line (CSL) under different stress states. However, a transitional behaviour has been found to contradict the critical state framework. Transitional soils have no unique NCL and CSL even up to very high stresses, and their mechanical behaviour is dominated by initial density, as shown in Figure 2-1 (Shipton & Coop, 2012). Specifically, transitional samples with different

initial densities have a family of NCLs or CSLs depending on their initial density. But transitional soils with the same initial density still follow the critical state mechanics, exhibiting a unique NCL and CSL. Similar to this lack of influence on monotonic loading, the initial density of transitional soils does not have much effect on cyclic loading (Cartwright et al., 2025).

Transitional behaviour can be quantified into different transitional degrees based on the extent of convergence of NCLs and CSLs. Ponzoni et al. (2014) introduced two factors m and P to quantify the degree of transitional behaviour by comparing the initial specific volume and final specific volume of loose and dense samples after compression or shearing tests, as shown in Figure 2-2. Factor m can be calculated from the compression curves of loose and dense samples, based on their specific volume at vertical stresses of initial and final states, using the Equation 2-1. The initial state is selected to avoid effects of sample disturbance at the start of the test, while final state corresponds to the maximum applied stress. For example, in Figure 2-2 (a) and (b), m is calculated based on 20 kPa and 7000 kPa. Li and Coop (2019) suggested that the factor m was not constant but varied with the final specific volume at different effective stress levels, as shown in Figure 2-3, potentially giving a curved relationship. As shown in Figure 2-2 (c) and (d), factor P is dependent on the projected specific volume at 1 kPa on the CSL for loose and dense samples (Γ_a and Γ_b) and their initial specific volume before consolidation (v_{0a} and v_{0b}), defined in Equation 2-2. Both m and P values range between 0 and 1, indicating a unique NCL characteristic of conventional soils and a fully transitional soil, respectively.

$$m = \frac{v_{final,loose} - v_{final,dense}}{v_{intial,loose} - v_{inital,dense}} \qquad \text{Equation 2-1}$$

$$P = \frac{\Gamma_a - \Gamma_b}{v_{0a} - v_{0b}}$$ Equation 2-2

Todisco and Coop (2019) emphasized that directly comparing factors m and P is meaningless. This is because both factors quantify the convergence at specific stress or strain levels within a test, but they are adopted in different types of tests, m for compression and P for shearing. Therefore, Todisco and Coop (2019) further developed factor m to create a 3D convergence surface, illustrating how the rate of convergence changes with both volumetric and shear strain, as shown in Figure 2-4. This surface allows for comparisons between compression and shearing tests. Todisco and Coop (2019) found that it was unlikely for the three soils studied to reach a unique volumetric state in triaxial or oedometer tests, and convergence occurred more rapidly with volumetric strain than with shear strain.

These studies indicated that the transitional degree varied among different soils. For soils with high transitional degree, the NCLs and CSLs are little convergent or even completely parallel. Some soils appear to have slowly but gradually convergent compression lines. Despite this gradual convergence, these soils are still classified as transitional soils because full convergence would require stresses or strains far beyond typical engineering practice. Additionally, their mechanical behaviour is dominated by the initial density, distinguishing them from traditional soils following the critical state framework.

The non-convergence must result from the persistence of soil fabric, as Todisco et al. (2018) suggested. The non-convergence of specific volume (v) appears to reflect non-unique fabric at critical states for samples with different initial density, as differences

in v can only arise from the variation in fabric. This non-unique fabric at critical state likely originates from a naturally robust fabric that depends on the initial density. This implies that a key problem of transitional behaviour is that transitional soils may lack the unique intrinsic properties traditionally used to quantify the effects of structure in natural soils (Coop, 2015). Further details on the soil fabric causing transitional behaviour will be introduced in Section 2.2.3.

In summary, the key characteristics of transitional behaviour are the dominance of the initial specific volume (v_i), the absence of unique NCL and CSL under monotonic loading and the variety of transitional degrees among different soils. The significant implication of transitional behaviour is that transitional soils may have non-unique fabric depended on initial density, suggesting non-unique intrinsic soil properties.

2.2.2 Transitional soils

Several soils with transitional behaviour have been identified, including gap-graded soils (Martins et al., 2001), reconstituted and natural well-graded clayey silts (Nocilla et al., 2006; Nocilla & Coop, 2008), well-graded sands (Altuhafi et al., 2010), well-graded coarse granular soils (Xiao et al., 2016) and decomposed volcanic rocks (Okewale & Coop, 2020). Sand with plastic fines (SPF) has been widely reported to have transitional behaviour in many studies (Martins et al., 2001; Ferreira & Bica, 2006; Shipton & Coop, 2015; Shipton et al., 2017; Todisco et al., 2018; Todisco & Coop, 2019). Soils with mixed mineralogy and/or mixed grading are more likely to have transitional behaviour (Shipton & Coop, 2015). Unfortunately, most studies of soil behaviour typically prepare reconstituted samples with similar values of v_i, so transitional behaviour could not be identified. The frequency of transitional soils could therefore be underestimated (Coop, 2015).

Transitional behaviour has been found to be significantly influenced by the fines content, however, grading alone is not a definitive indicator of transitional behaviour. Martins et al. (2001) suggested that sand with plastic fine had transitional behaviour typically with about 20-30% fines, although the proportion needed depended on the plasticity of the fines and the nature of sands. Carrera et al. (2011) investigated the effect of grading in silt-sand mixtures from the Stava tailings on the transitional behaviour. As shown in Figure 2-5, they observed transitional behaviour only in the mixture containing 50% sand and 50% silt. Additionally, they found that the one-dimensional NCL in the $e - lnp'$ plane moved downwards and became less inclined with increasing silt content. Li and Coop (2019) reported variability in the rate of convergence to the one-dimensional NCL from sandy to silty iron tailings. As shown in Figure 2-6, they found that the finest material achieved the NCL much earlier than the two other coarser materials.

Particle breakage can occur in transitional soils, but it is not a necessary feature of their behaviour. Altuhafi et al. (2010) found transitional behaviour in a subglacial sediment, which was already crushed to a critical fractal grading in-situ during glacial deposition and transport. The critical grading refers to a special fractal distribution where the soil packing is so stable that further compression does not easily lead to particle rearrangement or breakage. As shown in Figure 2-7, multiple compression curves are parallel and do not converge onto a single line even up to 250 MPa. Altuhafi and Coop (2015) found that poorly graded sands exhibit significant breakage and converge to a unique NCL, while critical grading sands of various mineralogies show little breakage and develop transitional behaviour, as shown in Figure 2-8. Shipton and Coop (2015) reported that no significant particle breakage occurred during testing of two transitional soil mixtures, quartz sand with non-plastic fines (SNF) and quartz sand with plastic

fines (SPF), as shown in Figure 2-9. Particle breakage was observed in a transitional soil mixture of crushable sand with plastic fines (Shipton et al., 2017), while Nocilla et al. (2006) did not find particle breakage for a transitional clayey silt. Therefore, Shipton et al. (2017) suggested that particle breakage is not a determining factor in transitional soils.

Since there is no definitive indicator to predict transitional behaviour and small changes in soil components can change this behaviour, there appears to be no simple method to predict transitional soils. Therefore, each soil has to be tested individually to identify transitional behaviour (Shipton & Coop, 2015).

2.2.3 Robust fabrics

Robust fabrics, as the potential reason for transitional behaviour, have been found not necessarily to result from sample preparation. Todisco et al. (2018) were the first to apply statistical parameters to the Pore Size Distribution (PSD) on Sand with Plastic Fine (SPF) samples, providing the evolution of the PSD during loading. Their findings suggested that the fabric that might relate to transitional behaviour was heterogeneous, as it covered a wide range of pore sizes. The differences between loose and dense samples remain after loading, as shown in Figure 2-10. They also tested the horizontal and vertical shear stiffnesses (G_{hh} and G_{hv}) by multi-directional bender elements, and the similar shear stiffnesses values shown in Figure 2-11 indicated an isotropic soil fabric. Moreover, they found that the stiffness was dependent on applied stress and poorly related to the sample density, similarly to the large strain behaviour. These observations suggested that the fabric linked to transitional behaviour did not result from the sample preparation, which typically induces structures with inherent anisotropy. Many previous studies have reported that sample preparation methods had no effect on the mechanical behaviour of transitional soils (Li & Coop, 2019; Li et al.,

2018; Nocilla et al., 2006; Shipton & Coop, 2012, 2015; Xu & Coop, 2017). Figure 2-12 provides an example where reconstituted samples prepared using different methods, including wet and dry compaction and the slurry method, exhibit very similar compression lines.

The robust fabrics that result in transitional behaviour have been found to differ from the natural structural elements that distinguish intact and reconstituted soils. Xu and Coop (2016) described the mechanical behaviour of a natural clayey loess, showing that the intact samples initially compressed beyond the NCL of the reconstituted samples and gradually converged towards it after yielding, as illustrated in Figure 2-13. Subsequently, Xu and Coop (2017) studied a silty loess with transitional behaviour. The presence of natural structure is clearly evident in Figure 2-14, based on the comparison between the intact soil and reconstituted soil with a similar initial specific volume (v_i). Later, Section 2.6 will introduce methods quantifying effect of intact structure distinguishing from the transitional behaviour that have been reported in the literature. Xu and Coop (2017) suggested that the transitional degree of an intact silty loess, quantified using m value method, was significantly higher than its corresponding reconstituted samples, as shown in Figure 2-15. However, this conclusion was not very certain due to the limited range of initial specific volume v_{20} for the intact specimens. However, this finding is consistent with the conclusions of Ponzoni et al. (2017) in Venice Lagoon sediments with transitional behaviour. Okewale and Coop (2020) found that the natural structure element in a transitional silty decomposed volcanic rock was broken down significantly less during compression than during shearing. This conclusion was drawn from the comparison of the m and P graphs between intact and reconstituted samples, as shown in Figure 2-16. This behaviour was distinct from that of the robust fabric responsible for the transitional behaviour.

2.2.4 Research gap

Although several studies have explored transitional behaviour, the characteristics of transitional behaviour in saturated soils remains incomplete. Additionally, due to the complexity of the mechanics of unsaturated soils, unsaturated soils are highly likely to have a different mode of transitional behaviour. Since no studies have yet investigated transitional behaviour in unsaturated soils, further research in this area is necessary.

2.3 Materials

2.3.1 Tailings

Tailings are mining waste after extracting the economic minerals, metals or coal from the ore. Due to the high demand of products from mining industries, several billion tonnes of tailings are produced per year and the most common storage method is tailings dams (Azcue, 2012). There have been 257 tailings dam failures recorded since 1915, with catastrophic environmental and human impact (Piciullo et al., 2022). The stability analysis of current engineering practice for tailings dams generally relies on the critical state line (CSL) that is determined for reconstituted tailings samples (Mmbando et al., 2021). This is because the characteristics of the CSL identify the soil potential for contraction or dilatancy hence also determines potential for static liquefaction (Carrera et al., 2011). Therefore, accurate CSLs for the tailings are required and any ambiguities in its location are a concern.

The origins of tailings and mineral sand fines necessarily mean that they will generally have mixed mineralogies and mixed gradings, which are typically the types of materials that have transitional behaviour (Coop, 2015). Li & Coop (2019) found a mild form of transitional behaviour at low-medium stresses in Iron tailings. But the behaviour tended

to be convergent like a conventional soil at pressures greater than 1MPa for the finer material and more than 10MPa for the coarser ones, as shown in Figure 2-6.

2.3.2 Loess

Loess in China covers 631 000 km^2, most of which is distributed on the Chinese Loess Plateau in north-central China (Liu, 1985). The Chinese Loess Plateau is the largest and thickest loess plateau on earth and partly covers the Chinese provinces of Gansu, Shaanxi, Shanxi, Henan, and Ningxia, as shown in Figure 2-17 (Xu et al., 2020). Since the plateau is formed by wind-blown sedimentation, the loess soils in the plateau have a common origin but variable particle gradings following the wind direction from northwest to southeast, from sandy loess, to silty loess, and clayey loess (Xu et al., 2020). Clear transitional behaviour has been found by Xu and Coop (2017) in a silty loess retrieved from Lanzhou, China, as shown in Figure 2-12 (a).

2.3.3 Mixture of kaolin and Leighton Buzzard sand

Artificial soil mixtures, mostly mixed or gap-graded natural soils, were widely employed in laboratory tests to study the fundamental behaviour of transitional soils. These mixtures have the advantage of eliminating complex effects, enabling controlled gradings and mineralogies and ensuring good experimental repeatability (Shipton & Coop, 2012). Transitional behaviour has been found in a gap-graded mixture consisting of 75% quartzitic sand and 25% kaolin (Martins et al., 2001; Shipton & Coop, 2015), as shown in Figure 2-18.

2.4 Unsaturated soil behaviour

2.4.1 Soil suction

Soil that has water partly filling the soil pores has an affinity to absorb more water, which is an isotropic pressure and is defined as soil suction. This soil suction is defined

as the total suction ψ and consists of the matric suction s and the osmotic suction π, $\psi = s + \pi$. These two suctions are commonly regarded as independent. The matric suction s relates to two main physical processes, capillarity and surface adsorption, and can be calculated as the pore air pressure u_a minus pore water pressure u_w, $s = u_a - u_w$. The principle of capillarity is linked to the surface tension of water, for example that fine soils usually have a higher capillarity than coarser soils. Surface adsorption is a process of taking water molecules into the substance of the clay particles and is strongly related to the type of clay minerals. Soils with high-activity clay minerals (e.g. montmorillonite) are able to maintain high degrees of saturation when their matric suctions are very high. The osmotic suction π can be expressed as a function of the salt concentration in the pore water. It is generally accepted that matric suction s rather than total suction ψ dominates the mechanical behaviour of unsaturated soils, although the dissolved salt in the pore water will result in some changes in the structure of soils (Alonso et al., 1987).

2.4.2 Soil-water retention behaviour

The Soil-Water Retention Curve (SWRC), also known as Soil-Water Characteristic Curve (SWCC), describes the suction behaviour with changes in water content. A range of SWRC expressions have been introduced to predict various soil properties, such as shear strength, permeability, and thermal coefficient (Barbour, 1998). A typical drying-wetting SWRC is shown in Figure 2-19. When the sample is continuously dried from a fully saturated state, the sample initially stays fully saturated as its suction increases, until air begins entering the largest pores at the air-entry point. When the sample begins to desaturate, the degree of saturation will eventually reach the residual value at very high suction and finally stay constant. The SWRC of clays with high plasticity usually has a hysteresis, since the suction or applied stress will rearrange the soil skeleton and

the processes of emptying (or refilling) water from (or into) voids will become not reversible. This means if desaturating a soil after wetting it to point A, the re-drying path will follow the primary drying curve rather than the main drying curve.

The shapes of the SWRC are affected by the soil structure and mineral composition. The soil structure, like the pore size, primarily influences the low suction range (0-100 kPa) of the SWRC. For example, the air entry value of samples prepared using the compaction method is significantly lower than that using the slurry method, as the slurry method results in a smaller largest pore size. The surface adsorption which is mainly determined by mineral composition is more effective at higher suctions in preserving water in soils. For example, soil with a high plasticity index tend to have a large water retention ability.

2.4.3 Stress variables

Single stress variable

The choice of appropriate stress variables is crucial in describing the constitutive behaviour. Early studies widely used a single effective stress, σ', to represent the partly saturated soil behaviour. Bishop (1959) proposed it by combining the total stress σ, pore air pressure u_a, pore water pressure u_w, and a factor dependent on the degree of saturation χ, as shown in Equation 2-3. However, Jennings and Burland (1962) highlighted a key limitation that the single effective stress could not describe the volumetric collapse often observed during wetting in unsaturated soil. This is because suction not only increases the inter-particle contacts but also provides the stabilising effect through the air-water interfaces. Coleman (1962) observed that the χ factor was strongly influenced by soil structure. Khalili and Khabbaz (1998) proposed to define the χ factor as a function of suction (s) with normalisation using the air entry value (s_e), as shown in Equation 2-4. When shear strength predictions based on this approach were

compared with experimental results from 14 published studies, the method showed excellent agreement with the measured values.

$$\sigma' = (\sigma - u_a) + \chi(u_a - u_w) \qquad \text{Equation 2-3}$$

$$\chi = \begin{cases} 1, & for\ s \le S_e \\ (s_e/s)^{\gamma}, & for\ s \ge S_e, and\ \gamma = 0.55 \end{cases} \qquad \text{Equation 2-4}$$

Separate stress variables

Burland and Ridley (1996) proposed to treat matric suction ($u_a - u_w$) and net stress ($\sigma - u_a$) as separate stress variables, as they have different mechanical effects. Suction contributes a stabilising effect, while net stress governs the grain slippage. This approach was adopted by Fredlund and Morgenstern (1977), who extended the Mohr-Coulomb failure envelope to include the suction variable, as shown in Figure 2-20. The shear strength of unsaturated soils is expressed in Equation 2-5, where τ is the shear strength, c' is the effective cohesion, φ' is the angle of friction related to net stress and φ^b is the angle of friction associated with matric suction. Fredlund et al. (1978) suggested that the φ' could be taken as equal to the angle of friction in the saturated condition, and considered it constant across all suction values. Fredlund et al. (1987) showed that φ^b was non-linear with respect to suction. Specially, φ^b equals φ' when the suction is below the air entry value, indicating saturated conditions, but decreases as suction increases, potentially approaching zero at high suction. Délage et al. (1987) observed that both φ' and φ^b could vary. Toll (2000) noted that φ' was influenced by the soil fabric and could be assumed to be equal to that in saturated state.

$$\tau = c' + (\sigma - u_a)\tan\varphi' + (u_a - u_w)\tan\varphi^b \quad \text{Equation 2-5}$$

Combined stress variable

Some authors used a combined stress to handle the effect of air and water phase. Normally, the equation of combined stress is similar to the Bishop's equation (Equation 2-3) using the net stress and matric suction but different weight factor of matric suction. Although suction is inside the combined stress, soil mechanical behaviour does not only depend on it and also depends separately on suction. This respects Burland's (1965) argument that the net stress and suction affected soil differently. Therefore, the combined stress is still not a true effective stress, and models using combined stress still need to include suction as an independent variable to describe unsaturated soil behaviour. Some studies used S_r as weighting factor as shown in Equation 2-6, and this combined stress is called Bishop's stress (Bolzon et al., 1996) or skeleton stress (Jommi, 2000). Murray (2002) proposed to use v_w/v with respect to the total volume, where v_w is the specific water volume and v is the specific volume.

$$\sigma' = (\sigma - u_a) + S_r(u_a - u_w) \quad \text{Equation 2-6}$$

2.4.4 Critical state framework for unsaturated soils

The critical state framework was originally established to describe the volumetric and shear behaviour of saturated soils (Schofield and Wroth, 1968). Building on this, Alonso et al. (1987) introduced an elasto-plastic model for unsaturated soils in terms of the variables q, $p - ua$, $ua - uw$, v and S_r. This work led to the development of an unsaturated critical state framework, named as the Barcelona Basic Model (BBM) (Alonso et al., 1990). It was further modified by many other researchers (Wheeler and

Sivakumar, 1995, Délage and Graham, 1995, Cui and Délage, 1996). A detailed discussion of unsaturated soil mechanics based on the critical state concept is presented in the following sections.

Elasto-plastic model

Alonso et al. (1987) proposed a conceptual framework to describe the volumetric behaviour of partly saturated soils under loading and collapse based on the theory of hardening plasticity. The Loading-Collapse (LC) yield surface can be projected onto the plot of suction s and net stress p'' as the yield locus, as shown in Figure 2-21, where $P'' = \frac{1}{3}(\sigma_1 + 2\sigma_3) - u_a$. For the region within the yield surface, both changes in suction and net stress will cause elastic behaviour and induce reversible (elastic) swelling or shrinkage. Any state point on the yield surface will cause irreversible (plastic) compressible volumetric strains as the state moves outside this locus. For example, sample P_{01} that already initially yielded on locus A_1B_1 will have its yield locus expanded to locus A_2B_2 after either loading at constant suction (Path L) or wetting at constant net stress (Path C). The plastic strains induced by Path L and Path C are the same, which is also equal to that induced by compression along the NCL (from p_{01}^* to p_{02}^*) for the corresponding saturated sample (zero suction). Figure 2-22 illustrates the method of deriving the yield locus (LC) from suction-controlled compression tests, which is to draw the points on the same elastic path from the constant suction compression curves.

The volumetric behaviour predicted by the conceptual framework is illustrated in Figure 2-23, involving loading at constant suction (Paths L1, L2 and L3) and wetting at constant net stress (Paths C1, C2 and C3). It can be seen from Figure 2-23 (b) that the yield stress increases as suction increases (from s_3 to s_1). If the sample is unloaded

following U3 after initial yield, only part of the strains will be recovered by swelling. Regarding the wetting paths, the amount of collapse (the change of specific volume) depends on the applied net stress, as shown in Figure 2-23 (c). Path C1 only induces swelling behaviour (increasing specific volume), since the sample is wetted at low net stress within the elastic zone. Sample C2 experiences first some swelling and then develops plastic compressive strains when the wetting path reaches the yield surface. Sample C3 is wetted at the highest net stress, which is very close to the yield stress, so it experiences the largest collapse with only plastic strains.

Barcelona Basic Model (BBM)

Alonso et al. (1990) proposed mathematical expressions for the elasto-plastic model for unsaturated soils under some assumptions. The expression of the Normal Compression Line (NCL) of unsaturated states evaluates the volumetric change in the $v - ln(p - u_a)$ plane, as shown in Equation 2-7. Under constant suction, v was assumed to change linearly with the logarithm of net mean stress $(p - u_a)$ during expansion of the LC yield curve. The intercept $N(s)$ and slope $\lambda(s)$ of the NCL are both defined as functions of suction, with a suction increase leading to a decrease of slope and increase of intercept. Alonso et al. (1990) also assumed a linear relationship between the strength and the mean net stress, as shown in Equation 2-8. Under constant suction, the yield surface was assumed to be elliptical, resulting in a constant stress ratio M, equal to that for saturated soils. Sivakumar (1993) later improved the BBM by allowing the critical state stress ratio (M) to vary with suction, which adds flexibility to the yield curve shape, as illustrated in Figure 2-24.

$$v = N(s) - \lambda(s) \ln(p - u_a) \qquad \text{Equation 2-7}$$

$$q = M\,(p - u_a) + p(s) \qquad \text{Equation 2-8}$$

Critical state parameters for unsaturated soils

Toll (1990) argued that the critical state stress ratio (M) was not constant for all suction conditions, and that the variation of critical state parameters was influenced by the soil fabric. Toll (1990) defined the critical states using five parameters in the $v-(p-u_a)$ plane and in the $q-(p-u_a)$ plane, as shown in Equation 2-9 and Equation 2-10. These parameters were expressed as functions of the degree of saturation for both a lateritic gravel (Toll, 1990) and a residual sandy clay (Toll and Ong, 2003).

In the $v-(p-u_a)$ plane, the intercept Γ_{aw} represented the v when both stresses equal unity. Assuming the soil is saturated at such low suction values, Γ_{aw} is taken to be equal to the intercept for the saturated soil. Figure 2-25 (a) shows that the suction contribution to the volumetric change represented by λ_w decreases as S_r reduces, while the influence of net stress λ_a becomes more significant. According to the capillary principle, water drains first from the largest pores as suction increases. At low S_r, water is therefore retained mainly in the fine pores within soil packets, while the larger inter-packet pores are filled with air. As a result, suction no longer significantly contributes to volume change, and small changes in net stress can cause large deformation through rearrangement of the soil fabric.

$$v = \Gamma_{aw} - \lambda_a \ln(p-u_a) - \lambda_w \ln(u_a-u_w) \qquad \text{Equation 2-9}$$

$$q = M_a(p-u_a) + M_w(u_a-u_w) \qquad \text{Equation 2-10}$$

Figure 2-25 (b) shows that the volumetric parameters follow a trend similar to the critical state stress ratios in that the suction related factor M_w decreases as S_r reduces, while the net stress component M_a becomes dominant. This is because when water

remains only within the soil packet, suction no longer acts between packets where shearing occurs. As a results, the soil packets may interact like dry grains, and the shear behaviour becomes increasingly governed by the net stress factor, which reflects inter-packet contact and friction.

2.4.5 Case study of unsaturated mechanical behaviour

Jotisankasa (2005) investigated the loading and collapse behaviour of an unsaturated compacted silty clay. His study is used as a case study here due to his extensive and thorough investigations. The volumetric behaviour of constant water-content oedometer tests and their estimated loading-collapse (LC) curves through the yield points are illustrated in Figure 2-26 (a) and (b). Samples with the low water content and high suction have relatively high yield stresses. The contours of constant suction isotropic Normal Compression Lines (NCLs) from triaxial tests are shown in Figure 2-26 (b). The NCLs for suctions between 10kPa and 100kPa are likely to converge towards the saturated NCL. This is a similar conclusion to Alonso et al. (1987) shown in Figure 2-22 (a). Figure 2-27 illustrates the results of the shearing experiments. It is evident that the samples with higher initial suctions are stiffer and reach higher peak deviatoric stresses, as shown in Figure 2-27 (a). The variations in volumetric strain during shearing are given in Figure 2-27 (b). The samples with lower initial suctions have a higher tendency to compress first and then tend to dilate less. Figure 2-27 (c) shows their failure envelopes at different cell pressures. The envelopes are evidently non-linear and may be characterised as nearly bilinear within suctions up to 1000 kPa. These two failure envelopes agree with the failure envelope model of Gan and Fredlund (1996).

2.5 Unsaturated experimental techniques

As previously stated, soil suction is a critical variable. It is one of the most significant determinants for the mechanical behaviour of partially saturated soils. Measuring or controlling suction is thus crucial when testing partially saturated soils. For saturated soils, the changes of water volumes are the same as the changes of total sample volume and are directly linked to the specific volume. In comparison, for unsaturated soils, extra devices are needed to measure the changes of total volume, due to the compressible pore air. Therefore, this section reviews suction measurement methods, suction control systems, and total volume measurement systems used in unsaturated tests.

2.5.1 Suction measurements

Suction measurements can be classified into direct and indirect methods (Ridley & Wray, 1996). For direct methods, the relevant quantity of the pore water energy or tensile stress is measured. The indirect methods measure other parameters linked to suction by calibrated relationships, such as relative humidity, resistivity, conductivity and moisture content.

Tensiometer

Bubble formation or cavitation will typically occur under negative water pressure in traditional pressure measuring systems, making the system unable to measure suction accurately. Ridley and Burland (1999) invented the suction probe, or Imperial College tensiometer, to measure directly the negative pore water pressure at atmospheric air pressure. As shown in Figure 2-28, it involves a 15 bar High Air Entry (HAE) ceramic porous stone, a small size water reservoir and pressure measurement device.

The porous stone serves as an interface between the soil and the water reservoir. It prevents pore air in the soil from entering the water reservoir but still allows water to flow through. The air-entry value of a porous stone is the maximum matric suction it can resist before pore air starts to enter the reservoir. This value is inversely proportional to the narrowest pore diameter within the porous stone. The low air entry porous stone normally has large pore sizes, giving air-entry value of around 20 kPa. The HAE porous stone has much smaller pores and therefore a higher air-entry value.

The suction probe can directly measure the suction so that it can be incorporated into the other apparatus to measure continuously suction during tests. The key limitation of the tensiometer with 15 bar porous stone is that suction values below about 100 kPa cannot be measured accurately.

Filter paper technique

Suction can be measured indirectly using the filter paper technique, which covers a wide range from 10 kPa to 100 MPa. As shown in Figure 2-29, dry filter papers are placed in direct contact with a soil sample inside an air-tight container. Over about one week, moisture equilibrium will be established between the sample and papers. Subsequently, the water content of the filter paper is measured. The suction of the sample was calculated using a calibration curve provided in ASTM D5298-16 for relationship between water content and suction of the specific filter paper brand.

2.5.2 Suction control systems

Axis translation technique

To address cavitation when measuring negative pore water pressure, Hilf (1956) proposed the axis-translation technique. This method involves raising the pore water pressure u_w equally with the pore air pressure u_a to a positive value while the suction

remains constant. Based on this principle, the pore water pressure can then be measured directly by the standard pressure transducer. This technique can be adopted in a triaxial apparatus, as schematically illustrated in Figure 2-30. The pore water pressure can be applied and measured at the base of the apparatus through an HAE porous stone, which is the same as that of the tensiometer. The pore air pressure can be applied through a low air-entry porous stone at the top of the sample, to keep the pore water pressure above atmospheric pressure (Javadi & Snee, 2001).

However, dissolved air could still pass through the HAE porous stone and form gathered air bubbles underneath it, which could result in severe errors when measuring the water volume changes. To solve this problem, Fredlund (1975) proposed a flushing system, the diffused air volume indicator (DAVI), to flush out the bubbles and measure the volume of the diffused air. As shown in Figure 2-31, it consists of a Lucite exit tube and a 10 cm^3 graduated burette, which are connected through a U-tube at the bottom. The DAVI should be connected to the base platen of the equipment with a constant water pressure difference of less than 70 kPa to allow flushing without causing cavitation. When water flushing through the base platen, any diffused air will accumulate in the burette and the extra water will flow into Lucite exit tube. The volume of diffused air can then be read from the burette.

Axis translation has been commonly used for directly controlling suction in research laboratories. However, this technique is usually valid when the degree of saturation is less than 80%. In the case of a higher degrees of saturation, there is no air permeability, and the increase of air pressure will result in volumetric strains (Bocking & Fredlund, 1980).

Osmotic technique

The suction control system using the osmosis technique was first developed by Kassiff and Ben Shalom (1971) for an oedometer apparatus. As shown in Figure 2-32, a typical oedometer apparatus with an osmotic technique incorporates a semi-permeable membrane to separate the sample and a macromolecular aqueous solution, such as Polyethylene Glycol (PEG). The principle is to allow water to pass through the membrane by osmosis until the soil suction equals the osmotic potential of the solution, and the osmotic potential can be controlled by the molar concentration of the solution. The osmotic system has the advantage of being able to perform tests at atmospheric air pressure and negative water pressure. An appropriate semi-permeable membrane can resist biodegradation in the PEG solution and sustain a constant suction of 750 kPa for two weeks (Cunningham, 2000; Colmenares, 2002). However, Colmenares (2002) found the suction in an oedometer apparatus was hard to control due to the difficulty in maintaining the contact between the granular material and the membrane. Cunningham (2000) also failed to control the suction when testing a reconstituted silty clay in triaxial shearing tests.

2.5.3 Volume measurement systems

The total volume change of an unsaturated sample includes the volume changes of both air and water. Due to the compressibility of the air phase, rather than measuring the natures of the two phases separately and calculating their sum, the total volume change is typically measured directly by global or local measurement methods.

Global measurements

One simple method for global measurement is to use laser scanner technique or photogrammetry technique, which require costly devices and sophisticated installation. Another way is to measure the volume change of the surrounding cell fluid. This was

first developed by Bishop and Donald (1961) in a double-walled cell (Figure 2-30), which can improve the measurement errors from the deformation of the cell chamber caused by the cell pressure. However, the double-walled cell still has two main limitations. Firstly, the cell may expand or contract as a result of temperature fluctuations, cell pressure variations and creep deformations. Secondly, the Perspex, commonly adopted as the material of the inner cell, can absorb water.

Local measurements

Local measurements determine the strains at certain locations on the samples. The main advantage of local measurements is accurate stiffnesses in the small strain range (Burland, 1990). Examples of local measurement devices are shown in Figure 2-33, namely the electrolevel inclinometer (Burland & Symes, 1982) and LVDTs (Cuccovillo & Coop, 1997) for measuring the axial strains, and an LVDT radial belt (Klotz & Coop, 2002) for measuring the radial strains. These strain-measuring devices all involve being attached directly onto the samples and monitoring the strains directly between two fixed points. Since the strain is measured between two fixed points, the shape of the samples has to be assumed, such as a right cylinder or a barrelled shape (Germaine & Ladd, 1988).

2.6 Microstructure

2.6.1 Soil structure

Intrinsic properties refer to properties of fully destructured soils and describe the inherent properties independent of natural states. These can be described by the Intrinsic Compression Lines (ICLs), which are the Normal Compression Lines (NCLs) of the fully destructed soils (Burland, 1990). Soil structure commonly is believed to consist of fabric and bonding, which affect the arrangement of soil particles, profoundly

affecting soil mechanical behaviour. The ICL can work as a reference state to quantify mechanical properties and assess the in-situ state for structured soils (Cotecchia & Chandler, 2000).

2.6.2 Normalization parameters

Burland (1990) proposed the void index I_v to highlight structure effects for intact clays through normalizing one-dimensional compression data, as shown in Equation 2-11. The parameters e^*_{100} and e^*_{1000} are the void ratios on the ICL at 100 kPa and 1000 kPa effective stresses, respectively, as shown in Figure 2-34 (a), while parameter C^*_c is the intrinsic compression index and the gradient of the one-dimensional ICL, as shown in Figure 2-34 (b). Thus, the normalized one-dimensional ICLs for various reconstituted clays define an almost unique line with two overlapping points but sometimes with slight differences of curvature as shown in Figure 2-34 (c) and (d). However, the void index of Burland (1990) can only be applied to the one-dimensional ICLs. A new parameter, normalized specific volume v_n generally defined by the isotropic ICL, was therefore proposed by Coop and Cotecchia (1995), as shown in Equation 2-12. The parameters λ^* and N^* are the gradient and the intercept (at1 kPa) of the ICL in the plane of specific volume and effective stress, which uses the double logarithmic scale ($lnv - lnp'$) to avoid the curvature of the ICL. This parameter allows the comparison for the isotropic and one-dimensional compression data and the shearing data. To identify further the structure effects, stress paths in shearing tests can be normalized by an equivalent pressure taken on the CSL, p'_{cs}, defined as Equation 2-13, assuming the CSL is unique for intact and reconstituted samples. The parameters $\lambda^*$and $\Gamma^*$are the gradient and the intercept (at 1 kPa) of the CSL in the $lnv - lnp'$ plane.

$$I_v = \frac{e - e^*_{100}}{e^*_{100} - e^*_{1000}} = \frac{e - e^*_{100}}{C^*_c}$$ Equation 2-11

$$v_n = exp\left(\frac{ln\, v - N^*}{\lambda^*}\right)$$ Equation 2-12

$$p'_{cs} = exp(\frac{\Gamma^* - ln\, v}{\lambda^*})$$ Equation 2-13

2.6.3 Stable and metastable structures

Since methods of directly measuring the fabric and the bonding are still not developed, a qualitative assumption is suggested to describe these two components, which is that the fabric provides a stable element to resist destructuration, while the bonding tends to be metastable (Coop et al., 1995). The schematic diagrams, shown in Figure 2-35, explain the effects of the fabric and bonding on the mechanical behaviour from an idealised compression and shearing behaviour for a natural clay, in which parameters v_n and p'_{cs} (p^*_{ie} in the figure) are used to highlight the effects of structure. Some studies on the microstructure of natural clays with stable structures indicated that some structural elements may remain even after very large strains or reconstituting (e.g. Fearon & Coop, 2000). Therefore, the state paths will not converge to the ICL or the CSL but stay in stable states as observed in the figure.

2.6.4 Experimental methods

There are several methods that have been used in the study of microstructure, for example, scanning electron microscopy (SEM) tests and mercury intrusion porosimetry (MIP) tests. The work by Jiang et al. (2014) on clayey loess is presented here as a case study, as it involved a detailed investigation and focuses on loess, which is also examined in this study.

MIP tests

MIP tests are widely used to measure the pore size distribution. By increasing pressure progressively, mercury is allowed to penetrate into the voids of the sample, from the larger voids to the smaller voids. The cumulative volume of mercury in a sample is continuously monitored, which is related to the cumulative pore volume. The pore size density can be calculated by deriving the cumulative pore volume with respect to pore diameter. This method assumes a cylindrical geometry of pores and Laplace's capillarity law for simplification. It should be noted that there are measurable minimum pore radii for MIP tests, due to the pressure limit of the apparatus.

Jiang et al. (2014) presented the pore size distributions for natural and reconstituted clayey loess samples using cumulative pore volume and pore size density, as shown in Figure 2-36. Two peak pore size densities were detected for both samples and defined as the inter-aggregate pore family and the intra-aggregate pore family. Both samples have nearly identical pore density and pore size for pores with radii less than 5 μm, due to the similar shapes of the cumulative and density curves. Figure 2-36 (b) provides the pore size distributions after 600 kPa isotropically consolidated triaxial tests for natural and reconstituted samples, which is well beyond the 200 kPa structural yield stress found in the oedometer tests. The reconstituted sample after testing had similar populations for the dominant macro-pores (inter-aggregate) and micro-pores (intra-aggregate) as the initial sample. In comparison, the populations of the dominant macro-pores for the intact sample decrease significantly after the test, which probably indicates that the metastable bonds in the natural sample may be destroyed during testing.

SEM tests

Scanning electron microscope (SEM) tests use an electron gun to emit a focused beam of electrons onto the surface of the soil sample under vacuum. The electrons interact with atoms of the samples, producing surface topography images.

Jiang et al. (2014) conducted SEM studies on the microstructure of natural and reconstituted clayey loess samples. The natural sample is characterised by connected assemblages and large pores (Figure 2-37 (a)), compared with the relatively smaller and uniform pores in a reconstituted sample (Figure 2-37 (b)). This indicates a more homogeneous fabric in the reconstituted sample in comparison with the natural sample, which probably results from the cementation bonds in the natural sample. As illustrated in Figure 2-37 (c) and (d), there are clear bonds between the particles or aggregates, which are the cementation bonds of carbonate and clays (Rogers et al., 1994).

Some other important structures have been found from SEM images. For natural samples, the macro-pores could be easily damaged upon compression and shearing loading by stresses larger than the yield stress (Jiang et al., 1999) and the aggregates then tend to be well-distributed granules after the tests (Jiang et al., 2014). However, the intra-aggregate pores (micro-pores) remain unchanged for both the natural and reconstituted samples (Cai & Dong, 2011). The structural anisotropy is characterised by a horizontal particle-orientation for both natural and reconstituted samples (Jiang et al., 2011).

2.7 Case study of transitional behaviour on saturated loess

Xu and Coop (2017) investigated the transitional behaviour of saturated silty loess in comparison with two other non-transitional loess soils. As their investigation was thorough and the transitional loess matches the materials studied in this present, their

work is used here as a case study. For convenience, some of the figures are repeated from earlier section of this chapter.

2.7.1 Compression behaviour

Compression curves

Nocilla et al. (2006) suggested that the clay content of soils could be a critical consideration in determining the existence of transitional modes. Xu and Coop (2017) obtained a similar conclusion for loess soils. Three types of loess soils from the northwest China were investigated, including clayey loess at depths of 20m and 50m retrieved from Xi'an with 20% clay (Xu & Coop, 2016), finer graded silty loess at a depth of 30m retrieved from Lanzhou with 10% clay (Xu et al., 2016) and a coarser and less well-graded silty loess at depths of 5m and 10m retrieved from Lanzhou with 5% clay (Xu & Coop, 2017). As shown in Figure 2-38, the existence of unique ICLs changes from clear to non-existent as the clay content increases from clayey loess to silty loess. Xu and Coop (2017) calculated the m factor to quantify transitional behaviour for the silty loess, as shown in Figure 2-39. The authors suggested the intact soil probably had a higher degree of transitional behaviour than the corresponding reconstituted soil, which is consistent with the finding of Ponzoni et al. (2014), as discussed earlier.

Effects of natural structure

The use of the void index I_v can help to highlight the relative effects of natural structure (Burland, 1990). Although the void index I_v method was originally proposed for sedimentary clays, Xu and Coop (2017) suggested that it still worked well for silty soils. A curved ICL for a silty loess soil was obtained by Xu and Coop (2017), the curvature of which is slightly smaller than that for the finer silty loess (Xu et al., 2016) and clayey loess (Xu & Coop, 2016) and is the opposite direction of that proposed by Burland

(1990), as shown in Figure 2-40. Since there is no unique ICL for transitional soil, it is difficult to quantify the structure effects for them (Ferreira & Bica, 2006). For a transitional silty loess, Xu and Coop (2017) proposed to use the ICL of the reconstituted specimens with similar specific volumes to the intact samples at the stress of 20 kPa. Although the choice of stress is arbitrary, the results still provided some useful information for comparison.

Natural structure effects for loess were highlighted by Xu and Coop (2017). As shown in Figure 2-40, the compression paths of intact loess soils cross the ICL and then tend to converge towards them. The natural structure effects become stronger as the loess becomes siltier. This was concluded based on the variations of intact compression paths, which included the distance between the curves to the ICL, the initial gradient before yield, the existence of clear yield point and the rate of destructuration after yield. The SCL of Burland (1990) introduced in Figure 2-40 is located quite far from the yield points and in-situ total vertical stresses of the transitional silty loess. On the contrary, those of the non-transitional finer silty and clayey loess are located quite close to the SCL (Xu & Coop, 2017). These indicate that the natural structures of the non-transitional clayey and finer silty loess probably have a similar common origin. The different mechanical behaviour of the silty loess suggests a different structure from the clayey and finer silty loess.

2.7.2 Shearing behaviour

Stress-strain behaviour

Xu and Coop (2017) conducted a series of shearing tests on transitional silty loess, comparing with the shearing behaviour of non-transitional clayey loess (Xu & Coop, 2016). As shown in Figure 2-41, the reconstituted and intact silty loess have the same gradient of CSL ($M = 1.395$), which is slightly higher than that for the clayey loess

($M = 1.25\ and\ 1.35$ for clayey loess at depths of 50m and 20m respectively). The stress-dilatancy relationships for silty and clayey loess shown in Figure 2-42 present different behaviours. The intact and reconstituted samples of silty loess have a similar behaviour, indicating a small influence of structure.

Shearing paths

The CSLs were identified from the groups of samples with similar v_i. Non-convergent CSLs have been found for both intact and reconstituted specimens for transitional silty loess and are highly dependent on the v_i of the specimens. As shown in Figure 2-43 (a), the CSLs for transitional silty loess are curved and much steeper than those for non-transitional clayey loess, which is likely to be the effect of a fabric component of structure. For simplicity, Figure 2-43 (b) and (c) assumed straight parallel CSLs for reconstituted and intact samples respectively, ignoring the curvature of the CSLs. These parallel CSLs indicate a clear and strong transitional mode. As shown in Figure 2-44, the P values confirm the strong transitional behaviour for the silty loess, and the intact samples probably have a higher degree of transitional behaviour ($P = 0.97$) than the reconstituted samples ($P = 0.34$).

Effects of natural structure

To identify structure effects, Figure 2-45 shows the normalized CSLs of the intact specimens (CSLi) and reconstituted specimens (CSLr) for the transitional silty loess using v_n (Xu & Coop, 2017). All the data were normalized using the isotropic ICL of group A illustrated in Figure 2-43. Although it is a slightly arbitrary choice for a transitional soil, the reconstituted samples for the chosen ICL should have a similar initial specific volume v_0 to the intact specimens. The normalized CSLs for intact and reconstituted specimens were obtained by grouping samples with a similar v_0 and plotting a normalized CSL for each group. Compared with the two unique CSLs for the

non-transitional clayey loess (Xu & Coop, 2016), a series of parallel normalized CSLs for the silty loess illustrated a clear transitional behaviour.

Structure effects can be seen from a comparison of group A reconstituted samples and group Y intact samples, which are considered to have a similar v_0. The isotropic compression paths of group Y reach outside the isotropic ICL of group A and then slowly converge toward it. The difference between the CSLi of group Y and the CSLr of group A is relatively small, compared with the non-transitional clayey loess which shows much clearer differences between the intact and reconstituted CSLs.

2.8 Literature review overview

2.8.1 Current research gaps

The mechanical behaviour of most soils can generally be described within the critical state framework. However, it has been found that soils with transitional behaviour have non-unique Normal Compression Lines (NCLs) and Critical State Lines (CSLs) for samples with different initial densities. This presents challenges to determine accurate and representative NCLs and CSLs for transitional soils. Since the characteristics of the NCL and CSL are critical for understanding various soil properties (e.g. compressibility, contraction or dilatancy, stability and liquefaction susceptibility), precise identification of the NCLs and CSLs is crucial for both research and engineering practice. For instance, the stability analysis of tailings dams in current engineering practice generally relies on the CSL determined from reconstituted tailings samples.

Although several soils, typically soils with mixed mineralogies or mixed gradings, have been identified to exhibit transitional behaviour, the characteristics of such behaviour in saturated tailings and loess soils remains incomplete. Additionally, the complex mechanics of unsaturated soils suggest that transitional soils in unsaturated states may

exhibit different modes of transitional behaviour. However, no studies have been conducted in this area so far. This highlights the need for comprehensive research into the transitional behaviour of both saturated and unsaturated soils.

Soil structure is believed to consist of fabric as a stable element and bonding as a metastable part, which profoundly affects the particle arrangement and the mechanical behaviour. Although the exact causes of transitional behaviour are still unclear, it is hypothesized that some stable structural elements persist even under large strains or reconstitution. Thus, to study the reasons for transitional behaviour, it is necessary to link microstructure to the macroscopic mechanical response and to investigate the effect of the microstructure.

Since the matric suction is the critical variable for unsaturated mechanical behaviour, it is necessary to understand the mechanical effect of suction on unsaturated soils with transitional behaviour. The Soil Water Retention Curve (SWRC) is essential for understanding suction behaviour in unsaturated samples. Filter paper tests can be used to measure indirectly the SWRC, and tensiometers equipped into a mould can be used to measure directly the SWRC. For suction measurements during mechanical tests, a tensiometer can be incorporated into the equipment. Alternatively, the axis translation technique can be used to avoid cavitation issues when measuring negative pore water pressure with a standard pressure transducer. The equipment using axis translation technique requires features such as independent regulation and measurement of pore air and pore water pressures, a pedestal with a High Air Entry porous stone and a flushing system, and a total sample volume change measurement system.

2.8.2 Research objectives

The primary objective of this study was to characterise the transitional behaviour of saturated and unsaturated soils. This was broken down into two sub-objectives:

Characterizing transitional behaviour in saturated soils

The first objective was to characterise the transitional behaviour of saturated soils. This was done by performing oedometer tests on saturated samples up to high stress levels in order to identify transitional behaviour through a family of NCLs. A series of triaxial tests followed to investigate the detailed transitional behaviour for the saturated soils through the non-unique NCLs and CSLs. Additionally, microstructure studies were carried out to help the interpretation of the mechanical responses.

Characterizing transitional behaviour in unsaturated soils

The second objective was to investigate the transitional behaviour of the same soils under unsaturated states. Filter paper tests were used for SWRC measurement. Unsaturated triaxial apparatus using the axis translation technique was designed to study the behaviour of unsaturated soils, comparing their behaviour in a saturated state. A series of constant suction compression and constant water content shearing triaxial tests were conducted to define the non-unique NCLs for given suction and non-unique CSLs corresponding to the suction attained at the end of each test. The microstructure of the unsaturated soils was also studied to help explain their mechanical behaviour.

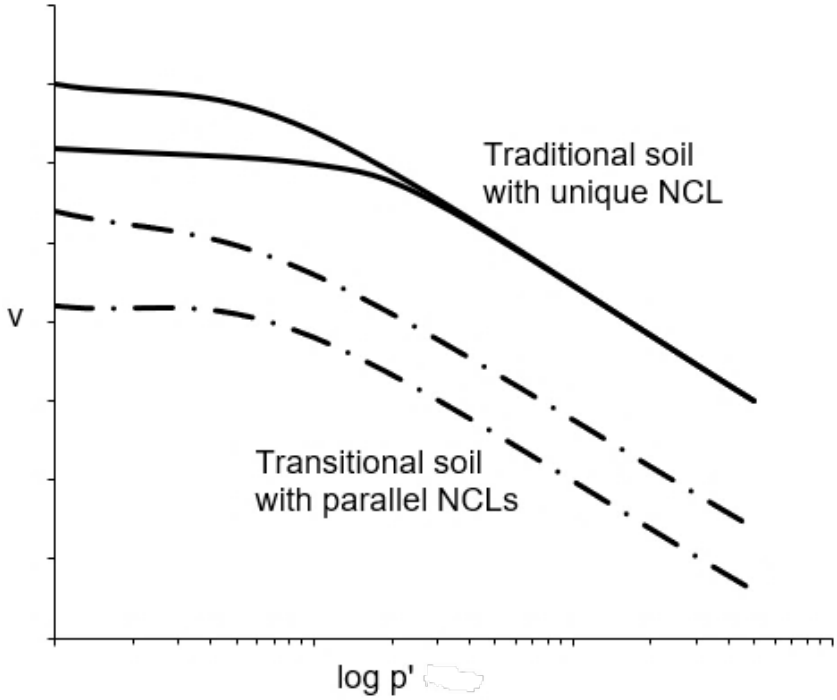

Figure 2-1 Compression behaviour of soil with transitional behaviour compared with traditional soil following critical state framework. (*V in figure is specific volume v.)

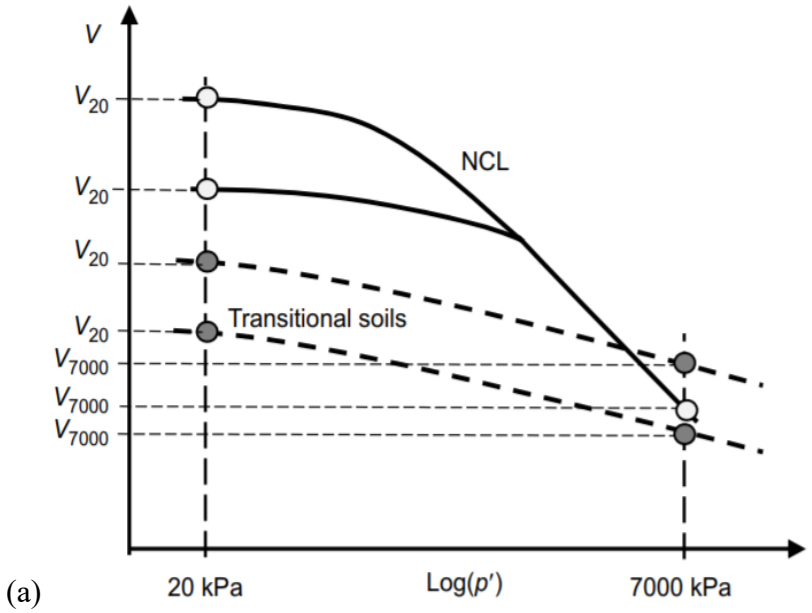
V
V_{20}
V_{20}
V_{20}
V_{20}
V_{7000}
V_{7000}
V_{7000}
NCL
Transitional soils
20 kPa
Log(p')
7000 kPa

(a)

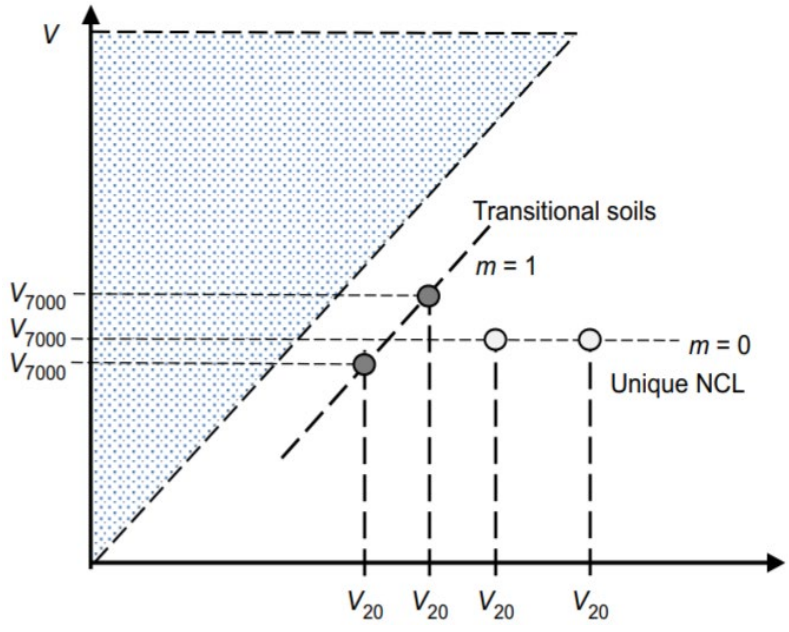
V
Transitional soils
m = 1
V_{7000}
V_{7000}
V_{7000}
m = 0
Unique NCL
V_{20}
V_{20}
V_{20}
V_{20}

(b)

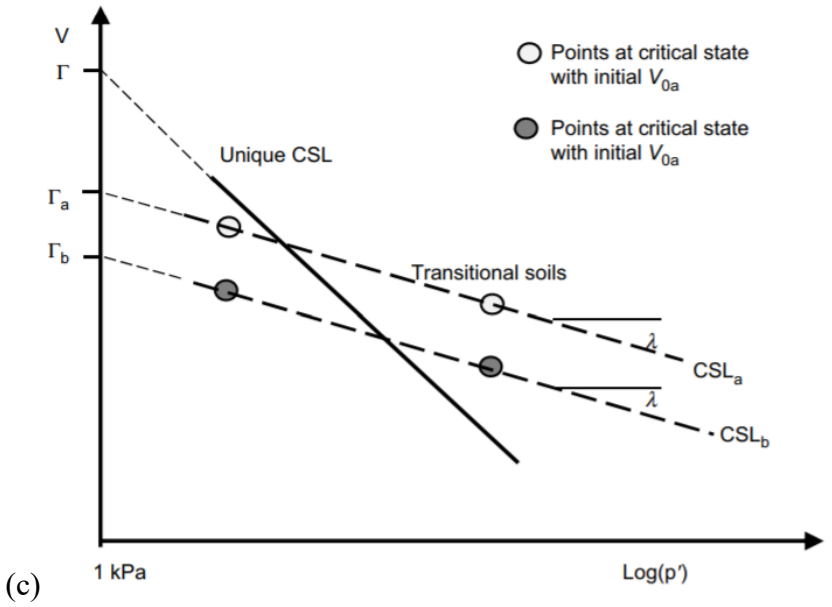

(c)

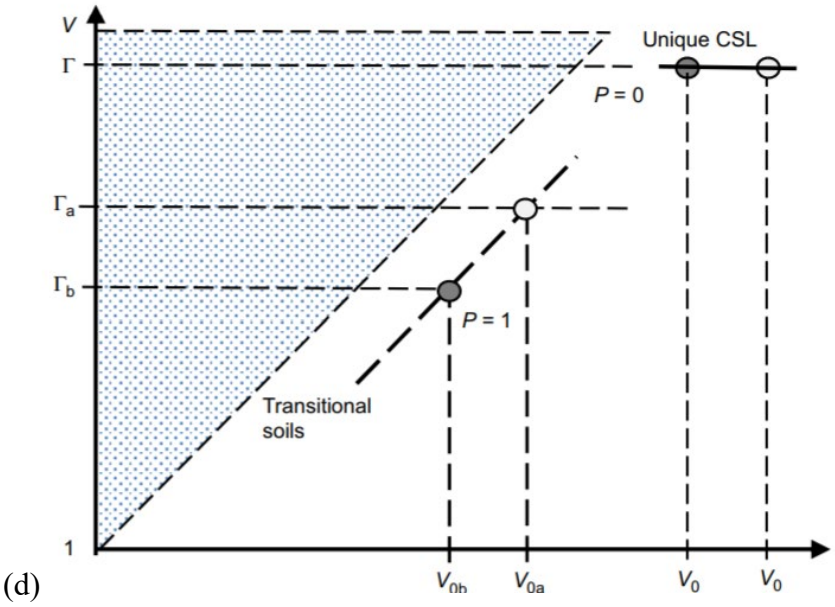

(d)

Figure 2-2: Schematic diagrams of (a) NCLs and (b) calculation of m value, and (c) CSLs and (d) calculation of P value (Ponzoni et al., 2014). (*V in figures is specific volume v.)

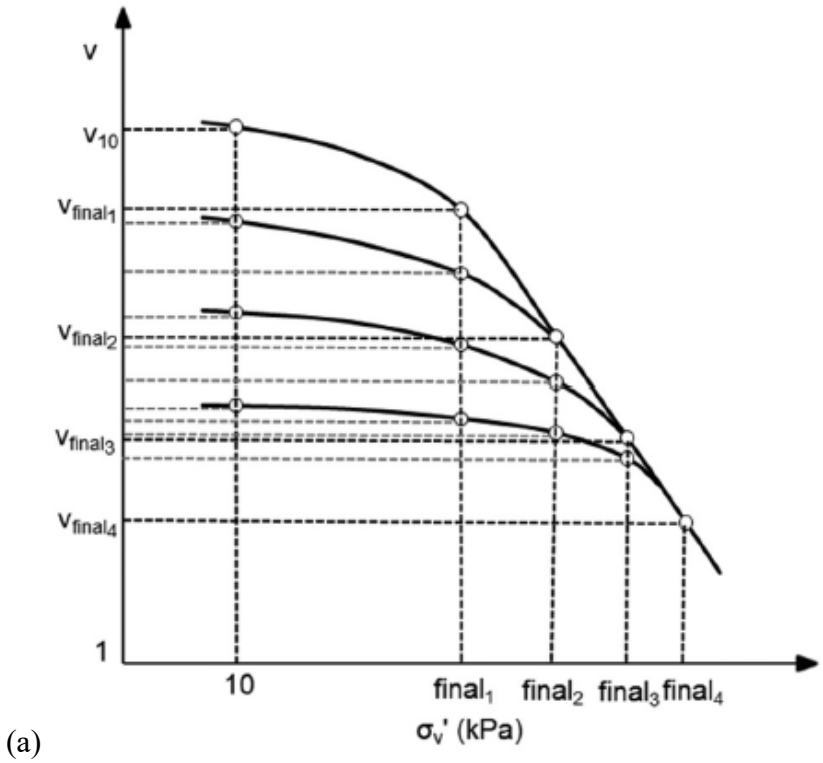

(a)

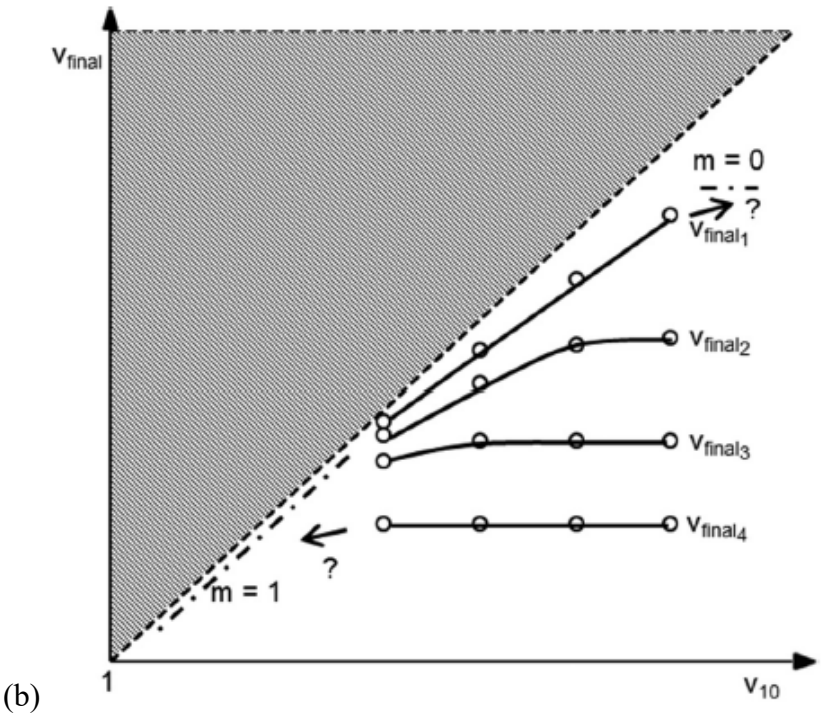

(b)

Figure 2-3: Schematic representation of the compression line illustrating the evolution of m values across varying stress levels (Li & Coop, 2019). (*V in figures is specific volume v.)

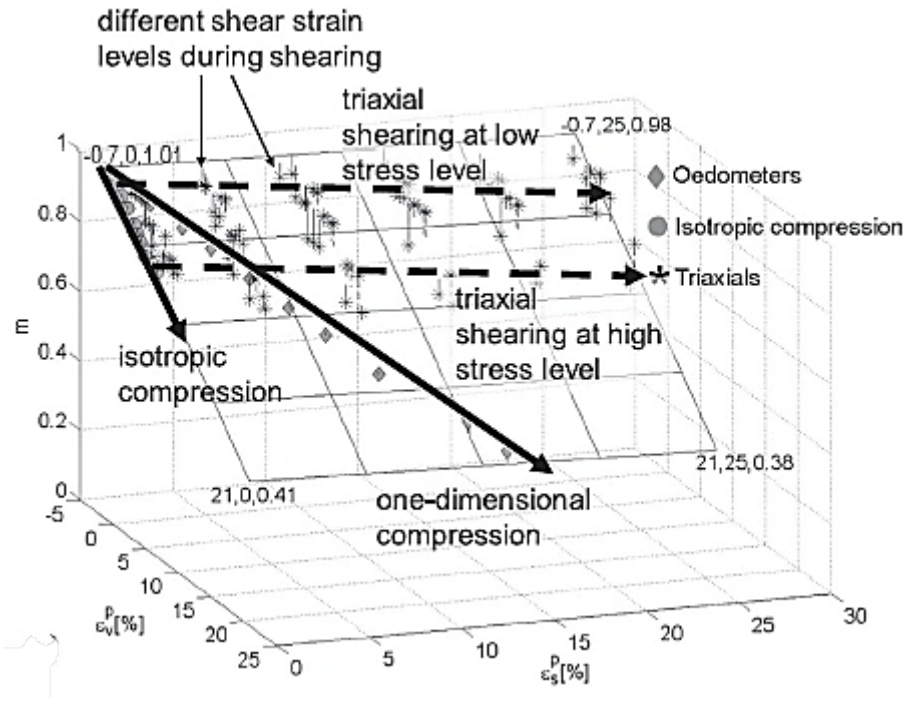

Figure 2-4: Convergence surface based on the m factor of crushed limestone (Todisco & Coop, 2019).

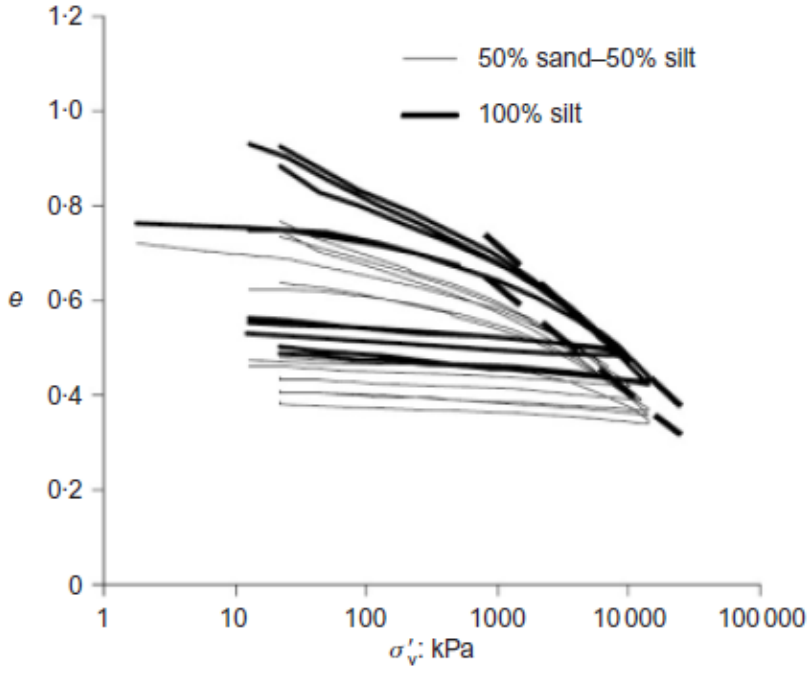

Figure 2-5: Oedometer compression curves with dotted lines marking the one-dimensional NCLs for soils from Stava tailings (Carrera et al., 2011).

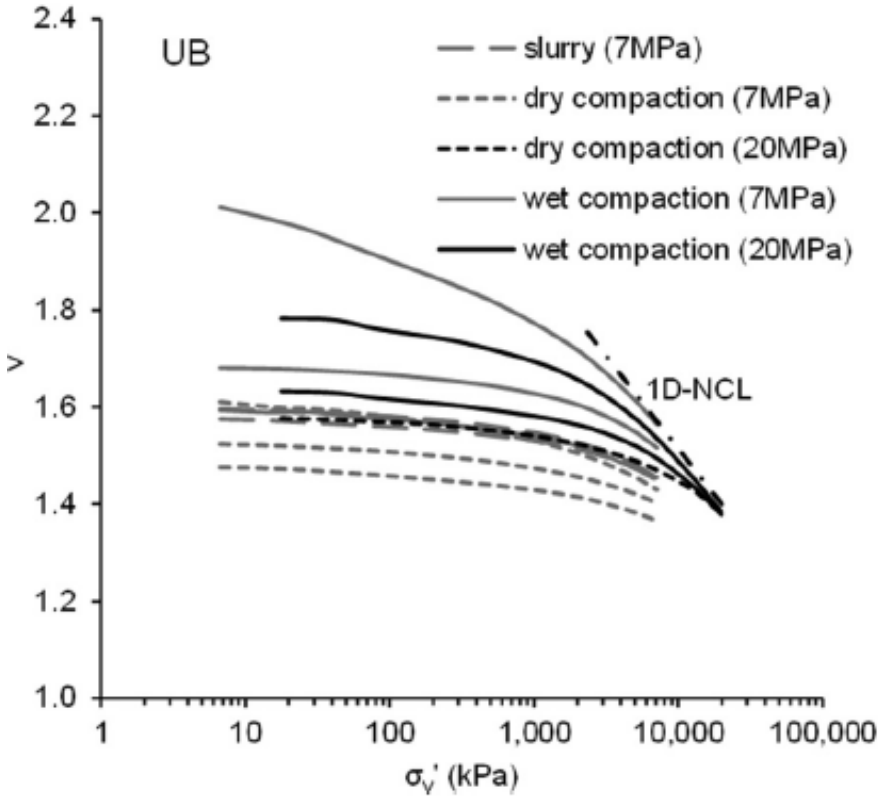
UB
slurry (7MPa)
dry compaction (7MPa)
dry compaction (20MPa)
wet compaction (7MPa)
wet compaction (20MPa)
1D-NCL
v
σv' (kPa)
2.4
2.2
2.0
1.8
1.6
1.4
1.2
1.0
1
10
100
1,000
10,000
100,000

(a)

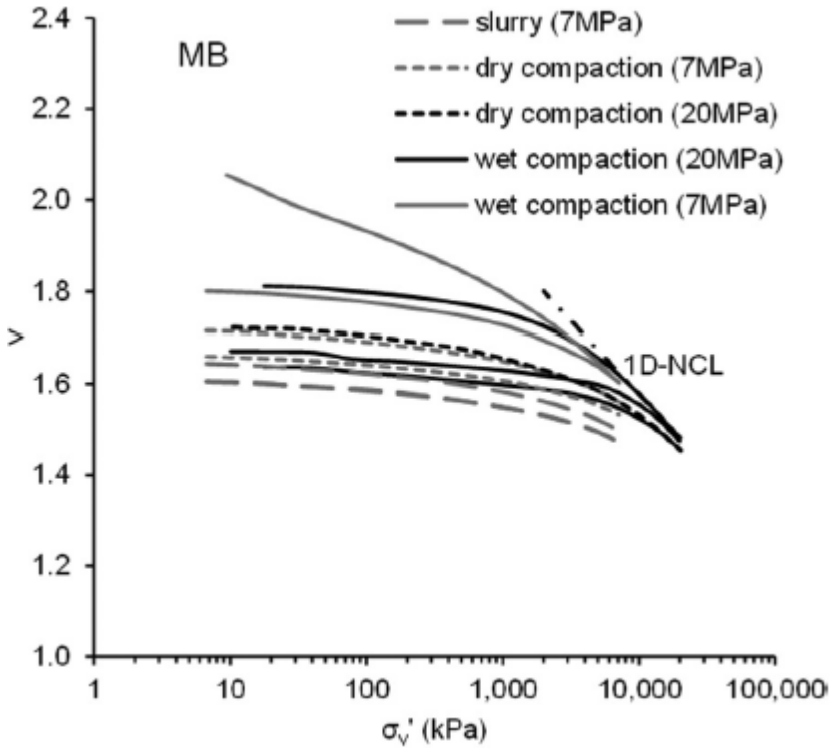
MB
slurry (7MPa)
dry compaction (7MPa)
dry compaction (20MPa)
wet compaction (20MPa)
wet compaction (7MPa)
1D-NCL
v
σv' (kPa)
2.4
2.2
2.0
1.8
1.6
1.4
1.2
1.0
1
10
100
1,000
10,000
100,000

(b)

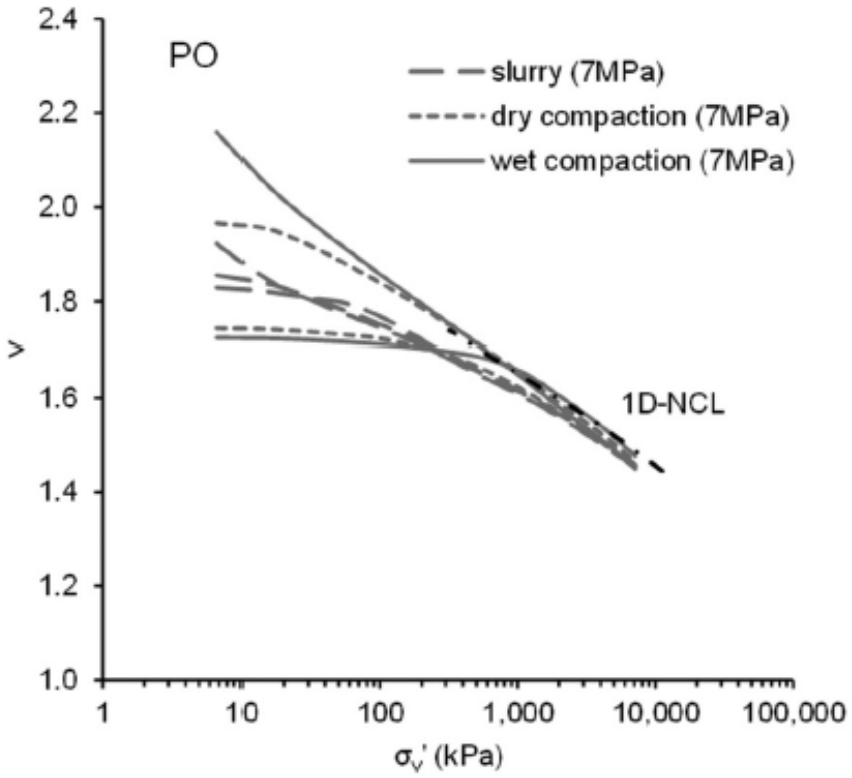

(c)

Figure 2-6 Compression curves from oedometer tests on Iron tailings from China for samples at three different locations: (a) sandy material from the upper beach (UB), (b) silty material from middle beach (MB), and (c) finer silty material from the pond (PO) (Li & Coop, 2019).

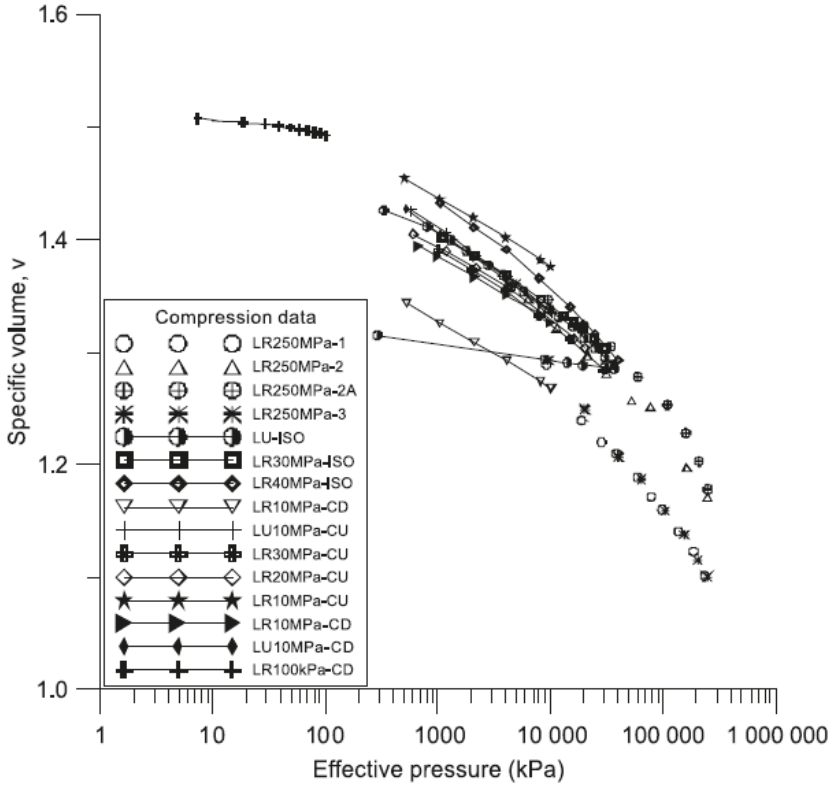

Figure 2-7: Isotropic compression tests on undisturbed specimens (LU) and remoulded specimens (LR) subglacial sandy sediment (Altuhafi et al., 2010).

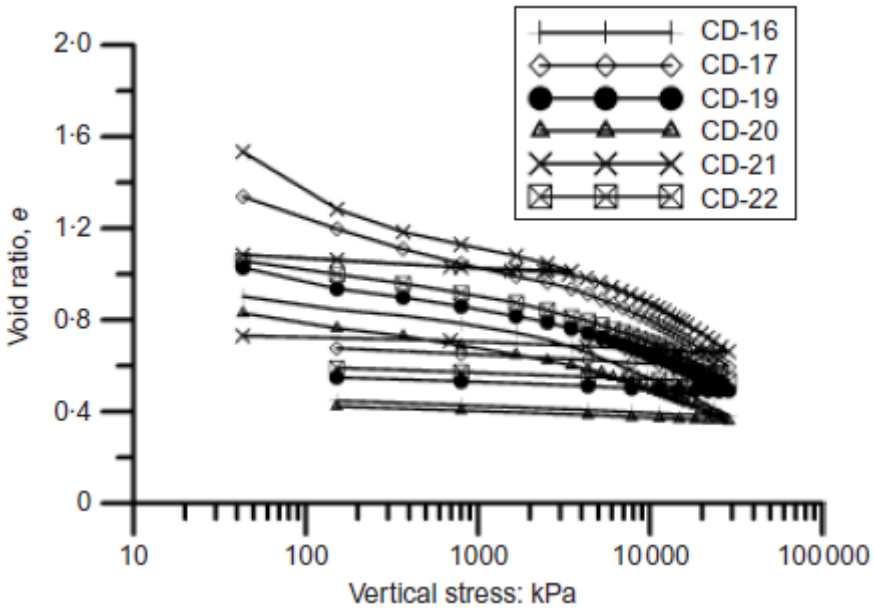

Figure 2-8: Compression curves for critical grading (CD) of Dog's Bay Sand (Altuhafi & Coop, 2015)

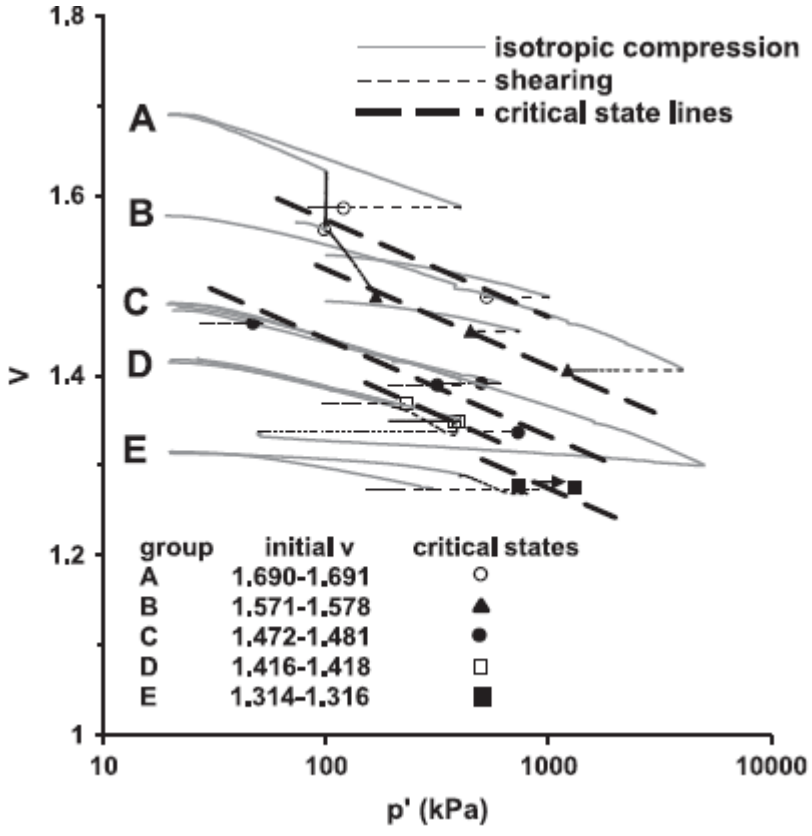

(a)

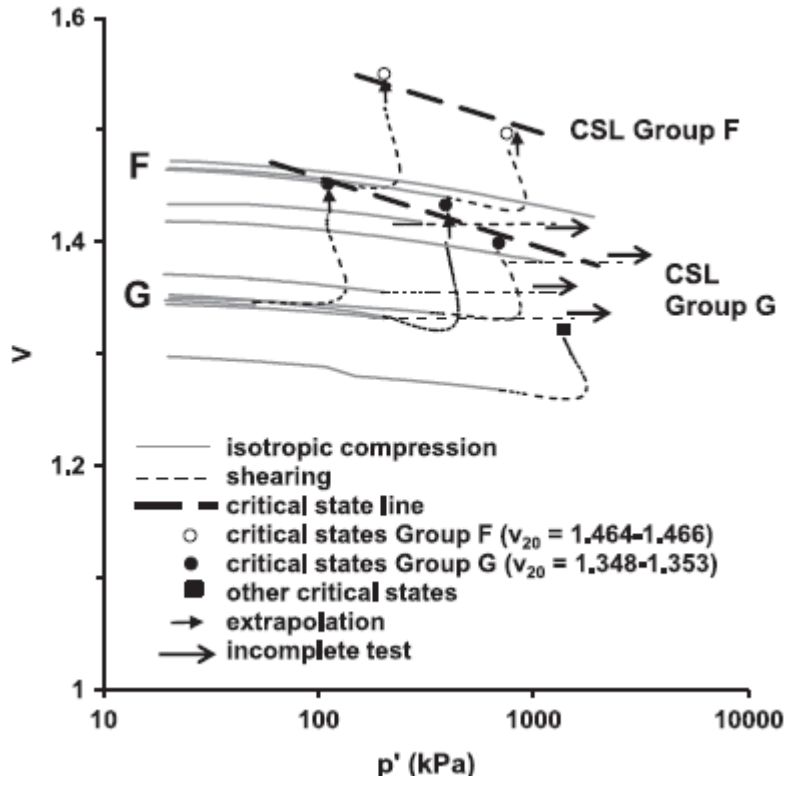

(b)

Figure 2-9: Isotropic compression and shearing behaviour of (a) Sand with Plastic Fine (SPF) and (b) Sand with Non-plastic Fines (SNF) soils (Shipton & Coop, 2015).

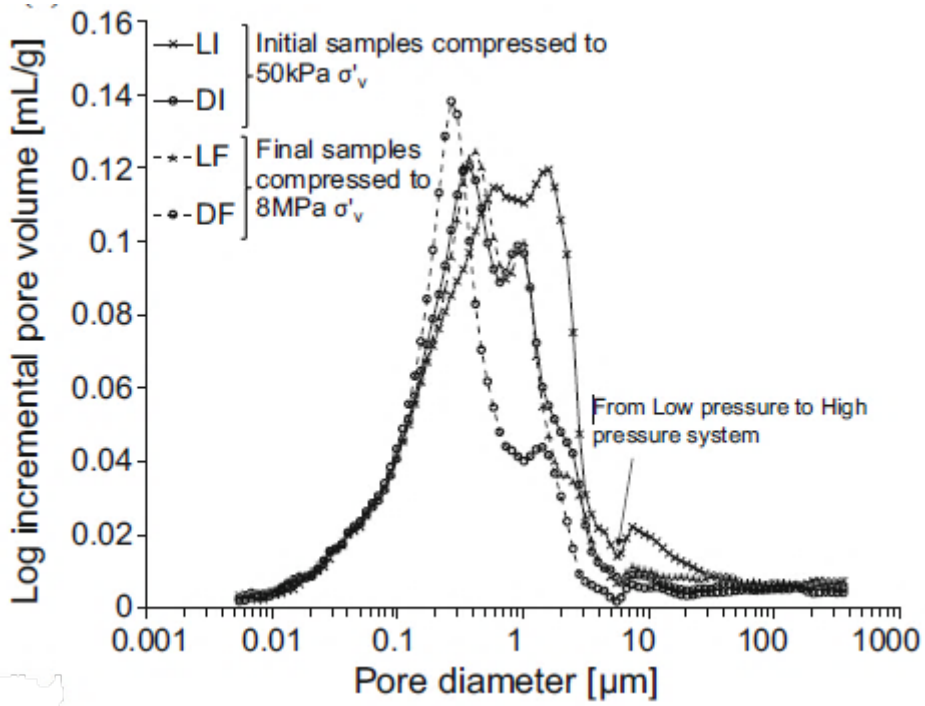

Figure 2-10: MIP results of loose and dense Sand with Plastic Fine (SPF) sample under 50kPa and 8MPa vertical stress in oedometer tests (Todisco et al., 2018).

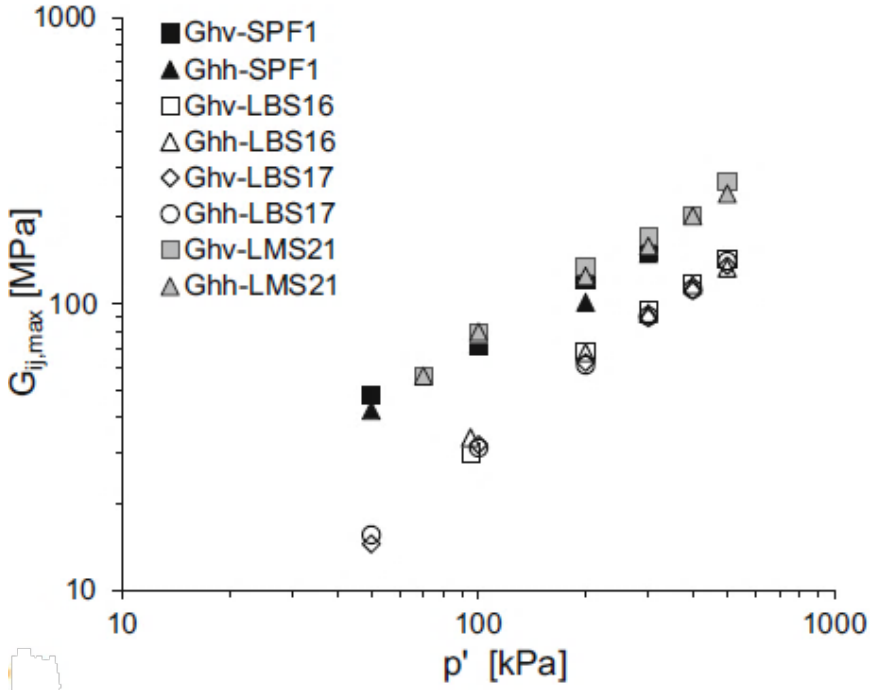

Figure 2-11: Vertical and horizontal elastic shear moduli (G_{hv} and G_{hh}) of the Sand with Plastic Fine (SPF) samples under isotropic compression (Todisco et al., 2018).

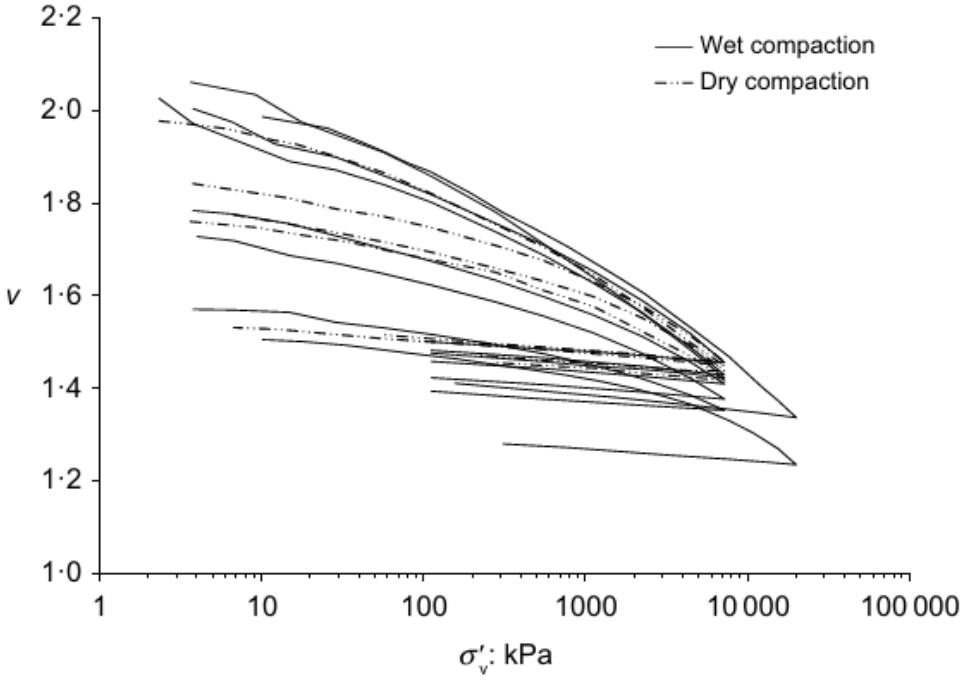

(a)

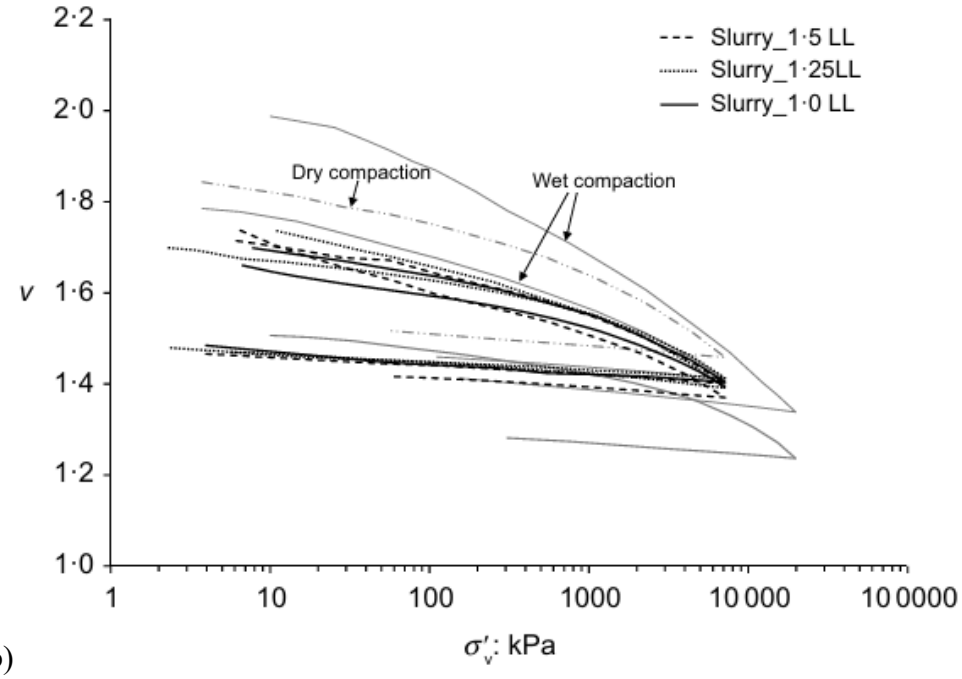

(b)

Figure 2-12: Oedometer compression curves of reconstituted silty loess prepared by (a) wet and dry compaction method and (b) slurry method (Xu & Coop, 2017).

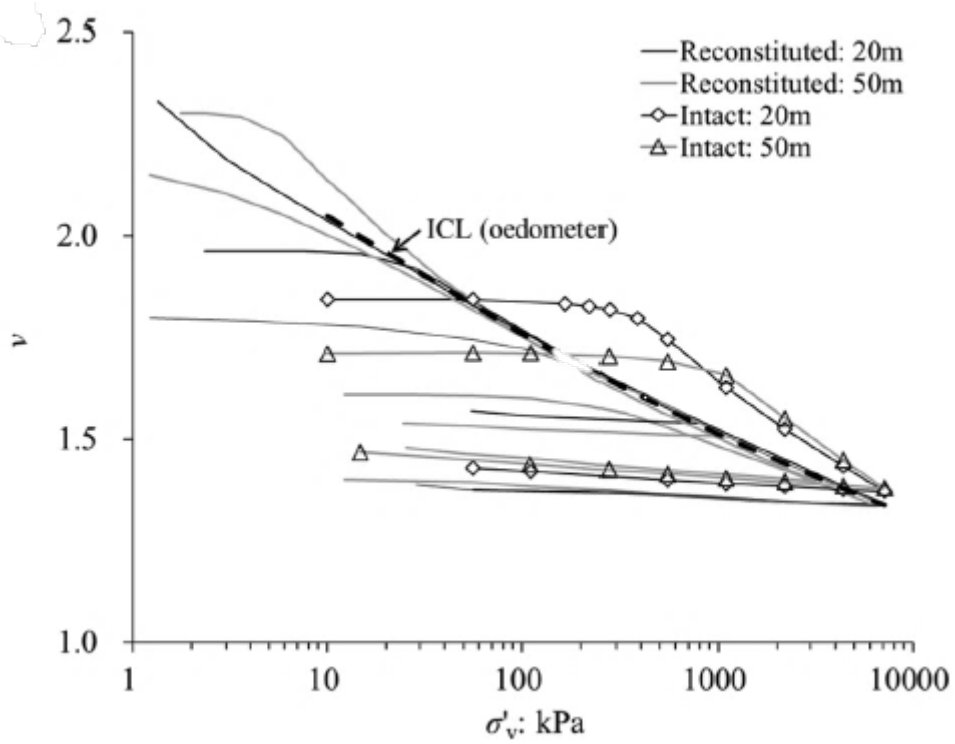

Figure 2-13: Compression curves of reconstituted and intact clayey loess in oedometer tests (Xu & Coop, 2016).

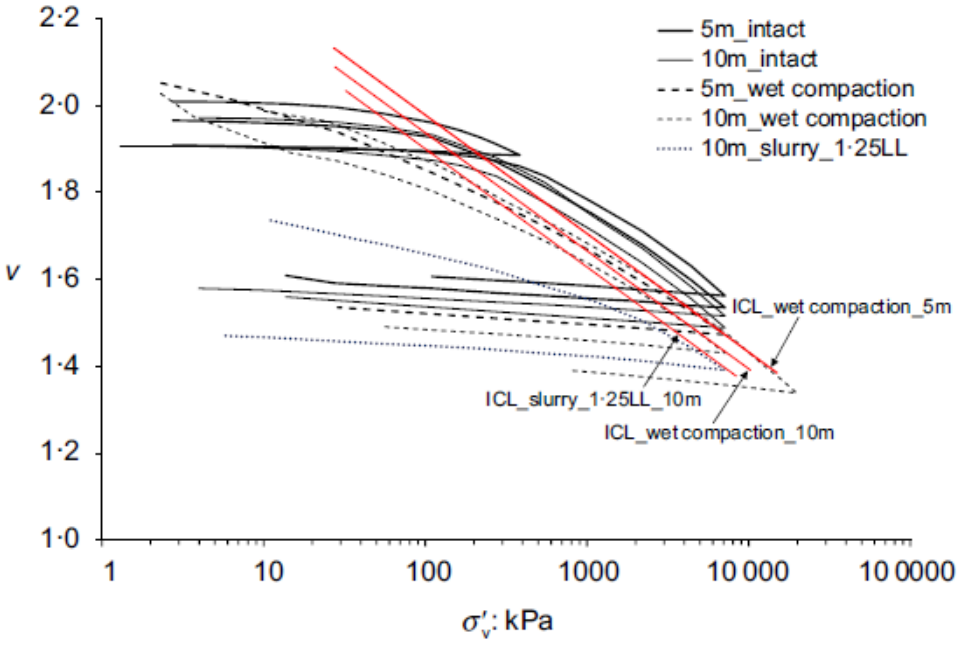

Figure 2-14: Compression curves of intact and reconstituted silty loess with transitional behaviour in oedometer tests (Xu & Coop, 2017).

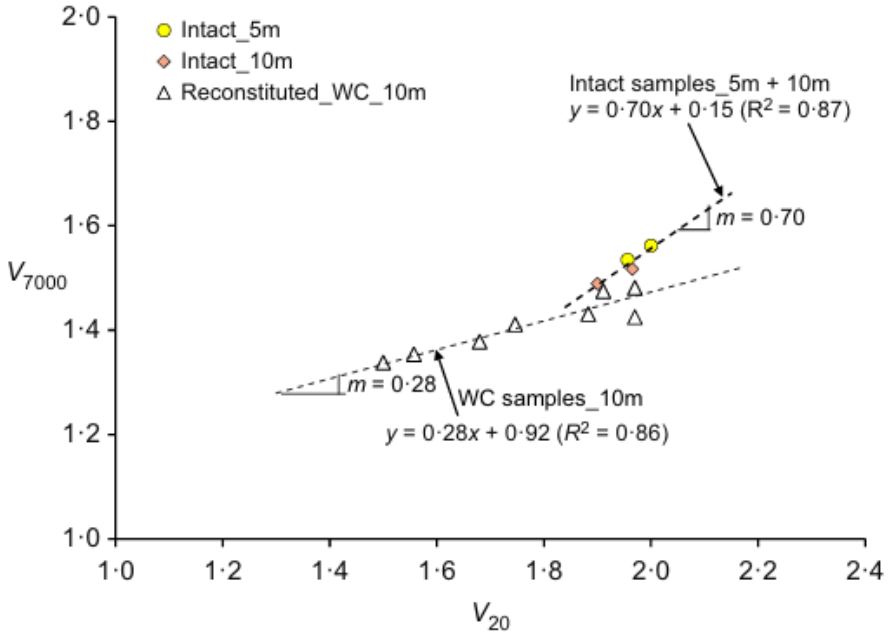

Figure 2-15: Quantification of the convergence of the compression curves by m value for the intact and reconstituted of silty loess (Xu & Coop, 2017).

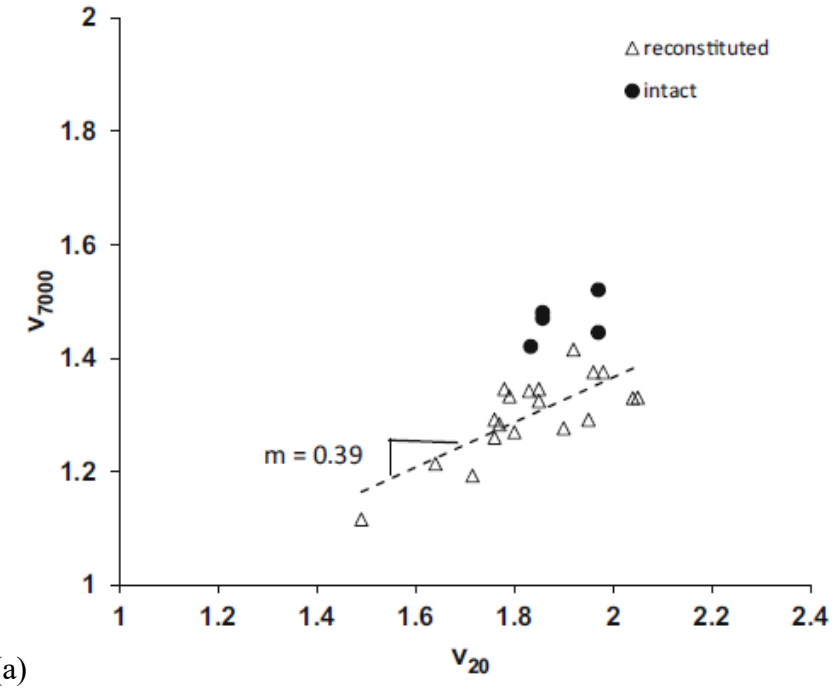

(a)

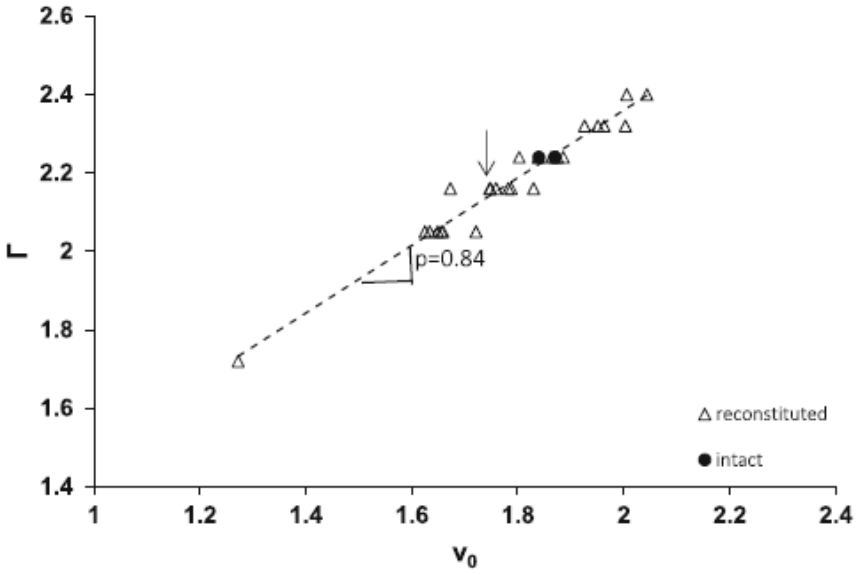

(b)

Figure 2-16: Degree of convergence (a) in compression through the m value and (b) in shearing through the P value on a silty decomposed volcanic rock (Okewale & Coop, 2020).

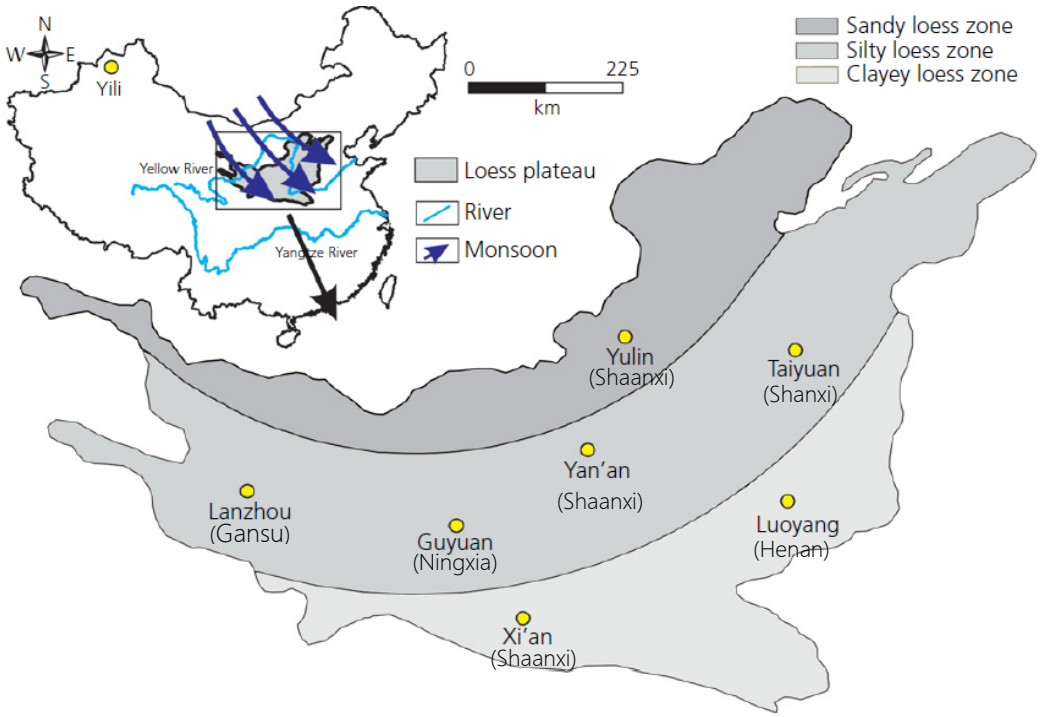

Figure 2-17 The loess soils on the Loess Plateau of China (modified by the author from Xu et al., 2020).

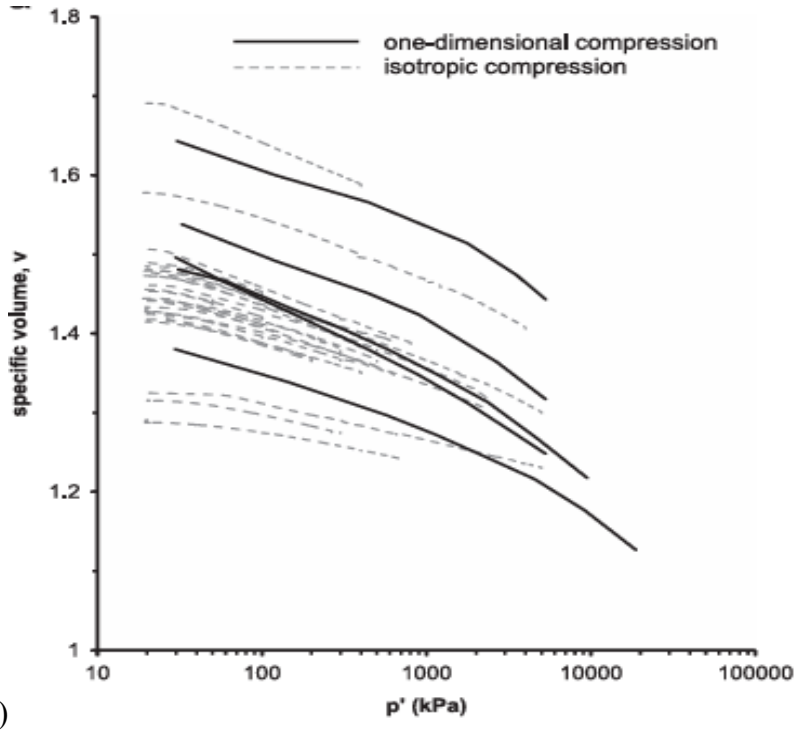

(a)

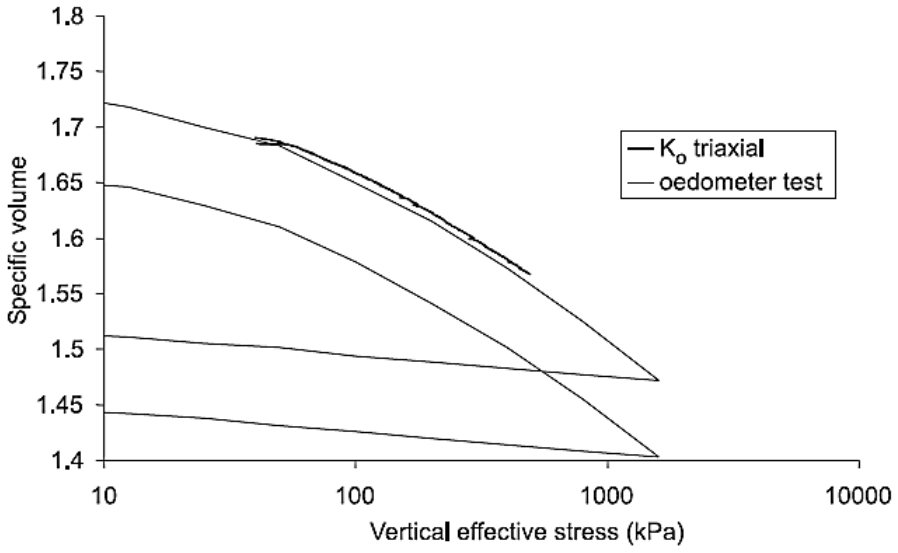

(b)

Figure 2-18 Transitional behaviour of SPF soils: (a) isotropic and one-dimensional compression data from Shipton and Coop (2015), and isotropic and ko compression data from Martins et al. (2001).

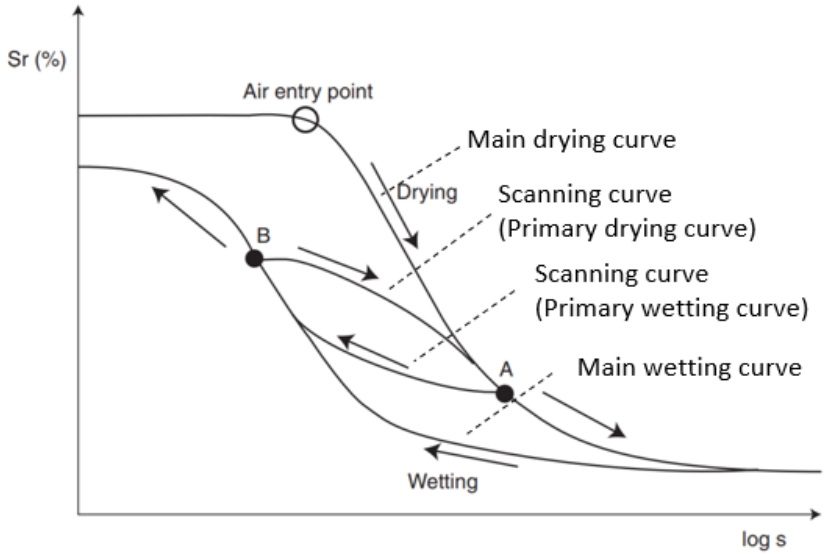

Figure 2-19 Hysteresis of soil water retention curves (Childs, 1969).

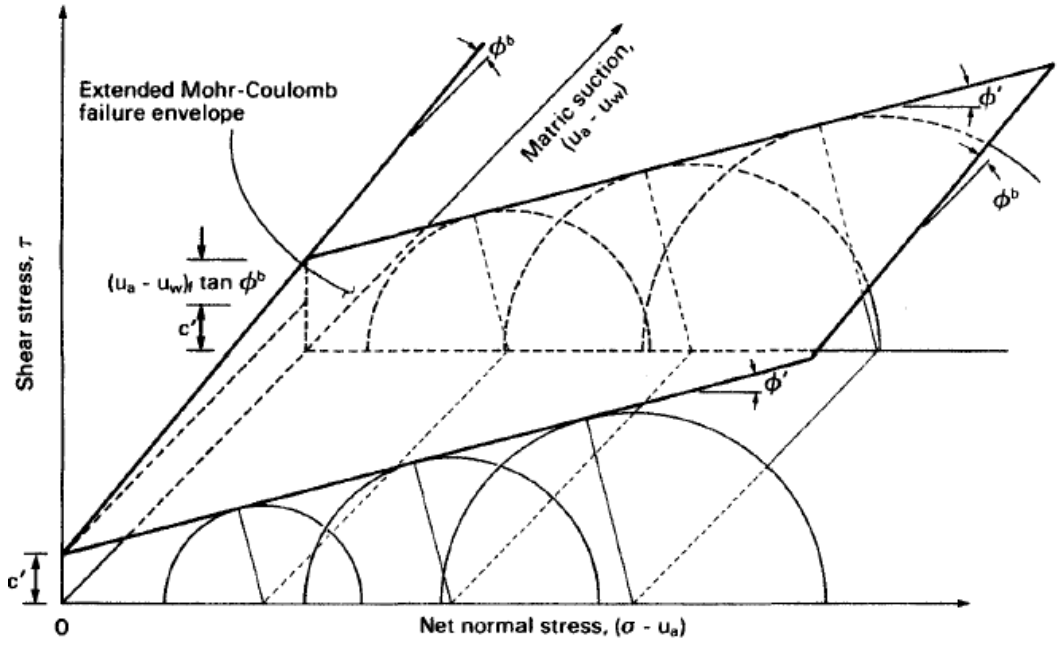

Figure 2-20 Extended Mohr-Coulomb failure envelope (Fredlund and Rahardjo, 1993).

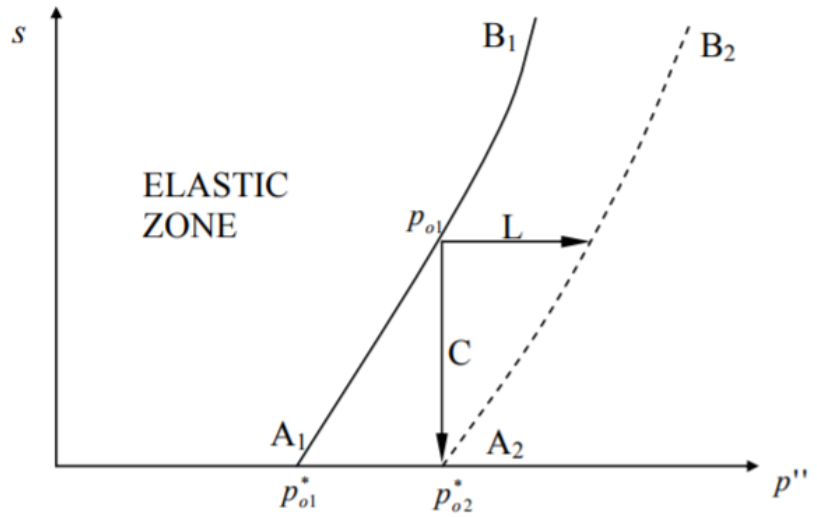

Figure 2-21 Loading-Collapse yield locus (Alonso et al., 1987).

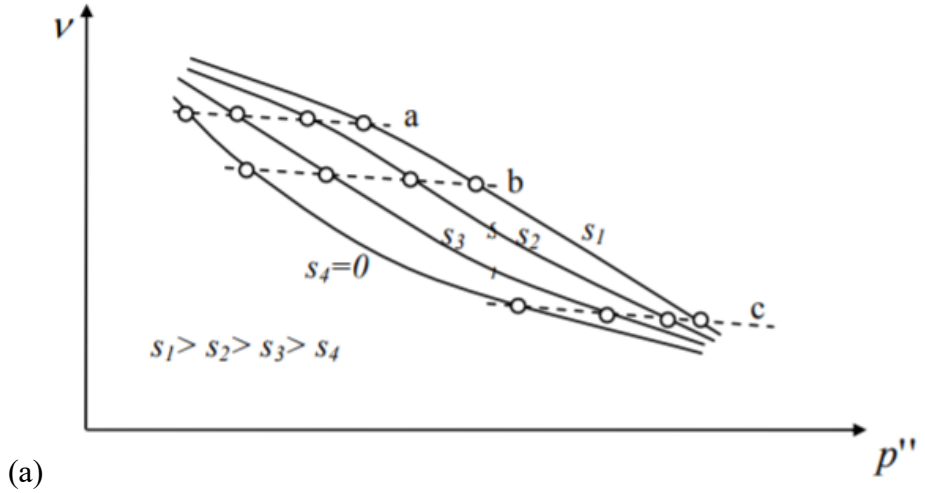

(a)

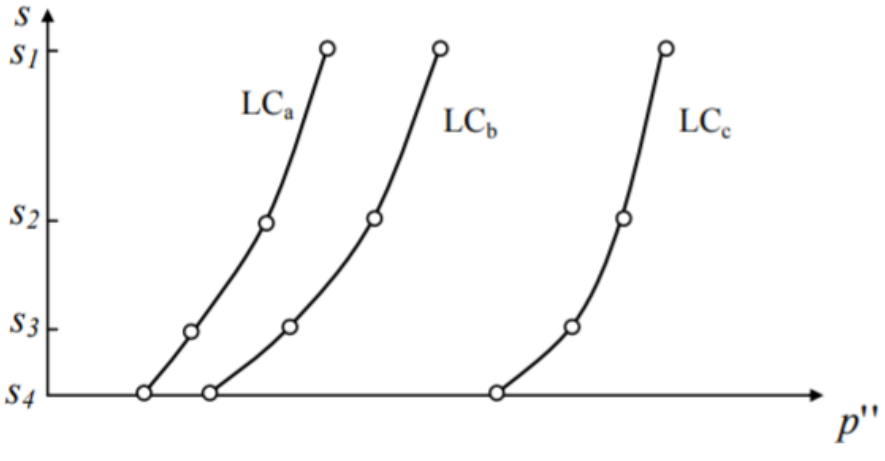

(b)

Figure 2-22 Relationship between compression curves for different suctions and yield loci (Alonso et al., 1987).

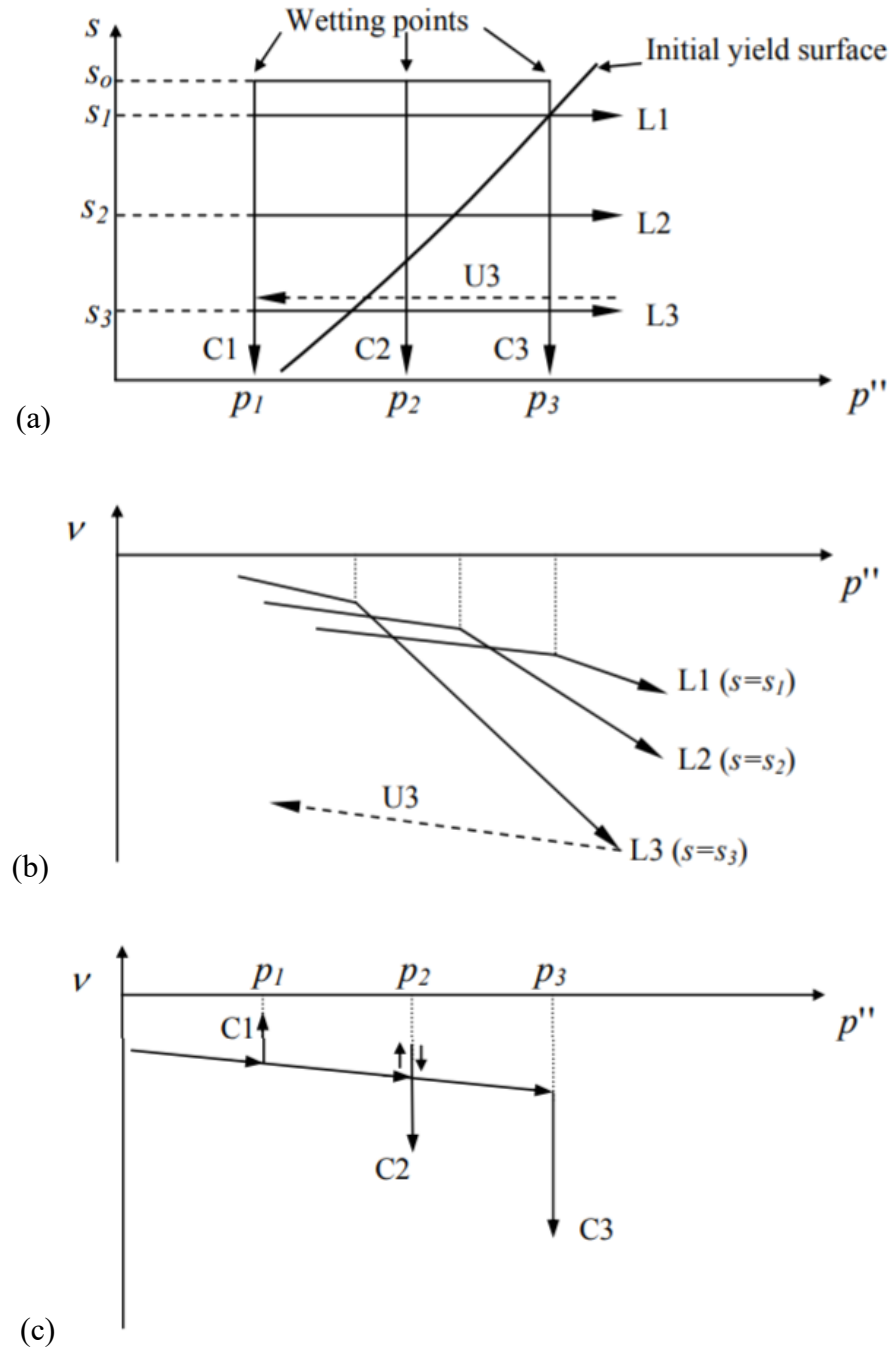

Figure 2-23 Deformation under loading and collapse behaviour (Alonso et al., 1987).

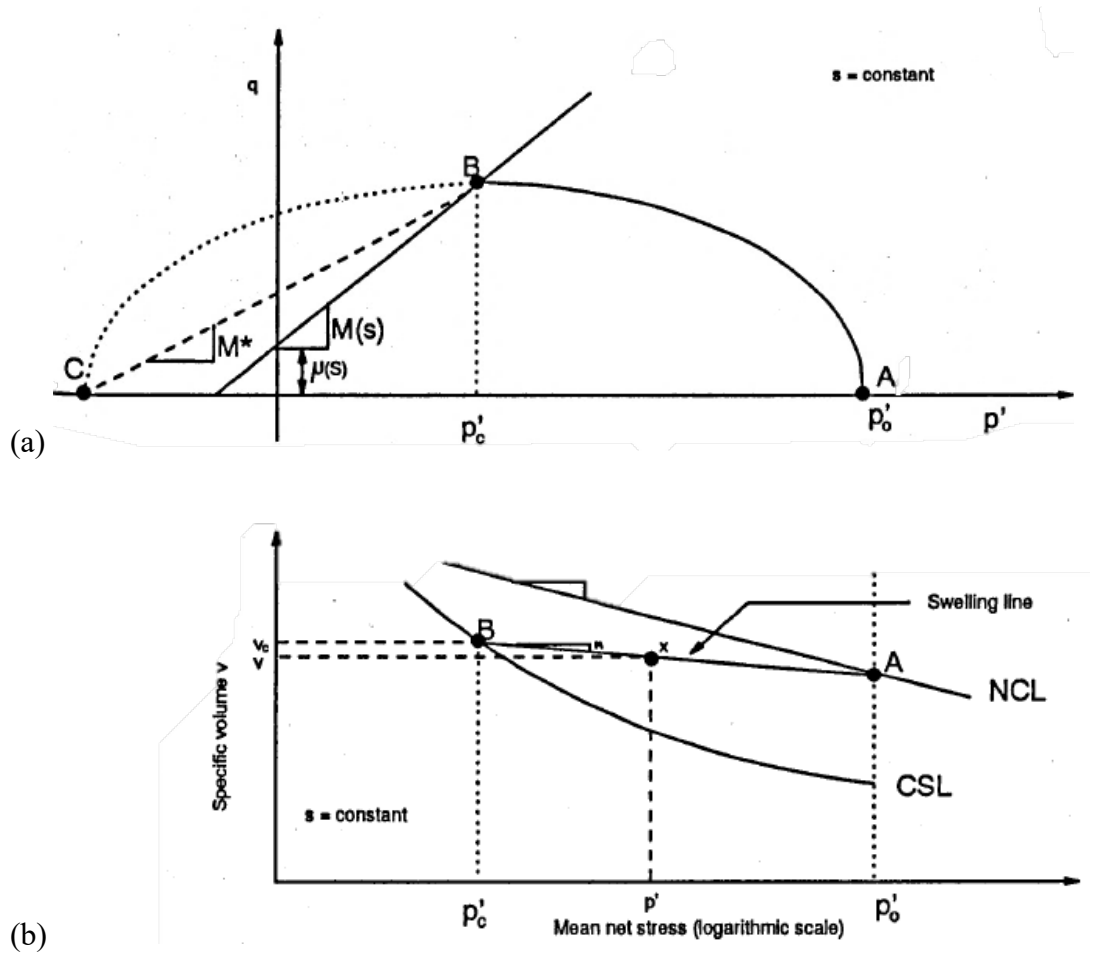

Figure 2-24 Modified Barcelona Basic Model (BBM) (Sivakumar, 1993).

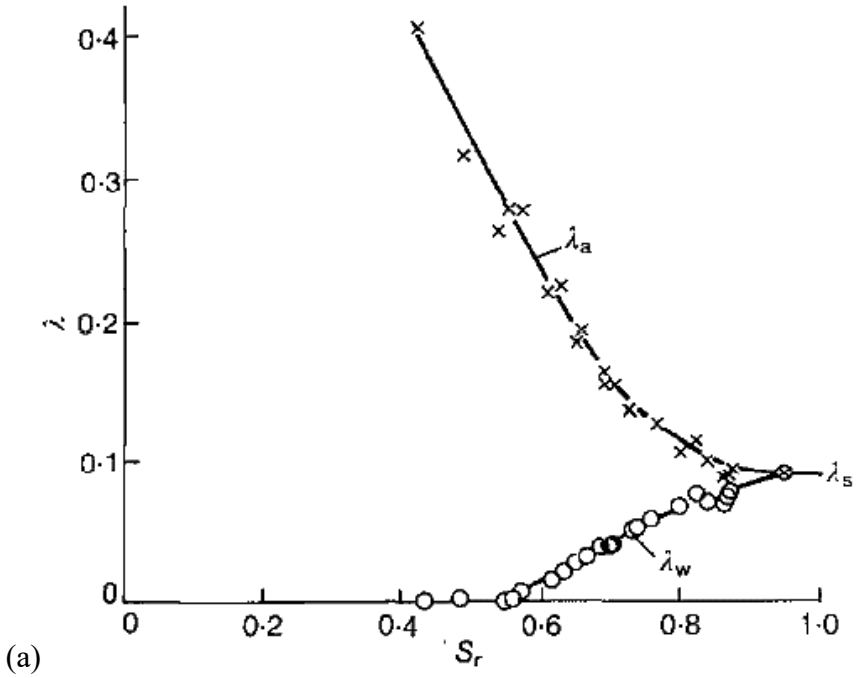

(a)

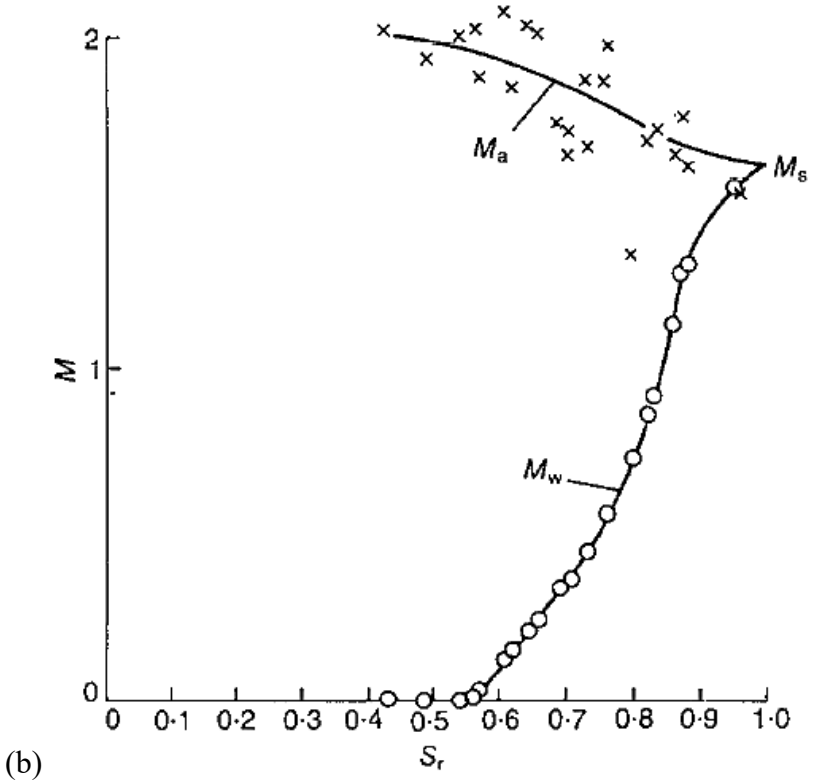

(b)

Figure 2-25 (a) Variation of the slopes and intercepts of the Normal Compression Line with the degree of saturation based on the equation $v = \Gamma_{aw} - \lambda_a \ln(p - u_a) - \lambda_w \ln(u_a - u_w)$; (b) variation of the critical state stress ratios with the degree of saturation based on equation $q = M_a(p - u_a) + M_w(u_a - u_w)$ (Toll, 1990).

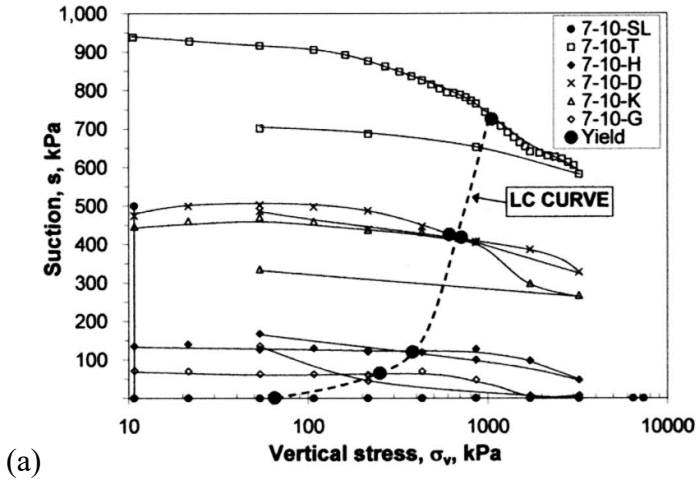

(a)

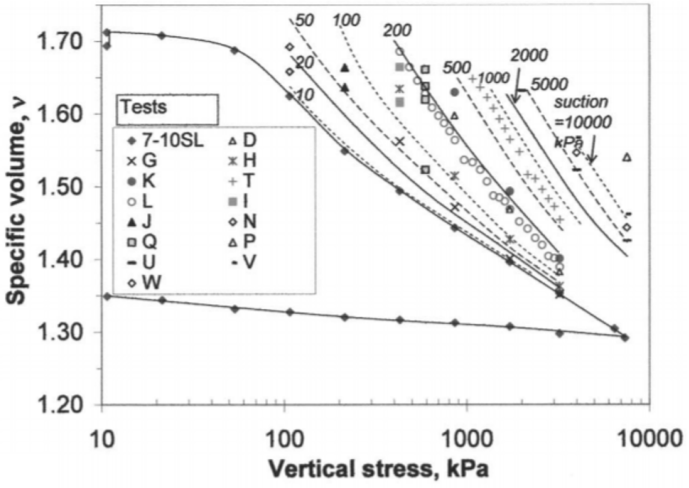

(b)

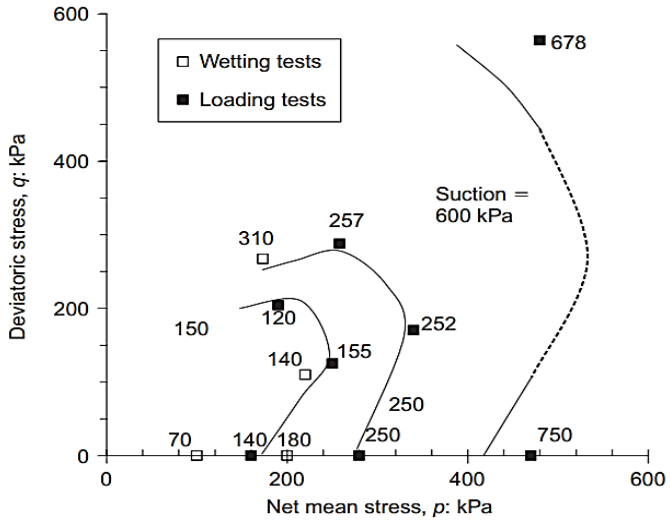

(c)

Figure 2-26 (a) Compression lines for constant water content oedometer tests, (b) contours of constant suction normal compression lines and (c) yield loci for a compacted silty clay (Jotisankasa et al., 2007).

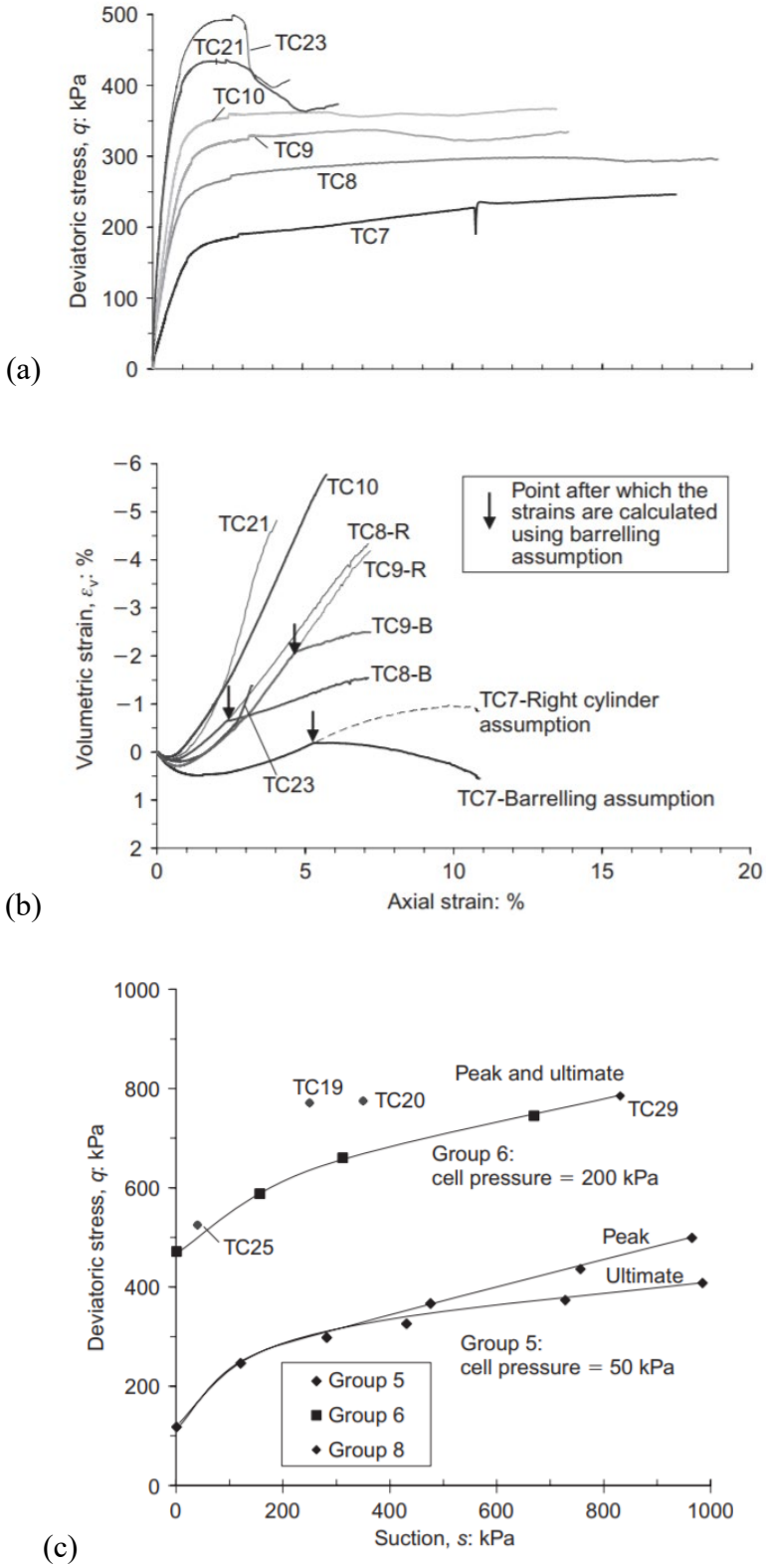

Figure 2-27 (a) Stress-strain behaviour, (b) volumetric behaviour and (c) failure envelopes for triaxial shearing tests on a compacted silty clay (Jotisankasa et al., 2007).

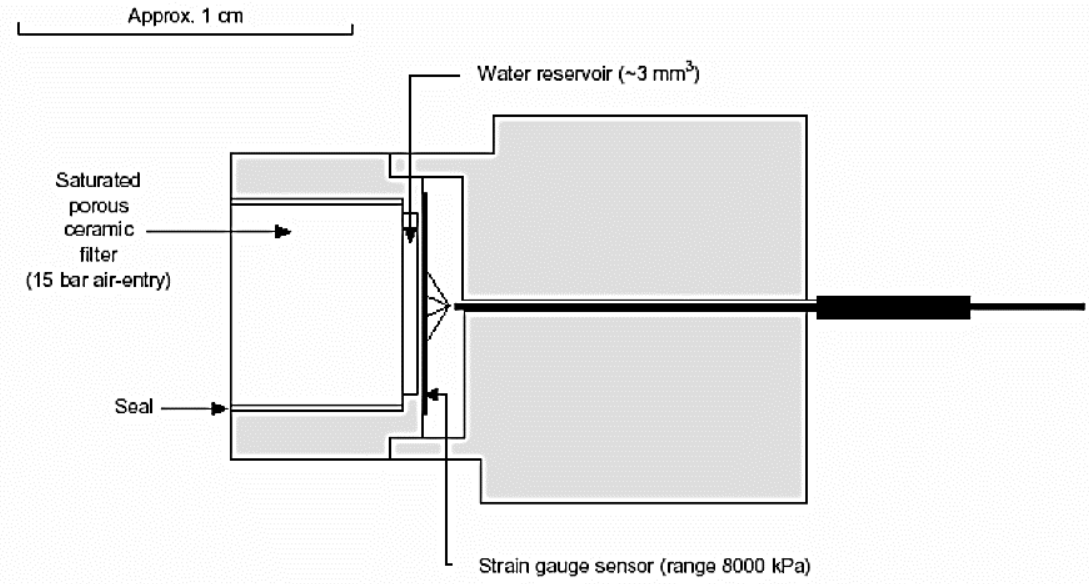

Figure 2-28 Schematic Imperial College tensiometer (Ridley & Burland, 1999).

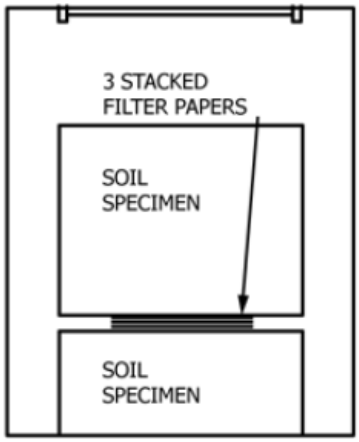

Figure 2-29 Setup for matric suction measurement using the filter paper technique (ASTM D5298-16).

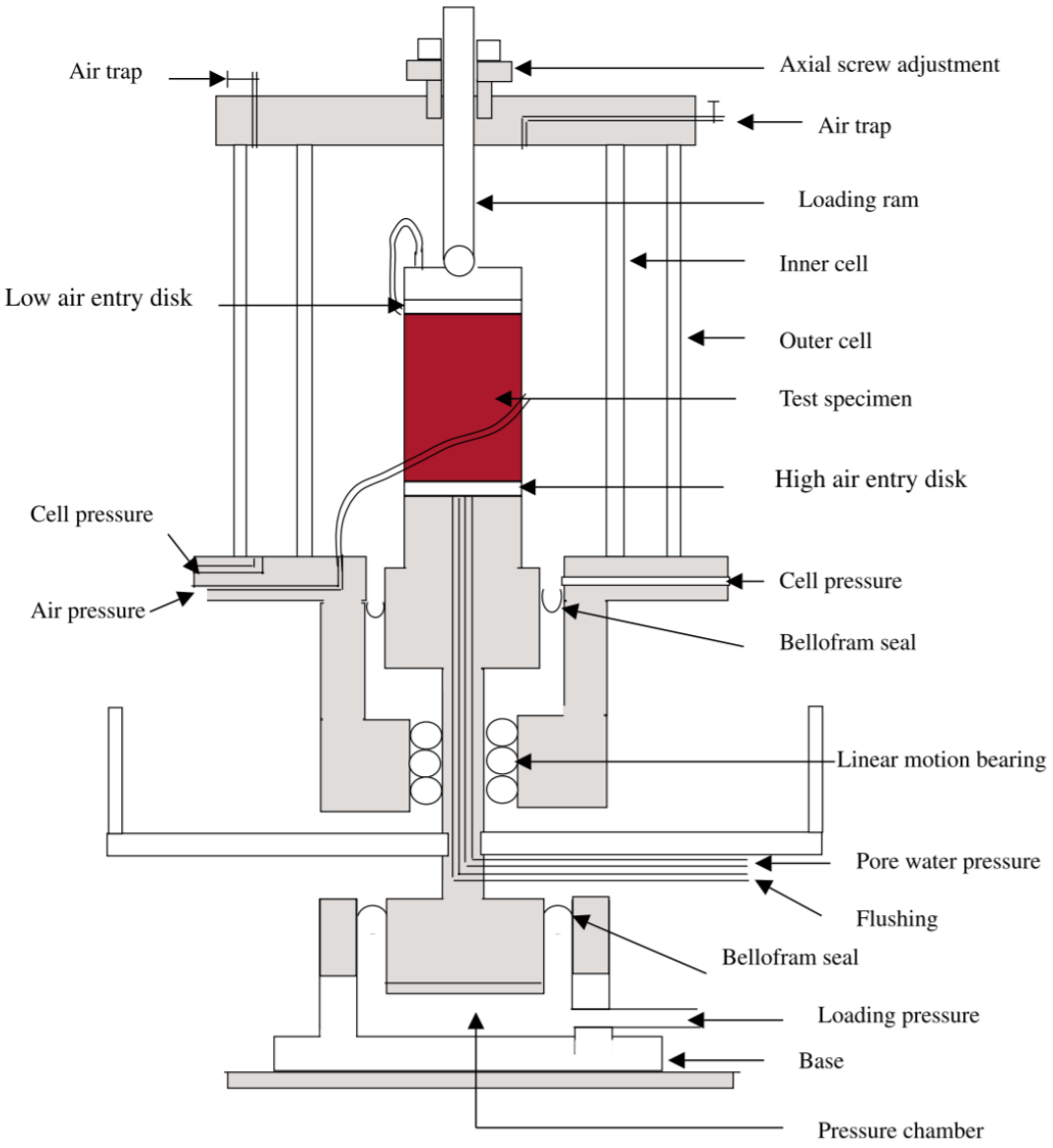

Figure 2-30 Suction-controlled double-walled triaxial cell using the axis-translation technique (Estabragh et al., 2004).

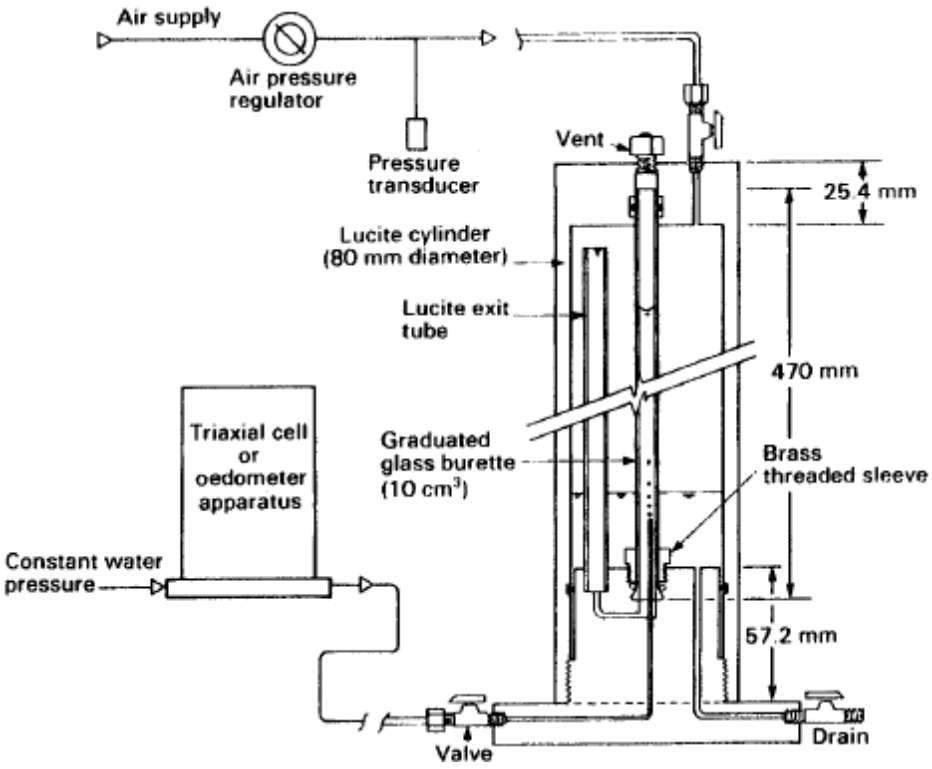

Figure 2-31 Diffused air volume indicator (Fredlund, 1975).

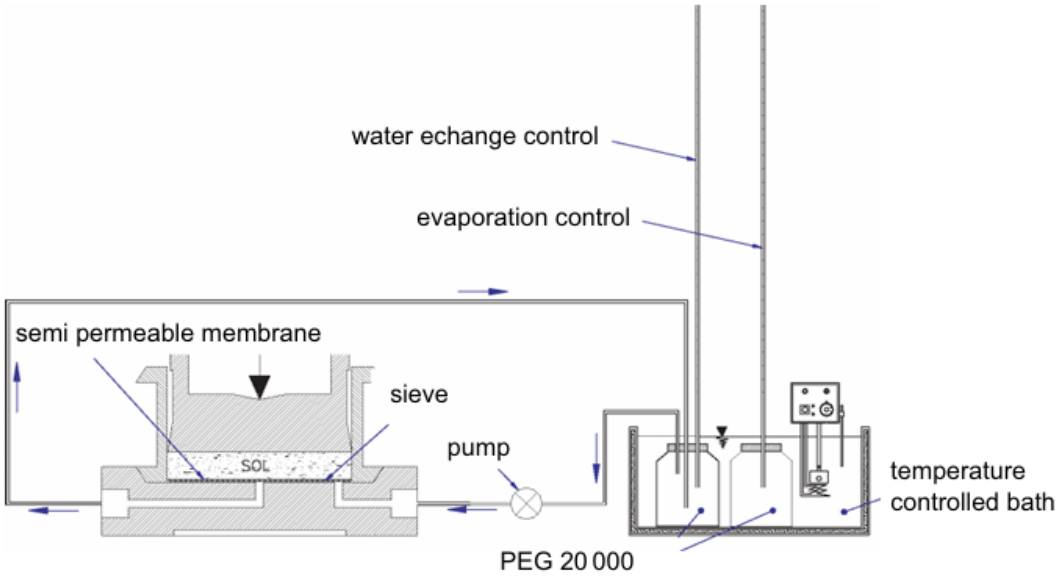

Figure 2-32 Osmotically suction-controlled oedometer apparatus developed at Imperial College (Délage & Cui, 2008).

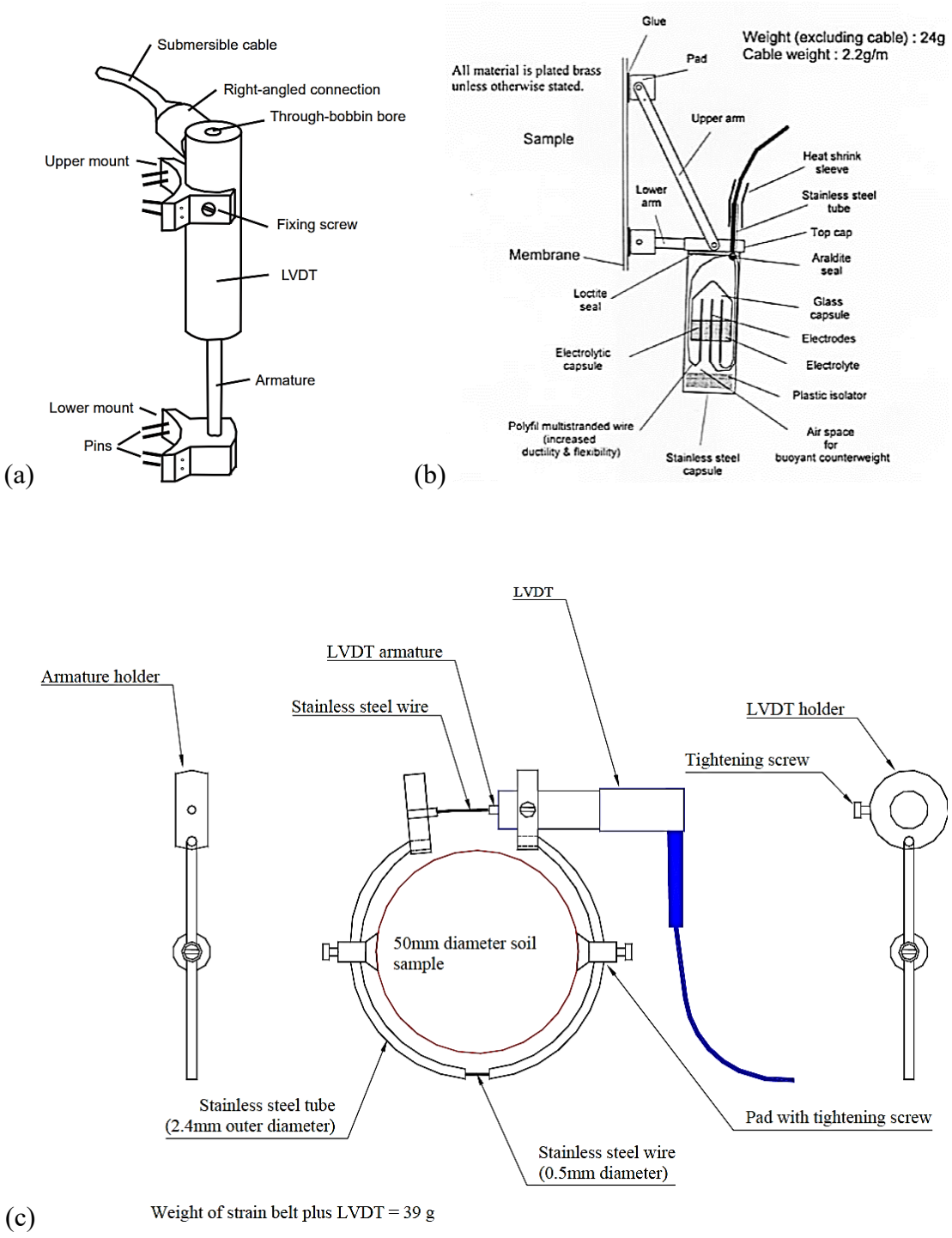

Figure 2-33 (a) LVDTs for axial strain measurements (Cuccovillo & Coop, 1997); (b) the electrolevel inclinometer (Burland & Symes, 1982) for axial strain measurements (after Kuwano, 1999); (c) a radial strain belt (Klotz & Coop, 2002) (after Jotisankasa, 2005).

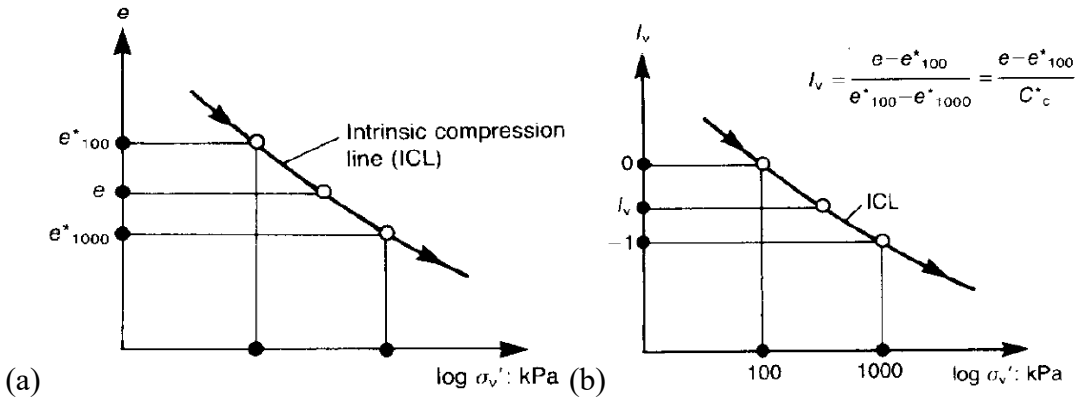

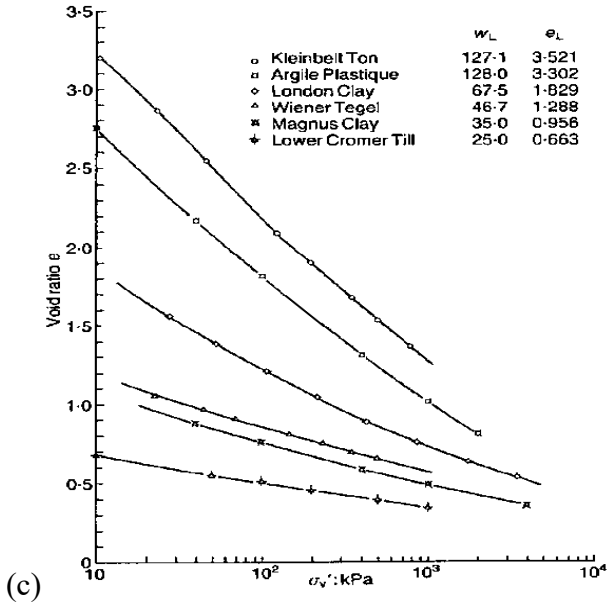

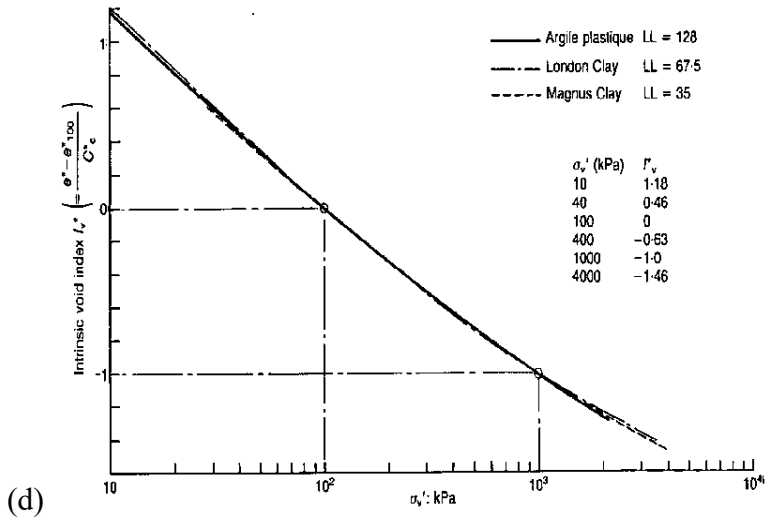

Figure 2-34 (a) The Intrinsic Compression Line (ICL) and (b) the normalized ICL based on void index; (c) one-dimensional ICLs for various reconstituted clays and (d) the corresponding normalized ICL based on void index (Burland, 1990).

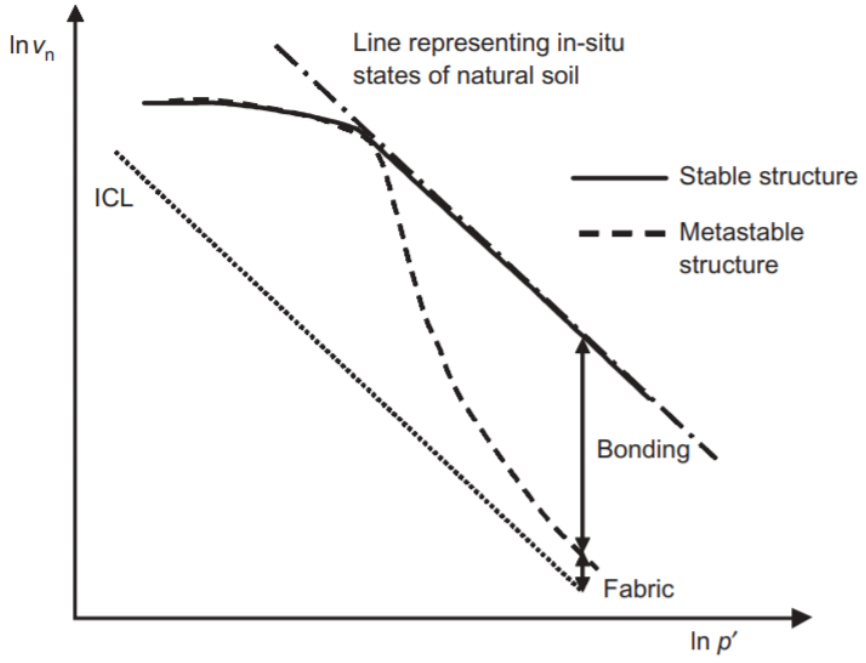

(a)

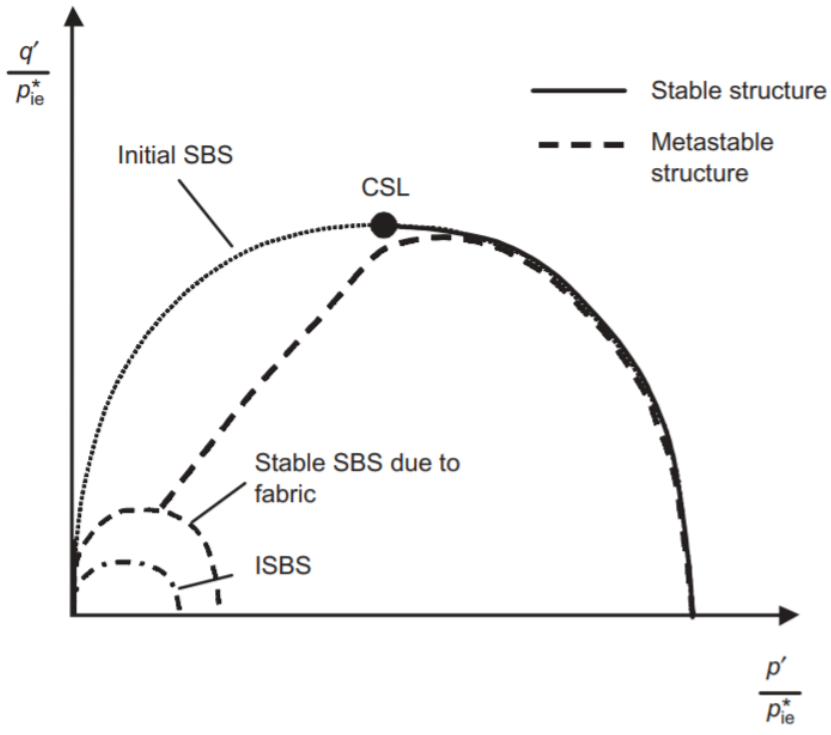

(b)

Figure 2-35 Schematic diagrams of idealised clay behaviour with the stable and the metastable structures in (a) compression and (b) shearing (Baudet & Stallebrass, 2004).

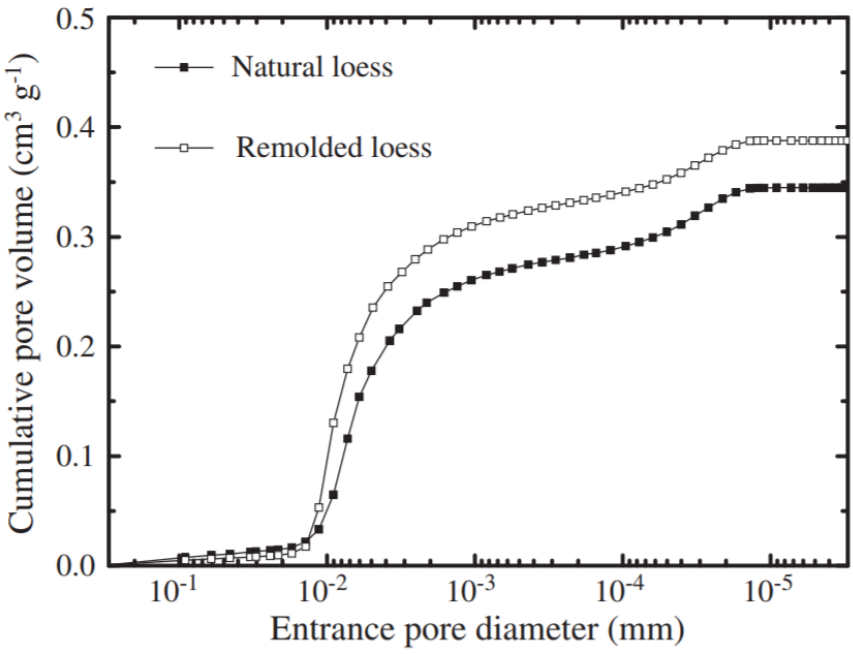

(a)

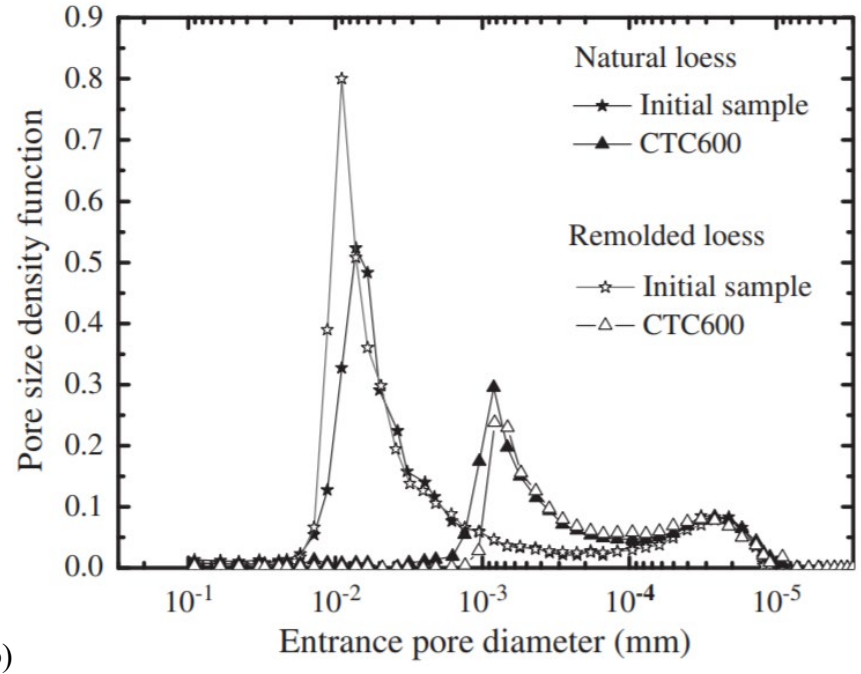

(b)

Figure 2-36 MIP results: (a) cumulative pore-volume curves for natural and remoulded clayey loess samples and (b) pore size density function before and after consolidated undrained triaxial tests (Jiang et al., 2014).

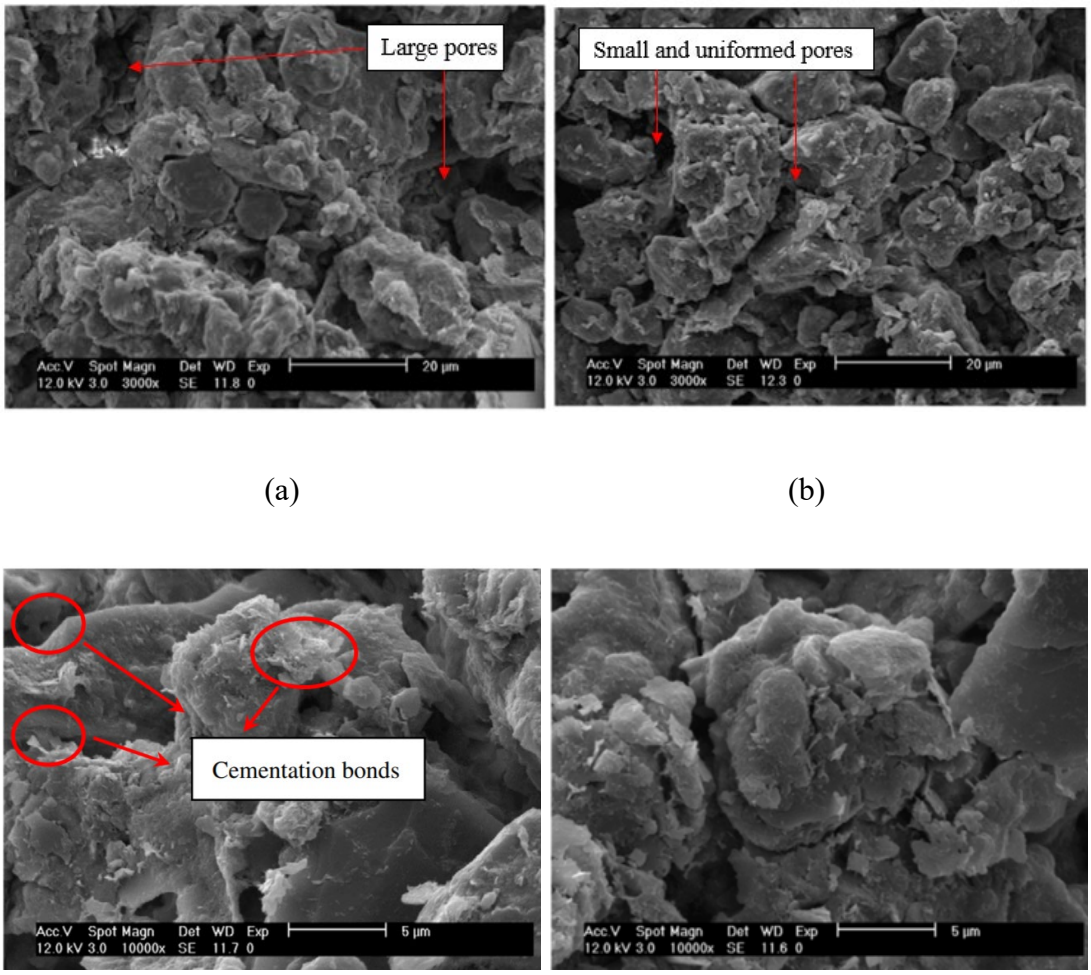

Figure 2-37 SEM images for clayey loess (a) natural and (b) remoulded loess in low magnification and the (c) natural and (d) remoulded loess in high magnification (Jiang et al., 2014).

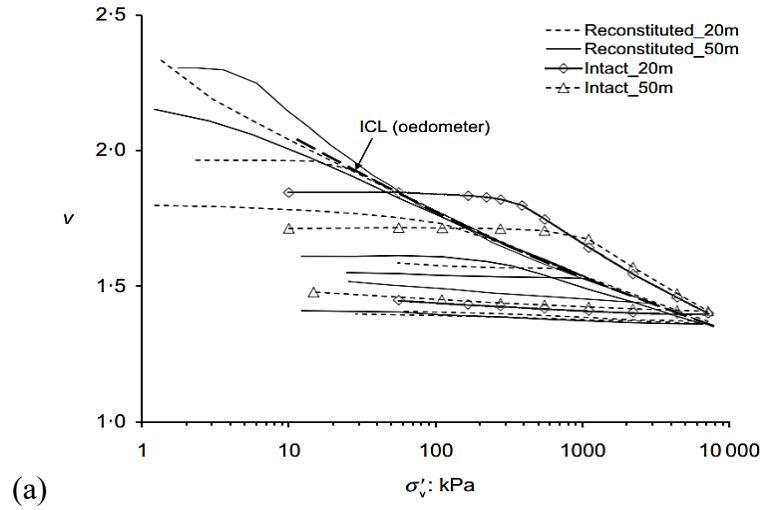

(a)

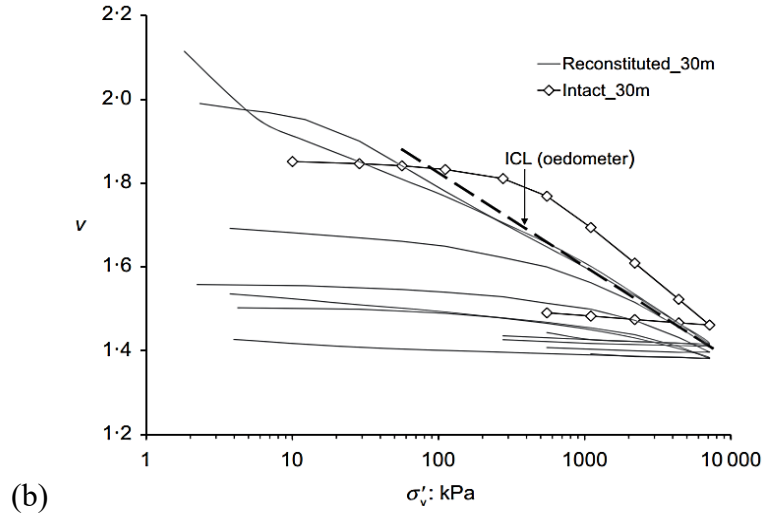

(b)

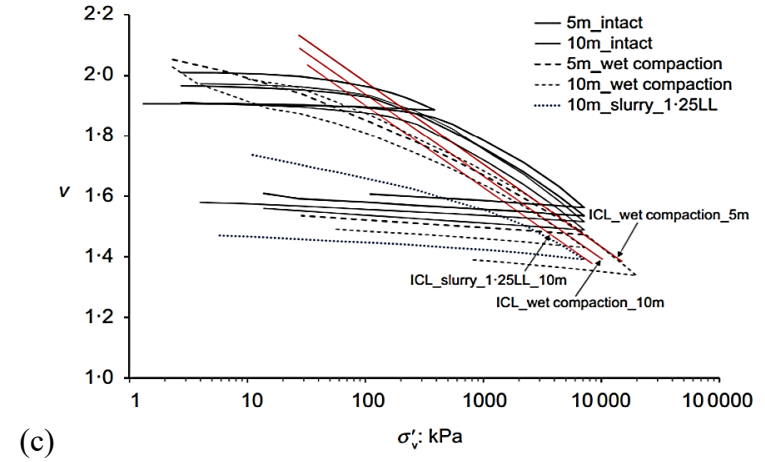

(c)

Figure 2-38 The oedometer compression curves and ICLs of (a) a non-transitional clayey loess with 20% clay (Xu & Coop, 2016), (b) a non-transitional finer silty loess with 10% clay (Xu et al., 2016) and (c) a transitional silty loess with 5% clay (Xu & Coop, 2017).

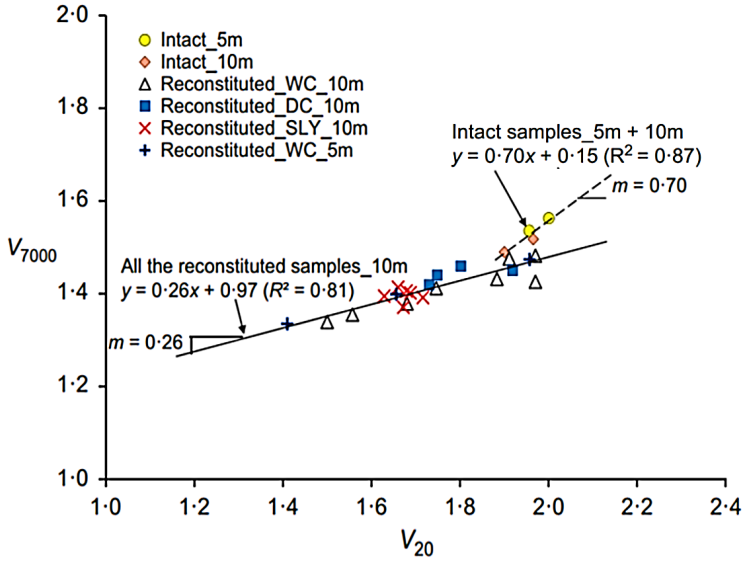

Figure 2-39 The m value for the reconstituted and intact samples of transitional silty loess (Xu & Coop, 2017).

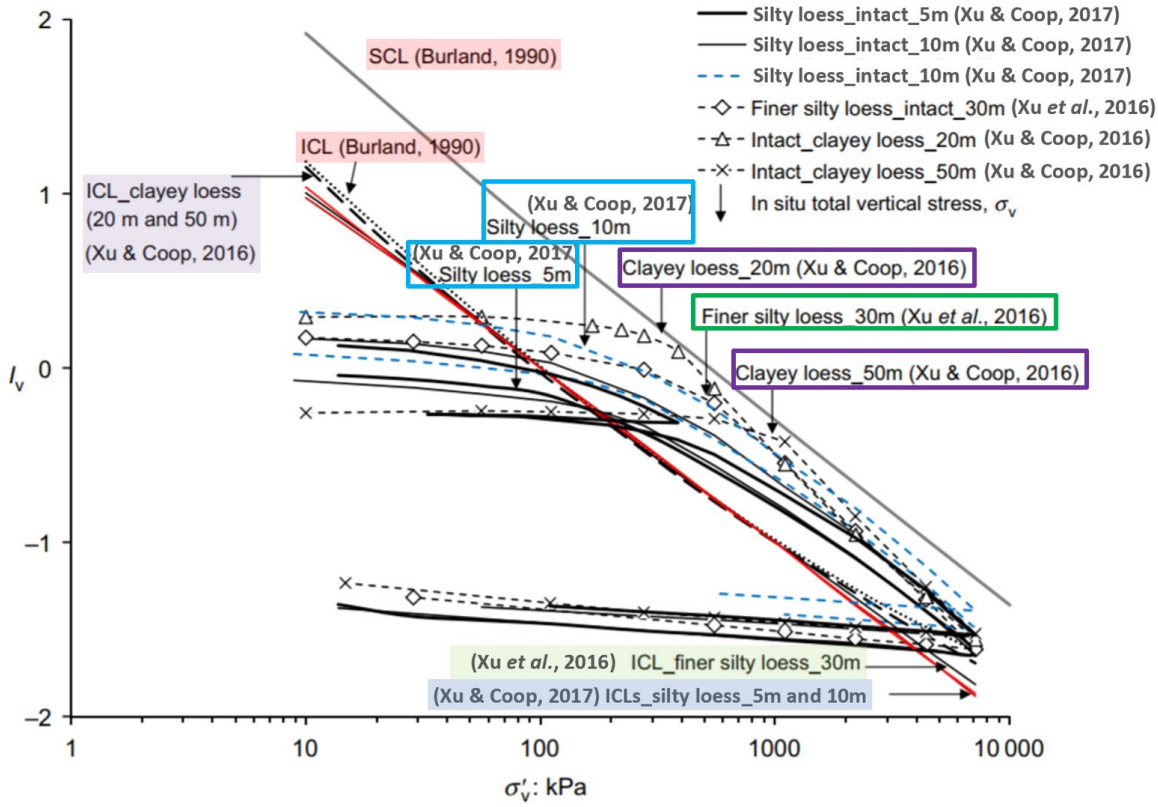

Figure 2-40 The ICLs and oedometer compression curves of a clayey loess at depths of 20m and 50m (Xu & Coop, 2016), a finer silty loess at a depth of 30m (Xu et al., 2016) and a silty loess at depths of 5m and 10m (Xu & Coop, 2017), comparing with the ICL and SCL of Burland (1990).

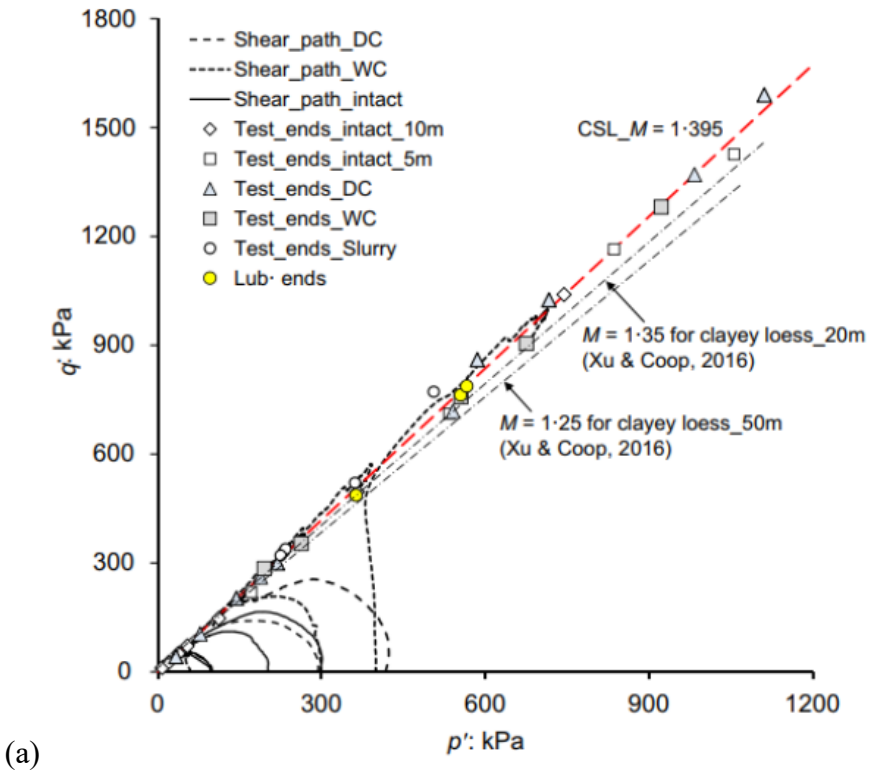

(a)

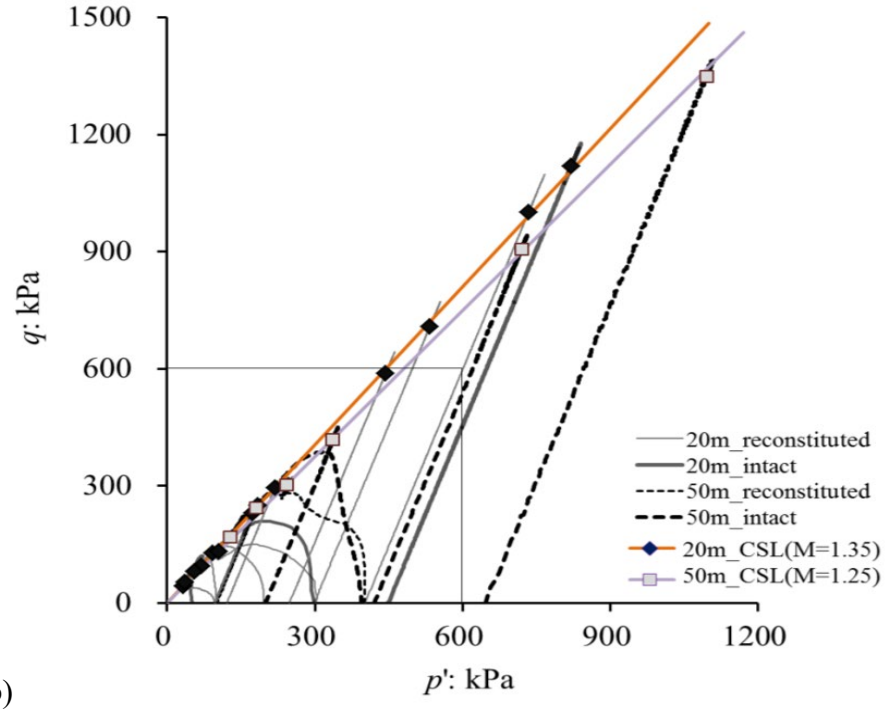

(b)

Figure 2-41 Undrained stress paths and critical state points for drained tests of (a) for transitional silty loess (Xu & Coop, 2017) and (b) for non-transitional clayey loess (Xu & Coop, 2016).

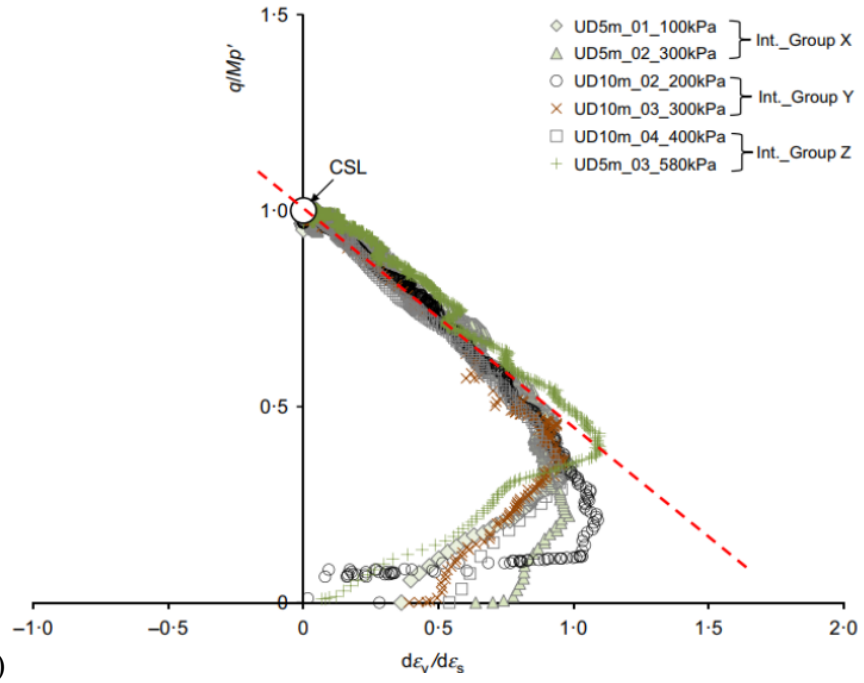
q/Mp'
1·5
1·0
0·5
0
CSL
UD5m_01_100kPa
UD5m_02_300kPa
Int._Group X
UD10m_02_200kPa
UD10m_03_300kPa
Int._Group Y
UD10m_04_400kPa
UD5m_03_580kPa
Int._Group Z
−1·0
−0·5
0
0·5
1·0
1·5
2·0
dεv/dεs

(a)

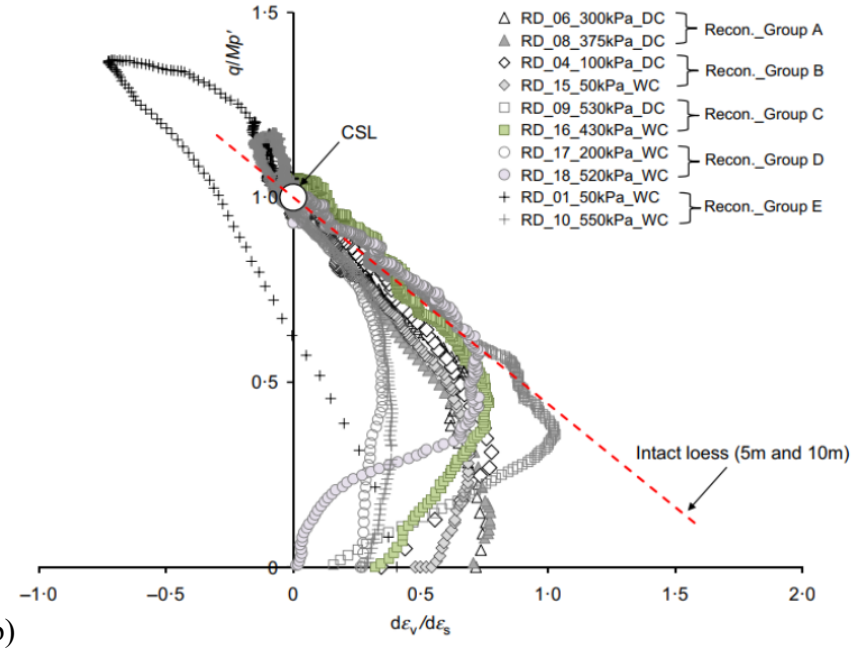
q/Mp'
1·5
1·0
0·5
0
CSL
RD_06_300kPa_DC
RD_08_375kPa_DC
Recon._Group A
RD_04_100kPa_DC
RD_15_50kPa_WC
Recon._Group B
RD_09_530kPa_DC
RD_16_430kPa_WC
Recon._Group C
RD_17_200kPa_WC
RD_18_520kPa_WC
Recon._Group D
RD_01_50kPa_WC
RD_10_550kPa_WC
Recon._Group E
Intact loess (5m and 10m)
−1·0
−0·5
0
0·5
1·0
1·5
2·0
dεv/dεs

(b)

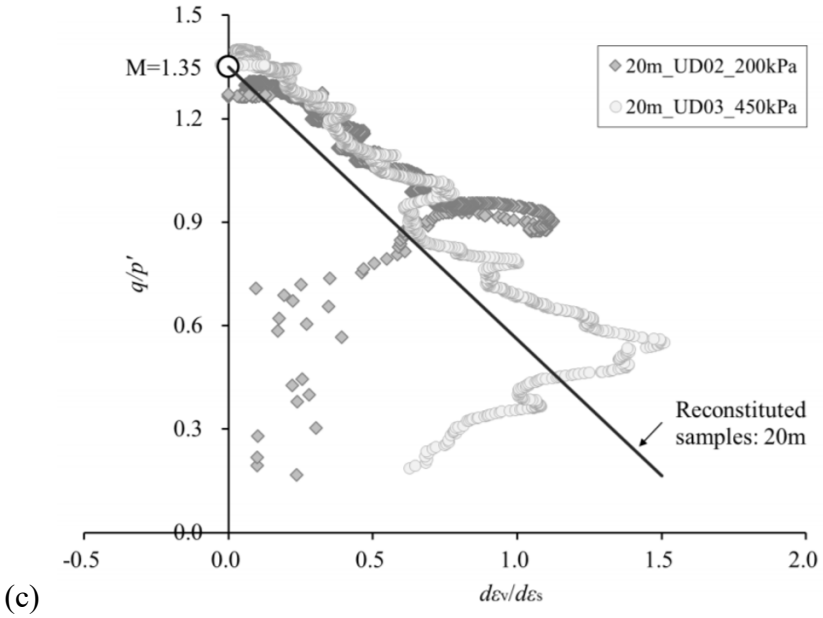

(c)

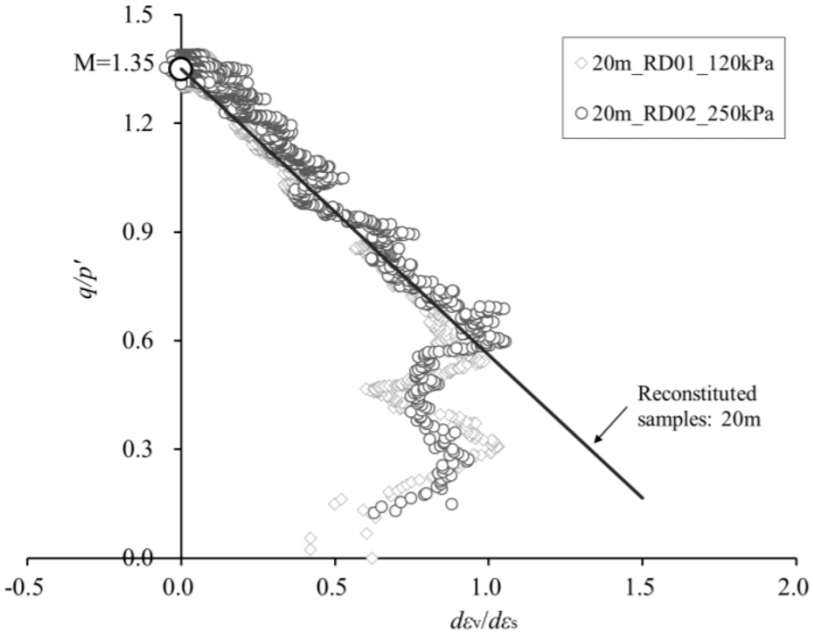

(d)

Figure 2-42 The stress-dilatancy during shearing of (a) intact and (b) reconstituted samples for a transitional SPF (Xu & Coop, 2017) and (c) intact and (d) reconstituted samples for a non-transitional clayey loess (Xu & Coop, 2016).

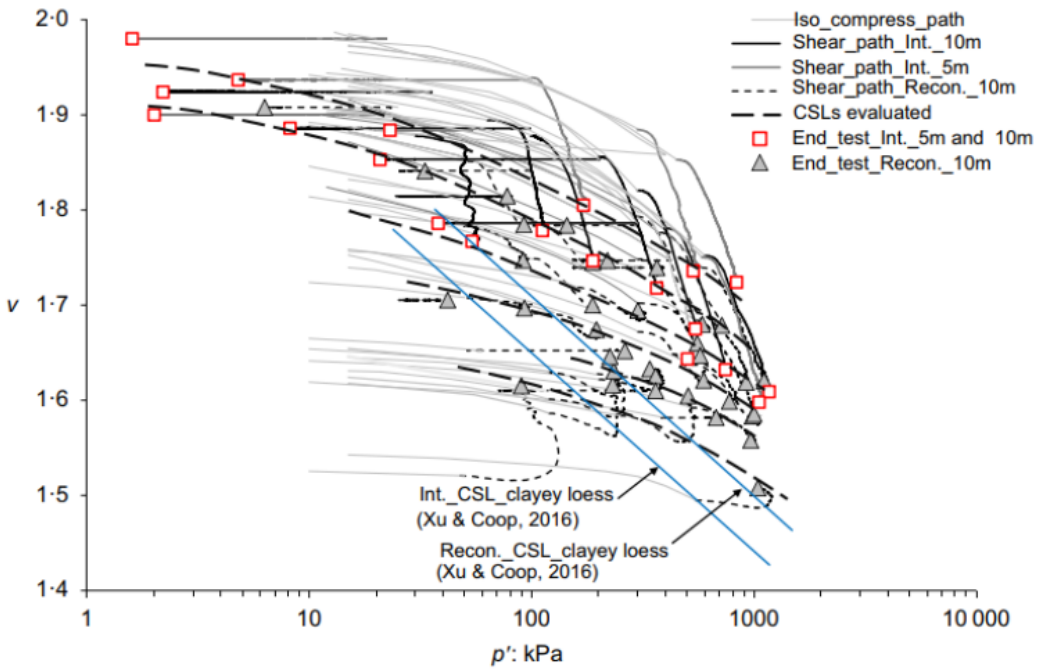
Iso_compress_path
Shear_path_Int._10m
Shear_path_Int._5m
Shear_path_Recon._10m
CSLs evaluated
End_test_Int._5m and 10m
End_test_Recon._10m
Int._CSL_clayey loess
(Xu & Coop, 2016)
Recon._CSL_clayey loess
(Xu & Coop, 2016)
v
p′: kPa

(a)

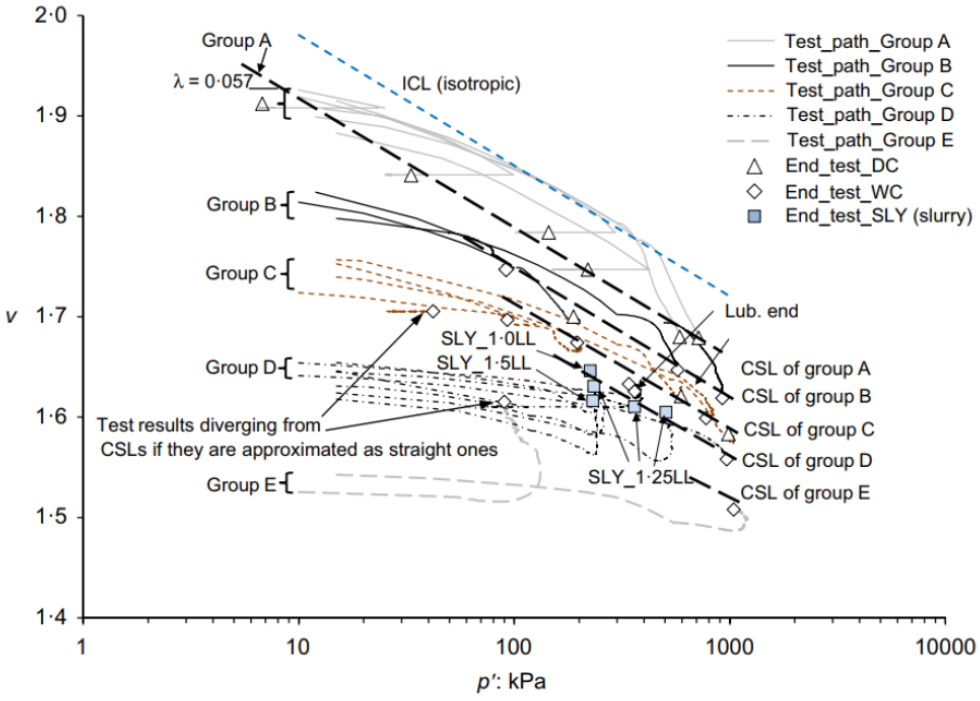
Group A
λ = 0·057
ICL (isotropic)
Group B
Group C
Group D
Group E
Test results diverging from
CSLs if they are approximated as straight ones
SLY_1·0LL
SLY_1·5LL
SLY_1·25LL
Lub. end
CSL of group A
CSL of group B
CSL of group C
CSL of group D
CSL of group E
Test_path_Group A
Test_path_Group B
Test_path_Group C
Test_path_Group D
Test_path_Group E
End_test_DC
End_test_WC
End_test_SLY (slurry)
v
p′: kPa

(b)

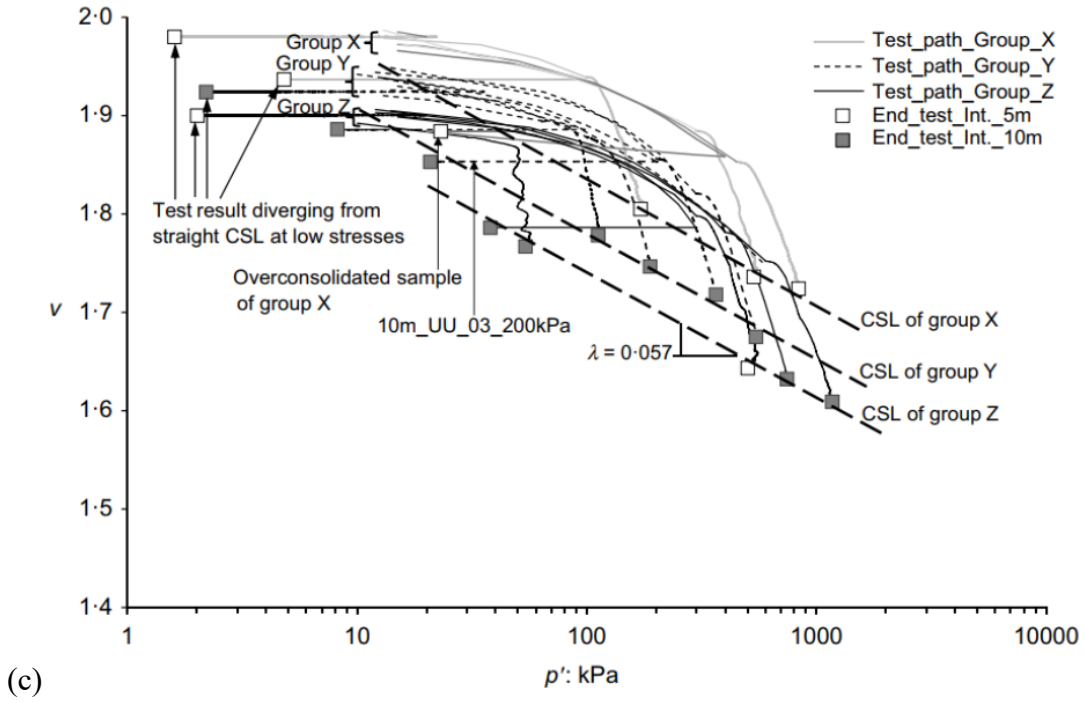

(c)

Figure 2-43 Critical states for a transitional silty loess in the volumetric plane of (a) intact samples at 10m and 5m depths and reconstituted samples at 10m depth; (b) straight parallel CSLs for all reconstituted samples and (c) all intact samples (Xu & Coop, 2017).

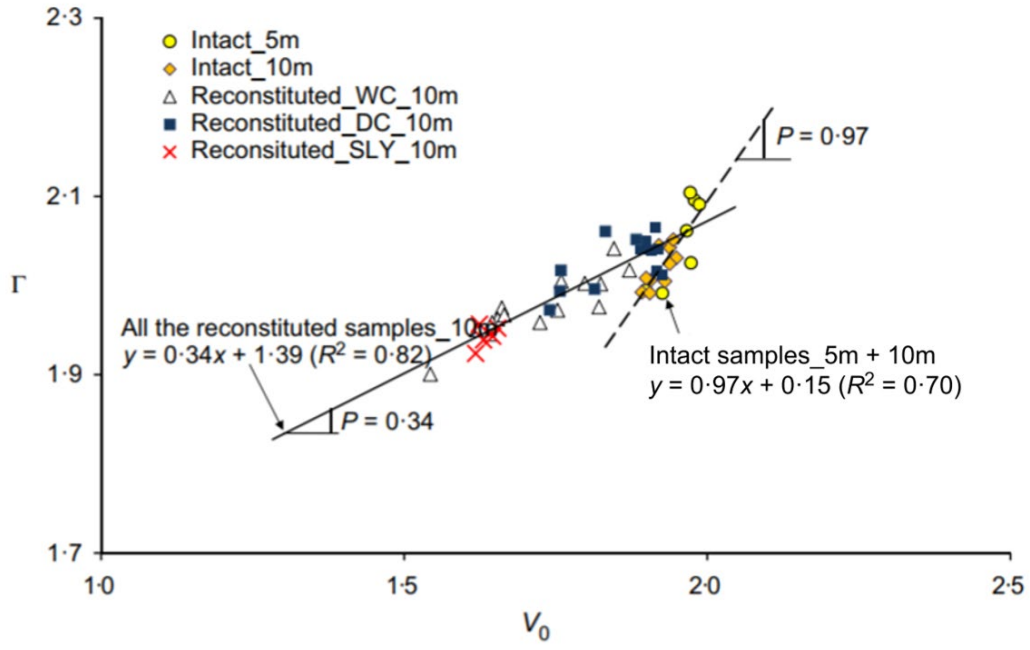

Figure 2-44 The P values for the reconstituted and intact samples of a transitional silty loess (Xu & Coop, 2017).

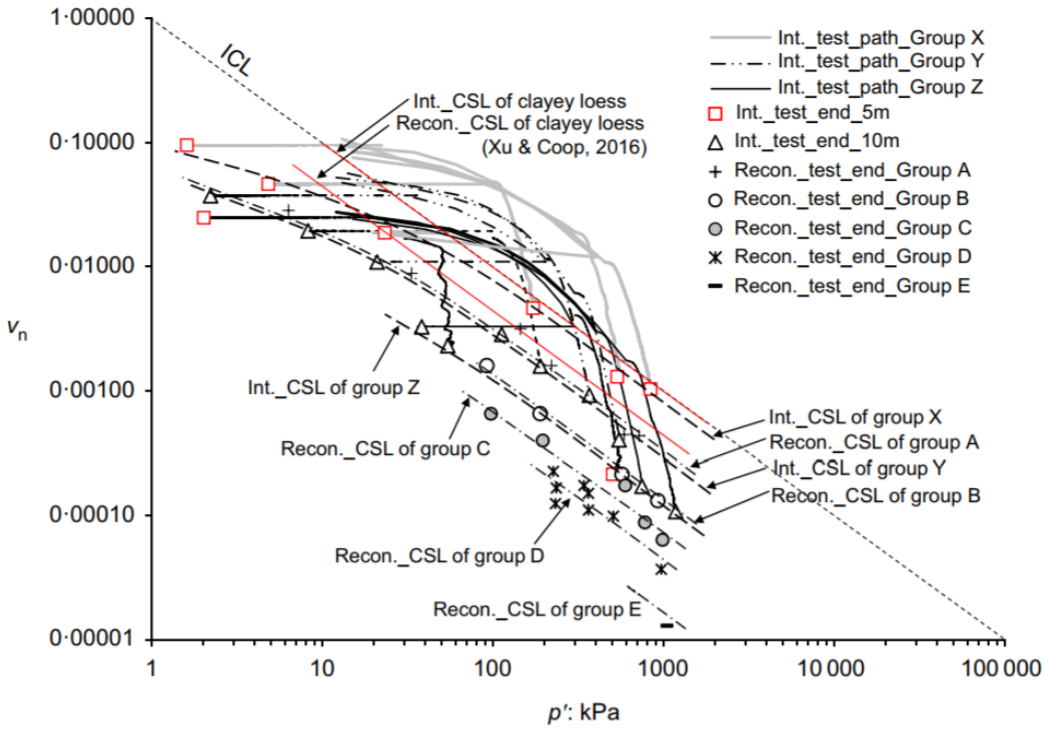

Figure 2-45 Normalised specific volume of the CSLs for the intact and reconstituted samples of a transitional silty loess using the isotropic ICL for group *A* (Xu & Coop, 2017).

CHAPTER 3 MATERIALS AND TEST PROCEDURES

3.1 Introduction

Soil materials that were expected to exhibit transitional behaviour were subjected to some characterisation tests to understand their basic soil properties. For the saturated samples, transitional behaviour was first identified through oedometer tests, and the transitional modes were further clarified by the triaxial tests. Transitional behaviour in unsaturated samples was also studied, with detailed apparatus and test procedures described in Chapter 4. The transitional behaviours for both saturated and unsaturated samples were expected to be explained through microstructural analysis using MIP tests and SEM tests. This chapter provides details on the soil materials tested and the procedures of these tests.

Section 3.2 introduces the materials tested, including tailings soils, a silty loess, and a kaolin-sand mixture. As described in Section 3.3, two sample preparation methods were adopted. The section also describes the calculation methods for determining the initial specific volume (v_i) of the prepared samples. Saturated oedometer tests were conducted on all soil samples, with the apparatus and test procedures detailed in Section 3.4. The primary focus of the saturated testing was the saturated triaxial tests. Section 3.5 provides a detailed explanation of the saturated triaxial tests, discussing the apparatus, calibration procedures, sample preparation, and test procedures for conventional triaxial tests and k_o compression tests, and also data analysis methods. The procedures for the MIP tests and SEM tests on freeze-dried samples used for microstructural analysis are explained in Section 3.6.

3.2 Materials

3.2.1 Tailings

The mineral tailings used in this study were retrieved from a mine about 100km south of Perth, Australia. These tailings were the by-product of rutile and zircon ore processing, which involved only a gravitational method and excluded crushing and the use of chemicals. The soil properties are summarised in Table 3-1 and the particle size distributions (PSD) are presented in Figure 3-1. The soil was separated into fine and sand components.

The fine part, known as slimes, was used in saturated tests and was named “fine mineral tailings” in this study. This focus was chosen because it represents the most critical portion of the tailings with respect to mechanical behaviour and stability concerns. The particle size distribution within tailings ponds typically varies both vertically and horizontally due to hydraulic sorting during deposition, resulting in complex stratification patterns. The finer tailings are of particular engineering significance, as their increasing concentration is associated with higher water retention, weaker sedimentation stratification, an elevated saturation line, and shorter dry beach lengths. These factors can all negatively impact the safety and stability of tailings storage facilities (Tian et al., 2024). Furthermore, previous research on transitional soils has shown that transitional behaviour is most often found in the finer portion of the grading (Coop, 2015), which further supports the focus on slimes in this study.

Transitional behaviour was observed in the fine mineral tailings, but the suction was found to be too high for the designed unsaturated triaxial apparatus. To address this problem, the fine mineral tailings were mixed with sand, and the mixture was named as “sandy mineral tailings”. Since transitional behaviour is often found in gap-graded soils, as presented in the literature review, the sandy mineral tailings as a mixture of

fine and sand was expected to be transitional. After testing different proportions of fines and sand, the sandy mineral tailings containing 60% sand and 40% fines were found suitable for the designed unsaturated triaxial tests and were therefore selected for the unsaturated tests. The details of component selection are provided in Section 6.2.2.

The PSD of the fine component (or fine mineral tailings) was obtained from sedimentation using a deflocculant. The sand component was analysed by wet sieving. The plastic and liquid limits (PL and LL) were 21.9% and 49.9% respectively for the fine component, which were determined by rolling thread and cone penetration tests. This indicated a medium plastic clay. As shown in Figure 3-2, X-ray diffraction showed that the predominant minerals present were kaolinite and quartz for the fines and sand components, respectively.

The specific gravity values (G_s) measured by pycnometer tests were 2.53 and 2.65 for fine and sand components, respectively. The G_s values used for sandy mineral tailings were calculated using the weighted harmonic mean of the specific gravities of the two components ($G_{s,a}$ and $G_{s,b}$), weighted by their respective dry mass fraction (x_a and x_b), as shown in Equation 3-1. This approach was derived by applying the total solid volume in terms of the component masses (m_a and m_b) and specific gravity, $V_{solid} = \frac{m_a}{G_{s,a}} + \frac{m_b}{G_{s,b}}$, to the equations of specific volume. This derivation works for all the equations of specific volume used in this study for both saturated and unsaturated samples, which will be shown in Section 3.3.3 later.

$$G_{s,mix} = \left(\frac{x_a}{G_{s,a}} + \frac{x_b}{G_{s,b}}\right)^{-1} \qquad \text{Equation 3-1}$$

3.2.2 Silty loess

A reconstituted silty loess was used in this study, retrieved from a depth of 10m in the Lanzhou region of Chinese Loess Plateau. The soil properties of the silty loess tested are summarised in Table 3-2 and the PSD is presented in Figure 3-3. Data were compared with a coarser silty loess previously tested by Xu and Coop (2017) that had a clear transitional behaviour. The G_s was 2.75 and the PL and LL were 18.3% and 29.7%. The PSD was measured by sedimentation method using a deflocculant. By comparison, the coarser silty loess also from a depth of 10 m in Lanzhou had a similar plasticity and G_s and only a slightly coarser grading. Given these similarities, the silty loess studied was expected to have transitional behaviour as well.

3.2.3 Mixture of kaolin and Leighton Buzzard sand

Transitional behaviour has been observed in a gap-graded mixture consisting of 75% quartz sand and 25% kaolin (Martins et al., 2001; Shipton & Coop, 2015). This artificial soil mixture is commonly used to study the fundamental behaviour of transitional soils in laboratory tests, as it eliminates more complex effects such as mineralogy on the mechanical behaviour and facilitates experimental repeatability (Shipton & Coop, 2012). A mixture of Leighton Buzzard sand and kaolin was used in this study and was expected to exhibit transitional behaviour as well.

The soil properties of the quartz sand and clayey kaolin used in this study are listed in Table 3-3, in comparison with those from Martins et al. (2001) and Shipton and Coop (2012). The kaolin used was sourced from the Bath Potter supplies. Its G_s was 2.65, and the PL and LL are 30.8 and 61.9, respectively. It mainly consisted of kaolinite (70%) and micaceous minerals (27%). The Leighton Buzzard sand employed was a rounded to sub-rounded quartz sand with a G_s of 2.67. Compared with those transitional

mixtures, the kaolin used here was more plastic or finer, and the quartz sand employed here was less angular.

Various proportions of quartz sand and kaolin were tested, and a mixture of 75% quartz sand and 25% kaolin exhibited the most obvious transitional behaviour. The G_s of this mixture was 2.655, calculated based on Equation 3-1. The PSD of this mixture is shown in Figure 3-4, compared to those from Martins et al. (2001) and Shipton and Coop (2012). The PSDs were measured by the sedimentation method using a deflocculant for the kaolin and by the wet sieving method for the sand.

3.3 Sample preparation

All the samples used in this study were reconstituted. Samples were prepared to achieve a wide range of v_i for investigating transitional behaviour. Since all the materials were originally dry and uniform, extra procedures like drying and sub-dividing were not needed to obtain representative reconstituted samples. Only the fine mineral tailings were a block, rather than in powder. The block was crushed with a grinding rod into small pieces, but not ground too severely to avoid changing the particle size.

Static compaction, as a common sample preparation method for achieving denser samples, was not used in this study because it can lead to uncontrolled over-consolidation of the samples. According to Shipton and Coop (2015), varying degrees of over-consolidation from the same initial specific volume do not affect the positions of NCL and CSL, as both are dependent solely on the initial specific volume prior to over-consolidation.

3.3.1 Slurry method

The slurry prepared with predetermined amounts of dry soil and water was placed directly into a sample mould. The wide range of v_i was achieved by using different

initial water content (w_i). The range of w_i used for different soils varied due to differences in plasticity. But for all the soils, the sample states resembled a dough for the lowest w_i and thick cream for the highest w_i. The slurry would have the soil and water segregated if too much water was added, and would crumble with too little water. Therefore, the range of v_i for a soil was decided by the range of w_i used, which was decided from trial and error. The required masses of the dry sample (m_d) and the distilled water (m_w) were calculated based on the w_i and expected v_i, using Equation 3-2 and Equation 3-3, where γ_d was dry unit weight, g gravity, Gs specific gravity, γ_w unit weight of water, and V volume of the specimen.

$$m_d = \frac{\gamma_d V}{g} = \frac{G_s \gamma_w V}{vg} \qquad \text{Equation 3-2}$$

$$m_w = m_d w = m_d \frac{v-1}{Gs} \qquad \text{Equation 3-3}$$

After calculation, the required amounts of the dry soil and water were thoroughly mixed, with extra care taken to break down any lumps using a spatula. The slurry was subsequently vacuumed in a desiccator until no more air bubbles were observed. Any amount of water lost during the vacuuming by evaporation was re-added. After being left overnight, the slurry reached a state of hydraulic uniformity and was ready to use. Slurries with high w_i were poured directly into the sample moulds. Since slurries with low w_i had no liquidity, they were pressed into the sample mould in small quantities at each time using a spatula. Extra attention was given to avoid any voids in the corners of the mould or in the sample. Details of the slurry sample preparation for oedometer and triaxial tests are presented later in Section 3.5.3.

Although the dense samples used water content lower than the liquid limit, meaning the mixture was no longer liquid, the term “slurry” is used here in a broader sense to describe the overall method. The maximum and minimum achievable specific volumes were determined through trial and error. The “slurry” was kept neither too wet, which could cause segregation of water and soil, nor too dry, which could lead to significant air entrapment. Slight unsaturation did occur in the dense samples at the start of testing, but any associated suction was likely minimal compared with the high stress applied.

3.3.2 Compaction method

It was found that the slurry method was unsuitable for certain cases so that a compaction method was adopted in this study as well. For instance, the mixture of quartz sand and kaolin at a high w_i prepared by the slurry method tended to segregate, and the compaction method addressed this problem. Additionally, samples prepared by the compaction method were more suitable for unsaturated tests in this study, compared to those using the slurry method. The specific samples and the reasons for employing the compaction method will be clarified and explained in each respective section. Consistency in the sample preparation method was maintained across the tests in each series to avoid any potential influence from sample preparation techniques.

The compaction method proposed by Ladd (1978) was adopted in this study. This method can give consistent results by achieving uniform and repeatable specimens. The test method was to compact a certain mass of moist sample to a predetermined height layer by layer. Since compacting the new top layer further densified the lower layers, the specimen in each layer was compacted to a lower degree of compaction than the expected final value, the ratio being defined as the under-compaction percentage (U). The U for the bottom layer was 10% for the densest specimen and 15% for the loosest specimen. The U for the top layer was 0% since the top layer should be compacted to

the expected density. The U_n was determined as the linearly increasing layer values n from the bottom to the top layers. The expected height from the bottom for each layer (h_n) was calculated based on the equation $\frac{h_t}{n_t}\left[(n-1)+\left(1+\frac{U_n}{1000}\right)\right]$, where h_t was the total sample height and n_t was the total number of layers. Although this method calculated the height of each layer with equal amounts of moist soil, the split mould available in the lab had equal heights for each of the three layers. The method was modified to calculate the amount of moist soil for each layer based on equal layer heights. The weight ratio of h_n for each layer, $\frac{h_n}{h_t}$, was used as the weight ratio of the moist soil mass for that layer m_n, such that $m_n = \frac{h_n}{h_t} m_t$, where m_t was the total sample mass.

A variety of w_i was used to reach a wide range of v_i in the compaction method, as for the slurry method. The w_i value was selected by trial and error, which will be explained later. Thus, the first w_i for a soil was randomly selected but always kept below the PL. The required amounts of dry soil and water were mixed and left overnight to allow for moisture equilibrium. Subsequently, the mixture was passed through a 1.18 mm sieve to break up any lumps, and any amount of water lost during equilibrium and sieving was re-added to the mixture.

Samples were prepared by static compaction in a split mould. The split mould had three layers with fixed equal height in each layer and a height of 78 mm in total. The detailed sample preparation for triaxial test using a split mould will be described later in Section 3.5.3. A volume control, rather than stress control, was employed to prepare samples to the desired v_i. A stress limit was considered for each soil to avoid any excessive pre-consolidation pressure. A higher w_i would be tried when the pressure limit was reached before the sample compressed to the designed height. This trial-and-

error process helped to select a suitable w_i, allowing the sample to be prepared within the specified pressure limit.

3.3.3 Calculation of initial specific volume and accuracy

A large error of the calculated v_i could result in an erroneous conclusion of non-convergent compression paths (Shipton & Coop, 2015). If the accuracy of the v_i calculated is much smaller than the difference of the final specific volumes (v_f) at a large stress level, it could be confidently concluded that compression lines are non-convergent. To illustrate this, an example of the oedometer compression curves for the fine mineral tailings is shown in Figure 3-5. Since the 0.4 difference in v_f at 8MPa cannot be caused by the ±0.013 accuracy of the v_i, it can be concluded that the compression lines for the fine mineral tailings are not unique. Therefore, it is important to estimate the accuracy of the initial v when assessing the convergence of the NCLs or the CSLs to determine the degree of transitional behaviour (Shipton & Coop, 2012, 2015; Rocchi & Coop, 2014).

Shipton and Coop (2012, 2015) proposed six different equations (Equation 3-4 to Equation 3-9) to calculate the v_i, which had some linkages between them but were as independent as possible. Each equation was based on different properties, namely initial bulk unit weight $\gamma_{bulk,i}$, initial dry unit weight γ_{di}, initial water content w_i, final water content w_f, final bulk unit weight $\gamma_{bulk,f}$, and final dry unit weight γ_{df}. In the equations, subscripts i and f stand for the initial and the final states, Gs the specific gravity, γ_w the unit weight of water, S_r the degree of saturation, γ_{bulk} the bulk unit weight, γ_d the dry unit weight, w the water content, and ε_v the overall volumetric strain. The calculated v_i $(\gamma_{bulk,i})$, v_i (w_i), v_i $(\gamma_{bulk,f})$ and v_i (w_f) would be incorrect for unsaturated samples. Rocchi and Coop (2014) proposed two equations (Equation 3-10

and Equation 3-11) to calculate v_i, $v_i(\gamma_{bulk,i}\ \&\ w_i)$ and $v_i(\gamma_{bulk,f}\ \&\ w_f)$, irrespective of the S_r. These equations were based on the combinations of the γ_{bulk} and the w.

$$v_i(\gamma_{bulk,i}) = \frac{(G_s - S_{ri})}{(\gamma_{bulk,i}/\gamma_w - s_{ri})} = \frac{(G_s - 1)}{(\gamma_{bulk,i}/\gamma_w - 1)} \quad \text{Equation 3-4}$$

$$v_i(\gamma_{di}) = \frac{G_s\gamma_w}{\gamma_{di}} \quad \text{Equation 3-5}$$

$$v_i(w_i) = \left(\frac{w_i G_s}{S_{ri}}\right) + 1 = w_i G_s + 1 \quad \text{Equation 3-6}$$

$$v_i(\gamma_{bulk.f}) = \frac{v_f}{1-\varepsilon_v} = \frac{(G_s - 1)}{(\gamma_{bulk.f}/\gamma_w - 1)(1-\varepsilon_v)} \quad \text{Equation 3-7}$$

$$v_i(\gamma_{df}) = \frac{v_f}{1-\varepsilon_v} = \frac{G_s\gamma_w}{\gamma_{df}(1-\varepsilon_v)} \quad \text{Equation 3-8}$$

$$v_i(w_f) = \frac{v_f}{1-\varepsilon_v} = \frac{w_f G_s + 1}{1-\varepsilon_v} \quad \text{Equation 3-9}$$

$$v_i(\gamma_{bulk,i}\ \&\ w_i) = \frac{\gamma_w(1+w_i)G_s}{\gamma_{bulk,i}} \quad \text{Equation 3-10}$$

$$v_i(\gamma_{bulk,f}\ \&\ w_f) = \frac{\gamma_w(1+w_f)G_s}{\gamma_{bulk,i}(1-\varepsilon_v)} \quad \text{Equation 3-11}$$

$$S_{ri} = \frac{G_s w_i \gamma_{bulk,i}}{\gamma_\omega G_s(1+\omega_i) - \gamma_{bulk,i}} \quad \text{Equation 3-12}$$

$$S_{rf} = \frac{G_s w_f \gamma_{bulk,f}}{\gamma_\omega G_s(1+\omega_f) - \gamma_{bulk,f}} \quad \text{Equation 3-13}$$

In this study, different v_i values were independently calculated for each specimen using these equations. Equation 3-4 to Equation 3-9 were used for saturated specimens, while Equation 3-5, Equation 3-8, Equation 3-10 and Equation 3-11were used for unsaturated specimens with their S_r calculated from Equation 3-11 and Equation 3-12. These equations for v_i were based on different properties calculated from independent measurements of volumes and weights of each specimen at the beginning and the end of the test. The mean of the v_i for each specimen was calculated from these v_i values. After discarding anomalous values with a deviation larger than ± 0.03, a new average v_i was calculated and used as the chosen v_i for the specimen. The accuracy of v_i for this specimen was determined by the maximum deviation from any non-discarded v_i values. The measurements required for each quantity in the equations of v_i and the details of the calculation based on these equations will be explained later in each type of test. Generally, the mean accuracy in this study was about ±0.013, slightly better than that achieved by Rocchi and Coop (2014), ±0.018.

3.4 Saturated oedometer tests

3.4.1 Saturated oedometer apparatus

The typical oedometer setup used is shown in Figure 3-6. It consists of a consolidation cell, a loading frame and deformation measurement. The loads added on the weight hanger were transmitted through the lever loading arm and the loading yoke into the consolidation cell. The specimen was placed in the consolidation cell and the loading cap at the top of the specimen transmits the loads vertically onto the specimen. The consolidation ring was laterally restrained by the locating ring at the base and the retaining ring with locking screws at the top. Base and top porous discs were used to allow the drainage of water from the specimen, and filter papers between the porous

stones and specimen were used to prevent soil from clogging the porous stones. The settlement of the specimen was measured by a dial gauge.

3.4.2 Test procedures

Sample preparations by slurry and compaction methods were described in Sections 3.3.1 and 3.3.2, including the procedures to obtain the appropriate w_i for the desired v_i and to prepare samples in sample moulds. This section is to describe the adopted procedures from Rocchi and Coop (2014) to obtain independent measurements of heights and weights of specimens at the beginning and the end of the tests. These measurements were used to calculate the v_i and the accuracy based on the equations described in Section 3.3. The measurements required for each quantity in the equations are listed in Table 3.4. Different methods were used to measure the initial sample weight and initial sample height in order to calculate $\gamma_{\mathrm{bulk,i}}$ and γ_{di}. A separate subsample was used to calculate $\mathrm{w_i}$. These ensured that $\gamma_{\mathrm{bulk,i}}$, γ_{di} and $\mathrm{w_i}$ were independent so that the corresponding v_i values were also independent. The same method was applied to the sample at the end of test, ensuring that the v_i values corresponding to the $\gamma_{\mathrm{bulk},f}$, $\gamma_{\mathrm{d}f}$ and w_f were independent as well. The procedures for obtaining these measurements are explained below.

After setting the oedometer cell in the loading frame with a dummy sample in, the dial gauge reading was recorded and later used to determine one value of the initial sample height. The weights of dry soil and water used were measured. Then, as demonstrated in Section 3.3, the sample was carefully prepared up to the top rim of the consolidation ring, as shown in Figure 3-6, to achieve the v_i desired. Therefore, another value of the initial sample height was equivalent to the ring height. The remaining moist soil was weighed again. The initial moist sample weight was calculated as the difference

between the weights of the moist sample before and after sample preparation. A subsample taken from the remaining moist soil was used to measure the w_i by weighing it before and after oven-drying. The moist soil was oven-dried and weighed. The weight of the dry soil used was determined by subtracting the sum weight of the oven-dried subsample and remaining soil from the total weight of the dry soil. After setting up the specimen, the initial gauge reading on the soil sample was recorded. Another initial height of the specimen was determined from the difference between the digital gauge readings on the dummy sample and soil sample.

After flooding the oedometer cell with water, loads were incrementally added or removed after each two hours to allow stabilisation. The gauge readings after each stabilisation were recorded to calculate the changes of volume strain. All the water in the consolidation cell was removed before unloading the final weight at around 10 kPa to avoid the sample absorbing excessive water. The specimen was taken out and weighed, which was the final moist weight of the sample. The average depth between the soil surface and the top rim was measured around the ring, which was used for one value of final height. Another final height was the initial sample height measured from the dummy sample subtracting the settlement. The specimen was oven-dried to determine the final dry weight of the specimen.

3.5 Saturated triaxial tests

3.5.1 Saturated triaxial apparatus

The triaxial system used in this study includes the triaxial cell, the measuring instruments, the pressure systems, and the data acquisition and the control systems, as shown in Figure 3-7.

Triaxial cell

A Bishop and Wesley triaxial cell was used. The cell top was fitted with a connection tube, an internal load cell and an external vertical linear variable differential transformer (LVDT). The connection tube was used to remove water from the suction cap, which connects the top platen to the adaptor fixed to the load cell. This connection aligned the sample with the adaptor, ensuring that the axial load was homogeneously transmitted on the sample. The load cell measured the deviator force, with the readings sent back to data logger. The external axial LVDT with 25 mm linear range measured the vertical displacement of the pedestal, which corresponded to the vertical displacement of the sample when the suction cap was connected to the adaptor. The cell body, made of a Perspex chamber, is filled with water to apply uniformly radial cell pressure to the specimen. The water was supplied from the lab water system through a distribution panel. Samples with a 38 cm diameter sit on the pedestal with a low air entry porous stone underneath. A side filter paper was placed around sample to accelerate the drainage. A latex membrane was used to separate the cell water from the specimen and sealed by O-rings at the top and bottom platens. There were two openings on the pedestal, one connecting to the back pressure system and the other for drainage. There were two additional lines on the cell base, one for the cell drainage and another connecting to the cell pressure system.

Local LVDTs

Two local axial LVDTs with a 12 mm linear range were installed diagonally opposite on the sample, with their mounts glued to the sample membrane. The armatures were free to move in the core so that the local strains between the mounts were measured. The local axial LVDTs were used in all saturated tests to obtain the stiffness at small strain levels during shearing. The local radial LVDTs were installed for unsaturated

tests and were also used in ko compression saturated tests. The supports of the local radial LVDTs were fixed to the pedestal diametrically opposite each other on the sample. Supports transferred the radial strain to a vertical armature displacement. The local radial LVDTs, larger than the axial ones, had a 25 mm linear range.

Pressure systems

The triaxial apparatus operated with a hydraulic pressure system, involving the cell, back and ram pressures. The water pressures were converted from air pressures through air-water interfaces. The interfaces for cell and axial pressure systems were rubber balloon cylinders. The ram was also driven by a constant rate of strain pump (CRSP) at a predetermined rate of displacement, which was controlled by computer. The Imperial College type volume gauge worked as the air-water interface for back pressure system. Additionally, it measured the pore water drained from sample through an incorporated LVDT. The air in the interfaces was supplied from the lab air system and regulated by air pressure controllers, which were computer-controlled. Water pressures in the interfaces were distributed to the corresponding pressure systems through a distribution panel. This panel was equipped with a pressure gauge, multiple isolating valves for each line, a water supply, a drainage line and several spare ports with valves. It allows for refilling or draining each interface and for checking the water pressure in each pressure line. The spare ports enabled to incorporate other water pressure equipment into the system if required. Pressure transducers were installed into the cell and back pressure lines near their ports. The ram pressure could only be checked through the gauge on the distribution panel.

Data acquisition and control systems

A datalogger was adopted to obtain and record highly accurate readings from pressure transducers in real time by automatically amplifying the input voltages and converting

analogue to digital signals. All local LVDTs had amplifiers that were connected to the datalogger for data recording. A software named TRIAX provided a programmable interface to scan automatically the datalogger and control the air pressure controllers. The recorded data from the datalogger were stored and analysed in the computer and were displayed on the screen to monitor the progress of tests.

3.5.2 Calibrations of saturated triaxial apparatus

Calibration of volume gauge

The volume gauge used in the back pressure line was an Imperial College type volume change device. In addition to functioning as the air-water interface, it also measured the pore water drained from sample through an incorporated LVDT. The calibration of the volume gauge was conducted by pumping known amounts of water into it and converting the voltage changes of the LVDT into the volume changes of water. A Bishop pump with 1.1024 cc/revolution was used, as shown in Figure 3-8. The volume gauge was connected to the Bishop pump through the distribution panel. Before calibration, the volume gauge was left under 750 kPa for a few hours to dissolve any trapped air and was flushed four times. The revolutions of the Bishop pump and corresponding voltage values of the volume gauge were recorded. It was found that the output voltage, over a range of ±5 V, was linearly proportional to the amount of water pumped across the entire range of 50 cc.

Calibration of local axial LVDTs

The voltages of the local LVDTs were first zeroed without their armatures to bring them to their reference state, ensuring that the linear range remained consistently in the same position. The local LVDTs were then directly mounted on a frame and calibrated using a micrometer with a resolution of 0.005 mm, in steps of 1 mm, as shown in Figure 3-9. A linear relationship was found between the applied displacement of 12 mm and the

measured voltage over a range of ± 5 V. This process identified the linear range on the armature and allowed the conversion of voltage to displacement within the software. In order to obtain small strain stiffness, the amplifiers of the LVDTs were adjusted to be close to 0V before shearing to optimize the resolution of the datalogger.

Calibration of local radial LVDTs

The local radial LVDTs used were larger than the local axial LVDTs. A schematic of the radial LVDT support is shown in Figure 3-10, following the design of Ackerley et al. (2016). The LVDT core was held vertically by a holding case and locked in place with a pin, while the armature rested on the upper face of an L shape arm. The round-end screw made a contact with the sample and moved along with the L shape arm as the radial displacement (Δr) occurred. This Δr was converted into the vertical displacement of the armature (Δd) through the pivoting of the L shape arm. The round-end screw could be adjusted forward or backward towards the sample to ensure horizontal movement at start of test for samples with any diameter. Since the two arms of the L shape arm were of similar length and the round-end screw began in a horizontal orientation, Δd was close to Δr. To ensure smooth movement of the L shape arm and good contact of the round-end screw with sample, an additional weight was attached at the end of arm. An adjustment column allowed for height adjustment, ensuring that the round-end screw contacted the sample at its mid-height. The entire assembly was seated on a base fixed on the pedestal, enabling it to move along with sample during shearing.

The same calibration on the axial LVDTs was conducted on radial LVDTs first to find the linear range of the armatures. This found that the radial LVDTs have a calibration of about 0.25 V/mm over their 25 mm and ± 3 V linear range. Then the calibration for the LVDT in its support was required, since the radial displacement was translated to the vertical LVDT armature through the L shape arm. A linear relationship between the

applied displacement Δr and measured displacement Δd was found over at least 4 mm range, which was symmetric with the position corresponding to a horizontal orientation of the round-end screw. This highlighted the importance of positioning the round-end screw horizontally at the start of the test. Since the length of the round-end screw will change the geometry of rotation mechanism, a series of calibrations were done on different lengths of round-end screw. Although it showed that the slope between the Δd and Δr changes less than 0.02% when the length changes 2 mm, the round-end screw was locked in place.

Apparatus compliance

A systematic error could occur in the vertical displacement measured by the external axial LVDT during deviatoric loading. This error could arise from the compression of components in the deviatoric loading path, such as the screw joint on the loading shaft and the filter paper, but it should only be significant at small strain levels. To address this, an axial compliance test was conducted on a metal dummy sample loaded to 500kPa deviator stress. This was under the assumption that the dummy sample was incompressible. The relationship between the vertical displacement (D) and the applied force (F) is plotted in Figure 3-11. The curve is fitted with an equation, $D = -3\times10^{-7}F^2 + 4.5\times10^{-4}F$, which was used to correct the readings of external axial LVDT.

Correction for membrane restraint

The latex membrane and side filter paper could impose a restriction effect and influence the radial stress when the sample barrelled, particularly at low stress levels. To avoid this, cuts were made across the strips of the side filter paper to reduce rigidity, and a correction for the latex membrane was applied to the cell pressure. Fukushima and

Tatsuoka (1984) proposed an equation for the additional radial stress, $\Delta\sigma_\gamma = -2 \cdot \frac{M\varepsilon_r}{D_i}$, where M is the extension modulus of the rubber membrane per unit width, ε_r is the radial strain of the membrane, and D_i is the initial diameter of the membrane. An M value of 3.6 kN/m was used in this study based on the membrane type. This correction was applied to all tests, though $\Delta\sigma_\gamma$ is typically only about 2 kPa at the largest radial strains.

3.5.3 Triaxial sample

Both slurry and compaction methods were used in this study. The preparation of the moist soil with appropriate w_i for the desired v_i for both methods was already described in Sections 3.3.1 and 3.3.2. This section gives the specific details on adopting these methods to prepare triaxial samples in sample moulds. The general calculation method of v_i was introduced in Section 3.3.3, and this section is about applying the calculation methods to the triaxial samples.

Slurry method prepared in consolidometer

More liquid slurries were prepared in a consolidometer. As shown in Figure 3-12, the consolidometer consists of a 38 mm tube, two platens with porous stones and a drainage line, a seating ring, and a water holder. Before assembly, a small amount of lubricating oil was applied into the inner wall of the tube and the side of the platens to reduce the friction during sample consolidation. The tube and the base platen were placed in the water holder, with the tube sitting on the seating ring. The slurry was poured directly into the tube, while holding and tapping the assembly to avoid trapping air. After the slurry was filled to the top, the top platen was placed, ensuring the top platen was free to rotate. Otherwise, the tube and top platen were cleaned, and the top platen was reapplied with lubricating oil. When the assembly was ready, a 0.5 kg weight was

placed on the top of top platen to consolidate the sample, with a dial gauge monitoring the settlement. The square root of time was plotted against the settlement to ensure the sample consolidated completely. The load was incrementally added up to 3 kg (26 kPa) in this method, which typically took about two weeks. To maintain the soil saturated during consolidation, the top platen was flushed daily with distilled water through the drainage line, and the water holder was kept filled up with water all the time.

After consolidation, the sample was extruded from the tube and placed in a sample holder. To prevent the sample from sticking to the holder, baby powder was spread on the inner surface of the holder. The sample was then trimmed to a height of about 76 mm, and the remaining sample was used to measure the w_i. The diameter and height of the sample were measured to calculate the initial volume of the sample, and the mass of moist sample was weighed. After the triaxial test, the sample was oven-dried and weighed, after weighing the mass of the moist sample. All these measurements were used to calculate the initial bulk unit weight ($\gamma_{bulk,i}$), the initial water content (w_i), the final bulk unit weight ($\gamma_{bulk,f}$), and the final water content (γ_{wf}). These values were relatively independent and used to calculate the v_i and accuracy as outlined in Section 3.3.3.

Slurry method prepared in split mould

When the slurry had a low w_i and lacked liquidity, it became difficult to place it into the tube of the consolidometer without voids so that a split mould was used in this case. The mould had a diameter of 38 mm and a height of 76 mm. The split mould, shown in Figure 3-13, was joined by screws in the middle, secured by retaining rings at the ends, and seated on a short platen. A piece of filter paper was placed inside the mould to prevent the soil from sticking in the mould. The slurry soil was pressed into the mould piece by piece in small quantities using a spatula and filled up to the top. Special care

was taken to press the soil into the corners and to avoid voids between sample pieces. After removing the sample from the mould and peeling the filter paper off, the sample was placed in a sample holder sprinkled with baby power. The sample was then trimmed to 76 mm, with the remaining sample used to measure the w_i. For very sticky samples, the filter paper was not removed until the sample was placed in the triaxial apparatus.

This process limited the maximum v_i achievable, compared with the oedometer sample, as overly soft samples are difficult to handle and prone to disturbance during sample transfer and assembly. For the samples with low v_i, mixtures were already strong enough to be handled gently, so these mixtures were placed directly into a split mould by hand. To avoid the formation of any macro-pores and non-uniformities in the dense samples, the paste was gently and quickly pressed against the bottom and sides of the mould. This technique is similar to that used in the preparation of Liquid Limit fall cone samples. Since the MIP data for the dense samples presented in Chapter 5 show no evidence of macro-voids, it can be concluded that air entrapment was negligible.

The diameter and height of the sample were measured to calculate the initial volume, and the mass of the moist sample was weighed to calculate $\gamma_{bulk,i}$. The rest of the moist soil and the subsample to measure the w_i were oven-dried and weighed as the m_r and m_w, respectively. To calculate the γ_{di}, the initial mass of dry sample was calculated by subtracting the m_r and m_w from the total dry soil used in sample preparation. After the triaxial test, the sample was weighed to calculate the $\gamma_{bulk,f}$ and oven-dried to calculate w_f. Then, v_i and its accuracy were calculated based on $\gamma_{bulk,i}$, w_i, γ_{di}, $\gamma_{bulk,f}$, and w_f.

Compaction method prepared in split mould

The split mould used in this method was the same as that for the slurry method but with different platens. Two sets of platens were used to prepare the sample in three equal height layers, as shown in Figure 3-14 (a). The first, second and the third layers were prepared by the combinations of two high platens, the one low and one high platen and the two low platens, respectively. The split mould was assembled with screws and retaining rings. After applying a small amount of lubricating oil to the inner wall of the mould, the required amount of moist soil for the first layer was placed into the mould with the high platen. Extra attention was taken in pushing the soil into the corners of the sample mould to avoid any voids. The sample was then statically compacted with the high platen on top. Before placing the second layer, the top surface of the previous layer was scarified, particularly along the edges, to ensure good connection with the next layer. The second and third layers were built in the same way as the first layer with the corresponding sets of platens.

A disk with a 7 mm height was placed at the bottom of the mould first before preparing soil sample, to reserve space for the subsample used for measuring w_i. After the three-layered sample was prepared, the disk was removed from the mould. As shown in Figure 3-14 (b), the required amount of moist soil for the 7mm height was then compressed on top of the prepared sample, separated by a filter paper. This subsample was representative for the measurement of w_i, as it underwent the same sample preparation process as the prepared sample. The same method used in the slurry method within the split mould was applied to calculate $\gamma_{bulk,i}$, γ_{di}, $\gamma_{bulk,f}$, and w_f. The v_i and its accuracy were then determined based on $\gamma_{bulk,i}$, w_i, γ_{di}, $\gamma_{bulk,f}$, the w_f.

3.5.4 Conventional triaxial tests

Sample setting-up

The pedestal was deaired by flushing the water from the supply through the back pressure and drainage lines. The back and cell pressures were set to zero when the water level in the cell reached the mid-height of the sample. The voltages of the local LVDTs were zeroed without their armatures to establish reference states. The measurement of the local LVDTs in mm were zeroed when the armatures were positioned at 0 V in the middle of the linear ranges. This process marked the positions of 0 V, allowing the armatures to be initially placed 5 mm above them, near the upper limit of the linear ranges.

After the sample was removed from the mould, it was placed on the pedestal with a low air entry porous stone and a filter paper underneath and with a top platen on top. A side filter paper was wrapped around the sample to assist the drainage of water from the top to the bottom. Grease was applied to the sides of the pedestal and top platen. The membrane was placed around sample using a membrane stretcher, and O-rings were placed on both the pedestal and top platen using an O-ring stretcher to seal the membrane.

The mounts of the two local axial LVDTs were glued to the membrane on opposite sides. A pair of mounts for each LVDT were positioned about 50 mm apart, covering about $2/3$ of the sample height. Once the glue had dried, the inner and outer distances between the two mounts were measured on both sides. The average of these measurements was used as the initial distance to calculate the local axial strain for that specific LVDT, referred to as gauge length. The LVDT body was fixed in the upper mount using a screw, with the armature resting on the lower mount. The LVDT body was positioned 5 mm above the pre-zeroed 0 mm position, providing about 11 mm

linear range for the LVDT. The LVDT cables were carefully arranged to ensure the sample was not tilted by the cables or disturbed during placement of the cell. For the radial LVDTs, the positions of the LVDTs on the support were already adjusted during calibration, and the round-end screws on the supports were oriented horizontally.

A small amount of grease was applied to the inner surface of the suction cap before it was placed on the top platen. Finally, the triaxial cell was closed and filled with water, and the computer system began recording data from all pressure transducers, volume gauge, load cell and LVDTs until the end of the test.

Saturation stage

The saturation began with 50 kPa back pressure and 70 kPa cell pressure. The back and cell pressures were increased to 100 kPa and 120 kPa at a rate of 50 kPa/hour, maintaining a constant 20 kPa effective stress. After that, the sample was allowed to stabilize for a day. Afterwards, with the back pressure line was closed and the cell pressure increased by 20 kPa. The B-value was calculated by dividing the change in pore pressure by the change in cell pressure after waiting for 10 minutes. The sample was considered saturated when the B-value exceeded 0.95. Typically, samples prepared by the slurry method were saturated under 100kPa back pressure, while samples prepared by the compaction method required the back pressure to be increased to 200 kPa. Stabilization of the sample, indicated by a stable volume gauge reading, generally took one day.

Before starting the test, the suction cap was connected. The ram pressure was increased to be slightly larger than the cell pressure, allowing the pedestal to float within the cell so the sample could move freely with minimal force applied. Then the Bishop pump was connected to the tube on the adaptor at the top of the cell. After zeroing the load

cell, the loading shaft was slowly screwed down until the adaptor was nearly in contact with top platen. As soon as the reading of the load cell began to rise, the suction cap was sealed to the adapter and top platen. The water trapped inside the suction cap was slowly sucked out by carefully unscrewing the Bishop pump handwheel, ensuring the applied load remained within $\pm$10 N. With the pedestal free to move vertically, the sample could move upward with applied deviator force less than 9 kPa. During suction cap connection, the back pressure line remained closed to minimize disturbance to the sample, while the cell pressure line stayed opened to the air-water interface to maintain constant cell pressure.

After the suction cap was connected, the Bishop pump was disconnected from the tube, and the ram pressure was adjusted so that the load on sample was about 0 N. The sample was then allowed to stabilize under the previous back and cell pressures, which typically took about half a day.

Compression stage

After the sample stabilised, the isotropic compression stage began. The ram pressure was controlled to maintain the load at 0 N, while the back pressure was maintained constant. The cell pressure was increased with rates of 1.5 kPa/hour, 2.5 kPa/hour, 3.5 kPa/hour and 4.5 kPa/hour for effective stress ranges of 20-50 kPa, 50-100 kPa, 100-200 kPa and 200-400 kPa. As a result, each compression stage took about 20 hours, 20 hours, 28.5 hours, and 44.5 hours, respectively. The sample was allowed to stabilise between each compression stage to ensure the compression rate was appropriate and to allow pore water to dissipate properly. Each stabilisation typically lasted one day.

Shearing stage

After the compression stages were complete, the sample was ready for shearing. The back pressure line was closed for the undrained shearing tests while the pore pressure was measured. For the drained shearing tests, the back pressure was maintained constant. The cell pressure for both cases was maintained at a constant value. The axial ram control was changed to the Constant Rate of Strain Pump (CRSP). The applied rates were 0.05 mm/hour, 0.1 mm/hour, 0.2 mm/hour and 0.4 mm/hour for axial strains in the range of 0-0.01%, 0.01-0.1%, 0.1-1%, and 1-25%, respectively. The data recording interval was adjusted to capture about 200 data points within each strain range. The entire shearing process typically took about 3 days.

After shearing, the drainage line was closed to lock the water content in the soil sample. The ram control was changed to the air-water interface with the pressure close to cell pressure, allowing the deviator force to be 0 N. The tube in the adaptor was then connected to the Bishop pump, and water was slowly pumped into the suction cap to disconnect it from adaptor. Once the suction cap was disconnected, the top loading shaft was screwed up to completely detach the suction cap. The ram pressure was further reduced to lower the pedestal in preparation for the next test, and the valve on the ram pressure line was closed to lock the pedestal in place. After reducing the cell pressure and draining the cell water, the sample was removed. It was then weighed in its moist state after removing the membrane and filter paper and again in a dry state after oven-drying.

3.5.5 k_o compression triaxial tests

The k_o compression triaxial tests were conducted to compare the results with those of the oedometer tests. The procedures for sample setup and saturation were the same as those used in the conventional triaxial tests. During the k_o compression stages, the cell

pressure was controlled to maintain a constant radial strain, as measured by the two local radial LVDTs. The sample was initially compressed at a rate of 0.04 mm/hour using the CRSP. When the cell pressure began to increase too rapidly, the rate was reduced to 0.01 mm/hour. The back pressure was kept constant throughout the process.

3.5.6 Data analysis

The volumetric strain (ε_v) was determined from the change recorded by the volume gauge and used to calculate the specific volume and total volume during compression and shearing. The corrections for the membrane restraint and apparatus compliance, as mentioned in Section 3.5.2, were applied to adjust the cell pressure and axial strain measured from the external LVDT during shearing. The sample height was determined using the corrected external axial strain, and the cross-sectional area was obtained by dividing the total volume by the current sample height. The deviator stress (q) was then calculated by dividing the deviator force by this cross-sectional area.

To calculate the stiffness at small strain levels, the local axial strain (ε_a) for each side was calculated by dividing the displacement measured from the local LVDT by the gauge length at the start of shearing. The tangent stiffnesses (G) for small shear strains were derived through the linear regression over short intervals of the q: ε_s plot, where ε_s represents the shear strain. The ε_s was calculated based on Equation 3-14, where ε_r is the radial strain. Since the local radial LVDTs were not installed for most of the saturated tests, the ε_r was calculated using Equation 3-15, which is applicable for both small and large strains.

$$\varepsilon_s = \frac{2}{3}(\varepsilon_a - \varepsilon_r) \qquad \text{Equation 3-14}$$

$$\varepsilon_r = 1 - \sqrt{\frac{1-\varepsilon_v}{1-\varepsilon_a}}$$ Equation 3-15

For the k_o compression saturated triaxial tests, the local radial LVDTs were used for strain control during testing. The sum of the measurements from both LVDTs represented the change in diameter, as these two measurements were not independent. The radial strain of the sample was calculated by dividing the change in diameter by the initial sample diameter.

3.6 Microstructure tests

3.6.1 Freeze-dried samples

Some samples after testing were used for microstructural analysis. The central part of the sample was carefully cut out, as it was considered free from boundary effects. To preserve it, the cut part with top surface marked was wrapped in cling film and then covered with melted wax, following with two additional layers of film and wax. This process was completed quickly to prevent water loss and preserve the microstructure. The samples were stored in a temperature-controlled lab room until they were freeze-dried.

To minimize disturbance to the microstructure during dehydration, the preserved samples were freeze-dried. This process was conducted at Ecole des Ponts ParisTech, France (ENPC), using the equipment shown in Figure 3-15. After unpacking, the samples were quickly cut into soil sticks measuring 10mm×5mm×5mm, with the top surface marked. The soil sticks were then ultra-quick frozen in liquid nitrogen, which was cooled to its freezing point (-210 ℃) under vacuum. This method of ultra-quick freezing converts pore water into crypto-crystalline ice without causing volume expansion

(Délage & Pellerin, 1984). Once frozen, the soil sticks were wrapped in tissue paper and placed in vacuum tubes for over 24 hours to complete sublimation of the ice.

3.6.2 MIP tests

Mercury Intrusion Porosimetry (MIP) test was utilized in this study to characterise the pore size distribution of the freeze-dried samples. The test was conducted at ENPC using a Micromeritics AutoPore IV 9500 Automated Mercury Porosimeter, as shown in Figure 3-16. This device had four high-pressure ports and two low-pressure ports. The penetrometer used for the test included a cell to hold the sample, a cap to close the cell and a stem through which mercury was injected. About 1g of freeze-dried sample was placed in the penetrometer. Initially, the penetrometer was put into the low-pressure port (3.6-200 kPa), where the mercury intruded into pores ranging from 352 μm to 6 μm in diameter. The low-pressure phase had 38 pressure stages, with an equilibrium time of 10 seconds per stage, taking about half an hour overall. Afterwards, the penetrometer was transferred to the high-pressure port, where pressures between 200 kPa and 227 MPa were applied, corresponding to entrance pore diameters between 6 μm and 5.5 nm. This high-pressure phase involved 63 data points with an equilibration time of 120 seconds per point, taking roughly 5 hours in total. After the test was completed, the device generated a report listing the pore diameter, cumulative pore volume, and incremental pore volume for each pressure stage. These data were used to plot the pore size distributions.

3.6.3 SEM tests

Scanning electron microscope (SEM) tests were conducted to analyse the fabric, particularly the particle orientation and pore structure of sample. These tests were conducted at the department of Earth Sciences at UCL, using the equipment shown in Figure 3-17 (a). The freeze-dried samples were broken to create vertical surfaces, with

the top sides clearly marked. The broken samples were sprayed with a layer of gold to improve the conductivity, as shown in Figure 3-17 (b). The coated samples were then mounted on a sample adapter for the SEM tests. Top sides were placed upward to ensure the orientations in the generated images could be identified correctly. The sample adapter, with maximum of 7 coated samples, was placed inside the SEM chamber, and each sample was observed in turn. Under vacuum, the electron gun emitted a focused beam of electrons onto the surface of the soil sample. The electrons interacted with atoms of the samples, producing the surface topography images on the monitor. The focus, contrast, and brightness were adjusted using the SEM software to produce clear images.

3.7 Summary

The oedometer and triaxial tests were performed to clarify the transitional behaviour of the saturated soil samples. Some of these samples after testing were examined in MIP and SEM tests for microstructural analysis to explore further the reasons behind the observed transitional behaviour. This chapter detailed the apparatus and test procedures used, while the results will be presented and discussed in Chapter 5.

Table 3-1 Material properties of tailings.

Tailings	Fine component	Sand component
$LL(\%)$	49.9	
$PL(\%)$	21.9	
Plasticity	Medium plastic	
Gs	2.53	2.65
D_{max}(μm)	64	3350
D_{50} (μm)	0.4	400
D_{min} (μm)	0.15	64
Soil type	Kaolinite clay	Quartz sand

Table 3-2 Material properties of loess soil studied, compared with a coarser silty loess with transitional behaviour (Xu & Coop, 2017).

Reference	This study	Xu and Coop (2017)
$LL(\%)$	29.7	26.8
$PL(\%)$	18.3	17.8
$I_p(\%)$	11.4	9.0
Plasticity	Low	Low
G_s	2.72	2.70
D_{max}(μm)	100.0	100.0
D_{50} (μm)	28.9	34.1
D_{min} (μm)	4.5	1.6
Soil type	Silty loess	Coarser silty loess

Table 3-3 Material properties of quartz sand and kaolin studied, compared with kaolin-sand mixtures with transitional behaviour from Martins et al. (2001) and Shipton and Coop (2012).

Reference	**This study**	**Martins et al. (2001)**	**Shipton & Coop (2012)**
		Kaolin	
Source	Commercial kaolin	Commercial kaolin	Speswhite kaolin
$LL(\%)$	61.9	39	62
$PL(\%)$	30.7	30	32
$I_p(\%)$	31.2	9	30
Plasticity	High	Medium	High
G_s	2.65	-	2.61
D_{max} (μm)	31.6	149.8	151.2
D_{50} (μm)	1.4	7.4	38.0
D_{min} (μm)	0.6	7.4	0.6
Soil type	clay	Silt	Silt
		Quartz sand	
Source	Leighton Buzzard sand	Sand of fluvial origin	Thames Valley sand
Description	Rounded to sub-rounded	Sub-rounded	Sub-rounded to sub-angular
G_s	2.67	-	2.67
D_{max}(mm)	1.18	2.01	1.17
D_{50}(mm)	0.77	0.65	0.80
D_{min}(mm)	0.21	0.17	0.41

Table 3-4 Measurements required for each quantity in equations to calculate initial specific volume for oedometer samples.

Equation	Quantity	Sub-quantity	Required measurements
Eq. 3.3 *Eq. 3.9*	$\gamma_{bulk,i}$	Initial weight	The difference of weights of the moist sample before and after setting up specimen.
		Initial height	The height of a dummy sample plus the difference of gauge readings on the dummy sample and specimen.
Eq. 3.4	γ_{di}	Initial weight	The difference of weights of total dry sample and sum weights of oven-dried subsamples and remaining sample.
		Initial height	The height of consolidation ring.
Eq. 3.5 *Eq. 3.9*	w_i		Based on moist and oven-dried weights of subsample.
Eq. 3.6 *Eq.3.10*	$\gamma_{bulk,f}$	Final weight	The weight of moist specimen in ring.
		Final height	The initial height calculated from dummy sample minus the settlement.
Eq. 3.7	γ_{df}	Final weight	The weight of oven-dried specimen in oedometer ring.
		Final height	The height of ring minus average depth between top rim of ring and surface of specimen.
Eq. 3.8 *Eq.3.10*	w_f		Based on moist and oven-dried weights of specimen in ring after test.
Eq. 3.6-3.8	ε_v		Settlement measured by the gauge divided by the initial height.

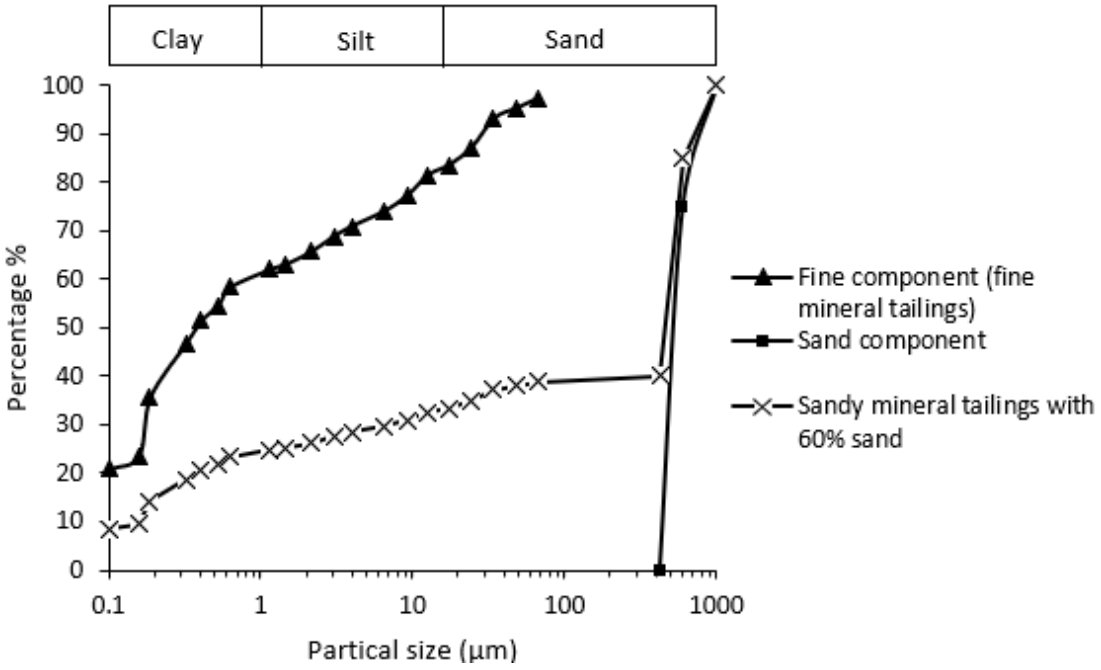

Figure 3-1 Particle size distribution of mineral tailings, including both fine and sand components, as well as the fine mineral tailings used for saturated tests and the sandy mineral tailings with 60% sand used for unsaturated tests.

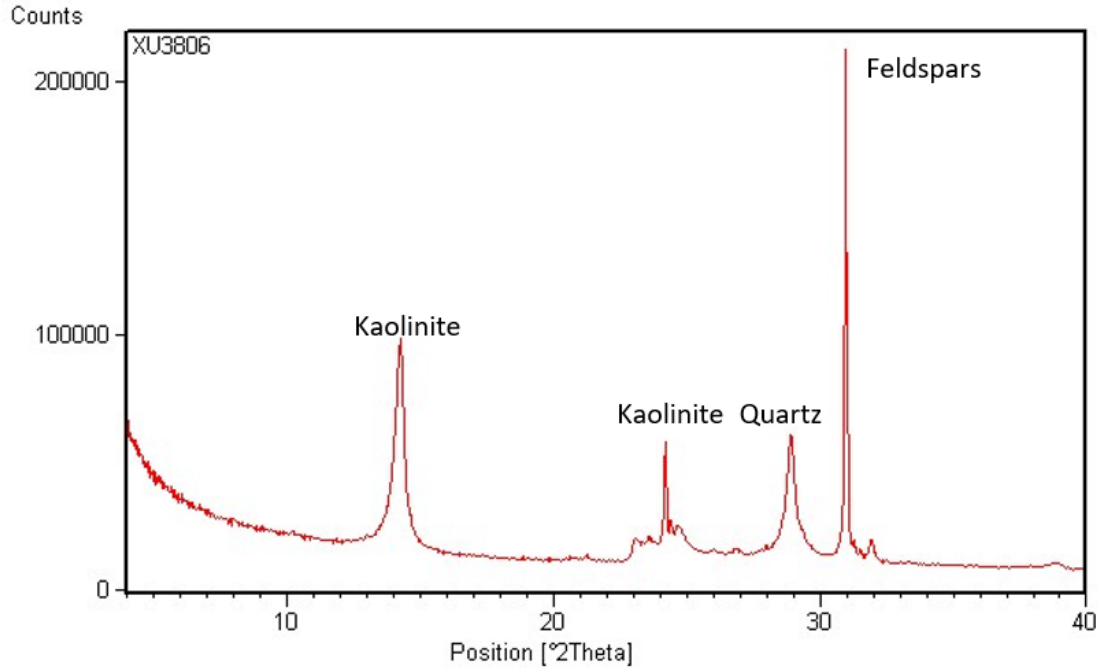

Figure 3-2 X-ray diffraction test on tailings soils.

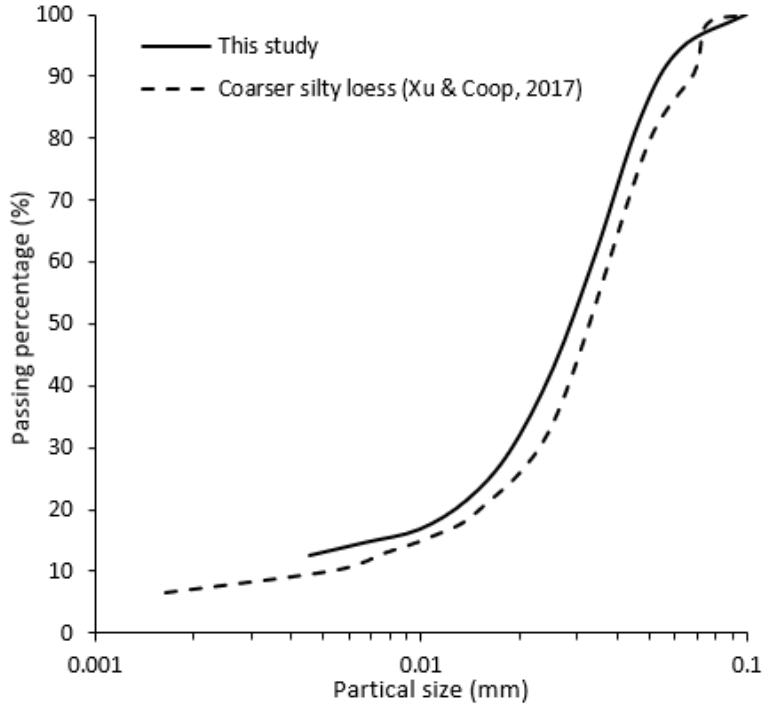

Figure 3-3 Particle size distribution of silty loess studied, compared with coarser silty loess with transitional behaviour (Xu & Coop, 2017).

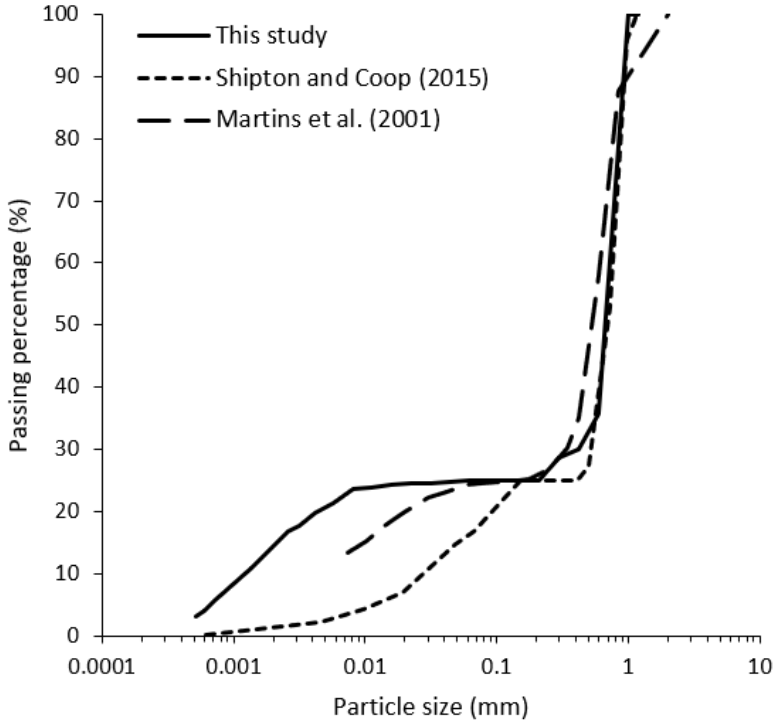

Figure 3-4 Particle size distribution of the mixture of 75% quartz sand and 25% kaolin studied, compared with those from Martins et al. (2001) and Shipton and Coop (2012).

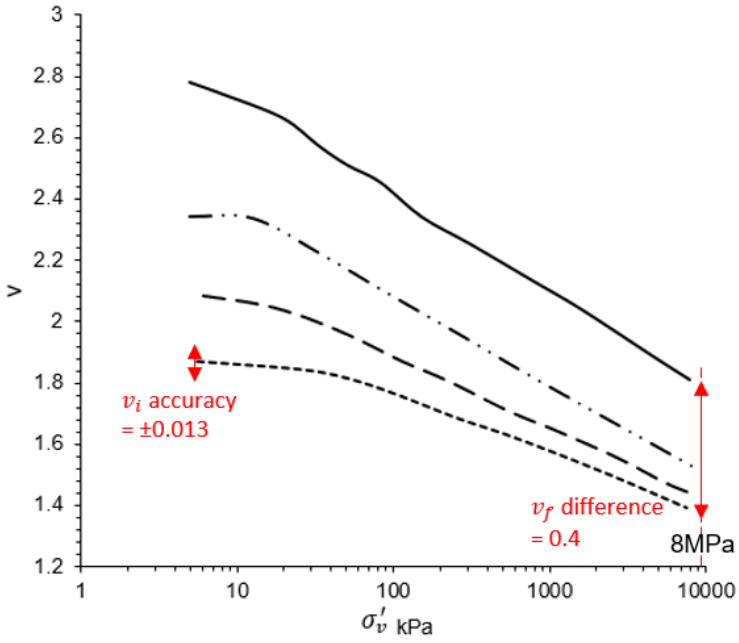

Figure 3-5 An example of the oedometer compression curve of fine mineral tailings, illustrating that the non-unique NCLs are not caused by the accuracy of the calculated initial specific volume.

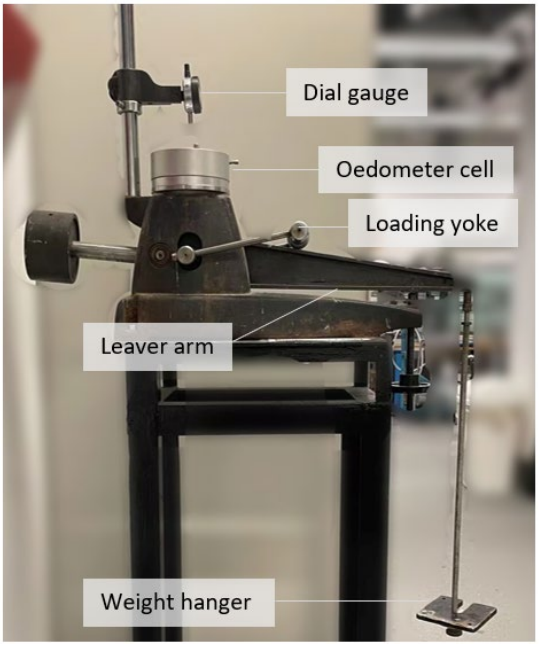

(a)

(b)

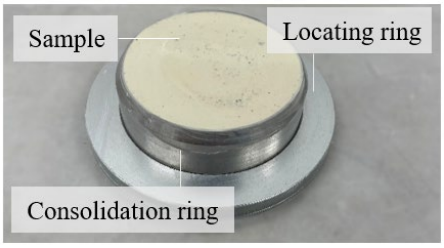

(c)

Figure 3-6 (a) Oedometer loading frame, (b) oedometer cell and (c) oedometer sample.

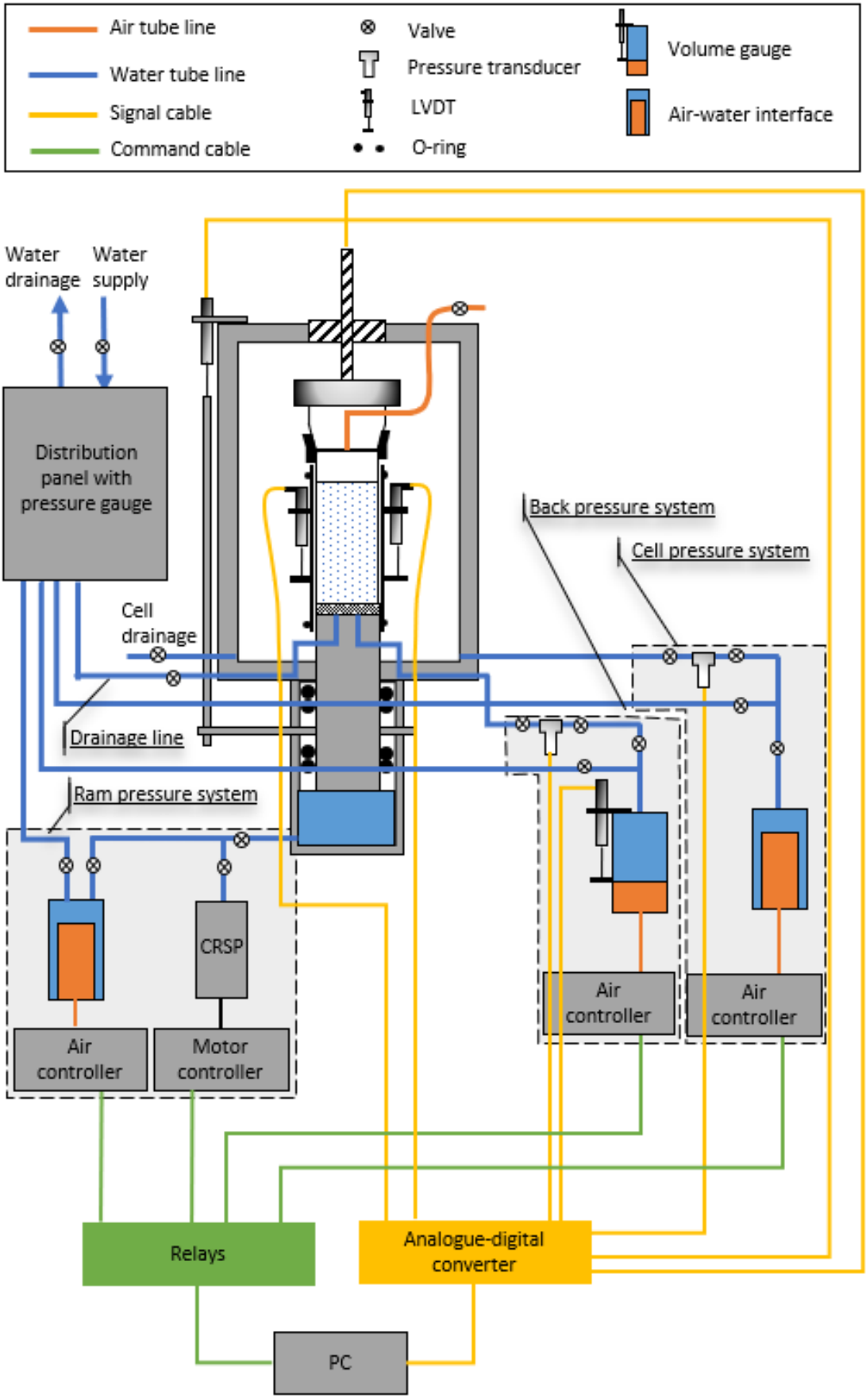
Air tube line
Water tube line
Signal cable
Command cable
Valve
Pressure transducer
LVDT
O-ring
Volume gauge
Air-water interface
Water drainage
Water supply
Distribution panel with pressure gauge
Cell drainage
Drainage line
Ram pressure system
Back pressure system
Cell pressure system
CRSP
Air controller
Motor controller
Air controller
Air controller
Relays
Analogue-digital converter
PC

(a)

(b)

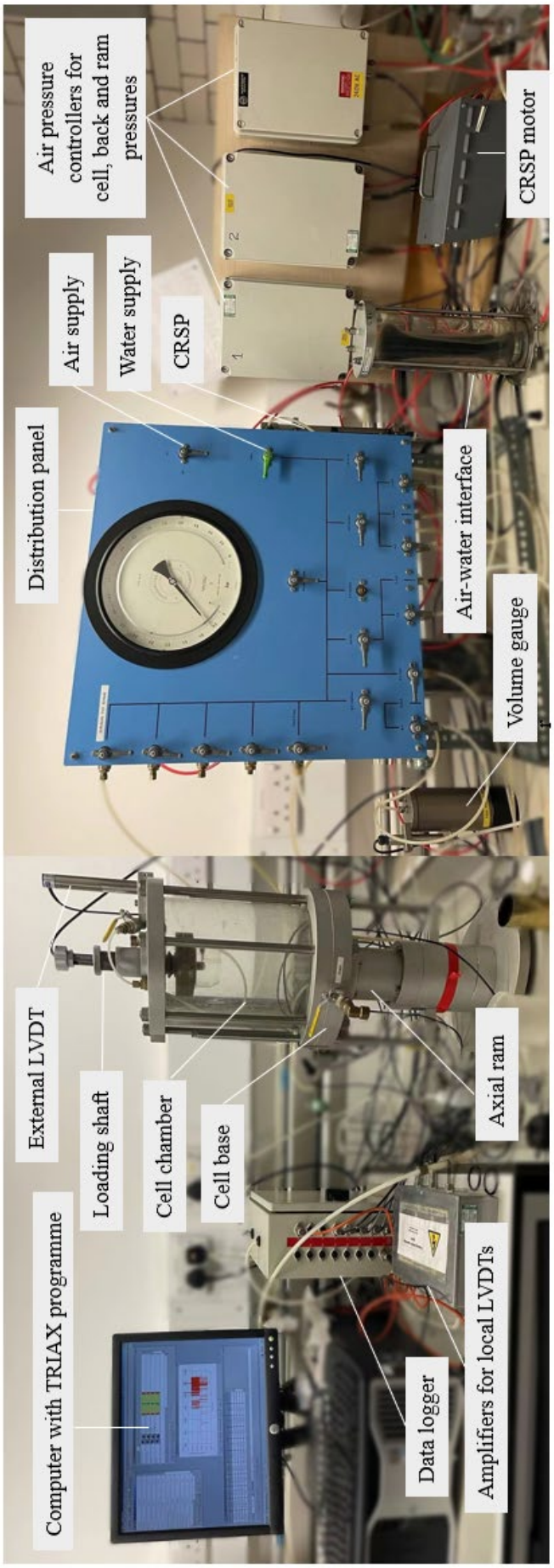
Computer with TRIAX programme
Data logger
Amplifiers for local LVDTs
Loading shaft
Cell chamber
Cell base
External LVDT
Axial ram
Distribution panel
Air supply
Water supply
CRSP
Air pressure controllers for cell, back and ram pressures
Air-water interface
Volume gauge
CRSP motor

(c)

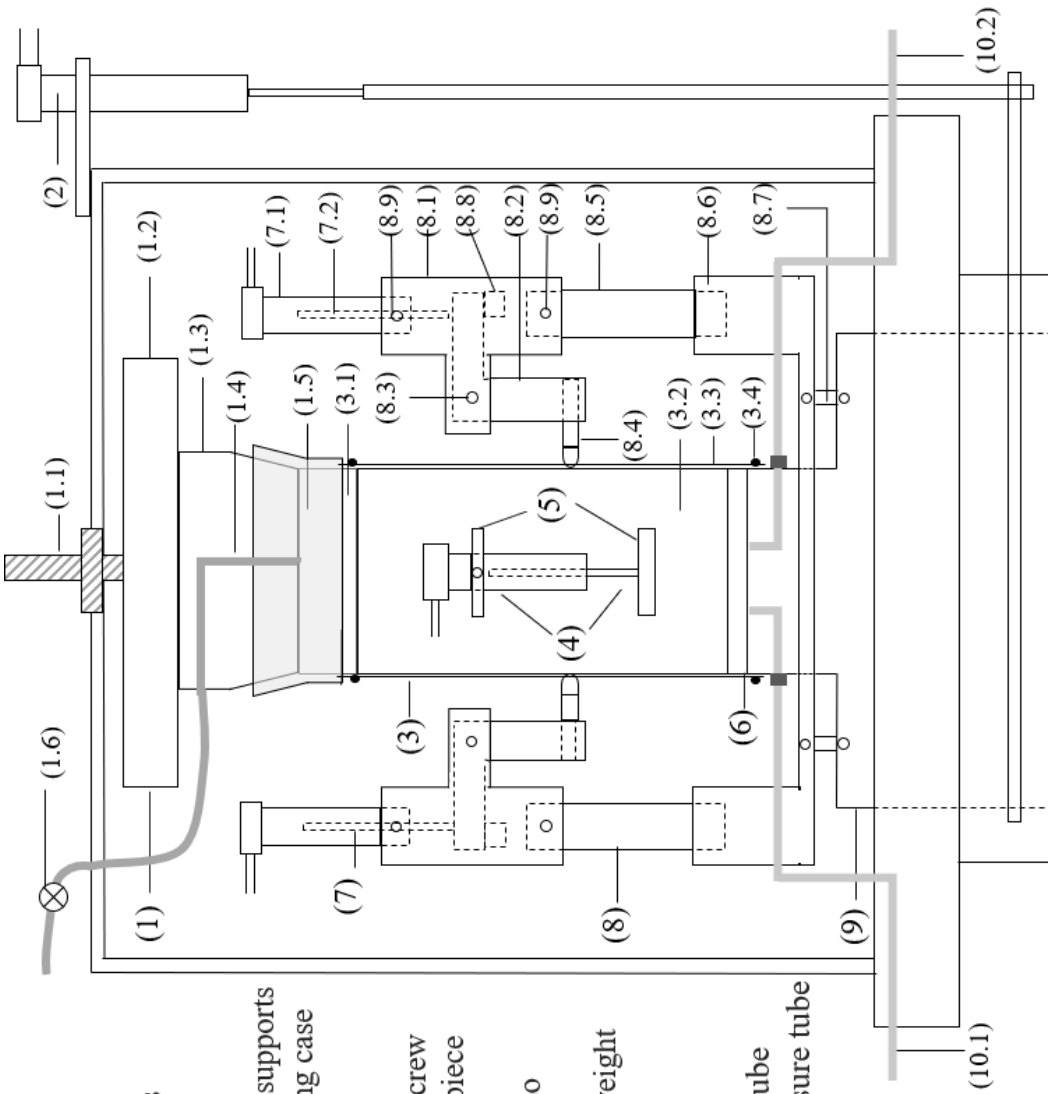

(1) Vertical loading system
- (1.1) Loading shaft
- (1.2) Load cell
- (1.3) Load adapter
- (1.4) Air tube line
- (1.5) Suction cap
- (1.6) Valve

(2) External LVDT

(3) Sample
- (3.1) Top platen
- (3.2) Soil sample
- (3.3) Membrane and side filter paper
- (3.4) O-rings

(4) Axial strain LVDTs

(5) Axial strain LVDT supports

(6) Low air entry porous stone

(7) Radial strain LVDTs
- (7.1) Core
- (7.2) Armature

(8) Radial strain LVDT supports
- (8.1) LVDT holding case
- (8.2) L shape arm
- (8.3) Pivot
- (8.4) Round-end screw
- (8.5) Adjustment piece
- (8.6) Support seat
- (8.7) Connection to pedestal
- (8.8) Additional weight
- (8.9) Screw

(9) Pedestal

(10) Drainage lines
- (10.1) Drainage tube
- (10.2) Back pressure tube

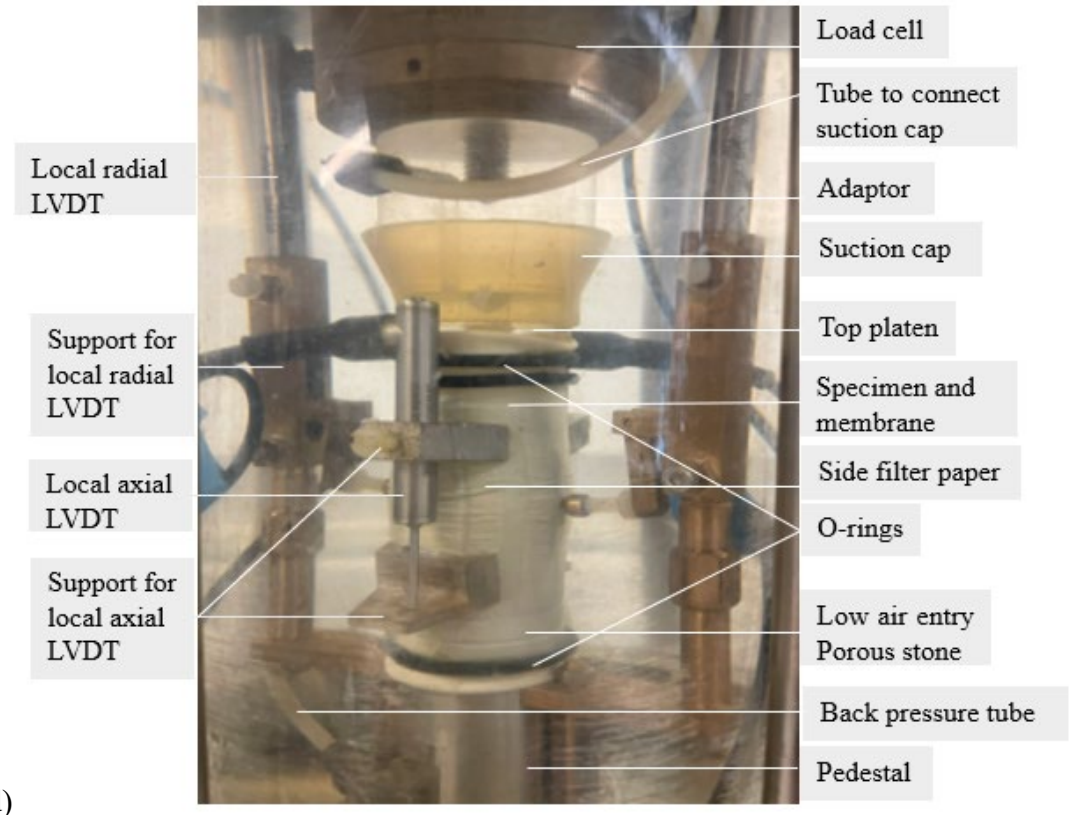

(d)

Figure 3-7 Saturated triaxial system: (a) schematic triaxial system, (b) photograph of triaxial system, (c) schematic cell, and (d) photograph of the details inside the cell.

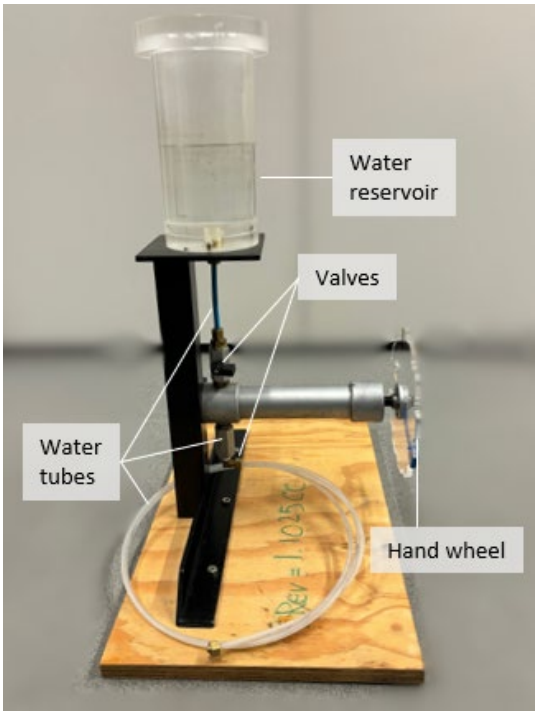

Figure 3-8 Bishop pump used to calibrate volume gauge.

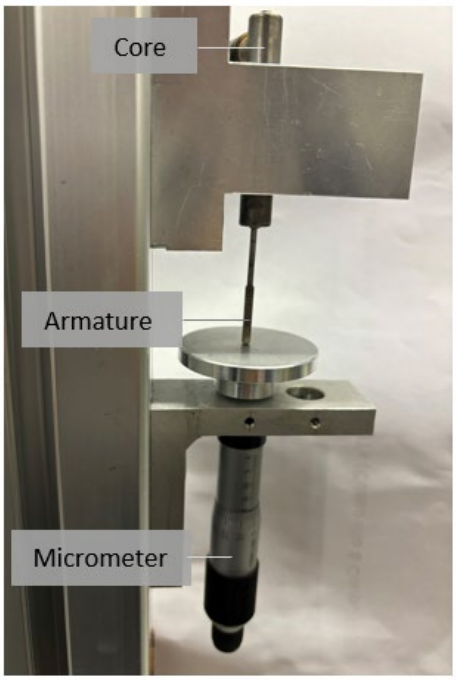

Figure 3-9 Micrometer and frame used to calibrate local axial LVDTs.

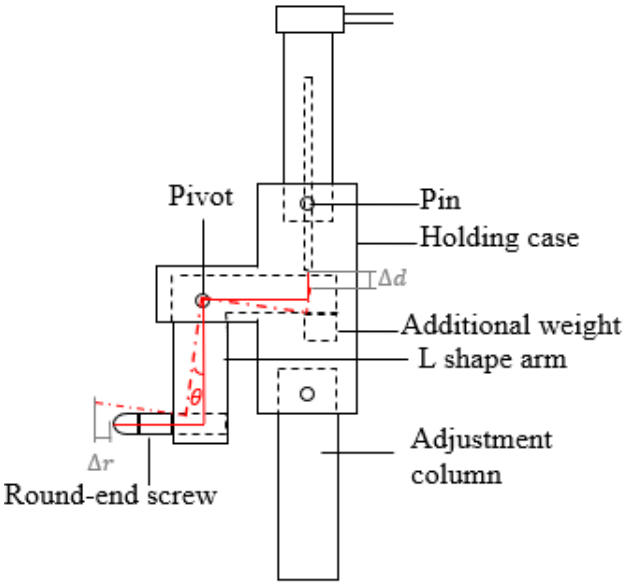

(a)

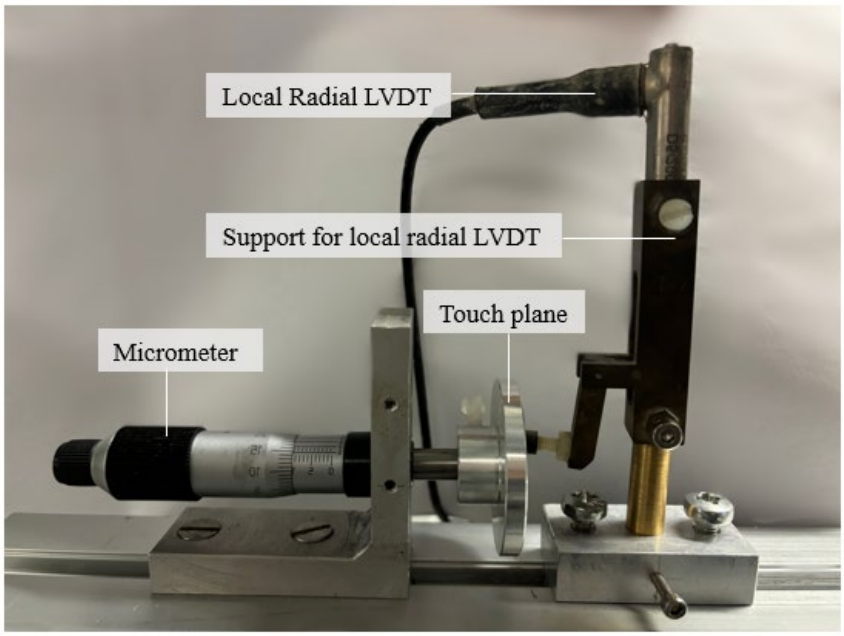

(b)

Figure 3-10 (a) Schematic of radial LVDT support, (b) photograph of the calibration of a radial LVDT.

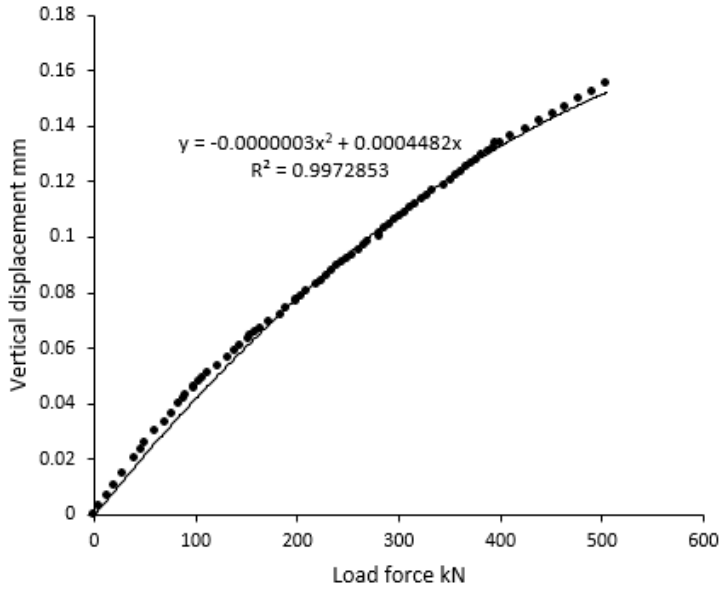

Figure 3-11 Calibration curve of vertical displacement due to applied deviator force from the compliance test.

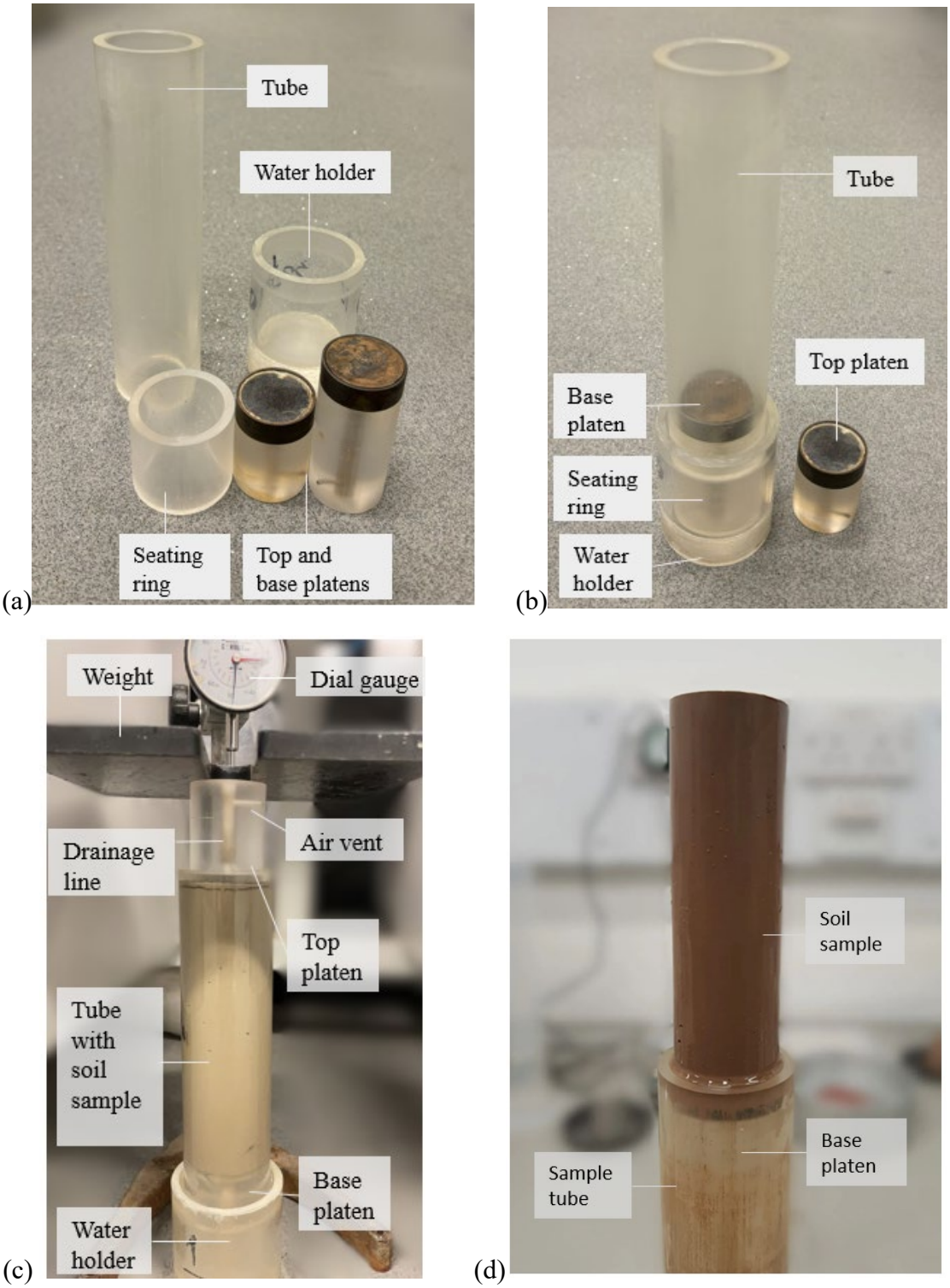

Figure 3-12 Sample preparation by the slurry method in a consolidometer: (a) components, (b) assembly, (c) sample consolidated, (d) sample extruded.

(a)

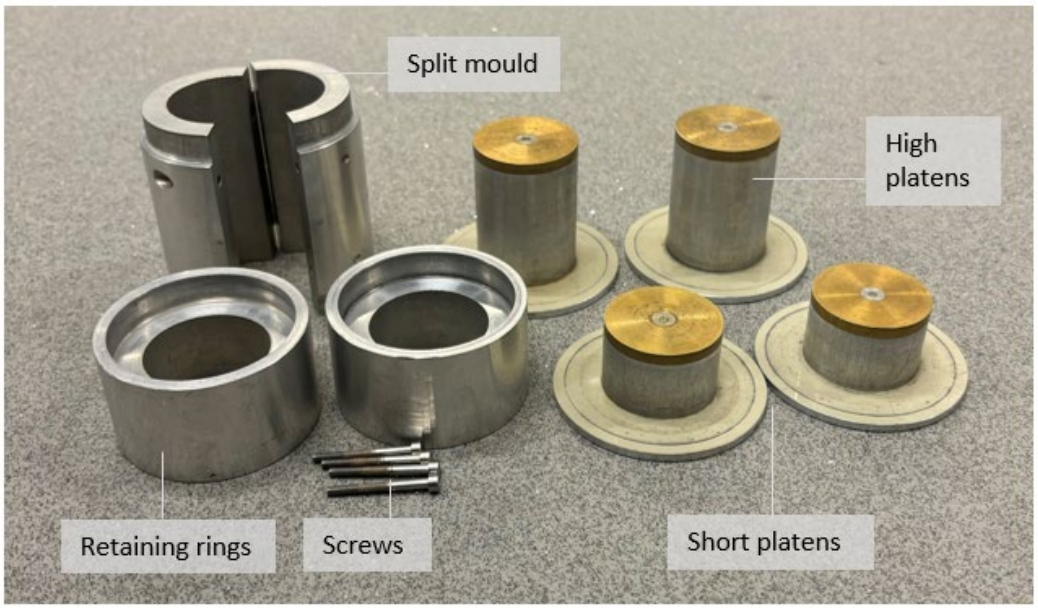

(b)

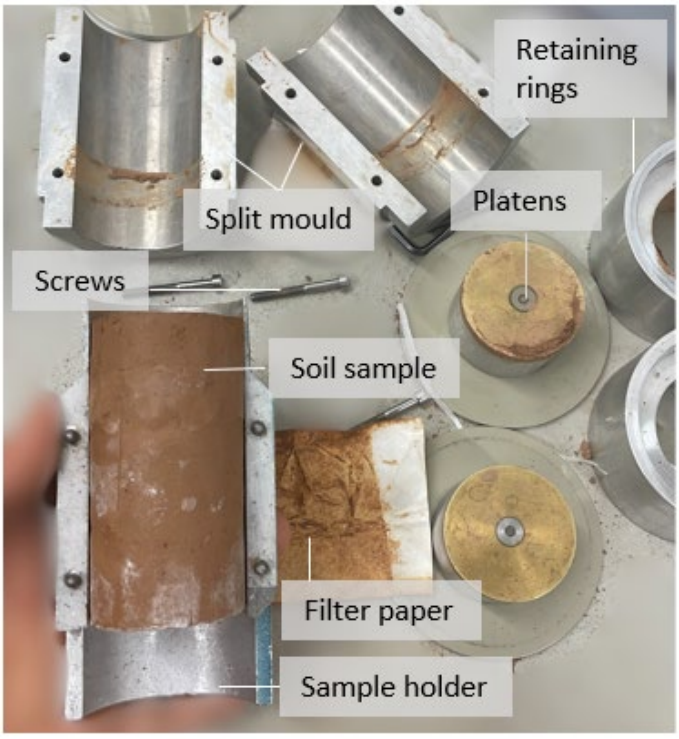

Figure 3-13 Sample preparation by the slurry method in a split mould: (a) split mould, (b) sample prepared.

(a)

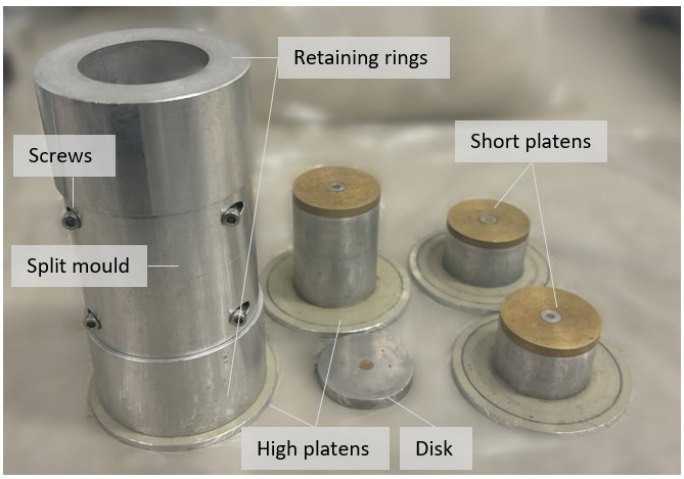

(b)

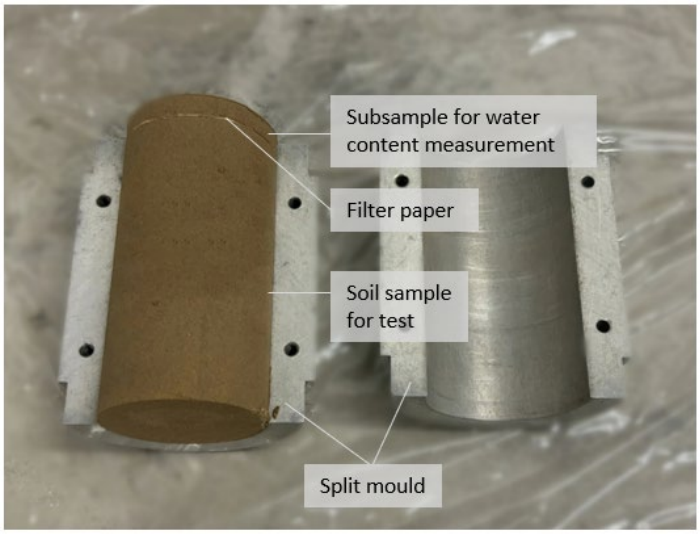

(c)

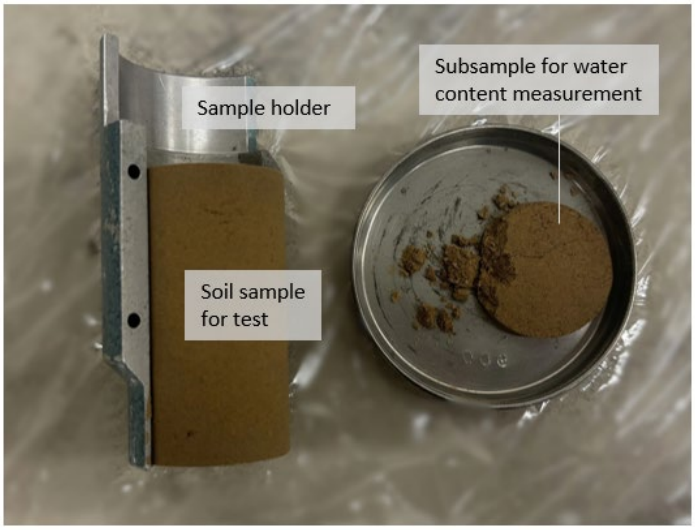

Figure 3-14 Sample prepared by compaction method in a split mould: (a) split mould, (b) sample for test and subsample for water content measurement and (c) sample in the sample holder and subsample in the tin.

(a)

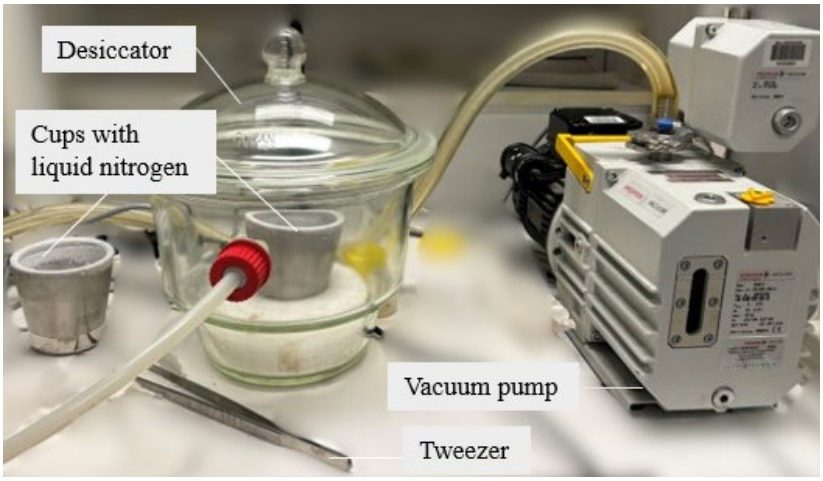

(b)

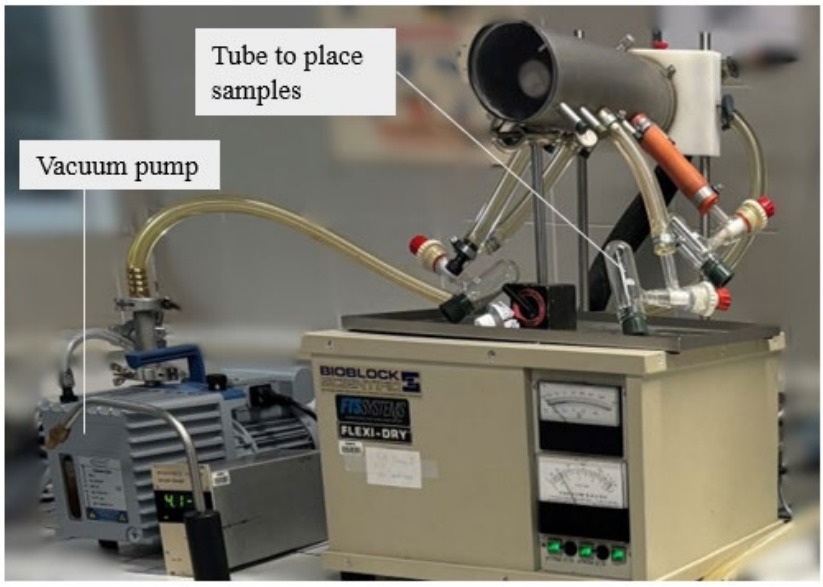

(c)

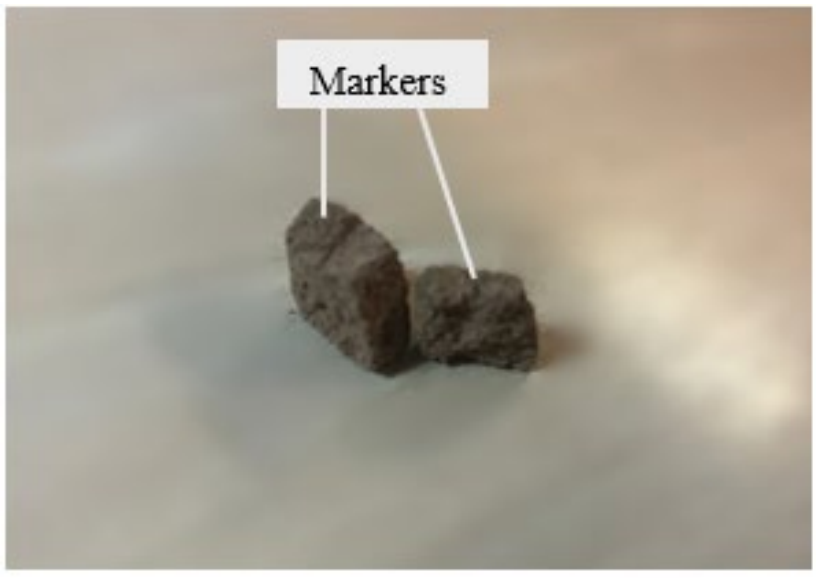

Figure 3-15 Dehydration of the samples by freeze-drying: (a) freezing sample using liquid nitrogen, (b) drying sample using vacuum, (c) freeze-dried samples.

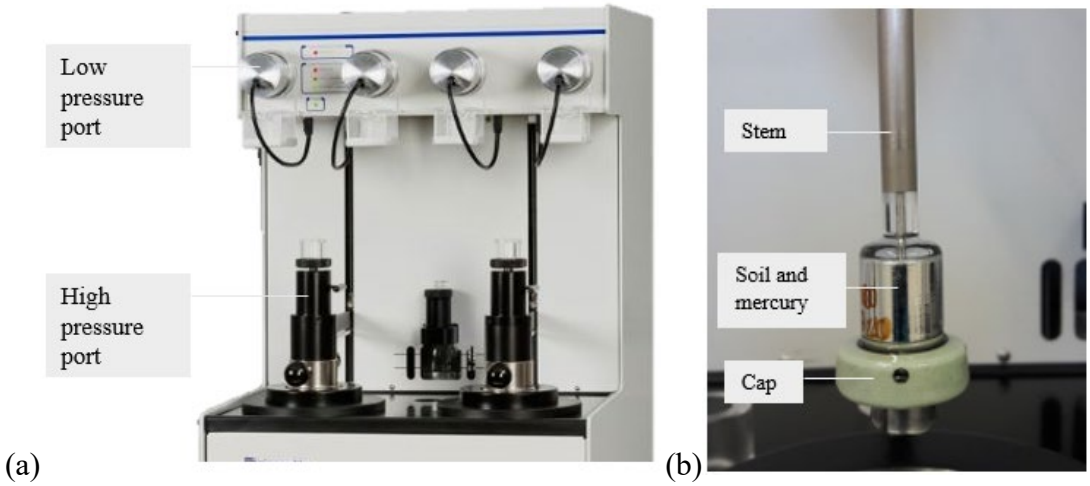

Figure 3-16 MIP test: (a) equipment and (b) penetrometer with sample in.

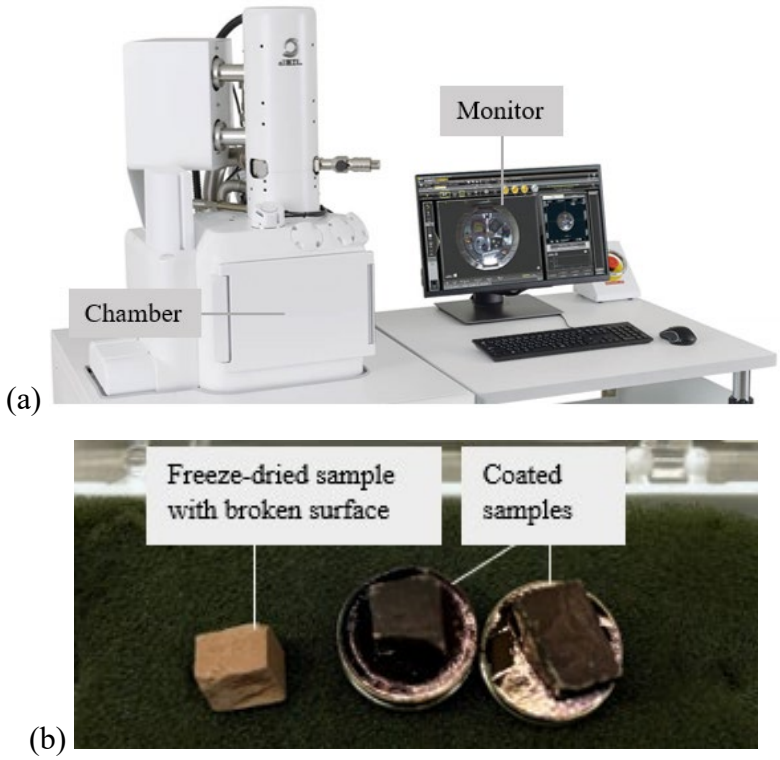

Figure 3-17 SEM test: (a) equipment and (b) samples.

CHAPTER 4 UNSATURATED TESTS

4.1 Introduction

This chapter presents the work conducted on unsaturated tests to study the transitional behaviour of unsaturated samples. To select soils with suitable suctions for the unsaturated tests, filter paper tests were conducted to determine the Soil Water Retention Curves (SWRCs) for different soils, as explained in Section 4.2. It was planned to use a tensiometer in this study for suction measurement as well, as presented in Section 4.3. A setup for SWRC measurement using the tensiometer was designed and built to complement the SWRC results obtained from filter paper tests. Additionally, an unsaturated oedometer apparatus equipped with a tensiometer was also designed for constant water content one-dimensional compression. Unfortunately, these tests could not proceed because the tensiometer was broken. The primary focus of this chapter was on unsaturated triaxial tests, carried out on a modified triaxial apparatus. Detailed instructions on converting a saturated triaxial apparatus to an unsaturated apparatus are provided in Section 4.4. This is followed by the system calibration procedures in Section 4.5 and system leakage detection in Section 4.6. The modified equipment was used for constant suction compression and constant water content shearing tests, with test procedures detailed in Section 4.7.

4.2 Filter paper tests

As mentioned in Section 2.4.2, the SWRC can be measured using the filter paper method. In this study, SWRCs were measured to select soils suitable for the unsaturated triaxial test using the modified triaxial apparatus, which is capable of maintaining and measuring suction up to 500kPa. Different soils were tested, including a loess soil, mixtures of kaolin and sand, fine tailings and sandy tailings. The sample preparation

method and initial specific volume (v_i) were considered as influencing factors on SWRCs. Additionally, the measured SWRCs for the selected soils were used to estimate the degree of saturation (S_r) for a given suction (s), enabling the preparation of a sample with a specific suction value for the unsaturated tests.

The sample was prepared in a 50mm diameter oedometer cell with a height of about 10mm. The sample preparation followed the oedometer test procedures outlined in Section 3.4.2, using both slurry and compaction sample preparation methods in Section 3.3. Since it is assumed that samples prepared using the same method are identical and consistent, samples used for each SWRC were prepared with the same initial water content (w_i) and v_i. After sample preparation, the sample was removed from the oedometer ring, and its size and mass were measured. The sample was either air-dried or wetted by spraying water onto its surface to achieve the desired S_r. The corresponding w for the desired S_r was calculated using Equation 3-12.

Whatman No. 42 filter paper was employed in this study, following a sample preparation method described by Jotisankasa (2005) and ASTM D5298-16 with modifications. In Jotisankasa's method, the sample was sandwiched between two filter papers and two Perspex discs, with the Perspex discs ensuring good contacts between the filter papers and the sample. To seal the sample, it was wrapped in three layers of cling film, placed in three sealed zip bags, and then transferred into a food container with a locking lid. Care was taken to avoid air entrapment in the cling film, and the zip bags were vacuum-sealed. To allow the sample to reach hydraulic equilibrium, the container was stored in a cool box and kept in a 20℃ room for 7-14 days.

In this study, the method was further modified by placing two half filter papers and one whole filter paper on each side, as illustrated in Figure 2-1, instead of single filter paper.

This design allowed for four measurements from the half filter papers in each test, with the additional whole filter paper used to protect the half filter papers from soil contamination. In cases where samples developed uneven surfaces during drying, the Perspex disc was omitted. Good contact between sample surfaces and filter papers was ensured by tightly wrapping cling film around the sample.

After the equilibrium period, suction was determined by measuring the water content of the filter paper (w_F). A precision scale with a resolution of 0.0001g was used for these measurements. The filter paper was transferred using a small zip bag. To minimize exposure, the entire transfer process took less than 5s, after which the bag was immediately sealed. If this process exceeded the time limit or if soil adhered to the filter paper, the measurement was discarded. The zip bag was weighed before and after placing the filter paper in it, with the same procedure followed for the remaining three half filter papers. Between uses, the moisture inside the zip bag was absorbed with tissue paper. The wet filter papers were then oven-dried for 2 hours to measure their dry weight, allowing the determination of the w_F. Any outlier among the four measurements was discarded, and the average of the remaining values was used as the final w_F for the filter papers. To convert the w_F of the filter paper to the suction (s) of the sample, the calibration equations obtained from Chandler and Gutierrez (1986) for initially dry filter paper were employed, $\log_{10} s = 4.84 - 0.0622 w_F$ for $w_F \leq 47$ and $\log_{10} s = 6.05 - 2.48 \log_{10} w_F$ for $w_F > 47$. The sample size and mass were measured to calculate the S_r corresponding to the measured suction.

The appropriate equilibrium time was determined by comparing the s measured from the filter papers within the same sample at different time intervals. Two half filter papers from one side were measured after 7 days, and another two from another side were measured after 14 days. The results indicated that the suction values from two

intervals showed minimal difference, demonstrating that 7 days were sufficient to reach hydraulic equilibrium for the tested soils.

4.3 Tensiometer tests

4.3.1 Tensiometer

The principle of the tensiometer was introduced in Section 2.5.1. A tensiometer purchased from Geo-Technologies Ltd was used in this study. It had a 14 mm diameter and a capacity of $\pm$1.5MPa, as shown in Figure 4-2 (a). It was employed for suction measurements in the SWRC tests and unsaturated oedometer tests. The tensiometer was equipped with an amplifier and powder supply, as illustrated in Figure 4-2 (d). The signals were stored in the data logger and transmitted to the computer as voltage readings. A voltage reading software was used to convert these to pressure values through the calibration equation from measurement. Although the tensiometer was already pre-calibrated and had a calibration curve from the manufacturer, it was calibrated again before use and a new calibration curve was generated. The calibration was conducted by pressurising in 200 kPa intervals up to 1 MPa, with the voltage readings recorded against the pressure readings from pressure transducer.

A saturation block was used to saturate the tensiometer, as shown in Figure 4-2 (d). This block had a hole to hold the tensiometer, which was fixed in position by four screw clamps and sealed by an O-ring at the bottom of the hole. The block was connected to a pressure pump on one side to pressurize the tensiometer and a valve on the other side to release pressure to the atmosphere. Before saturation, the saturation block was flushed with deaired water from the pressure pump, with the valve open. The tensiometer was then placed into the block and submerged in water, while the valve remained open to release water pressure. The screws were gently tightened to mount

the tensiometer, while the voltage reading was monitored to ensure it did not change more than 200 mV. The saturation block was then flushed again, and the valve was closed once the water flowed out from the air valve. After this process, the tensiometer was ready for saturation.

For saturation, the tensiometer was slowly pressurized up to 1MPa by the pressure pump in 200kPa intervals. For the initial saturation, this pressurisation process lasted for two weeks, followed by cavitation-saturation cycles to enhance the capacity of tensiometer. To induce cavitation in the tensiometer, it was exposed to atmosphere pressure, causing the voltage reading to rapidly decrease, until the reading suddenly jumped to 0 V and stabilized. After each cavitation, the tensiometer was immediately placed back into water and re-saturated in the saturation block. Since the tensiometer was not completely dried after cavitation, two days were sufficient to re-saturate it. After three cavitation-saturation cycles, the capability of tensiometer was around 700 kPa. During tests, the tensiometer was re-saturated after cavitation as soon as possible. Saturation normally took two days if the tensiometer was not fully dried. Otherwise, it required two weeks of saturation, followed by cavitation-saturation cycles to regain the capacity.

4.3.2 Setup for SWRC tests

Test apparatus

As mentioned in Section 2.4.2, the SWRC can be measured using a tensiometer for samples undergoing either discrete or continuous drying. Discrete drying can provide more accurate measurements but may miss the details of the SWRC. Continuous drying can offer a complete SWRC but may introduce errors due to uneven moisture distribution. Achieving good hydraulic equilibrium in continuous drying requires an optimal sample height, allowing for rapid evaporation. Meanwhile, the mass of the

sample must be sufficient to ensure measurable changes in water content during drying. In this study, a setup was designed for both discrete and continuous drying methods, modified from the designs of Toker et al. (2004) and Lourenço et al. (2011). The discrete drying method was intended to verify results from continuous drying and to determine the appropriate sample height.

A sample mould used for sample preparation and testing was designed with a top lid and a bottom hole, as shown in Figure 4-2 (b). The mould was about 53mm in diameter and 50mm in height. The top lid can be opened to expose the sample's top surface during drying or wetting and can be closed for hydraulic equilibrium. The bottom hole was fitted with an O-ring, ensuring a tight fit for the tensiometer and preventing any loss of sample moisture. The mould was set in a metal seat with a plug to close the bottom hole during sample preparation. When the sample was ready for testing, the tensiometer was immediately mounted in the mould, and the set was transferred to a plastic support, as shown in Figure 4-2 (c).

During testing, the sample mould sitting on the support was placed on the scale, with the prepared sample inside and tensiometer inserted. Readings from both the scale and the tensiometer were automatically recorded by the computer. To prevent any contact with the scale that could lead to errors in mass readings, the tensiometer cable was rested and secured on a support.

Test procedures

The sample was prepared using the compaction method as described in Section 3.3.2, similar to the oedometer sample preparation introduced in Section 3.4.2. This method was chosen over the slurry method for unsaturated samples, and the reason behind this choice is provided in Section 4.7.3. The first trial for the sample height was 10mm to

evaluate its suitability for the continuous drying. The specimen was statically compacted to a height of 10mm in the mould sitting on the mould seat. Water was then sprayed onto the top surface to saturate the sample, which was left for at least one day to achieve hydraulic equilibrium. Then, the height and mass of the sample were measured to calculate the w_i and S_{ri} based on Equation 3-12.

After saturating the tensiometer, a paste of the tested soil was applied on the top of it to ensure good contact of its porous stone with the sample. Then, it was mounted in the sample mould and placed in contact with the sample surface. The sample mould covered with the lid was then transferred to a mould support and placed on the scale. Hydraulic equilibrium between the paste and the sample was confirmed when the reading stabilised, indicating the tensiometer was ready for measurement. Once the suction readings stabilised, the readings from both the scales and the tensiometer were recorded. The lid was then opened to initiate the continuous drying of the sample. Manual photographs of sample's height and diameter were taken every three hours to estimate sample volume change through digital analysis. This method was intended to be improved with automated image capture every half hour for future tests. The 1080p image resolution provided an accuracy of up to 0.1mm. In the trial test, the changes in diameter and height were about 1mm. The scale readings and the volume change from digital analysis were used to calculate the S_r. The test was stopped after the tensiometer reached cavitation.

The results from the trial test on the 10mm height sample during continuous drying are shown in Figure 4-3. It shows that the mass began to change at the start of test but the suction remained unchanged for the first 15 hours. As a result, the SWRC curve differs significantly at the start of the test from the result of the filter paper method, which was validated by the consistent results presented in Chapter 6. This indicates poor hydraulic

equilibrium at start of the test in the 10 mm height sample. Plans were made to test a thinner sample in the next trial of continuous drying or just do a discrete drying test. Unfortunately, the tensiometer was broken later so that the tests could not continue.

4.3.3 Unsaturated oedometer apparatus

An unsaturated oedometer equipment was designed for the constant water content unsaturated oedometer test, equipped with a tensiometer for suction measurement. The design was modified from Jotisankasa (2005) and is illustrated in Figure 4-4. The equipment was modified from a traditional oedometer apparatus. A new top cap was designed with a hole fitted with an O-ring and a clamp consisting of a plate and two bolts, to secure and seal the tensiometer. The gap around the top cap was sealed with latex rubber. Unfortunately, the tests could not proceed as the tensiometer broke.

4.4 Unsaturated triaxial equipment

4.4.1 General layout of the system

An unsaturated triaxial system was modified from the saturated triaxial system introduced in Section 3.5.1 using the axis translation technique. The modified system was capable of performing the suction-controlled and constant water content tests. As shown in Figure 4-5 (a), the system consisted of mainly a cell, a pressure measurement and control system, and a strain and volume measurement system.

As mentioned in Section 2.5.2, the axis translation technique is used to increase pore air and pore water pressures equally. This allows the pore water pressure to become positive, preventing cavitation while maintaining the desired suction value. To implement this, an air pressure line was added to the top platen, supplied by an air pressure controller and measured by an air pressure transducer. The pedestal was equipped with a High Air Entry (HAE) porous stone and wavy groove, while a low air-

entry porous stone was used on top of the sample. The principle of both porous stones is the same as that described in Section 2.5.1. A half ball was used in place of the suction cap. Compared with the saturated triaxial system, no changes were made to the pressure measurements and control systems for back, cell and ram pressures.

The water volume change was measured using the volume gauge for back pressure, similar to the saturated system introduced in Section 3.5.1. Air volume change was not easy to measure due to the compressibility of air, so total volume was measured instead. For the total volume measurement, local LVDTs and a volume gauge were used instead of double cell mentioned in Section 2.5.3, as the local LVDTs also allow measurement of small-strain stiffness. Four LVDTs were used to measure both the axial and the radial strains. A volume gauge was equipped in the cell pressure line to measure the total volume change by measuring the volume change of cell water. Detailed explanations of the elements and procedures are provided in the subsequent sections.

4.4.2 Modified pedestal

An HAE porous stone is essential to prevent air from passing through into the pore water system when the suction is less than its air entry value. The higher the air entry value of the HAE porous stone, the larger the suction value it can withstand. But this comes with a lower permeability, meaning the tests can last longer. Considering time efficiency, a 5-bar HAE porous ceramic disk from the Soilmoisture company was used, with a diameter of 27 mm, a thickness of 7 mm, and a capacity of 500 kPa suction. As shown in Figure 4-6, the HAE porous stone was glued into the pedestal, using a resin from the Soilmoisture company specially designed for the porous stone. To get a strong bond between the porous stone and pedestal, extra care was taken to avoid bubbles in the resin by heating it and gluing the stone using the resin and an O-ring together. Since

the saturated HAE porous stone has the optimum permeability, it must be saturated at the start of each test. Details of the saturation process are provided later.

As explained in Section 2.5.2, pore air may still diffuse into the pore water system through an HAE porous stone and accumulate underneath it. To address this, a wavy groove was designed under the porous stone to trap any diffused air bubbles and provide a smooth path for flushing them out. The wavy groove was 2mm in width and connected to the back pressure line and drainage line. The flushing system connected to pedestal will be introduced later.

4.4.3 Modified top platen

Since the unsaturated samples were so stiff that the suction cap was no longer able to align the sample to load cell, a half ball was used instead and placed on top of a top platen modified with a conical hole, providing a freely rotating flat surface. This design ensured a uniform vertical load, even for slightly tilted samples. Air pressure was applied to the top of the sample through the modified top platen, as shown in Figure 4-7 (a). A push-fit joint was replaced with a nut and olive connection to prevent potential leakage from incorrect positioning. The nut of the connection was permanently joined on the top platen, eliminating the possibility of it accidentally unscrewing during sample assembly. As a result, the air tube line was permanently joined to the top platen, and a special O-ring stretcher with an opening was used to pass through the tube, as shown in Figure 4-7 (b). The air tube was slightly heated with a heat gun to curve it into position inside the cell. An air pressure transducer and a manual controller were added to measure and regulate the pressure. Before each test, the air pressure line was blown dry, and the transducer was zeroed to atmospheric pressure.

To prevent water from evaporating from the sample into the air pressure line, a low-air entry porous stone was used on top of the sample. Although some water was found in the air pressure line after tests, it was likely condensed water from the air rather than the pore water from the sample, as no water was observed in the section of tube closest to the sample.

4.4.4 Flushing system

As mentioned in Section 2.5.2, a diffused air volume indicator (DAVI) can be used to measure the volume of diffused air, which is necessary in order to correct the measurement of water volume change. The principle of the DAVI is to flush the base of the pedestal with a maximum pressure gradient of 70 kPa and collect the diffused air into a burette to measure the air volume.

A flushing system, as shown in Figure 4-8 (a), was designed by the author. It consists of a 100ml twin burette volume change apparatus and a Bishop pump, as illustrated in Figure 4-8 (b) and Figure 3-8. Water from the back volume gauge was flushed to the twin burette apparatus through the pedestal, and then flowed into Bishop hand pump through the pressure panel. A small pressure gradient was created by rotating the Bishop hand pump slowly, ensuring a pressure difference less than 70 kPa.

In the twin burette flushing system, the left burette reading h_L reflected the water change volume, and the right burette reading h_R included both water and air change volume. Therefore, the diffused air volume was calculated by the difference in readings between the two burettes, $h_R - h_L$. The system allowed for two-way flushing, as both the Bishop hand pump and twin burettes could reverse the water flow direction. The total diffused air volume was the sum of the reading changes after each flushing. With

the twin burettes graduated at 0.2ml intervals, this system provided greater accuracy compared to the DAVI, which uses a burette graduated at 10ml.

Before building the twin burette flushing system, a simpler flushing system was used to estimate the volume of diffused air over time and assess the frequency of flushing required. As shown in Figure 4-8 (c), this system involved directly connecting the Bishop hand pump to the pedestal through the pressure panel, creating the pressure gradient by rotating the Bishop pump. The transparent water tube was monitored during flushing to observe the diffused air, and the volume could be roughly estimated. The inner diameter of water tube was 2.6 mm, meaning an air bubble with 9.4 mm length in the tube would correspond to 0.05mL volume. This resolution was even smaller than that of the twin burette flushing system. A dummy test under 200kPa suction was flushed daily using the simple flushing system for seven days, but no air bubbles were even observed. Therefore, the twin burette flushing system was not built or used and correction for diffused air was unnecessary for any test.

4.4.5 Total volume measurement system

A total volume measurement for unsaturated samples during testing is essential to calculate the specific volume and the degree of saturation. The volumetric strain (ε_{vol}) can be calculated from the axial strain (ε_a) and radial strain (ε_r). As in the saturated triaxial tests, the axial strains were measured using a pair of symmetric local LVDTs attached to the sample membrane, and the radial strains were measured with another pair of local LVDTs held by a set of radial strain supports, as introduced in Section 3.5.2.

The accuracy of the volumetric strain calculated from local LVDTs was verified in saturated triaxial tests, including isotropic compression and shearing stages. The system

performed well during isotropic compression and at small strain levels during shearing (typically $\varepsilon_a < 5\%$), so the local LVDTs were used in these cases. However, it became less accurate at large strain levels during shearing. The details of these verifications will be explained later.

Due to the limitation in measuring volumetric strain using local LVDTs at large strains during shearing, a cell volume gauge, the same as for the back volume gauge, was used. It was fitted parallel with the existing cell pressure line, as shown in Figure 4-5 (a), providing supply of cell pressure and measurement of cell water volume change. Testing the cell volume gauge in saturated triaxial tests revealed that while it was less accurate at small strain levels, it performed well at large strain levels. Therefore, the total volume change in shearing stages at large strains was determined using the cell volume gauge. The details of this performance will be explained later.

4.5 Calibrations for total volume measurement

4.5.1 Calibration using local LVDTs

Calibration for compression data

The calculation of total volume change during isotropic compression is explained using the loess saturated test T1 as an example, shown in Figure 4-9. The axial strain (ε_a) and the radial strain (ε_r) were the average values of the two local axial LVDTs and two local radial strains, respectively. The volumetric change (ε_{vol}) was calculated by Equation 4.1, which should work for both small and large strains. The volumetric strain calculated based on back volume gauge (VG) was used for comparison, since it should be equal to total volumetric strain in a saturated test. There is a small gap at about p'=60 kPa, resulting in about 0.7% difference out of 7.1% total volumetric strain. This resulted from the samples disturbance when connecting the suction cap and straightening the

sample. This disturbance should not be observed in unsaturated tests, since the suction cap would not be used. Besides this disturbance, the local LVDTs work well for the calculation of total volume change in isotropic compression.

$$\varepsilon_{vol} = \varepsilon_a + 2\varepsilon_r - \varepsilon_r^2 + \varepsilon_r^2\varepsilon_a - 2\varepsilon_r\varepsilon_a \qquad \text{Equation 4-1}$$

Calibration for shearing data

The calculation of total volume change during shearing is explained using the loess saturated test T3 as an example, as shown in Figure 4-10. There is a clear difference between the initial and the external axial strains at large strain levels, beyond 2% and especially beyond 10%, which is normal because that the local axial LVDTs only measure the central section of the sample. Therefore, the external axial strain was considered more representative for the whole sample at large strains and was used for the calculation of total volume strain. For radial strain, both the radial LVDTs were consistent and the average value was the total radial strain.

Since the sample would not be a right cylinder at large strains, the correction was made based on a barrelling assumption. The sample diameter at the end of the test was measured. As shown in Figure 4-11, the diameter at 7 different elevations (n=7) was measured, recorded as D_i (i=1 to 7). The lowest value of D_i is named as the threshold diameter D_t, which is either D_1 or D_7. Before the diameter measured from radial LVDTs during testing reaches D_t, the shape is assumed to be a cylinder. Beyond that, the barrelling correction was applied to the ε_r, using a method similar to that of Klotz and Coop (2002) and Jotisankasa (2005).

This barrelling correction assumes that the diameter ratio for each elevation $x_i = \frac{D_i - D_t}{D_{(n+1)/2} - D_t}$ remains constant during the whole shearing stage. This equation means that for each layer the difference between the diameter at the given elevation and the

threshold is always proportional to the difference between the diameter at the mid-height elevation and the threshold during shearing. Then ε_r is corrected by the equation $\varepsilon_r^t + AX \cdot (\varepsilon_r^m - \varepsilon_r^t)$, where ε_r^t is the radial strain at the threshold point, ε_r^m is the measured radial strain at the mid-height and $AX = \frac{1}{2n-2}(x_1 + x_n + 2\sum_{i=2}^{n-1} x_i)$ is the weighted average ratio of x_i. The AX normally ranges from 0.5 to 0.6.

The cross-sectional area in the deviatoric stress calculation used the average value of the corrected ε_r and the ε_r^m. Equation 4-1 was still used for the corrected ε_{vol} but used the corrected ε_r. The calculated ε_{vol} with and without correction are plotted in Figure 4-10 (c), compared with the ε_{vol} based on the back volume gauge. After the barrelling correction, the corrected ε_{vol} fits very well at the small strain levels (before 2%) but can be very wrong at large strain levels. Therefore, the barrelling correction method can work well at small strain levels.

In summary, local LVDTs work well in isotropic compression and shearing at small strains, while other methods should be used for large strain levels.

4.5.2 Calibration using cell volume gauge

To measure the total volume change, a cell volume gauge was also used because LVDT-based measurements become unreliable at large strain levels during shearing. Three effects were considered for the calibration, including cell pressure, ram displacement and time. Then these calibrations were applied to a dummy sample for testing. Details are below and results in Figure 4-12.

The first step of the calibration conducted on the cell volume gauge was the same for the back volume gauge shown in Section 3.5.2, which was to flush the system and define the linear range of voltage and water volume for the volume gauge.

Calibration for cell pressure change

During the compression stage, the cell pressure can change significantly and the pressure changes will cause immediate volume change in the cell volume gauge because of its expansion. This will not happen in shearing, since the cell pressure will be constant. Loading and unloading were conducted to calibrate the effect of cell pressure on the volume gauge change. It can be seen from Figure 4-12 (a) that overall the regression line of first loading is consistent with that of second loading and the maximum difference between two times loading up to 800 kPa is only 0.8 cc. The calibration equation used in the data analysis is $y = -1.53 + 6.71^{-2}x - 6^{-5}x^2 + 3^{-8}x^3$, where y is the cell volume gauge reading in cc and x is the cell pressure in kPa. This error will affect the calibration during isotropic compression, which will be discussed later when applying it to the data.

Calibration for ram displacement

During shearing, the constant rate of strain pump (CRSP) moves the ram up with a constant rate of displacement, displacing the cell water. The calibration was done on the five rounds of loading and unloading. As shown in Figure 4-12 (b), all five rounds are very consistent and the axial displacements for all arounds are linear with the cell volume gauge change, following regression equation $y = -2.826x + 0.0974$, where y is the cell volume gauge reading in cc and x is the axial displacement in mm.

Calibration for time

The time of effect was conducted at a constant 500kPa cell pressure over three days, and the results are shown in Figure 4-12 (c). There is a quick volume increase at the start of 12 hours, following as a gradual increase with a slight cycle. The initial rapid volume changes up to 0.5cc results from the cell pressure application and the

corresponding expansion of tubing and the triaxial cell. Since this increase stops after a few hours, it is excluded from the time-related data correction.

The small cyclic volume changes are due to the temperature fluctuations in the laboratory room and steel volume gauge, as shown in Figure 4-12 (d). The magnitude of volume change was about $\pm 0.1cc$ corresponding to $\pm 1.0℃$ variation of room temperature over 24 hour cycles. The variation was not considered to affect the volume change significantly during shearing at large strains, since the cycle is not large compared with total volume change. It is noted that the cycle may lead to an error for isotropic compression and shearing at small strain levels, although the cell volume gauge would not be used in these cases and local LVDTs would be used instead.

A steady increase of volume with time was also observed besides the cyclic change. This may result from many reasons, including the water absorption of the Perspex cell chamber, system leakage or possible air bubbles dissolving. It was later confirmed as small system leakages mostly, which will be explained later. The curve was fitted well with the linear regression line if the temperature effect was ignored, $y = 0.016x$, where y is the cell volume gauge reading in cc and x is the time in hours. This rate of time effect was used only in this section. A new ratio after fixing the leakage was adopted for the correction of unsaturated tests, which will be introduced later.

Calibration for isotropic compression data

The calibration for cell pressure and time effects were applied to both loading and unloading stages of isotropic compression on a saturated sample, as shown in Figure 4-13. Since it is a saturated sample, the back volume gauge change should be the total volume change, which should be equal to the calculation from the cell volume gauge. For the loading stage, the calculated total volume change from the cell volume

gauge considering the effects of cell pressure and time is compared with the measurement of the back volume gauge. There is a difference of 0.4 cc out of 3.9 cc total volume change at the end of compression. Some fluctuations due to temperature change give a maximum error of 1.5 cc out of 3.9 cc total volume change. For the unloading stage, a difference is about 0.24 cc out of 0.3 cc total volume change. Since the local LVDTs perform better, they were used for the total volume change during isotropic compression.

Calibration for shearing data

For the shearing data, the effects of the ram displacement and time were considered since the cell pressure was constant, as shown in Figure 4-14. The back volume gauge is also used for comparison. The cell volume gauge calibrated for ram displacement and time has a similar trend to the back volume gauge, with about 0.5 cc difference out of 4.3 cc total volume change at the end of shearing, corresponding to 0.6% difference out of 5.6% total volumetric strain. Given a specific volume of 1.8, the resulting error would be just about 0.01, which was acceptable.

In summary, the cell volume gauge works well at large strains during shearing, considering the effects of ram displacement and time.

4.6 System leakage

4.6.1 Leakage tests

A leakage test is very important for a new system. For the leakage tests, back and cell volume gauges were tested first, when they were isolated from the rest of the system. It can be seen from Figure 4-15 (a) and (b) that both back and cell volume gauges have a linear increase of 0.035 cc/day and 0.012 cc/day, respectively. This change is very small and linear, which means they were considered acceptable. Then the whole system was

tested on a dummy sample and the cell was pressurised directly through the cell volume gauge. As shown in Figure 4-15 (c), the cell volume gauge could not stabilise even after 6 days and had significant volume change in total (around 5.6 cc). This indicated that there was a small leakage in the system, but it was difficult to identify where it occurred.

Small leakages normally occurred at tube joints, in components that water flows through (e.g. valves), or in broken components (e.g. broken LVDTs and broken LVDT cables inside the cell). Since there were many potential leakage points and each leakage test took at least 24 hours, leakage testing was extremely time-consuming.

Each component was checked one by one. The system was pressurised by back and cell volume gauges with a large pressure difference, and the valves in between were turned on one by one during each leakage test. The volume change in the volume gauges under constant pressure was used to detect leakages, rather than pressure changes for an isolated volume. This is because even a small temperature change can cause large pressure variation in rigid components like the triaxial cell or volume gauge.

An example of leakage testing on the back pressure line is shown in Figure 4-15 (d). To isolate the back pressure line from the air pressure line first, the modified top platen was replaced by a traditional top platen. The back volume gauge reading was recorded when the valves next to the back volume gauge were turned on one by one. There was not much volume change until turning on the final valve. Therefore, the leakage point can be any component between this valve and the pedestal, and the only way to identify it was to tighten them sequentially. But tightening compression joints sometimes made leakage worse due to the deformation of the compressed olive. So, it took a long time to spot and fix the leaking joints. After fixing them, a clear stabilisation of the back

volume gauge was observed in Figure 4-15 (e), indicating that the back pressure line was now leak-free.

Many other specific leakage tests like this were conducted based on the cell volume gauge reading as well. In the end, the cell volume gauge had a linear change with time, 0.00051 cc/hr or 0.012 cc/day, as shown in Figure 4-15 (f). This rate was acceptable and used as the new time-effect correction for the unsaturated tests.

4.6.2 Leakage points

Overall, there were many leakage points spotted in the system:

The new valve on the pressure line of the new cell volume gauge was found to leak due to its poor quality, and some old valves in the back pressure line leaked as well due to ageing. The local LVDTs leaked a few times, because of rusted bodies and broken cables. The replacements were subjected to new leakage checks.

There was leakage in the compression joint connecting the new pedestal to the back pressure line so that the cell water flowed into the back volume gauge. Tightening the compression joint was tried first, but the leakage became worse due to deformation of the compressed olive. It was fixed by changing the compression joints.

The modified top platen leaked cell water into the air pressure line and the sample, because of a loose screw joint between the air tube and the top platen. This was found because the leaking water was found in the air pressure line. The screw joint used to screw into the top platen was glued into the top platen instead, to avoid any potential leakage in the future. A separate leakage test was done by placing soap bubbles around the joint and applying air pressure, checking if bubbles stayed still.

Small cracks in the HAE porous stone were observed in the pedestal, which could adversely affect the performance of the porous stone. These cracks occurred when the

cell pressure decreased rapidly at the end of tests but the pore pressure decreased slowly due to the low permeability of HAE porous stone. Then, a very sudden large pressure difference resulted in the cracks. The HAE porous stone was replaced, and in subsequent tests the cell pressure was decreased slowly to ensure a maximum 50 kPa pressure difference on the porous stone.

4.7 Test procedures for unsaturated triaxial tests

4.7.1 Porous stone saturation

As mentioned in Section 4.4.4, to achieve the best performance of the HAE porous stone, the drainage system should be flushed first and the porous stone should be carefully saturated. Water from the Bishop hand pump was flushed to the back volume gauge through the groove in the pedestal, as shown in Figure 4-8 (c). The air bubbles in the groove then accumulated in the back volume gauge and were released by emptying and refilling the back volume gauge in four cycles once it was fully filled. Four rounds of flushing normally were required to deair the drainage system, judged by observing no more air bubbles in the transparent tubes.

After flushing the system, the cell was pressurised at the maximum cell pressure 800 kPa overnight with the drainage line and back pressure line closed. This high cell pressure was meant to diffuse the air in the HAE porous stone into the cell water. Then the porous stone was flushed with the cell water by setting the back pressure to 50 kPa, creating a pressure difference with the cell pressure. The back volume gauge readings during flushing were recorded so that the permeability was calculated, which was derived from the slope of volume gauge reading with time. Saturation was finished when the permeability was constant. One day of saturation was required for the very first test, and overnight saturation was sufficient for the subsequent tests.

4.7.2 Sample selection and preparation

Some criteria are required for unsaturated samples used in the unsaturated triaxial equipment with a 5 bar HAE porous stone. First, the suction value during the test should be smaller than 500 kPa so that the HAE porous stone could work properly. Second, the air entry value of the sample should be relatively low so that the sample could have a wide range of workable suctions. Third, the permeability of the sample should be relatively high so that the test could be completed within an acceptable duration.

The sample selection and sample preparation were based on the Soil Water Retention Curve (SWRC) of samples, and the details of the whole process will be shown in Section 6.2 along with the SWRC results of the samples. Here is an example of tailings to explain the principle.

The fine tailings used for the saturated tests was considered for unsaturated test, but the SWRC of the fine tailings prepared by slurry preparation has an air entry value (AEV) larger than 500 kPa. Therefore, the sample type and sample preparation were both adjusted to meet the criteria. A sandy sample would have smaller AEV than the clayey sample and sample prepared by the compaction method could have a smaller AEV than the slurry method, so the sandy tailings prepared by the compaction method were used. Different proportions of fine and sand were considered, including 75%, 60% and 50% sand. The tailings samples with 60% sand and prepared by the compaction method had an AEV lower than 100kPa and had a wide range of suction states below 500kPa. The duration of the unsaturated triaxial test on this material was about 1 month, which was acceptable. Therefore, the sandy tailings with 60% fine sand were selected for unsaturated tests, and the compaction method was used to prepare the sample in a split mould, as described in Section 3.3.2. Then, the prepared sample was sprayed with water on the surface or was dried in the atmosphere to achieve a certain water content,

corresponding to the required suction value estimated from its measured SWRC. After being left for one day to reach equilibrium with cling film covering, the sample was ready for testing.

4.7.3 Test stages

Unsaturated triaxial tests conducted in this study include sample setting-up, suction application and stabilisation, constant suction compression, constant water content shearing, and sample dismantling. The test procedures in each stage are described as follows.

Sample setting-up

The HAE porous stone was always kept with water on top to avoid any desaturation until the sample was set up. The back and cell pressure transducers were zeroed when the water level was about the position of the mid-height of sample. Due to the low permeability of the HAE porous stone, it normally took many hours for the back pressure to stabilise before zeroing it. The modified top platen and the air pressure line were dried by blowing through with air. The air pressure transducer was zeroed when connected to the atmosphere.

The initial wet mass and size of the sample were measured just before placing it on the pedestal. After removing the excess water from the pedestal, the sample was placed on the top of it with a filter paper beneath and a low air entry porous stone on top. After placing grease around the pedestal and top platen, the side filter paper, the membrane and O-rings were placed in sequence, similar to that in the saturated tests as introduced in Section 3.5.4. The same procedures for saturated tests was adopted for zeroing and setting up the local LVDTs. Extra care was taken in placing the modified top platen to

avoid dragging sample and disturbing the local LVDTs. The half ball was finally placed on the top platen.

Suction application and stabilisation

After filling the cell with water and closing the cell, the initial readings from the volume gauges and local LVDTs were recorded by the computer. The cell, back and air pressures were manually increased to 50 kPa, 30kPa, and 10 kPa respectively, in sequence. The suction was then slowly built up to 100kPa by increasing all the pressures to the desired values in 1 hour, 220 kPa, 200 kPa and 100kPa for the cell, air and back pressures respectively.

All the pressures were then maintained at constant values during the suction stabilisation stage. The back volume gauge and local LVDTs were used to check for stabilisation. Due to the difficulty in achieving perfect equilibrium throughout the sample, the stabilisation was assumed to be complete when the water volume change was smaller than 0.1 cc/day, following the standard adopted by Sivakumar (1993). Normally, the stabilisation stage took a minimum 3 days and sometimes up to 10 days.

Constant suction compression

Constant suction compression was conducted by holding the air and back pressures constant and gradually increasing the cell pressure to the required value. To speed up the test, the cell pressure was ramped at 1kPa/hour for the first 100 kPa increment, 2 kPa/hour for the next 200 kPa increment and 3 kPa/hour for the remaining increment. Compression was paused between each stage for stabilisation, allowing the excess water pressure throughout the sample to dissipate and checking whether the increment rate was appropriate. Each stabilisation normally took 2 days and showed minimal change in the back volume gauge or local LVDT readings. This indicated that excess

pore water was not significant and that the increment rate was appropriate. The whole compression stage took about 10 days to increase the cell pressure from 220 kPa to 750 kPa.

Constant water content shearing

For the constant water content shearing, the back pressure line was closed for a constant water content condition. The cell and air pressures were maintained constant. The local LVDTs were all zeroed to 0mV at their current positions to ensure the best resolution at the start of shearing. The loading shaft on the top of the cell was screwed down to just contact the half ball. After setting up the ram to the CRSP control, shearing commenced. The sample was sheared under displacement control at the increment rates of 0.05mm/hr for ε_a=0.001%-0.01%, 0.1mm/hr for ε_a=0.01%-1%, and 0.15mm/hr for ε_a=1%-25%. These slow rates were considered adequate to allow equilibrium of pore water pressure. The entire shearing stage typically lasted around 15 days.

Sample dismantling

At the end of the test, the deviatoric force was removed from the sample by bringing down the axial ram. The air pressure was reduced to zero and the back pressure line was kept closed. The cell pressure was decreased gradually to allow the back pressure underneath the HAE porous stone to decrease, in order to avoid the back pressure larger than the cell pressure by more than 50 kPa and breakage the HAE porous stone. Then, the sample was ready for dismantling.

The final wet mass and dimensions of the sample were measured immediately after removing the membrane. These values were used to calculate the bulk unit weight and the barrelling correction factor as mentioned in Section 4.5.1. Three parts of the sample (top, middle and bottom) were cut out for the water content measurement, which was

also used to evaluate the change in water content during the test. The rest of the sample was preserved for SEM and MIP tests. These soil properties at the start or the end of the tests were used to evaluate the initial specific volume, as introduced in Section 3.3.3.

4.7.4 Data analyses

The radial strain was the summed value of the two local radial LVDT displacements divided by the diameter of sample. The axial strain was the average local axial strain based on their respective gauge lengths. The calculation of the total volume change of sample was discussed in Section 4.5. The total volume strain was calculated based on local radial and axial strains following the Equation 4-1 in the suction application and stabilisation stage, compression stage and the initial 3% axial strain of the shearing stage. For large strain levels in the shearing stage, the total volume strain was calculated from the cell volume gauge and corrected for the ram displacement and time. The current ν and total volume were calculated based on the total volume strain. The cross-sectional area was calculated by dividing the current volume by the current height. The w was calculated based on the change in the back volume gauge reading and the calculated final water content.

4.8 Summary

This chapter presented the equipment development and test procedures for unsaturated tests used to investigate unsaturated transitional behaviour. Filter paper and tensiometer tests were conducted to determine the Soil Water Retention Curves, which informed the selection and preparation of the unsaturated triaxial samples. The unsaturated triaxial system was modified from a conventional saturated triaxial system using the axis translation technique to enable suction-controlled testing. This chapter establishes

the experimental foundation for the analysis of unsaturated transitional behaviour discussed in Chapter 6.

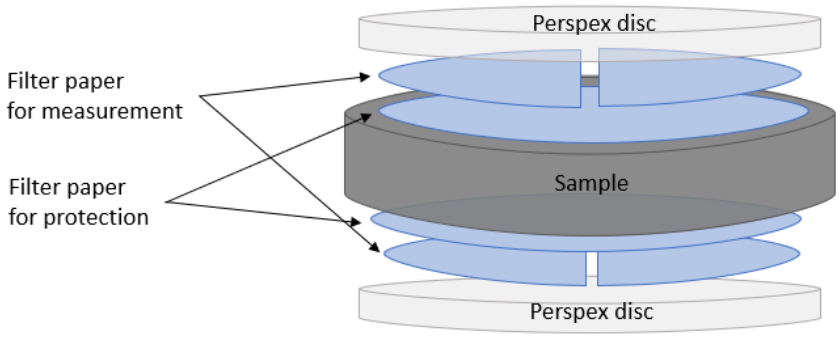

Figure 4-1 Sandwiched sample in filter paper tests.

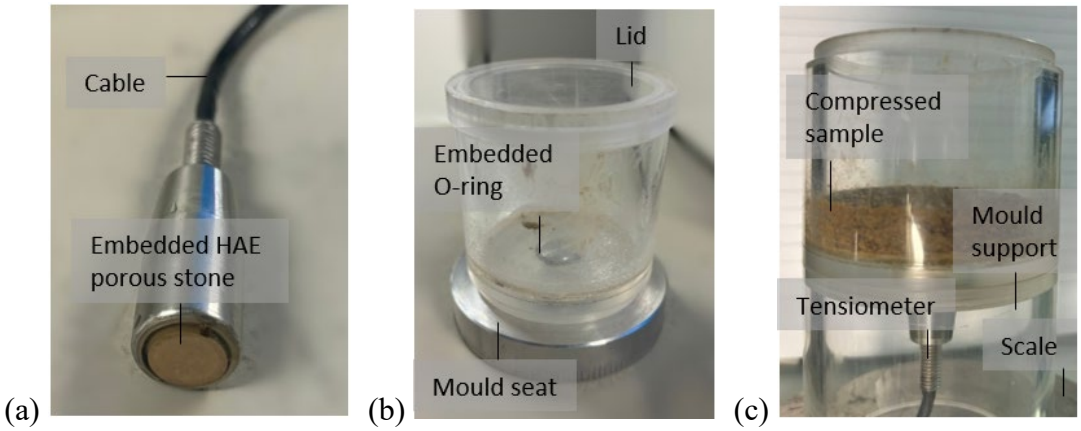

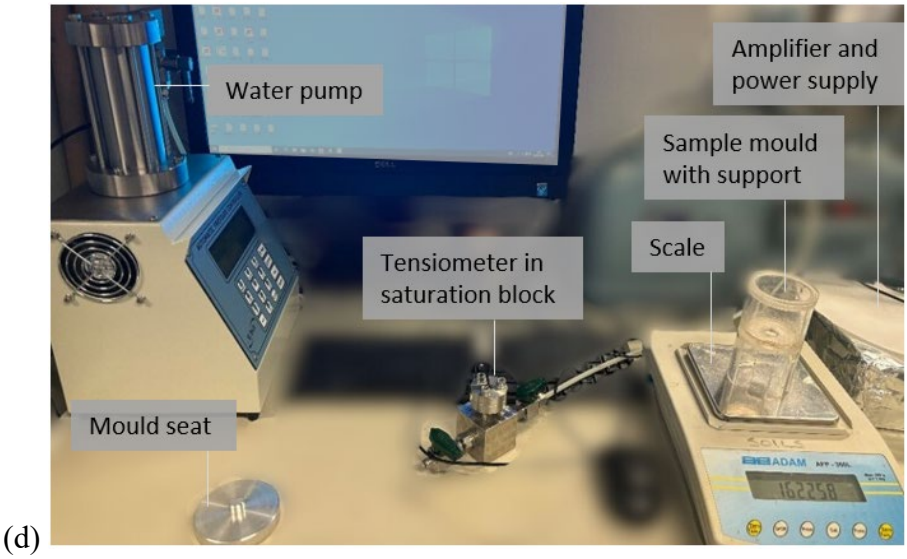

Figure 4-2 Setup for SWRC testing using a tensiometer: (a) tensiometer, (b) mould for sample preparation, (c) mould for suction measurement, (d) overall system setup.

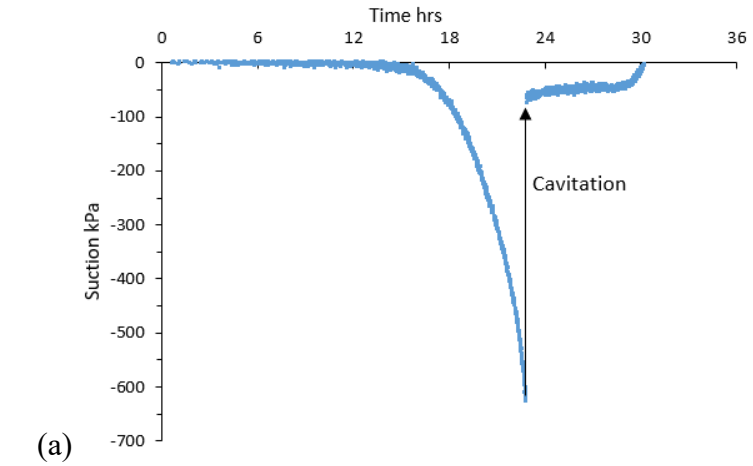

(a)

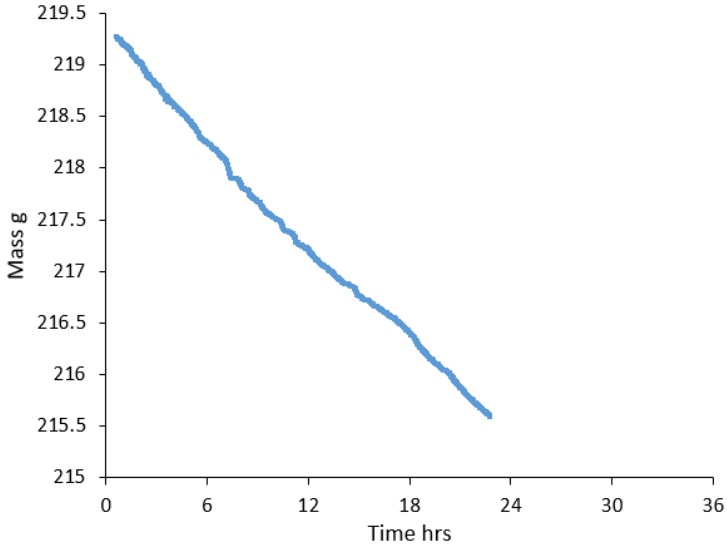

(b)

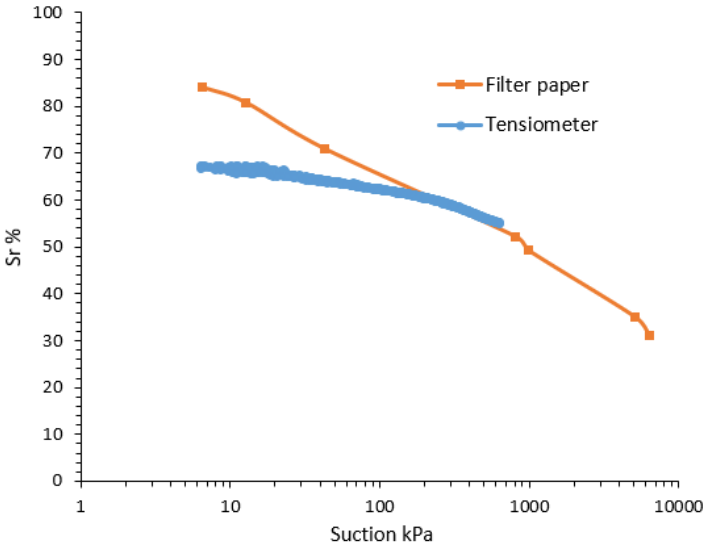

(c)

Figure 4-3 Results for SWRC measurement based on tensiometer test during sample desaturation: (a) suction change, (b) mass change, and (c) SWRC.

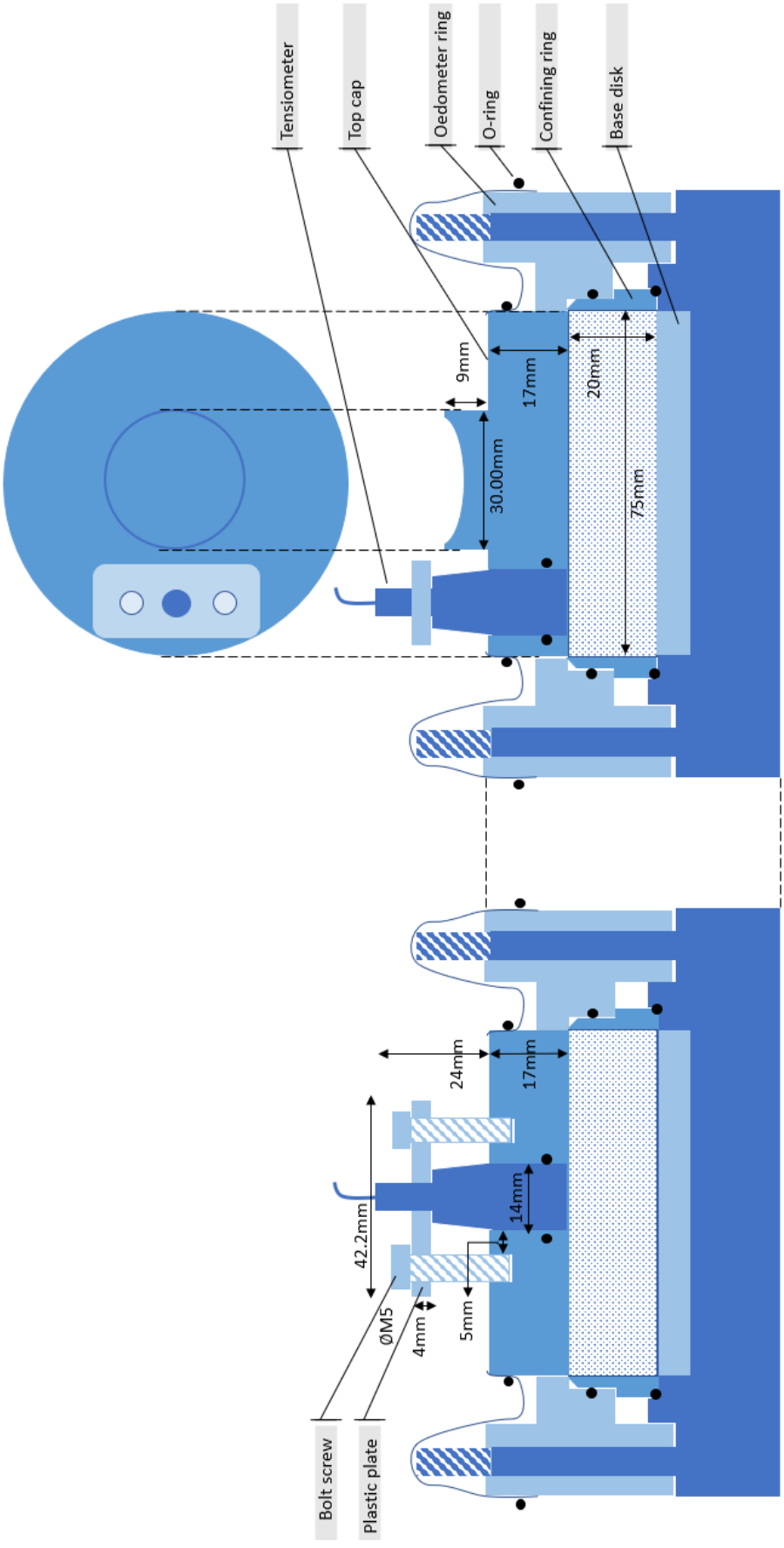

Figure 4-4 Schematic design of the unsaturated oedometer tests.

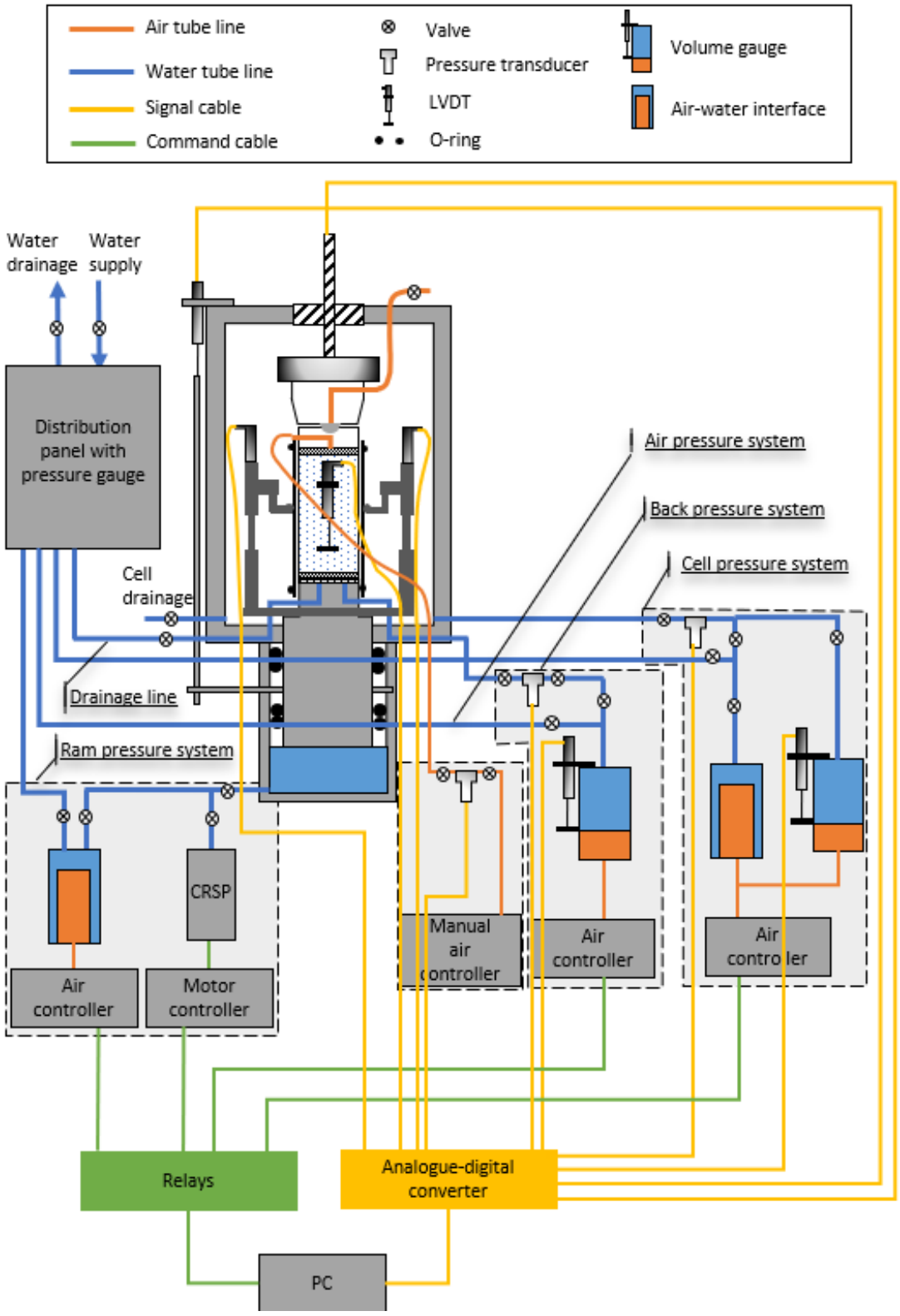
Air tube line
Water tube line
Signal cable
Command cable
Valve
Pressure transducer
LVDT
O-ring
Volume gauge
Air-water interface
Water drainage
Water supply
Distribution panel with pressure gauge
Cell drainage
Drainage line
Ram pressure system
Air pressure system
Back pressure system
Cell pressure system
CRSP
Air controller
Motor controller
Manual air controller
Air controller
Air controller
Relays
Analogue-digital converter
PC

(a)

(b)

(1) Vertical loading system
    (1.1) Loading shaft
    (1.2) Loading cell
    (1.3) Load adapter
    (1.4) Air tube line
    (1.5) Valve
    (1.6) Half ball
    (1.7) External LVDT
(2) Modified top platen
    (2.1) Top platen
    (2.2) Air tube line
(3) Low air entry porous stone
(4) Axial strain LVDTs
(5) Axial strain LVDT supports
(6) Sample
(7) Radial strain LVDTs
    (7.1) Core
    (7.2) Armature
(8) Radial strain LVDT supports
    (8.1) LVDTs holding case
    (8.2) L shape arm
    (8.3) Pivot
    (8.4) Round-end screw
    (8.5) Adjustment column
    (8.6) Support seat
    (8.7) Joint to pedestal
    (8.8) Additional weight
    (8.9) Screw
(9) Pedestal
    (9.1) HAE porous stone
    (9.2) Wavy groove
(10) Drainage lines
    (10.1) Drainage tube
    (10.2) Back pressure tube

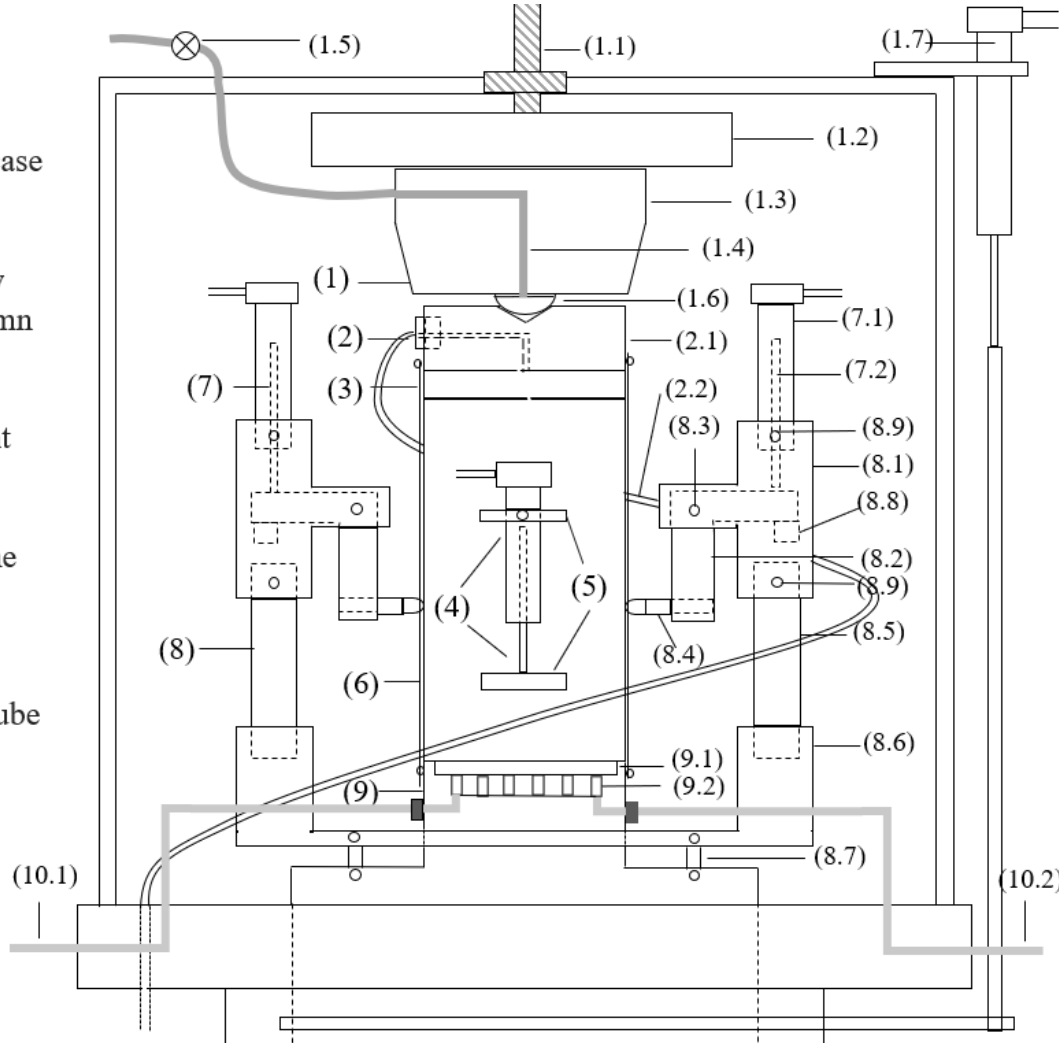

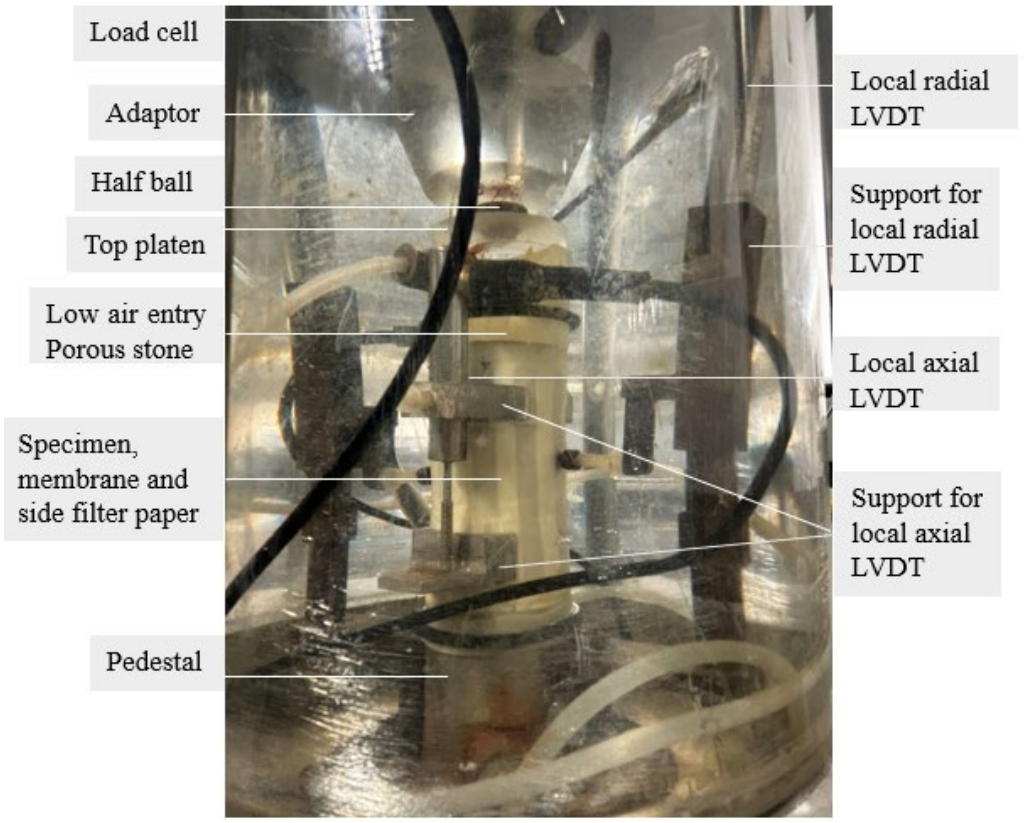

(c)

Figure 4-5 (a) Layout of the unsaturated triaxial system, (b) schematic of cell, and (c) photograph of the cell.

(a)

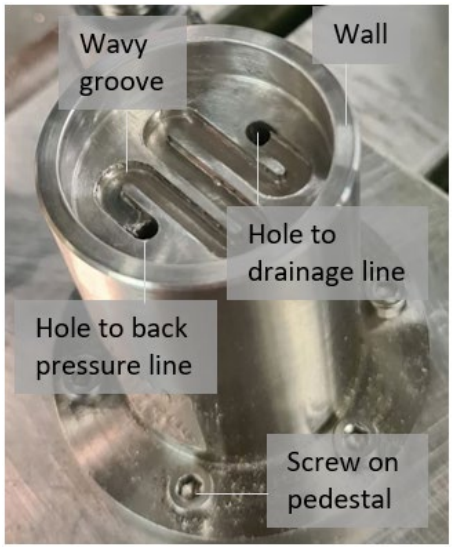

(b)

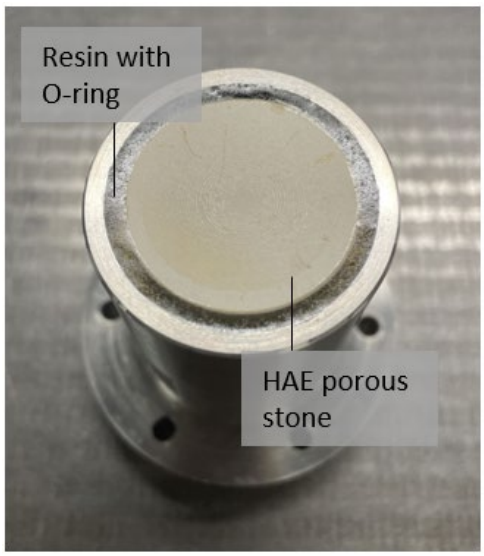

Figure 4-6 Modified pedestal: (a) HAE porous stone and (b) wavy groove.

(a)

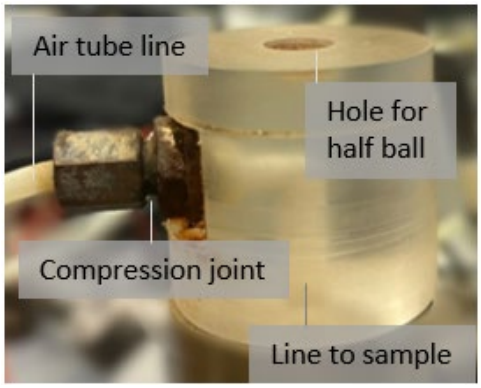

(b)

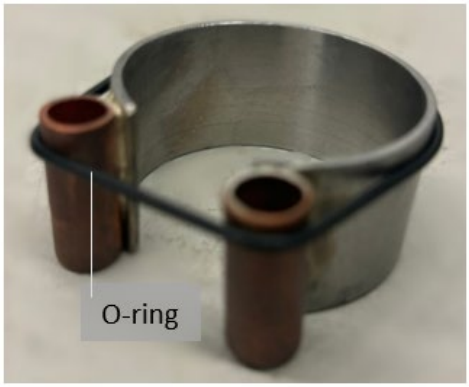

Figure 4-7 Modified top platen for air pressure: (a) top platen, and (b) O-ring applying tool.

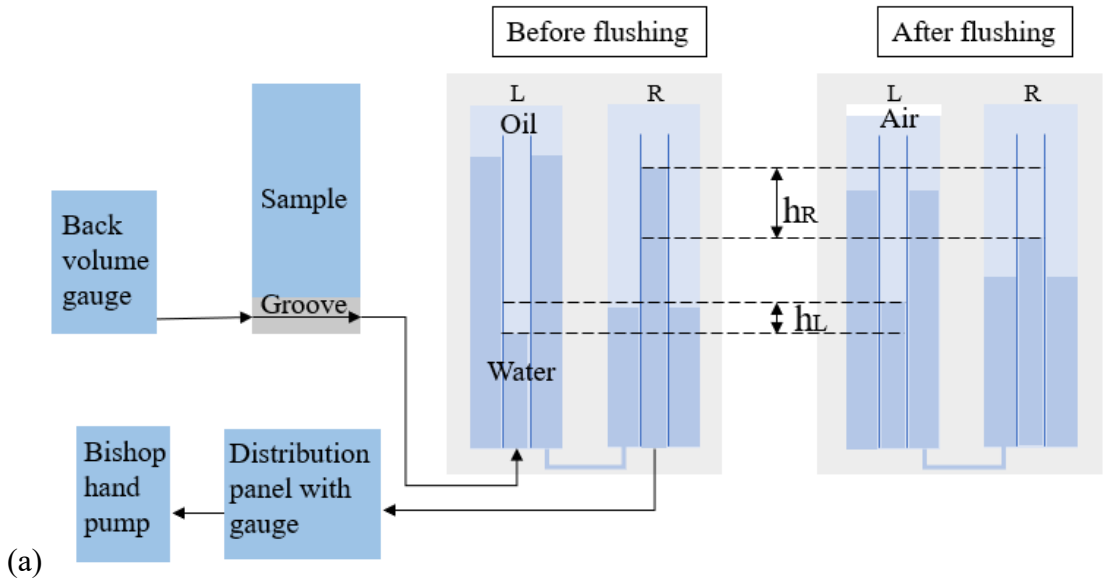

(a)

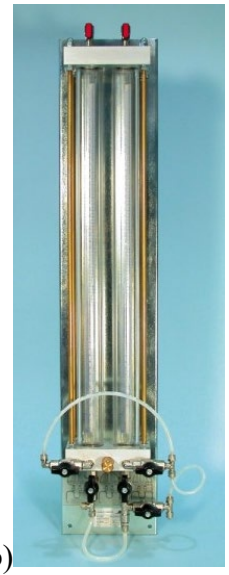

(b)

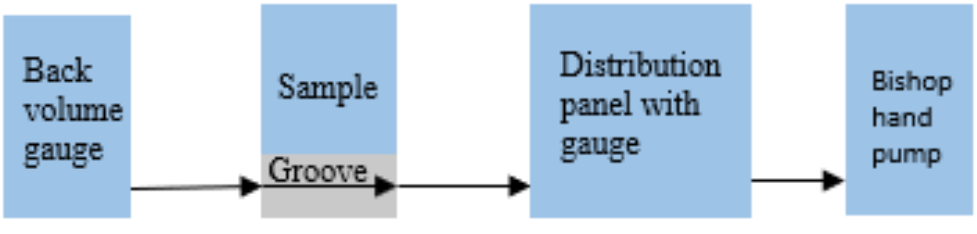

(c)

Figure 4-8 Flushing systems: (a) schematic of twin burette flushing system, (b) twin burette apparatus from ELE international company, and (c) schematic of a simple flushing system.

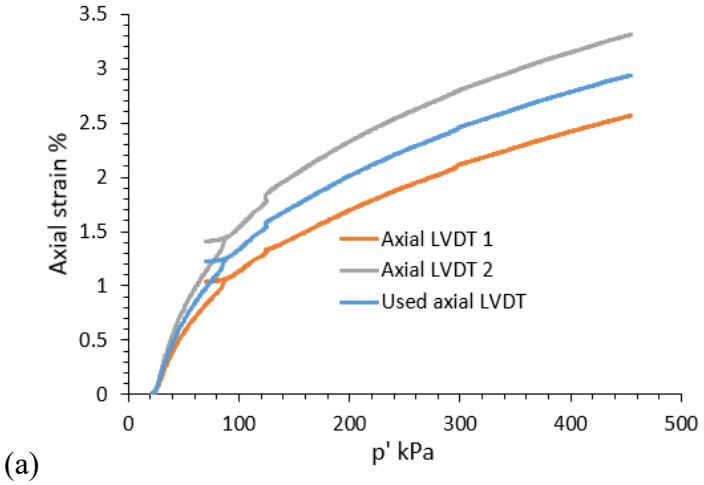

(a)

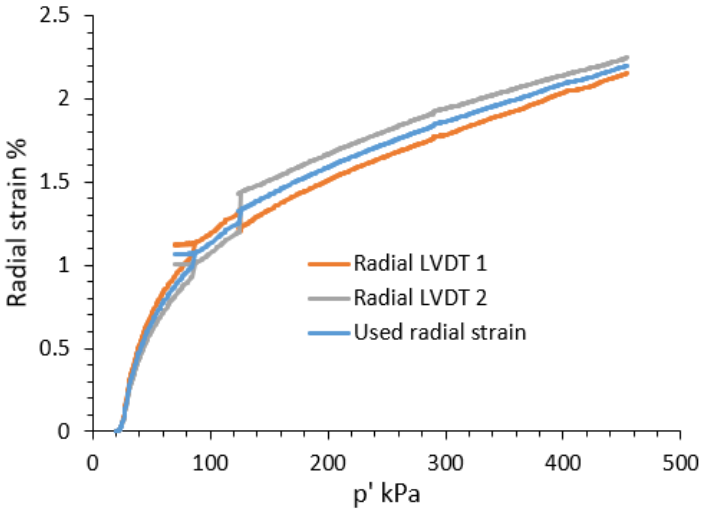

(b)

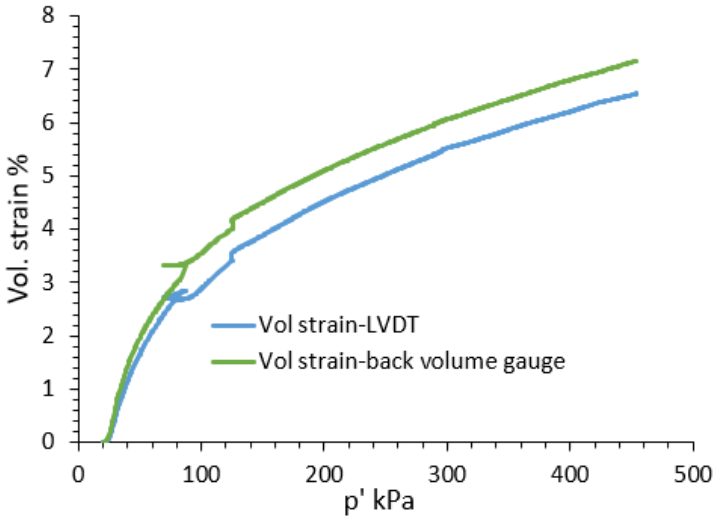

(c)

Figure 4-9 Calculation of total volume using local LVDT during isotropic compression of loess saturated test T1 as an example: (a) axial strain (b) radial strain, (c) calculated total volumetric strain.

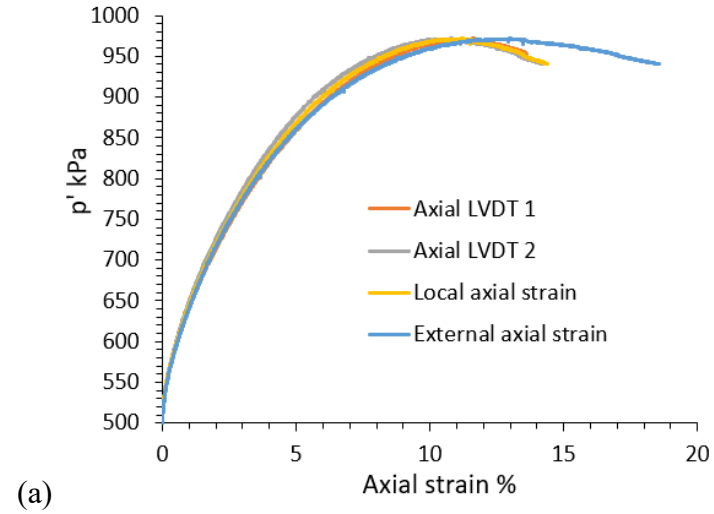

(a)

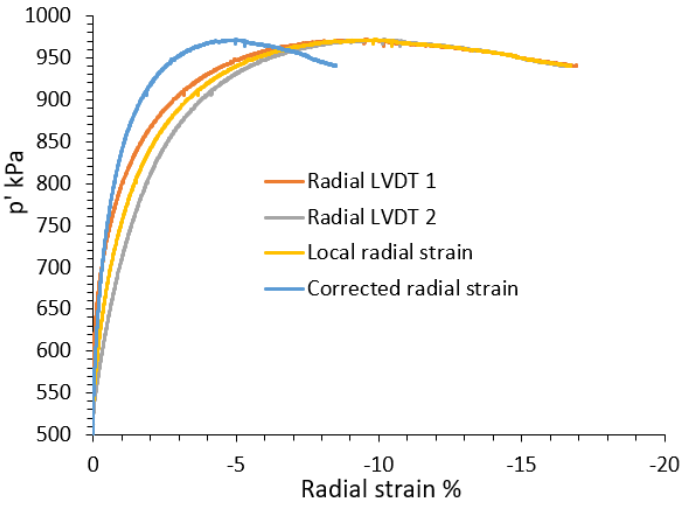

(b)

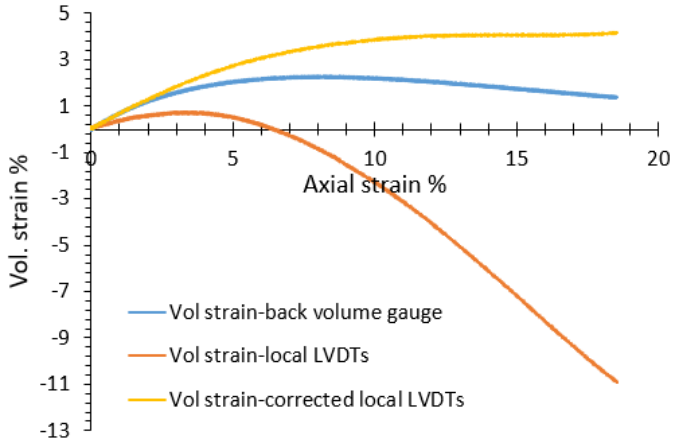

(c)

Figure 4-10 Calculation of total volume through local LVDT during shearing of loess saturated test T3 as an example: (a) axial strain (b) radial strain, and (c) calculated total volumetric strain.

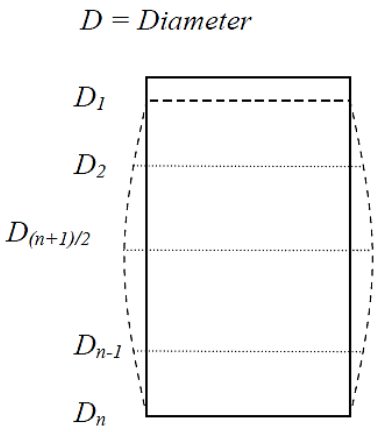

Figure 4-11 Barrelling shape assumption (Jotisankasa, 2005).

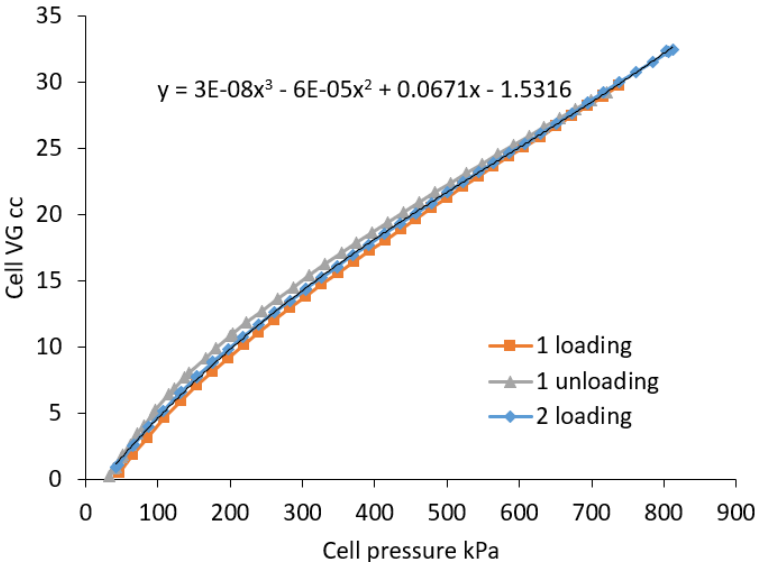
y = 3E-08x³ - 6E-05x² + 0.0671x - 1.5316
Cell VG cc
Cell pressure kPa
1 loading
1 unloading
2 loading
0
5
10
15
20
25
30
35
0
100
200
300
400
500
600
700
800
900

(a)

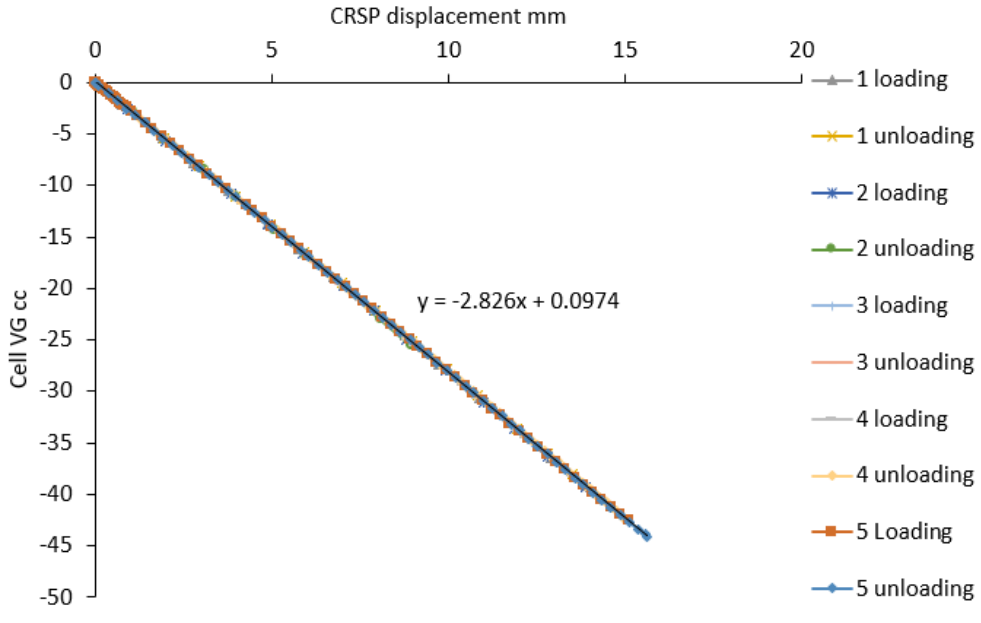
CRSP displacement mm
Cell VG cc
y = -2.826x + 0.0974
1 loading
1 unloading
2 loading
2 unloading
3 loading
3 unloading
4 loading
4 unloading
5 Loading
5 unloading
0
5
10
15
20
0
-5
-10
-15
-20
-25
-30
-35
-40
-45
-50

(b)

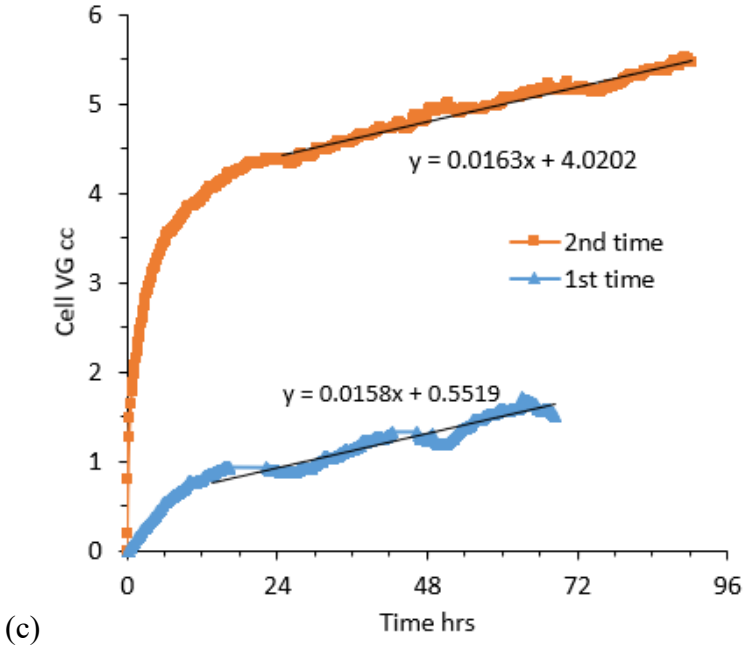

(c)

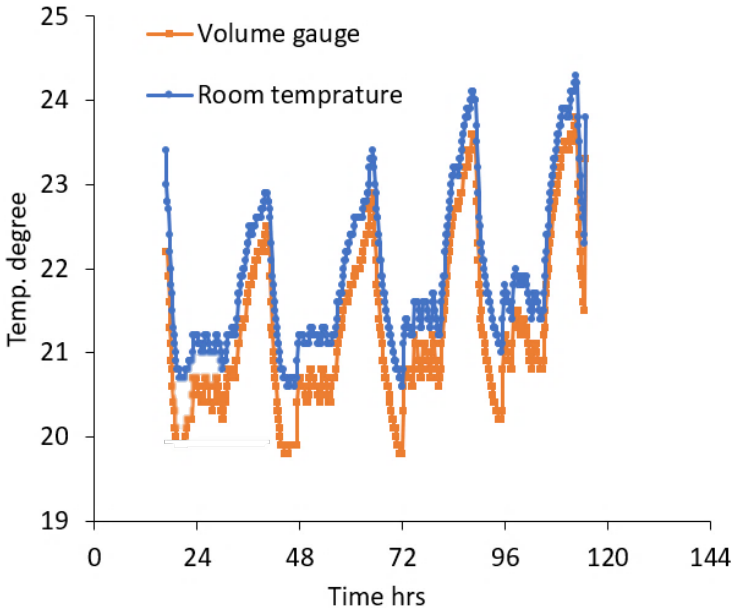

(d)

Figure 4-12 Calibration of cell volume gauge for effects of (a) cell pressure, (b) ram displacement, (c) time, and (d) temperature.

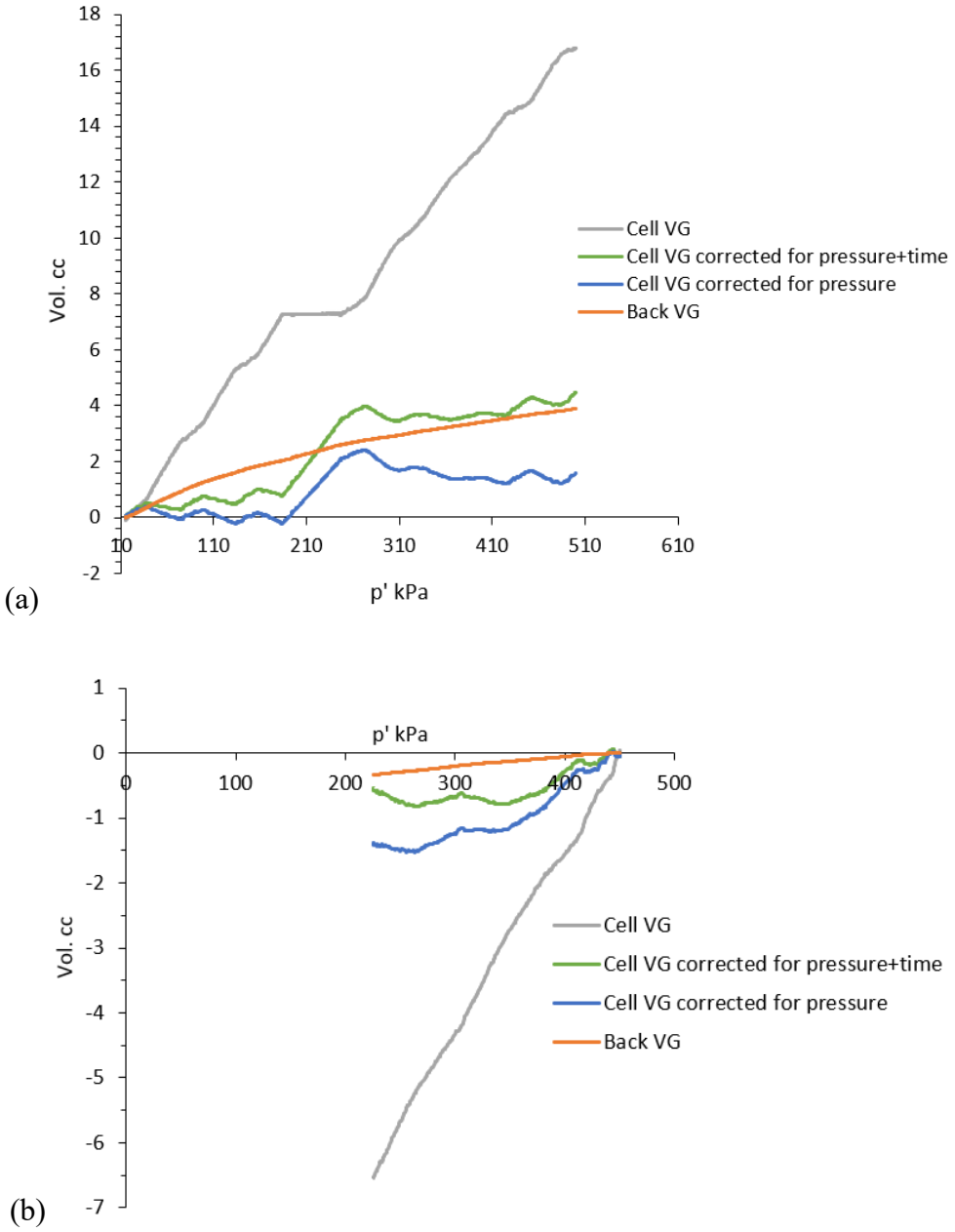

Figure 4-13 Calibration of cell volume gauge for isotropic compression (a) loading stage of saturated loess test T2 and (b) unloading stage of saturated loess test T1 as examples.

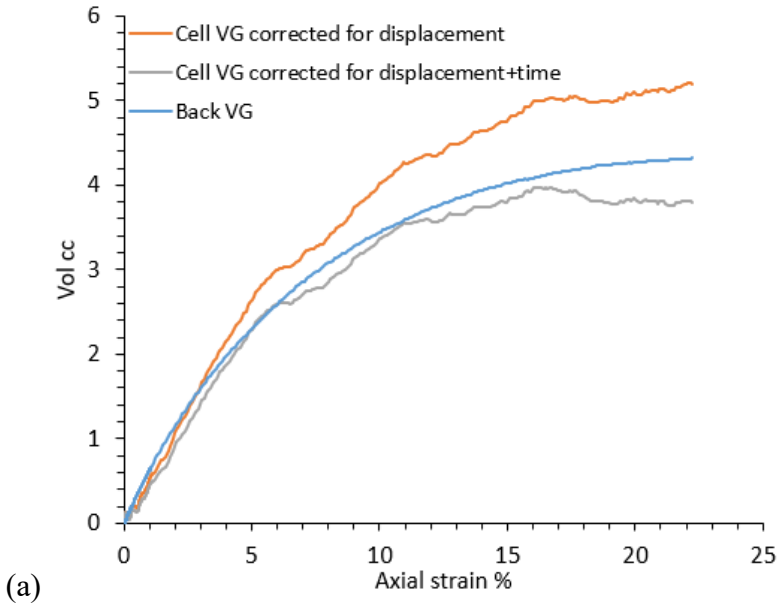

(a)

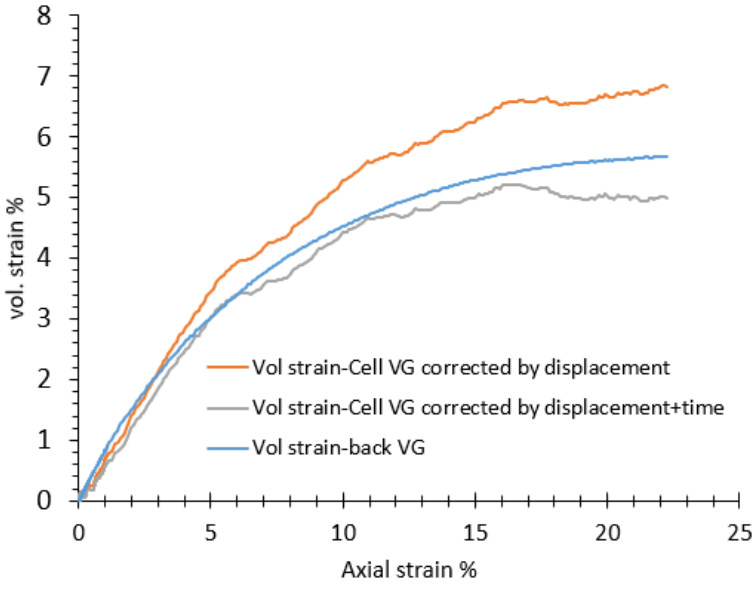

(b)

Figure 4-14 Calibration of cell volume gauge for shearing of saturated loess test T2 as an example: (a) the volume change for calibrations and (b) the volumetric strains for calibrations.

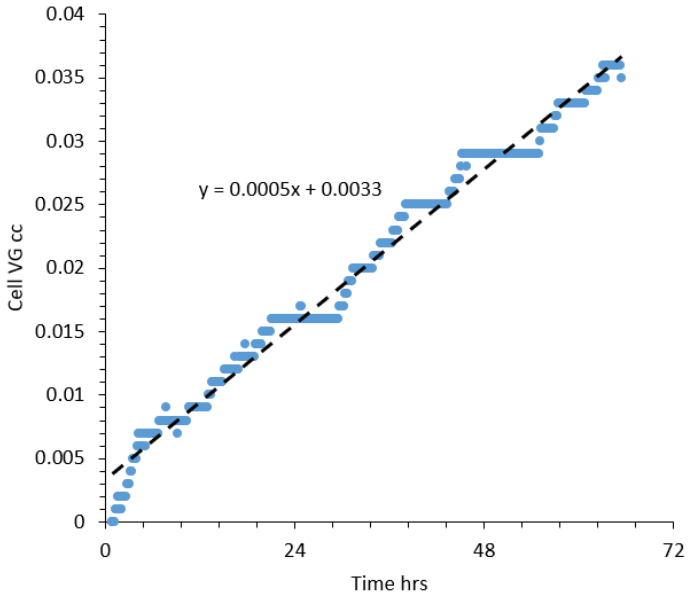
y = 0.0005x + 0.0033
Cell VG cc
Time hrs
0.04
0.035
0.03
0.025
0.02
0.015
0.01
0.005
0
0
24
48
72

(a)

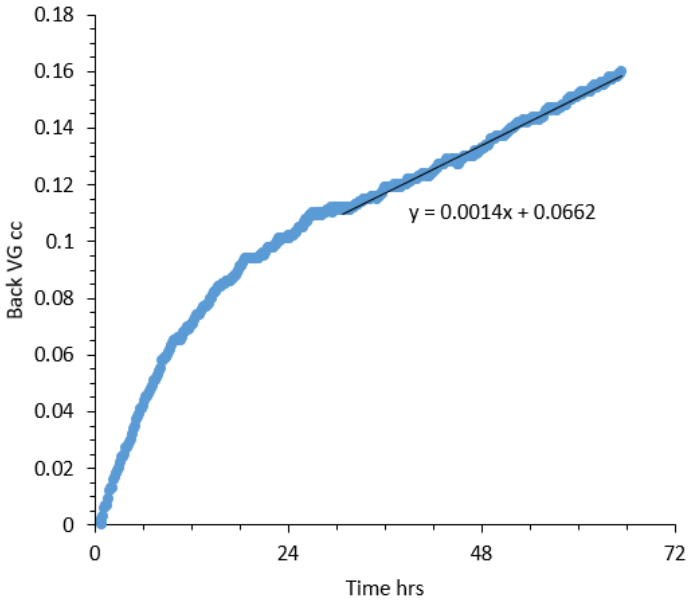
y = 0.0014x + 0.0662
Back VG cc
Time hrs
0.18
0.16
0.14
0.12
0.1
0.08
0.06
0.04
0.02
0
0
24
48
72

(b)

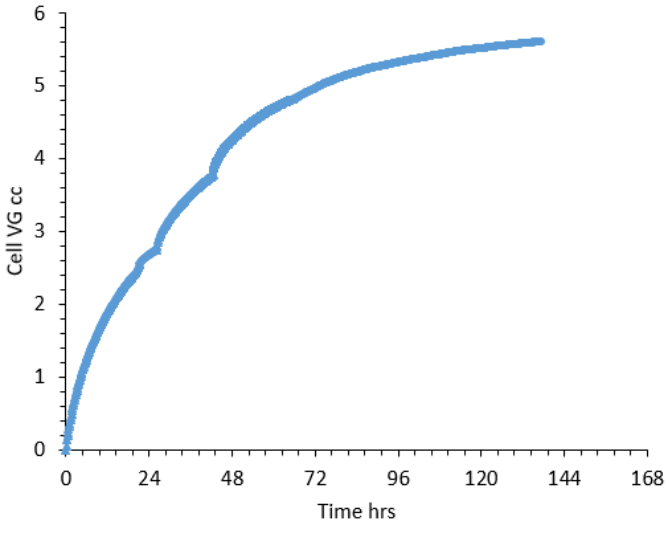
Cell VG cc
Time hrs
6
5
4
3
2
1
0
0
24
48
72
96
120
144
168

(c)

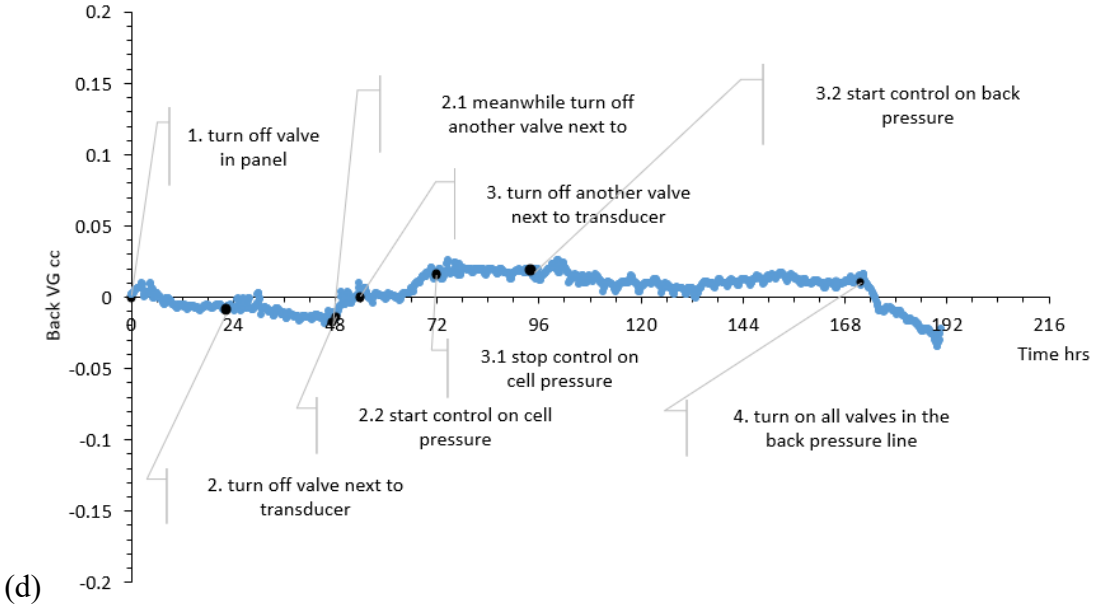

(d)

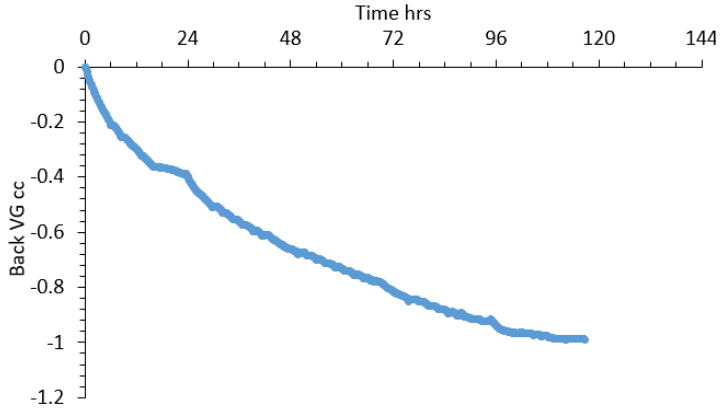

(e)

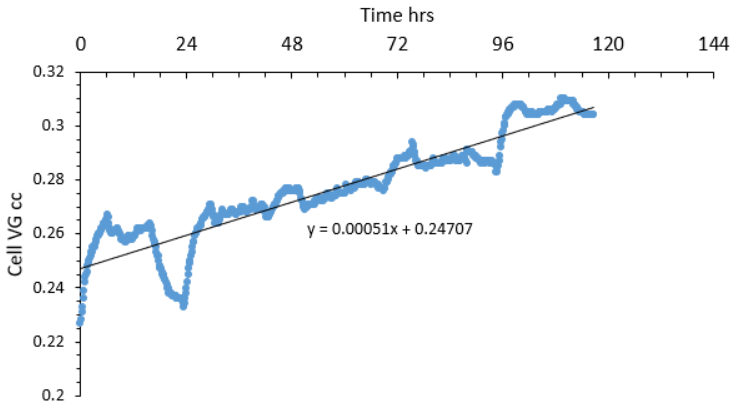

(f)

Figure 4-15 Results of leakage tests: (a) cell volume gauge and (b) back volume gauge isolated check; system check using (c) cell volume gauge and (d) back volume gauge; (e) back volume gauge and (f) cell volume gauge isolated check after fixing the leakage points.

CHAPTER 5 ANALYSIS OF SATURATED TESTS

5.1 Introduction

To investigate the transitional behaviour of saturated soil, a series of oedometer and triaxial tests were conducted on samples across a wide range of initial specific volume (v_i) values. Microstructure tests were further conducted on samples tested to analyse soil structure and explain the transitional behaviour. This chapter presents the results from these tests and discusses the characteristics of the transitional behaviour observed. Four soils were studied, including mixtures of kaolin and Leighton Buzzard sand, silty loess, sandy tailings, and fine tailings, each detailed in its respective section, from Section 5.2 to Section 5.5. Transitional behaviour was identified in all four soil materials, with a more detailed study on this behaviour in the fine tailings in Section 5.5.

5.2 Mixture of kaolin and sand

5.2.1 Mixtures with different components

Different proportions of kaolin and Leighton Buzzard sand were tested to identify the mixtures exhibiting the most pronounced transitional behaviour. These mixtures included 85% sand with 15% kaolin (85SK), 80% sand with 20% kaolin (80SK), 75% sand with 25% kaolin (75SK), 70% sand with 30% kaolin (70SK), and 65% sand with 35% kaolin (65SK). One dense sample and one loose sample for each mixture were prepared with the slurry method with targeted v_i values of 2.1 and 1.4 and were named (XX)SK(Y), where XX is the percentage of sand and Y is l or d, representing loose or dense state, as summarised in Table 5-1. Their compression behaviours are shown in Figure 5-1 (a). It is clear that the compression lines of 85SK and 80SK completely converged at about 8 MPa, but the 70SK and 65SK show similar non-convergence. It

is evident that the 75SK, containing 75% sand with 25% clay, exhibits the most pronounced transitional behaviour.

The m value proposed by Ponzoni et al. (2014) was employed to quantify the convergence of the compression paths. This value was determined by plotting the relationship between the v at an initial low stress level (v_i) and that at a final high stress level (v_f) for each compression curve. The gradient of this relationship represents the m value, as introduced in Section 2.2.1. As shown in Figure 2-2, if a unique normal compression line is generated, samples with different v_i converge to the same v_f, resulting in *m=0*. In cases when the difference in v_i remains constant, indicating parallel compression curves, the m value would be 1. Therefore, the closer the m value is to 1, the stronger the transitional behaviour of the soil.

For the oedometer tests on mixtures with various proportions, the m values shown in Figure 5-1 (b) were calculated based on the v_i at σ_v' =30 kPa and the v_f at σ_v' =8000 kPa. This initial stress level was chosen to avoid the initial sharp decrease observed in some tests before σ_v' =30 kPa, which might be caused by air trapped in the sample boundary. It is clear that the 75SK mixture has the highest m value (m=0.53), and it therefore was selected for further study. As mentioned in Section 3.2.3, Martins et al. (2001) and Shipton and Coop (2015) studied transitional behaviour for Sand with Plastic Fines (SPF) consisting of 75% quartzitic sand and 25% kaolin. They reported degrees of transitional behaviour of 0.67 and 0.89, respectively. The relatively high transitional degrees compared with mixture studied are likely due to differences in soil properties, as shown in Table 3-3.

5.2.2 Mixture with 75% sand and 25% kaolin

The slurry sample preparation was first used for the mixture 75SK to achieve a wide range of v_i by varying the w_i. Samples OM2 to OM5 had v_i from 1.60 to 1.34 with w_i ranging from 22.6% to 11.3%, as shown in Table 5-2. Their one-dimensional compression lines did not converge at stresses up to 5.4 MPa, as shown in Figure 5-2 (a) representing clear transitional behaviour. Difficulties arose in preparing looser samples using higher w_i. Very high w_i values, from 60.4% to 33.9%, were used for samples OM6 to OM12, but their compression lines became concentrated at similar positions, as shown in Figure 5-2 (b). This is because when the water content becomes too high, some of the added water does not bind with the soil and instead remains as gravitational water. This indicates the difficulty of using slurry method to achieve a high v_i value for certain soils.

The compaction method was used instead to reach a higher v_i with w_i about 10.8% for sample OM1. Its compression line was very similar to those of samples with very high w_i (samples OM6 to OM12), and it did not converge with the other compression lines. This indicates that the sample preparation method does not affect the compression behaviour of transitional soil, as introduced in Section 2.2.3, and this agrees with many previous studies (Li & Coop, 2019; Li et al., 2018; Nocilla et al., 2006; Shipton & Coop, 2012, 2015; Xu & Coop, 2017). Although mixture 75SK exhibited clear transitional behaviour, it was not selected for further study, as other soils with higher transitional degrees were identified later.

5.3 Silty loess

5.3.1 Compression behaviour

Oedometer tests

For the silty loess, the slurry sample preparation was initially used in four oedometer tests. Samples OL1 to OL4 were prepared using w_i from 38.1% to 15.9% for v_i ranging from 2.02 to 1.67. However, the difficulty of using higher w_i to prepare higher v_i was also observed in loess, and it was even worse than in the mixture of sand and kaolin 75SK. As shown in Figure 5-3 (a), the compression lines for the slurry samples OL1 to OL3 are very concentrated, although their compression lines still do not converge with that of the sample OL4 up to 5.4 MPa vertical stress.

Since the compaction method was able to create samples with a wide range of v_i easily for the mixture of sand and kaolin 75SK, this method was tried on loess to prepare samples OL5 to OL8. The v_i varied from 2.20 to 1.66 with w_i ranging from 9.8% to 12.1%, as shown in Table 5-3. The four compression lines reach their non-unique Normal Compression Line (NCL) and show non-convergence up to 5.5 MPa vertical stress, as shown in Figure 5-3 (b). These compression lines have varied yield stresses, ranging from less than 2 kPa for the loosest sample OL5 to 2000kPa for the densest sample OL8. This variation results from differences in the initial water content, leading to a phenomenon similar to varying degree of preconsolidation. The degree of transitional behaviour was quantified using m values, calculated based on the varied initial states (σ_v' =30, 250, 1000, and 2500 kPa) and the final state at the maximum applied pressure (σ_v' =5500 kPa). The selected initial states correspond to the yield stresses of each tests, checking the influence of sample preparation on transitional behaviour. The influence of sample preparation was later concluded in the study on sandy tailings (Section 5.4.1) that it only affects the mechanical behaviour before

yielding and would not affect the transitional behaviour. This conclusion agrees with the previous studies (Li & Coop, 2019; Li et al., 2018; Nocilla et al., 2006; Shipton & Coop, 2012, 2015; Xu & Coop, 2017).

As shown in Figure 5-4 (a), the m values range from 0.23 to 0.73, indicating a strong influence of compaction method on the compression behaviour before yielding. This suggests that the m value to quantify the transitional degree should be determined from the compression behaviour after yielding to eliminate influence of sample preparation. For comparison, the transitional silty loess prepared by the slurry method in Xu and Coop (2017) exhibited an m value of 0.26, calculated based on the initial state at 20 kPa and the final state at 7000 kPa. The silty loess in this study therefore shows a comparable degree of transitional behaviour. Due to the clear transitional behaviour, this silty loess was used for the further study. Additionally, since the compaction method was ultimately chosen for sample preparation in the unsaturated tests, as previously mentioned, the compaction method was consistently used for the loess sample in both saturated and unsaturated tests.

Triaxial tests

Three triaxial tests were conducted on samples prepared using the compaction method, with v_i varying from 2.13 to 1.69 with w_i ranging from 9.4% to 21.2%, as summarised in Table 5-3. The loosest sample TL1 was isotropically compressed up to 450 kPa and then unloaded to 230 kPa. The densest sample TL3 underwent isotropic compression to 260 kPa, unloading to 75 kPa and subsequent reloading to 500 kPa. The medium density sample TL2 was directly isotropically compressed to 500 kPa. Their isotropic compression behaviour is illustrated in Figure 5-3 (c).

The transitional behaviour was clearly demonstrated by the lack of convergence in the compression lines up to an effective stress (p') of 550 kPa. TL1 exhibited a very linear compression line starting from very low stress level, suggesting it had reached its NCL. TL2 reached its NCL at around 200 kPa, while TL3 appeared to reach its NCL at a high stress level of around 400 kPa. Both tests showed NCLs with quite similar slope to that of TL1. The transitional degree was quantified by m values, calculated using the same initial states as those in the oedometer tests (σ_v' =30 and 250 kPa) and the final state at the maximum applied pressure ($\sigma_v' = 450$ kPa). As shown in Figure 5-4 (b), the m values of 0.97 and 0.83 show little variation between the two initial stress states. The m values obtained from the triaxial tests are notably different from those of the oedometer tests.

To compare the one-dimensional and isotropic compression behaviour, the σ_v' from the oedometer tests was converted to p' by estimating the k_0 value using $k_0 = 1 - sin\phi'$, based on the results from triaxial shearing tests. The dense and medium density samples TL2 and TL3 exhibited compression behaviour similar to that of samples with comparable initial densities in the one-dimensional tests. However, the loose sample TL1 displays a flatter compression line compared to the corresponding one-dimensional test. This contrasting trend suggests a greater degree of transitional behaviour in isotropic compression than in one-dimensional compression. This difference was also observed in other samples and will be explained later.

5.3.2 Shearing behaviour

After isotropic compression, the samples were sheared in drained conditions in order to reach higher stress levels at the end of the tests, which would provide the critical stress states at higher stresses. As shown in Figure 5-5 (b) and (c), TL1 and TL2 reached stable volumetric states and stress ratios (q/p'), indicating reaching critical states by

the end of the tests. Both tests had a consistent M value of about 1.31 and a linear failure envelope in the p': q plane, as shown in Figure 5-5 (d). TL3, however, failed to reach the critical state before the end of test due to the displacement limitations of the apparatus, showing an unstable volumetric strain and stress ratio. The volumetric and stress-strain behaviour were extrapolated using hyperbolic extrapolations. Both extrapolated values stabilised at around 30% axial strain, and the stress ratio reached the same M value and failure envelope as the other two tests.

The critical state points of the three tests are plotted in the $v - lnp'$ plane, as shown in Figure 5-5 (a). For conventional soils, samples sheared from the same initial p' should reach the same critical state point at the end of test, represented by the same v value at the same p'. Since TL3 reached the same p' value as the TL2, this supports the good extrapolation on TL3 data. However, it is unlikely that the TL3 reached the same v value of TL2 due to the small total volumetric strain of TL3. In the critical state framework, there should be a unique CSL and its slope in the $v - lnp'$ plane should be similar to that of NCL. However, the end points of the TL1 and TL2 tests remain far apart, making them unlikely to converge into a single CSL with a slope matching that of the NCL. Instead, it appeared more probable that each test has an individual CSL, as indicated in Figure 5-5 (a).

5.3.3 Microstructure analysis

Scanning electron microscope (SEM) and mercury intrusion porosimetry (MIP) tests were conducted to investigate the potential reasons from soil fabric for the transitional behaviour. The detailed testing methods for both tests are provided in Section 3.6. It should be noted that only vertical surfaces were examined in the SEM tests.

Loess samples with high and low v_i (LH and LL) were prepared for testing. They were one-dimensionally compressed in oedometer tests to σ_v' of 50 kPa, 500 kPa and 8 MPa through oedometer tests, resulting in six specimens (LH50, LH500, LH8M, LL50, LL500, and LL8M). Three dense samples LL have an average v_i of around 1.68, and loose samples LH have an average v_i of around 2.15, corresponding to the oedometer tests OL8 and OL5 shown in Figure 5-3. The compression behaviour of these samples is consistent with the oedometer tests results, and the corresponding compression data are presented in Figure 5-6.

MIP tests

Cumulative pore size distributions were obtained from the MIP tests, and the pore size distribution (PSD) was derived through the linear regression over short intervals of the cumulative pore volume and pore diameter. As shown in Figure 5-7 (a), all three PSDs of LH loose samples show a sharp single-peak distribution with peak at around 1 μm. As the vertical stress increases from 50 kPa to 8 MPa, the pore volume in the range of 0.1–1 μm increases, due to collapse of larger pores in range of 1-3 μm shifting the distribution toward smaller sizes. Overall, the structure becomes less open during loading, but some structural pores persist, especially above 1 μm. The PDSs of the LL samples are broader and flatter than those of LH samples but also have peaks at around 1 μm, as shown in Figure 5-7 (b), indicating a multiscale pore structure in LL samples. With increasing vertical stress, there is a moderate shift in peak location but the peak persists even at 8 MPa.

Figure 5-7 (c) directly compares the PSDs of LH and LL samples at 50 kPa and 8 MPa. At 50 kPa, LH50 sample has significantly more pores in the 1-4 μm range than LL50 sample, indicating a more open structure in LH50 and denser packing in LL50. After compression to 8 MPa, the pore volume under 1 μm in LH8M became similar to LL8M,

suggesting that fine-pore structures of both samples under compression are similar. However, pore volume differences at 8 MPa persists that LL8M sample maintained a distinct peak at around 3 μm but the peak of LH8M was flatter in the 1-10 μm range.

These results suggest that although compression reduces overall pore volume in both LH and LL samples, the non-convergence of pore structures, especially the persistence of 3 μm pores in LH, explains why samples with different initial densities do not converge to a unique specific volume even under high stress. This supports the identified transitional behaviour in this silty loess because the material retains microstructural differences despite the high stresses.

SEM tests

Scanning Electron Microscopy (SEM) was used to further investigate the microstructural differences between high and low v_i samples (LH and LL), complementing the MIP results. Samples were taken after one-dimensional compression to vertical effective stresses of 50 kPa and 8 MPa.

For the loose sample at 50 kPa (LH50), the SEM image in Figure 5-8 (a) shows clearly defined silt grains covered by loosely packed and randomly oriented clay particles. These clay aggregates may be montmorillonite, which can form this honeycomb-like fabric under loose and saturated conditions. After compression to 8 MPa (LH8M), as shown in Figure 5-8 (b), the silt grains are still distinguishable and coated with a layer of clay particles, but the clay particles appear less flocculated. These observations aligned with the MIP data. The observed open structure in LH50 samples agrees with the dominant pore size at around 3 μm, and the remaining open but less flocculated structure in the LH8M sample aligns with the persistent dominant pores after loading.

In contrast, the dense sample at 50 kPa (LL50), as shown in Figure 5-8 (c), exhibits a more compact silt grains with less visible inter-particle space. The clay particles are more aligned, and the honeycomb-like fabric observed in LH50 is absent. After loading to 8 MPa (LL8M), Figure 5-8 (d) reveals a further denser structure. The silt particles are tightly and uniformly packed, and the clay aggregates appear closely compressed. The SEM images confirm that the initial density has a lasting influence on microstructure after high loading. The persistence of loosely packed silty and clay particles in LH samples suggests that difference on microstructure between LH and LL cannot be eliminated by compression. This supports the MIP findings and provides additional evidence of the transitional behaviour observed in this silty loess studied. The non-convergent void ratio results from the different soil structures from different initial densities, which could not be erased by up to 8MPa compression.

5.4 Sandy tailings

As mentioned in Section 4.7.2, the fine tailings were not suitable for the unsaturated tests due to their very high suction. Instead, a sandy tailings consisting of 60% sand and 40% fines and prepared using the compaction method, was found to be suitable for use in further unsaturated tests. Therefore, saturated tests were also conducted on these sandy tailings, and the results are presented here for comparison with the unsaturated tests shown in the next chapter. However, the fine tailings remain ideal for studying saturated transitional behaviour and thus are the primary focus of the saturated testing presented in the next section.

5.4.1 Compression behaviour

Oedometer tests

Both slurry and compaction methods were used to prepare samples for oedometer tests, as shown in Table 5-4. The slurry samples covered a wide range of v_i from 2.021 to 1.550 by varying the w_i values. The compression lines reached individual NCLs and did not converge up to vertical stress of 2500 kPa, as shown in Figure 5-9 (a), indicating clear transitional behaviour. For samples prepared by the compaction method, three samples from medium-dense to dense (OSTc3, OSTc4 and OSTc5) had clear non-convergent compression lines up to 5.6 MPa. Lower w_i values were used in samples OSTc1 and OSTc2 to reach higher v_i values than the OSTc3. However, their compression lines collapsed onto that of OSTc3, as shown in Figure 5-9 (b). This issue will be discussed later.

The degree of transitional behaviour was quantified using m values, calculated based on the initial state on $\sigma_v' = 100$ kPa and final state on $\sigma_v' = 2500$ kPa, as shown in Figure 5-9 (c). The slurry samples (OSTs) showed a larger m value of 0.58 compared to 0.38 for the compacted samples (OSTc), indicating a greater transitional degree in OSTs. This difference may result from pre-consolidation effects introduced during sample preparation. When recalculated from a higher initial state $\sigma_v' = 250$ kPa, the m values increased to 0.72 for the OSTs and 0.56 for the OSTc, which are higher than those calculated from $\sigma_v' = 100$ kPa. Although this increase confirmed that the sample preparation affects the initial compression state, the similar m values between two methods overall suggest comparable compression behaviour regardless of preparation method. Although the slurry samples showed slightly a greater transitional degree, the compaction method was adopted for the further study on sandy tailings, due to its suitability for the unsaturated tests.

Isotropic compression tests

As transitional behaviour had already been identified by oedometer tests, triaxial tests were conducted to characterise further the transitional behaviour, particularly the NCLs and CSLs. Three triaxial tests were conducted on compacted samples with v_i ranging from 1.43 to 1.84, corresponding to w_i values from 13.3% to 8.8%, as shown in Table 5-4. Loose samples TST2 and medium density sample TST3 were isotropically compressed to p'=500 kPa, while dense sample TST1 was compressed to p'=350 kPa and unloaded to p' =70 kPa. All three tests reached individual NCLs at around p'=100 kPa, as shown in Figure 5-10 (a), demonstrating non-unique NCLs due to transitional behaviour.

To compare oedometer and triaxial compression behaviour, the vertical stresses σ_v' from the oedometer tests were converted to effective stress p' using k_0 value calculated from the M value obtained through triaxial shearing, following $k_0 = 1 - \sin\phi'$. Compared with triaxial compression, the oedometer compression lines were steeper, especially for samples with high v_i, and showed greater convergence. This behaviour was also observed in the silty loess, as shown in Figure 5-3 (c). Todisco and Coop (2019) reported that the oedometer compression of crushed limestone exhibited slightly more convergence than isotropic compression, which attributed to the additional shear strain in the oedometer tests. As shown in Figure 2-4, when the convergence parameter reaches m=0.5, the required plastic volumetric strains are about 10% for isotropic compression and 12% for oedometer compression, indicating a difference of about 2% between two tests (Todisco and Coop, 2019). However, the difference observed in this study is considerably larger, suggesting that other factors may also be influencing the convergence. Therefore, this difference was further examined through k_0 compression tests in the triaxial system.

Triaxial k_0 compression tests

It is believed that triaxial k_0 compression tests provide more reliable one-dimensional compression results than the oedometer tests due to the better saturation of the samples and the absence of sidewall friction. These tests were conducted by controlling the radial strain to be zero through adjustment of the cell pressure. Two samples, KSTH and KSTL, were prepared to one high v_i of 1.76 and one low v_i of 1.38, similar to the triaxial isotropic compression samples TST2 and TST1 and oedometer samples OSTc1 and OSTc5.

As shown in Figure 5-10 (b), both k_0 compression lines reached their own one-dimensional NCLs around p'=100 kPa and followed trends similar to the isotropic compression lines. Notably, the loose sample KSTH does not show the collapsing compression line seen in OSTc1, suggesting that this collapse was due to the limitations of oedometer tests rather than an issue of sample preparation. End friction at the bottom and top surfaces of the sample may have occurred in triaxial isotropic compression tests, possibly leading to an hourglass-shaped sample. However, the closely aligned compression behaviour of the triaxial isotropic and k_0 tests suggests that the effect of end friction in the triaxial tests was minimal. This consistency also indicates that triaxial k_0 tests provides more reliable one-dimensional compression behaviour than oedometer tests.

Initially, the difference between the oedometer and triaxial k_0 compression behaviour was believed could be attributed to using an inaccurate k_0 value. As mentioned before, the k_0 value used was based on the M value. The corresponding stress ratio (q/p') was calculated based on $q/p' = \frac{3(1-k_0)}{1+2k_0}$. This stress ratio matched the linear stress path of loose sample KSTH, as shown in Figure 5-10 (c), but the dense sample KSTL followed

a curved and lower stress path. This was modelled with a quadratic function up to $p' =$ 650 kPa, $q = 0.1969\, p' + 0.0005 p'^2$. This equation was used to recalculate the k_0 as a function of p', assuming k_0 remained constant beyond 650 kPa. The oedometer results corrected using the new k_0 are shown in Figure 5-10 (d). Notably, the compression lines beyond 650 kPa are critical, as they strongly relate to the determination of the NCLs. Although the exact k_0 values beyond 650 kPa were uncertain, the compression lines only shifted slightly to higher stress states so that the influence of k_0 on the interpretation of the compression behaviour is very limited.

Secondly, the potential influence of sidewall friction in the oedometer ring was also considered as a possible reason for the difference between the two tests. If sidewall friction were absent, the actual vertical stress on the specimen would be lower, and the corresponding volume change would be greater. This would result in a lower position in the $v - lnp'$ plane, but the effect of this on the gradient of the compression line is unknow.

5.4.2 Shearing behaviour

The shearing behaviour of sandy tailings is shown in Figure 5-11. Samples TST2 and TST3 reached critical states at around 20% axial strain in drained shearing, observed as stable states in terms of stress ratio and volumetric behaviour in Figure 5-11 (a) and (b). Both tests reached a similar failure envelope in the $q - p'$ plane, corresponding to M=1.16. However, due to high over-consolidation, sample TST1 sheared under undrained conditions was still far from reaching its critical state, as the pore water pressure was far from the stabilisation, as shown in Figure 5-11 (c). Therefore, the CSL of sample TST1 could not be defined. The strongly dilative behaviour of TST1 observed in the $p' - q$ plot in Figure 5-11 (d) was attributed to over-consolidation.

For conventional soils, there should be a unique CSL so that samples sheared in drained condition from the same p' would converge at a single point in the $v - lnp'$ plane. However, it is clear from Figure 5-11 (e) that the critical state points of TST2 and TST3 remained far apart and are likely to have their individual CSLs, indicating a transitional behaviour. The estimated CSLs are plotted in Figure 5-11 (e), with slopes adopted from their respective NCLs.

5.4.3 Microstructure analysis

Oedometer compressed samples and triaxial k_0 compressed samples were tested to study the potential reasons for the different compression behaviour from the two tests. Loose and dense oedometer samples (OSTH and OSTL) have average v_i values of 1.77 and 1.43, corresponding to the oedometer tests OSTc1 and OSTc5 shown in Figure 5-10 (b). High v_i and low v_i oedometer samples (OSTH and OSTL) were compressed to σ_v' of 100 kPa, 1170 kPa and 5500 kPa, corresponding to p' of 70 kPa, 790 kPa and 3700 kPa. This resulted in six specimens, namely OSTH100, OSTH1170, OSTH5500, OSTL100, OSTL1170, OSTL5500. Oedometer samples that had experienced 100 kPa and 5500 kPa vertical stresses (OSTH/OSTL100 and OSTH/OSTL5500) were used to study the compression effects on soil structure to examine the potential reasons for transitional behaviour. The compression behaviour of these samples used for microstructure analysis is consistent with the results of the oedometer tests, and the corresponding compression data are presented in Figure 5-12.

The triaxial k_0 compression loose sample KSTH and dense sample KSTL have average v_i values of 1.76 and 1.37, similar to those of the oedometer samples OSTH and OSTL. They were compressed to a p' of 650 kPa, which is close to the vertical stresses of 1170 kPa applied to oedometer samples OSTH/OSTL1170. These samples are

therefore compared to study the difference of soil structures under the two testing types and to study the potential reasons for the difference between the two tests.

MIP tests

The pore size distributions (PSD) of the oedometer samples are presented in Figure 5-13. At 100 kPa, both samples exhibit bimodal distributions, with dominant pores around 0.03 μm and 3 μm. As the vertical stress increases from 100 kPa to 5500 kPa, the dominant macro-pores (around 3 μm) significantly reduce in volume, while the micro-pores near 0.03 μm slightly increase, indicating the collapse of inter-aggregate structures. This consistent evolution across both densities suggests a similar microstructural response to compression. Comparing the two densities, as shown in Figure 5-13 (c), OSTH100 contains a larger volume of macro-pores in the 3-10 μm range compared to OSTL100, indicating a looser initial structure. Even after compression to 5500 kPa, OSTH5500 retains slightly looser than OSTL5500, representing by slightly more macro-pores around 50 μm and micro-pores around 3 μm. Figure 5-14 compares the triaxial k_0 compression samples KSTH and KSTL with oedometer samples OSTH1170 and OSTL1170 compressed to a similar stress level. Generally, the triaxial k_0 samples retain a greater volume of macro-pores across both densities, suggesting less structural compression compared to the oedometer samples. The PSDs are quite similar in the low v_i samples, with only minor differences in the 10-40 μm range. However, the difference is substantial in the high v_i samples, for example, KSTH still retains a large volume in the 1-300 μm range. These observations align with the mechanical behaviour that oedometer compression induces greater volumetric strain than triaxial k_0 compression, particularly in loose samples.

SEM tests

Figure 5-15 (a) and (b) show low-magnification SEM images of the loose and dense samples under 100 kPa (OSTH100 and OSTL100), respectively. In both samples, the sand grains do not appear to be in direct contact and are dispersed within a continuous clay matrix, and macro-pores can be observed between the clay aggregates and sand particles. The loose sample OSTH100 displays more inter-aggregate pores between clay aggregates, suggesting a more open structure. The dense sample OSTL100 shows more compressed and less open clay aggregates than the loose sample OSTH100. These microstructural features align with the MIP results, which indicate macro-pores at around 100 μm in both samples and a slightly higher volume of pores around 6 μm in the OSTH100 sample. After compression to 5500 kPa, as shown in Figure 5-15 (c) and (d), the clay aggregates in both samples become slightly less random and less flocculated, and the general microstructures of the loose and dense samples are similar. These observations are consistent with the MIP results, which show that the Pore Size Distributions (PSDs) of both samples are similar and there is only a small reduction of inter-aggregate pores around 3 μm after loading.

Figure 5-15 (e) and (f) present SEM images of the oedometer samples OSTH1170 and OSTL1170, and Figure 5-15 (g) and (h) show the corresponding triaxial k_0 samples KSTH and KSTL. The loose and dense oedometer samples show similar microstructures of clay aggregates, with the dense sample having more closely packed clay aggregates. This matches the MIP results that the dense sample shows slightly lower pore volume at around 1 μm. In contrast, the microstructures of clay aggregates in the triaxial k_0 samples are notable different from those of the oedometer samples. Both loose and dense triaxial samples show more open structures with increased inter-aggregate pores, and the clay aggregates appear more flocculated, especially for the

loose sample. This aligns with the MIP findings that the loose triaxial sample (KSTH) displays a bimodal PSD with a dominant pore size around 3 μm, suggesting a loose structure. This feature is absent in the oedometer sample OSTH1170, confirming a structural difference. This observed structural difference between two tests helps explain the volumetric strain differences between the two tests. There are more compressed and uniform fabric in the oedometer samples, and the triaxial k_0 tests lead to less structural rearrangement and preservation of the initial fabric.

5.5 Fine tailings

Due to its most pronounced transitional behaviour, the fine tailings were selected as the main focus for the study of transitional behaviour in the saturated state. All tests conducted on the fine tailings are listed in Table 5-5. It should be noted that triaxial tests T1-T8 were conducted by Dr. Abi Cartwright, a former PhD student at UCL, and the remaining tests continued from her work (Cartwright, 2022).

5.5.1 Compression behaviour

One-dimensional compression

It can be seen from Figure 5-16 (a) that the compression curves for the oedometer samples with lower v_i are initially flatter than those with higher v_i. Subsequently, all compression paths reach their individual normal compression lines (NCLs) with fairly similar slopes which do not converge even up to 8 MPa. The m value proposed by Ponzoni et al. (2014) was employed to quantify the convergence of the compression paths. Li and Coop (2019) extended the technique so that the factor m could be calculated at multiple final stress levels to assess the trend in convergence across different compression states.

For the oedometer tests, the m value is calculated here based on v_i at effective stress p' of 30 kPa (v_{30}) and v_f at p' of 2000 kPa (v_{2000}) and 7000 kPa (v_{7000}). The choice of using p' rather than vertical stress σ_v' is to enable consistent comparison between one-dimensional and isotropic compression conditions. The initial low stress was chosen as 30 kPa to minimise the effects of any potential sample disturbance during sample preparation and setting up, as well as any potential pre-consolidation in the dense samples resulting from small suctions. The σ_v' was converted to p' by adopting a k_0 value estimated using $k_0 = 1 - sin\phi'$. Figure 5-17 (a) illustrates that the m values decrease slightly, from 0.66 to 0.55, as the final stress level increased from 2000 kPa to 7000 kPa. The m values for many reconstituted soils with transitional behaviour have been calculated in previous studies, for example, m=0.26 (for v_{7000}) for a silty loess (Xu and Coop, 2017) and m=0.23 and 0.26 (for v_{6000}) for a silt and a silty clay (Ponzoni et al., 2014). Compared with these typical transitional soils, the tailings in this study have a high degree of transitional behaviour. Additionally, the relationship between v_{30} and v_{final} may be curved, representing non-constant m values among samples with different initial densities. The m value for samples with higher v_{30} are higher than that for those with lower values. This is because denser samples experience less volumetric strain and reach a slightly flatter one-dimensional NCL at higher stress levels compared with looser samples.

Isotropic compression

As oedometer tests had already been used to examine the transitional behaviour in compression, the triaxial tests were only compressed to lower stress levels primarily to study the mechanical behaviour in shear. Reconstituted samples were prepared with 38mm diameter and 76mm height using the slurry preparation method.

The isotropic compression tests were conducted to 50 kPa, 100 kPa, 200 kPa or 400 kPa, as shown in Figure 5-16 (b). Although most of the tests reached their individual straight NCLs, it is noteworthy that some tests either may not reach or only just reach their NCLs. This is primarily attributed to the compression of dense samples to relatively low stresses in some cases. This was evident from the fact that test T13CU100D, with a similar v_i to samples T10CD50C and T14CU50C, only reached its NCL at about 50 kPa, which was the stress these two tests were compressed to.

As expected, the isotropic compression behaviour shows a similar non-convergent trend to the one-dimensional compression curves. The degree of convergence is further quantified by the m value based on v_i at p' of 30 kPa (v_{30}) and the v_f at p' of 100 kPa (v_{100}), 200 kPa (v_{200}), and 400 kPa (v_{400}), as shown in Figure 5-17 (b). The m values are almost constant for all samples with different v_{30} at each stress level and m values decrease with increasing stress, 0.72 for v_{100}, 0.63 for v_{200}, and 0.48 for v_{400}. This indicates that the convergence is independent of the v_i and increases only slowly with the stress level. The constant m values for samples of all densities in the triaxial tests may be attributed to the narrower range of v_i achieved, compared to the oedometer tests, where the greater range of v_{30} gives a curvature to the v_{final} : v_{30} relationship. Generally, isotropic compression has larger m values than one-dimensional compression, indicating less convergence in isotropic compression. This is consistent with the compression behaviour observed in silty loess and sandy tailings, as shown in Figure 5-3 (c) and Figure 5-10 (a).

Triaxial k_0 compression

As with the sandy tailings, due to the clear differences between the one-dimensional and isotropic compression behaviour, k_0 compression tests were conducted in the

triaxial apparatus to investigate the reason. Samples were prepared as "slurries" at two different w_i values (89.3% and 35.0%) in order to obtain distinct initial densities, using the same preparation method as in the other triaxial samples. As shown in Figure 5-16 (c), the k_0 compression lines from the triaxial tests closely align with the isotropic compression lines. The small jump in the path of the loosest sample was due to some initial difficulty in controlling zero radial strain on a very soft specimen. The better agreement of the triaxial k_0 compression lines with the isotropic compression lines suggests that the k_0 compression lines from the triaxial tests are more reliable than the oedometer ones in the $v - lnp'$ plane. This is consistent with the findings in sandy tailings, as shown in Figure 5-10 (b).

5.5.2 Shearing behaviour

With a wide range of v_i and compressed to various stress levels p_0', the specimens were then either sheared undrained or drained. The intention was to provide a wide distribution of critical states in the $v - \ln p'$ plane in order to investigate the locations of the CSLs.

Most of the triaxial tests were sheared up to about 20% axial strain to reach reasonably constant stress states defined as critical states. Due to the limited axial strain available in a Bishop and Wesley triaxial apparatus and the relatively large strains that occurred in isotropic compression, some tests did not meet this condition. Hence, a small hyperbolic extrapolation was applied to the volumetric strain for drained shearing tests and to the pore pressure for undrained shearing tests up to 25% axial strain. The applied extrapolations were relatively minor and the details will be discussed below.

The critical states are plotted in the $v - \ln p'$ plane, as shown in Figure 5-18, along with the isotropic compression paths, shearing paths and the extrapolations applied. It is

clear that neither a unique NCL nor CSL can be identified. The differences in the overall locations of compression lines and critical states are much larger than the inaccuracy of v_i, which is around ±0.013. Therefore, the non-uniqueness of the NCLs and CSLs does not result from errors in the calculation of v_i. Non-unique NCLs and CSLs are commonly found in laboratory investigations in which the grading is changed by adding fines (e.g. Carrera et al., 2011) but here it must be emphasised that the grading is unique and unchanged. The grading was also checked after testing and was found to be unchanged.

5.5.3 Quantification of transitional behaviour

NCL and CSL parameters

In the critical state framework, the NCL and CSL for a plastic soil are typically linear in $v - \ln p'$ plane with the same slope, defined as $v = N - \lambda \ln p'$ and $v = \Gamma - \lambda \ln p'$ respectively, where N and Γ are the intercepts at 1 kPa and λ is the slope. To obtain deeper insights into the transitional mode, the locations and equations of the NCLs and CSLs were carefully analysed and identified as described in detail below.

A rigorous study of the critical state parameters was conducted to contribute quantitative insights into the transitional behaviour. The specimens were first divided into four groups A-D based on their initial specific volumes defined by the value at 30kPa, v_{30} during isotropic compression, as shown in Figure 5-18. This choice of v_{30} rather than v_i is made to avoid potential errors generated from disturbance during sample preparation and assembly. Then the individual NCLs for each test were identified, as well as their parameters λ and N.

As illustrated in Figure 5-19 (a) and (b), the parameters λ and N generally exhibit a linear trend with v_{30}, except for a few scattered data points. This scatter can be

explained by the volumetric behaviour in Figure 5-18. The tests with lower λ than the average value within their density group were compressed to the relatively low stress level of 50 kPa. This probably suggests that these specimens did not reach their respective NCLs. The tests also show vertical tails after isotropic compression in the $v - \ln p'$ plane. This indicates significant pore water dissipation, due to slightly too rapid compression rates for these loose specimens. Subsequently, the λ and N of NCL for each group were determined as the average values from the individual NCLs within their respective group. It can be seen from Figure 5-19 (a) and (b) that they fit well with the regression line derived from the individual data. Figure 5-18 plots the average NCLs for each group estimated in this way. It can be seen that the NCLs for each group are a reasonably good fit, considering the variations in v_i among specimens within each group. Therefore, it can be concluded that both the slopes and the locations of these NCLs are representative of their respective groups.

Within the critical state framework, the slope of the NCL is generally consistent with that of the CSL. Therefore, the gradients of the individual CSLs for each sample are initially assumed to be the same as those for their respective NCLs. Figure 5-19 (c) presents the intercept Γ of individual CSLs calculated based on the defined individual gradients and the average values calculated as the representative Γ for the CSLs within each group. It is clear that the Γ exhibits a linear relation with v_{30}, except for the outlier data points from the tests mentioned above. The average Γ values for the CSLs within each group closely align with the regression line derived from individual data. Hence, it seems reasonable to adopt the λ of the individual NCLs as the gradient of the individual CSLs and to use the average Γ values within each group as the representative Γ for the CSL within that group. Figure 5-18 (b) illustrates the CSLs for each group, determined based on the established parameters. Most of the critical states are well

fitted with the estimated CSL for each group, except for the over-consolidated T10CD50C and T14CU50C in Group C.

P value

Ponzoni et al. (2014) proposed the *P* value to quantify the degree of transitional behaviour during shearing. This method calculates *P* as the ratio of the difference in v (Δv_0) to the difference in Γ ($\Delta\Gamma$), $P = \frac{\Delta\Gamma}{\Delta v_0}$, as shown in Figure 5-20(a). The *P* value can range between 0 and 1 in this case. *P=1* indicates that the CSLs are offset by the same amount as specific volume (Δv_0), signifying perfectly transitional behaviour. When soil exhibits a unique critical state line, $\Delta\Gamma$ is equal to 0, resulting in *P=0*. This method only applies when the NCLs or CSLs for each density group have same gradients, as the case shown in Figure 5-20(a) that the NCL or CSL of loose sample (NCL_1 or CSL_1) is equal to the that of dense sample (NCL_2 or CSL_2).

However, the NCLs or CSLs for each density group do not have same gradients in this study, as shown in Figure 5-20 (b) that the slope of NCL or CSL for loose sample (λ_1) is not equal to that for dense sample (λ_2). In this case, the difference in $\Delta\Gamma$ could be greater than the difference in specific volume (Δv_{0_NCL}), causing the P value to exceed 1, so that Ponzoni's calculation method of P value cannot quantify the convergence of the CSLs anymore. Therefore, a modified P value was developed to be the ratio of the difference in specific volume on the NCLs ($\Delta v_{p'\_NCL}$) and CSLs ($\Delta v_{p'\_CSL}$) at the same stress level (p'), $P = \frac{\Delta v_{p'\_NCL}}{\Delta v_{p'\_CSL}}$. The *P* value still ranges from 0 to 1, representing a unique CSL and perfectly transitional respectively. This method requires a precondition that the CSL has the same slope as the corresponding NCL, for example, the CSL_1 and CSL_2 have the same slopes as the NCL_1 and NCL_2 respectively, so that the P value can remain independent of the chosen p'.

The modified *P* value was used to quantify the transitional behaviour. The chosen p' is 30 kPa since most samples reach their NCL before 30 kPa, as shown in Figure 5-18(a), so that the difference of v_{30} from different compression lines equals that of $\Delta v_{p'\_NCL}$. Figure 5-20 (c) presents the v_{30} on NCLs and CSLs (v_{30_NCL} and v_{30_CSL}) for each specimen, and the slope represents the *P* value. It is notable that the *P* value is approximately 0.83 with some small scatter for the reasons mentioned above. This *P* value indicates a very high degree of transitional behaviour, especially compared with other typical reconstituted transitional soils such as a loess with *P=0.34* (Xu and Coop, 2017).

Effect of extrapolations

Incomplete tests or poor data extrapolation are commonly cited as reasons for the apparent non-convergence of critical states. The purpose of the study on extrapolation effects is to prove that the non-convergence is an inherent feature of transitional behaviour. The absence of a unique CSL is evident in Figure 5-21. If there were a unique critical state line for the soil, specimens undrained shearing starting with the same specific volume should end at the same p'. Most of the specimens achieved reasonably stable p' values by the end of the tests, but Figure 5-21 (a) demonstrates that the differences in final p' values among specimens in each density group are too large to converge. The existence of a unique critical state line in drained shearing would imply that the specimens sheared from the same initial p' should attain the same final v. However, Figure 5-21 (b) reveals that although there is some reduction in the differences in the v , it is not possible for all of these tests to converge to the same v at 25% axial strain, especially given the ±0.013 accuracy of v_i. Although hyperbolic extrapolations are applied to some tests, the extrapolations give similar curves of v and

very little change of p'. Hence, the lack of convergence of CSLs in the $v - p'$ plane should not result from the extrapolation.

5.5.4 Stress-strain behaviour

Stress-strain behaviour

The stress-strain behaviour is shown in Figure 5-22, including stress ratio q/p' responses, changes of pore water pressure normalised by the initial effective confining pressure $\Delta u/p'_0$ and volumetric strain ε_v. Generally, the undrained tests exhibit significantly greater stiffness compared to drained tests at similar stress levels. For undrained shearing, Figure 5-22 (a) and (b) show that the dense specimens (Groups C and D) have slight peak strengths with a peak $\Delta u/p'_0$. The loose specimens (Groups A and B) have strain-hardening behaviour and compressive pore pressures. This suggests a slight effect of initial density on stress-strain behaviour, but much less than that for a conventional sand, for example. In drained shearing, all tests have strain-hardening and contractive behaviour and a density impact is not strongly evident, as shown in Figure 5-22 (c) and (d). Two samples, T14CU50C and T10CD50C, do not follow the overall trend and have a behaviour similar to a typical over-consolidated clay or dense sand. This is because these tests did not reach their NCLs during isotropic compression as mentioned previously. Generally, samples with any initial density are predominantly compressive and strain-hardening. Even the densest samples in Group D do not give the strong dilative and strain-softening behaviour that would be expected from a conventional soil with a unique CSL. Therefore, this minimal effect of initial density results from the transitional behaviour.

Stress paths

Figure 5-23 presents the stress paths and estimated CSL in the $q - p'$ plane. It can be seen that the estimated CSL has a small curvature so that the CSL gradients *M* for tests

with the lower p_0' are slightly higher than those with a higher pressure. The non-unique *M* is consistent with the variation of the ultimate stress ratios q/p' shown in Figure 5-22 (a) and (c). The estimated CSL fits reasonably the critical state points and corresponds to $q' = 1.23p' - 4.23 \times 10^{-4}p'^2$. After normalising the stress ratio by the M, Figure 5-24 illustrates that most of the final normalised stress ratios are close to 1, representing a reliable estimation of the CSL. From the lower stress value *M=1.23*, the critical state angle of shearing resistance ϕ' is 30.7°. This normalised stress ratio is used to build the state boundary surface, a fundamental element of the critical state framework.

Effect of extrapolations

As mentioned previously, hyperbolic extrapolations are applied to five tests in order to approach reasonably constant stress states or constant volumes. One undrained test, T11CU50B, is extrapolated slightly as shown in Figure 5-22 (a) and (b). Four extrapolated drained shearing tests have reasonable small changes for the stress ratios q/p' at the large strains as shown in Figure 5-22 (c). Although the volumetric states probably are not quite stable yet in Figure 5-22 (d), their estimated critical states fit well with the estimated CSL in the $q - p'$ plane, as shown in Figure 5-23. Therefore, it is evident that the extrapolation method works well and the curved CSL does not result from extrapolation.

5.5.5 State boundary surface

The stress paths are further normalised by *M* and an equivalent pressure taken on the CSL (p_{cs}') in Figure 5-25 to build the state boundary surface. State boundary surfaces have not previously been identified for transitional tailings. The p_{cs}' is defined as $\exp\left(\frac{\Gamma - v}{\lambda}\right)$. The *M*, λ and Γ values used for each test are generated from their individual

CSLs. The equations for these parameters defined above were not used, because they would introduce additional scatter arising from the difference between the equation and the real data.

This normalisation ensures that all the CSLs lie at (1,1). The NCLs for different tests are slightly scattered, as shown in Figure 5-25 (a). The initial p'/p'_{cs}, the NCLs, for four tests, are located at smaller values than for most of the tests. It is highly likely that these tests have not quite reached their NCLs since they have relatively low v_i and were compressed to relatively low p'_0. There is still some scatter of initial p'/p'_{cs} values for tests definitely on their respective NCLs. This is probably because the slopes of CSLs were assumed to be equal to those of their individual NCLs, which is not necessarily accurate. But the small scatter means the assumption is still acceptable. Therefore, a state boundary surface (SBS) is identified from the average value of the initial p'/p'_{cs} values for samples on their NCLs. The stress ratio between the CSLs and the estimated isotropic NCL is about 2, which is similar to that of many clays. But there is a possible slight peak on the wet side of SBS, which is a feature of sand (Coop and Lee, 1993), possibly due to the low plasticity of the soil. The undrained tests plot inside the SBS, meaning that Rendulic's principle is also not obeyed, another feature that is more typical of sands.

The differences between the undrained and drained tests are clear in the normalised paths as shown in Figure 5-25 (a). The undrained tests reach the Hvorslev surface and then change direction abruptly toward the CSL. The drained tests are more gently curved and reach a gross yield at small stress ratio of about $q/Mp'_{cs} = 0.3$, which agrees with the yielding in the $v - lnp'$ plot (Figure 5-18), except for sample T10CD50C. Since T10CD50C did not reach its NCL, its normalised stress path behaves

like a sample sheared from the dry side and it reaches the Hvorslev surface rather than Roscoe surface.

The initial p'/p'_{cs} value is related to the spacing between the NCL and the CSL. To study the density effect, Figure 5-25 (b) highlights the normalised stress paths for tests in the same density group. It is clear that the median initial p'/p'_{cs} for the denser groups C and D are significantly larger than that for Groups A and B at about 1.7. Hence, the SBS is probably smaller for denser samples. This agrees with the smaller spacing of the NCL and CSL for the denser groups on Figure 5-18.

5.5.6 Stress-dilatancy behaviour

As shown in Figure 5-18, whether a transitional soil exhibits contractive or dilative behaviour depends on whether it has reached its own individual NCL yet. For example, the dilative response observed in sample T14CU50C occurs because the sample has not yet reached its NCL. For comparison, sample T8CD400C, which belongs to the same density group (Group C) but was compressed to a higher effective stress (400 kPa) and had already reached its NCL, did not exhibit any dilative behaviour.

Figure 5-26 (a) plots the stress-dilatancy behaviour for the drained tests. The shear strains ε_s used are total strains rather than plastic strains, but the elastic component is small. It is calculated as $\varepsilon_s = \frac{2}{3}(\varepsilon_a - \varepsilon_r)$, where $\varepsilon_r = 1 - \sqrt{\frac{1-\varepsilon_v}{1-\varepsilon_a}}$, which is valid for both small and large strains. Values of ε_a and ε_v were calculated from the measurements of the local LVDTs and the volume gauge, respectively. The values of dilatancy $d\varepsilon_v / d\varepsilon_s$ are calculated as regressions over short intervals of the ε_v: ε_s plot. Since the rate of dilation is calculated as the ratio of two small increments, the plot of dilatancy has some scatter especially in the small strain range. All paths initially reach a straight relationship with similar slopes at similar small strain levels. Except for test

T10CD50C, which did not reach its NCL, all other tests only have compressive behaviour and tend towards the same critical state $q/Mp' = 1$ at large strains. Sample T10CD50C reaches the linear relationship at a higher stress ratio in comparison to other tests and shows volumetric dilation with a slight peak strength at larger strains, as expected.

To compare the dilatancy behaviour for undrained shearing tests, Figure 5-26 (b) presents the stress paths normalised by the p_0'. Most samples for all initial densities have an evident and similar overall contractive tendency. Sample T14CU50C that has not reached its NCL is much less contractive initially and more dilative subsequently than the other tests. Some tests show evident phase transformation points (PTPs), highlighted as the enlarged points shown in figure. There are slight differences between the looser and denser samples, but this is much less than the effect of density would be on a conventional sand with a unique CSL, for example.

Figure 5-26 highlights the key principle of transitional behaviour that these tailings with any initial density are predominantly contractive with a unique stress-dilatancy relationship, and this results from the transitional behaviour.

5.5.7 Stiffness

The tangent stiffnesses (G) for small shear strains are derived through the linear regression over short intervals of the q: ε_s plot. The tangent shear modulus, rather than the secant value, is used since it better describes the evolution of stiffness. The ε_s used is total strains rather than plastic strains as the elastic component would be small. The degradation of G with ε_s is shown in Figure 5-27, with the data points starting at about ε_s =0.001% due to the limited accuracy of the local LVDTs. The stiffness degradation curves have a consistent pattern for tests with the different p_0'. The trend of stiffness

degradation can also be roughly observed from the undrained shearing behaviour in Figure 5-22 (b) at small strain levels between 0 to 1%. The stiffness degradation is slightly unusual compared to many soils in that the soil is initially stiff but undergoes a very rapid decay. A distinct yielding occurs before 0.005% shear strain, and this is consistent with the stiffness behaviour where degradation begins at about 0.003% shear strain. The stiffness reduction occurs rapidly at small strain levels, mostly up to 0.1% shear strain. Beyond 0.2% shear strain, the stress ratio curves tend to become less steep and more linear indicating that the tangent stiffness values have become relatively small and stable. None of the shearing curves reaches a peak q value before 1% shear strain, so there is no negative stiffness.

The stiffness behaviour is interpreted by extracting data from Figure 5-27 at particular ε_s as shown in Figure 5-28. The variation of stiffness for each strain level shows converging lines in $logG: logp'$, which can be represented by $G = A(p')^n$. Figure 5-29 (a) indicates that there is no consistent difference between drained and undrained tests, which agrees with the results of Shipton and Coop (2015) for transitional behaviour. It has been widely found that the specific volume has an important influence on stiffness for both clays (Viggiani and Atkinson, 1995) and sands (Jovičić and Coop, 1997). However, this does not seem to be the case for this transitional soil since the stiffness contours are independent of the density as shown in Figure 5-29 (b), which is also consistent with the results of Shipton and Coop (2015). It is suggested that the lack of effect of density on stiffness is again a feature of transitional behaviour.

5.5.6 Microstructure analysis

Transitional behaviour is believed to be related to robust elements of soil fabric that will not be completely broken down even under high stress or strain levels, and Todisco et al. (2018) used MIP to examine the soil structure of a transitional soil. MIP and SEM

imaging have been used here to examine the pore size distribution and possible particle orientations, respectively. Two loose and dense samples, with the same v_i as samples K1 and K3 shown in Figure 5-16, were triaxial k_0 compressed in p' of either 30kPa or 450kPa, resulting in four samples (K1-30, K1-450, K3-30, and K3-450). The trimmed subsamples were then freeze-dried for the MIP and SEM tests. The freeze-drying followed the ultra-quick technique of Délage and Pellerin (1984) in which the ice sublimates under vacuum to avoid any volumetric change to the samples.

MIP tests

From the MIP tests, as shown in Figure 5-30, the cumulative pore size distributions (PSDs) for the loose and dense samples at 30 kPa show the greatest difference in the 0.1–10 μm range, reflecting a reduction in inter-aggregate pores and a less open structure in the dense sample, which is consistent with the SEM observations. When comparing samples compressed to 30 kPa and 450 kPa, the most significant pore volume loss also occurs within the 0.1–10 μm range, confirming that 1D compression causes collapse of the open structure observed in the SEMs. Comparing the loose and dense samples at 450kPa, the main differences in the PSDs are observed around 2μm and 0.05μm. The small difference at 2μm agrees with the SEM images, representing a slightly greater number of inter-aggregate pores in the dense sample. Although higher magnification images (not shown here) were also captured, it was not possible to identify meaningful differences in fabric at the 0.05μm scale from single individual frames. The similarity in PSDs above 0.05μm for both densities suggests both fabrics tend toward a similar mildly oriented structure under high stress. This is consistent with the similarly oriented domains observed in SEM images for two samples. Therefore, the relatively slow convergence of the PSD above 0.05 μm results in the slow

convergence of the compression data, and the persistent divergence of the MIP curves below 0.05 μm accounts for the incomplete convergence of the specific volumes.

SEM tests

The SEM images with frame sizes of about 25μm and 2μm were taken from broken (split) vertical surfaces, as shown in Figure 5-31. They clearly show the difference in initial density at 30kPa with a more open fabric for the looser sample. In the loose sample (K1-30), the clay particles exhibit a more flocculated arrangement, forming some bookhouse-type open aggregates with abundant inter-aggregate pores. Despite this, local regions of more oriented and stacked aggregates are also present. The bookhouse aggregate is a structure with randomly oriented domains in edge-to-face contact, and the stacked aggregate is a structure with oriented domains in face-to-face contact, as shown in Figure 5-32. The dense K3 sample at 30 kPa (K3-30) shows a more tightly packed fabric, although the overall structure remains largely open. At 450kPa, the initially dense sample (K3-450) shows a greater number of inter-aggregate pores of around 2μm in size, aligned along oriented domains. However, no major differences are observed between the oriented domains for the initially loose and dense samples.

In summary, the microstructural data indicate that transitional soils begin with distinctly different initial fabrics, which are generally similar in appearance, but with a highly open structure in loose samples and a more compact structure in dense samples. Following 1D compression, both evolve into slightly more aligned fabrics, but it is clearly the pore fabric below 0.05 μm that causes the transitional behaviour.

5.6 Conclusions from saturated tests

A series of oedometer and triaxial tests were conducted on mixtures of kaolin and Leighton Buzzard sand, silty loess, sandy tailings, and fine tailings to investigate

saturated transitional behaviour. Transitional behaviour was observed in all four materials, with the transitional degree m and P summarised in Table 5-6. Fine tailings were selected among them for a detailed investigation due to the most pronounced transitional behaviour, although the fine tailings later were found to be unsuitable for the designed unsaturated triaxial equipment. Detailed reasons and test results for the fine tailings in the unsaturated tests are provided in Section 6.2.1. The conclusions presented below are based on the fine tailings, as the findings for the other three soils are consistent with those derived from the fine tailings study.

- Oedometer tests identify a lower degree of transitional behaviour compared with isotropic compression tests, and the k_0 compression tests carried out in the triaxial apparatus are more consistent. This suggests that triaxial k_0 compression tests provided more reliable insight into their one-dimensional compression behaviour than conventional oedometer tests.
- The transitional mode is identified by non-unique NCLs and CSLs and quantified by parameters m and P, and the values represent a high transitional degree for this tailings. Building on the work of Ponzoni et al. (2014), the calculation method of the P value was modified to quantify the transitional degree for a more general situation in which the NCL or CSL has a different gradient for different initial density groups.
- The intercepts and slopes of the NCL or CSL vary roughly linearly with the initial density as quantified by ν_{30}. As the initial specific volume for the samples decreases, the slopes of the NCLs or CSLs decrease and the spacings between the NCLs and CSLs decrease. Previously the initial density was generally believed to have no effect on transitional behaviour, and for example Shipton

and Coop (2015) had suggested that the spacing of these lines was simply constant for all initial densities.

- Apart from this effect of the initial density on the NCL/CSL spacing, the influence of initial density is slight, since samples with any initial density predominantly have compressive and strain-hardening behaviour. In comparison, a conventional soil would be much more affected by the initial density since the densest samples would strongly dilate to reach a unique CSL and hence show strain-softening behaviour. The initial density has no effect on dilatancy behaviour and stiffness, again features seen in the transitional behaviour of other soils but not previously observed for tailings.
- There have been very few comprehensive investigations into the transitional behaviour of soil. In this study, the State Boundary Surface (SBS), small strain stiffness, and stress-dilatancy behaviour of tailings were investigated for the first time.

For engineering practice, the hydraulic deposition process in tailings ponds often results in complex stratification patterns. In addition to grading variability, differences in initial water content and drainage conditions during deposition contribute to spatial heterogeneity in initial density across the deposit. While previous research has largely focused on how the variations in grading influence critical state behaviour, less attention has been paid to the role of the initial density. This study highlights that the initial density alone can influence the compression behaviour and critical state behaviour for transitional tailings. Neglecting this transitional behaviour may lead to an underestimation of compressibility. Dry stacking is gaining favour as a means of disposal, but the implications of this research would be that if the tailings were

transitional, even placing it in a denser state by dry stacking may do little to reduce their compressible behaviour. This, however, needs considerably more research.

Table 5-1. Summary of oedometer tests on mixtures of kaolin and Leighton Buzzard sand in different components using slurry sample preparation method.

Sample	Component (sand+kaolin)	ν_i	Test
85SK	85% +15%	2.064	85SKl
		1.455	85SKd
80SK	80% +20%	2.045	80SKl
		1.519	80SKd
75SK	75% +25%	2.106	75SKl
		1.369	75SKd
70SK	70% +30%	1.883	70SKl
		1.407	70SKd
65SK	65% +35%	2.068	65SKl
		1.394	65SKd

Table 5-2. Summary of oedometer tests on the mixture of 75% sand and 25% kaolin.

Sample	Sample preparation	ν_i	w_i%
OM1	Compaction	2.106	10.8
OM2	Slurry	1.597	22.6
OM3	Slurry	1.458	19.2
OM4	Slurry	1.429	15.1
OM5	Slurry	1.339	11.3
OM6	Slurry	2.191	60.4
OM7	Slurry	2.021	56.6
OM8	Slurry	1.999	45.2
OM9	Slurry	1.983	45.2
OM10	Slurry	1.945	45.3
OM11	Slurry	1.849	35.0
OM12	Slurry	1.819	33.9

Table 5-3 Summary of oedometer tests and triaxial tests on silty loess.

Sample	Test	Sample preparation	ν_i	w_i%	p' kPa
OL4	Oedometer	Slurry	2.045	38.1	2545
OL2	Oedometer	Slurry	1.854	30.8	2545
OL1	Oedometer	Slurry	1.733	23.3	2545
OL3	Oedometer	Slurry	1.696	15.7	2545
OL6	Oedometer	Compaction	1.951	11.3	2545
OL7	Oedometer	Compaction	1.756	12.0	2545
OL8	Oedometer	Compaction	1.654	12.1	2545
OL5	Oedometer	Compaction	2.195	9.8	2545
TL1	Triaxial	Compaction	2.129	9.4	450→230
TL2	Triaxial	Compaction	1.820	15.7	500
TL3	Triaxial	Compaction	1.688	21.2	260→75→500

Table 5-4 Summary of oedometer tests, triaxial k_0 compression tests and triaxial tests on sandy tailings.

Sample	Test	Sample preparation	ν_i	w_i%	p' kPa
OSTs1	Oedometer	Slurry	2.021	40.42	1420
OSTs2	Oedometer	Slurry	1.660	25.68	1420
OSTs3	Oedometer	Slurry	2.297	53.01	1420
OSTs4	Oedometer	Slurry	1.550	20.46	1420
OSTc1	Oedometer	Compaction	1.746	10.06	1690
OSTc2	Oedometer	Compaction	1.798	10.88	3715
OSTc3	Oedometer	Compaction	1.614	11.99	1690
OSTc4	Oedometer	Compaction	1.483	12.59	1690
OSTc5	Oedometer	Compaction	1.422	13.00	3715
KSTH	Triaxial k_0	Compaction	1.764	8.80	650
KSTL	Triaxial k_0	Compaction	1.376	13.5	650
TST1	Triaxial	Compaction	1.432	13.34	350→70
TST2	Triaxial	Compaction	1.835	8.83	500
TST3	Triaxial	Compaction	1.650	10.70	500

Table 5-5. Summary of oedometer tests and triaxial tests on fine tailings using slurry sample preparation method.

Sample	v_{30}	Group	Drainage	p_0' (kPa)
O1	2.59	____	____	____
O2	2.24	____	____	____
O3	2.01	____	____	____
O4	1.84	____	____	____
K1	2.23	____	____	____
K2	1.90	____	____	____
K3	1.80	____	____	____
T1CD100A*	2.234	A	CD	100
T2CD200A*	2.254	A	CD	200
T3CD50A*	2.189	A	CD	50
T4CD400A*	2.207	A	CD	400
T5CU50A*	2.305	A	CU	50
T12CU100A	2.240	A	CU	100
T16CU50A	2.224	A	CU	50
T6CU300B*	2.049	B	CU	300
T15CU50B	2.029	B	CU	50
T11CU50 B	2.108	B	CU	50
T8CD400C*	1.969	C	CD	400
T10CD50C	1.948	C	CD	50
T14CU50C	1.937	C	CU	50
T7CU200D*	1.875	D	CU	200
T13CU100D	1.905	D	CU	100

Note: CD and CU are consolidated drained and consolidated undrained tests; v_{30} is specific volume at p'=30 kPa; p_0' is mean effective stress before shearing; *Triaxial tests T1-T8 were from Dr. Abi Cartwright (Cartwright, 2022).

Table 5-6. Transitional degree m and P values for tested soils in saturated tests.

Soils		m or P values
* m values for v_i at $\sigma v_i'$ or p_i' and v_f at $\sigma v_f'$ or p_f' are shorten as $m^{\sigma v_i'}_{\sigma v_f'}$ for oedometer tests and $m^{p_i'}_{p_f'}$ for isotropic compression tests. * P value at p' is shorten as $P_{p'}$ for triaxial shearing tests.		
Mixture of kaolin and sand in different proportion		
Oedometer tests and slurry samples	85SK	$m^{30}_{8000} = 0.17$
	80SK	$m^{30}_{8000} = 0.28$
	75SK	$m^{30}_{8000} = 0.53$
	70SK	$m^{30}_{8000} = 0.32$
	65SK	$m^{30}_{8000} = 0.19$
Silty loess		
Oedometer tests and compacted samples	OL5-OL8	$m^{30}_{5500} = 0.23$ $m^{250}_{5500} = 0.32$ $m^{1000}_{5500} = 0.50$ $m^{2500}_{5500} = 0.73$
Iso compression and compacted samples	TL1-TL3	$m^{30}_{450} = 0.83$ $m^{250}_{450} = 0.98$
Sandy tailings		
Oedometer tests and slurry samples	OSTs1-OSTs4	$m^{100}_{2500} = 0.58$ $m^{250}_{2500} = 0.72$
Oedometer tests and compacted samples	OSTc3-OSTc5	$m^{100}_{2500} = 0.38$ $m^{250}_{2500} = 0.56$
Fine tailings		
Oedometer tests and slurry samples	O1-O4	$m^{30}_{2000} = 0.66$ $m^{30}_{7000} = 0.55$
Iso compression and triaxial shearing	T1CD100A-T16CU300B	$m^{30}_{100} = 0.72$ $m^{30}_{200} = 0.63$ $m^{30}_{200} = 0.48$
Triaxial shearing and slurry samples	T1CD100A-T16CU300B	$P_{30} = 0.83$

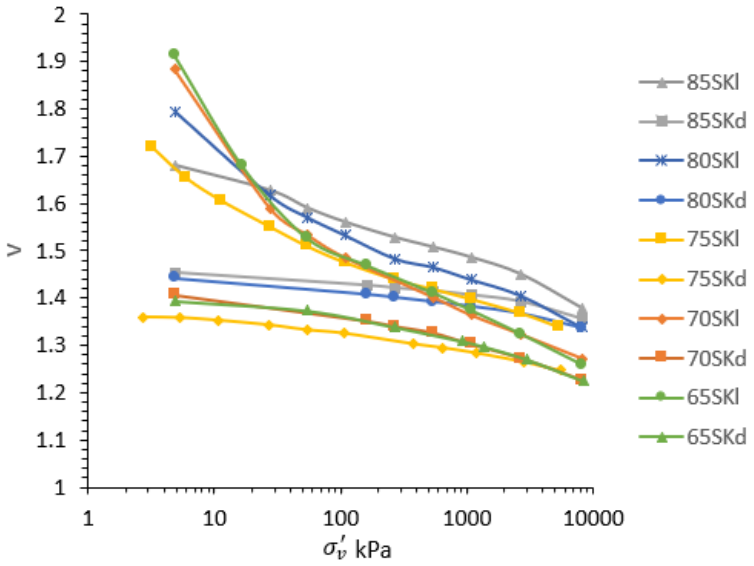

(a)

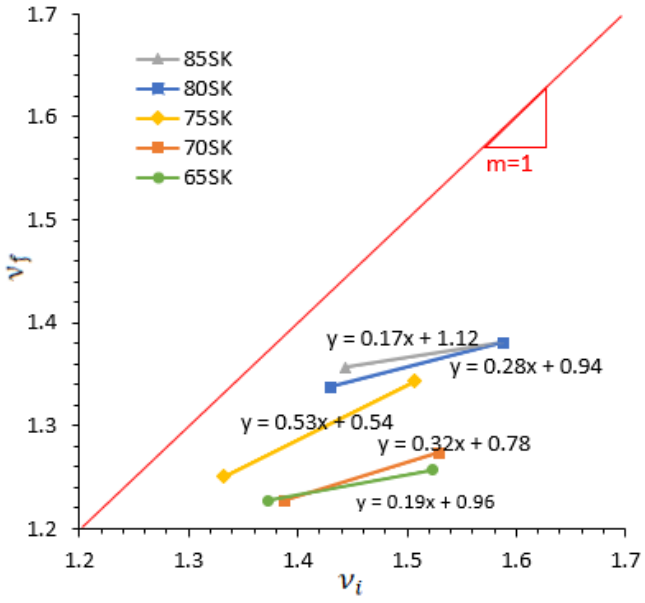

(b)

Figure 5-1 Compression behaviour of mixtures of sand and kaolin: (a) one-dimensional behaviour and (b) transitional degree m of the mixtures with sand and kaolin in different proportions.

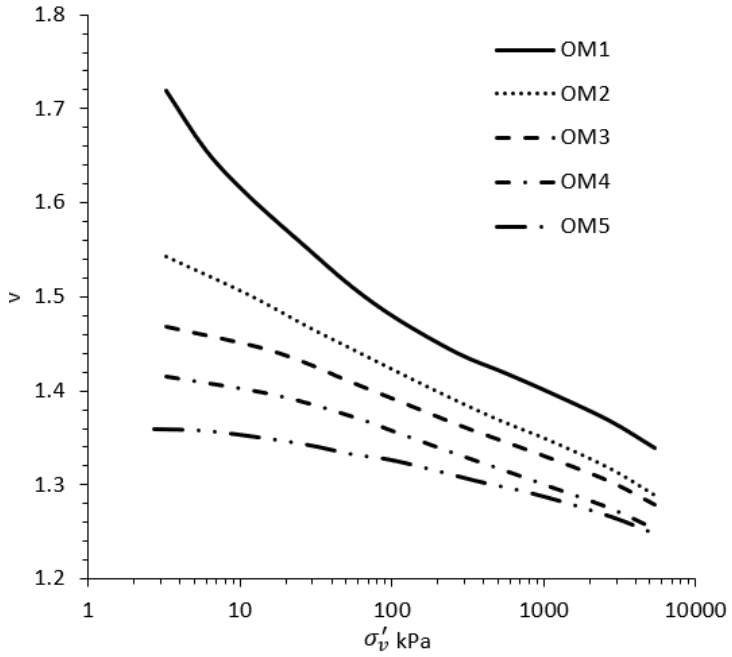

(a)

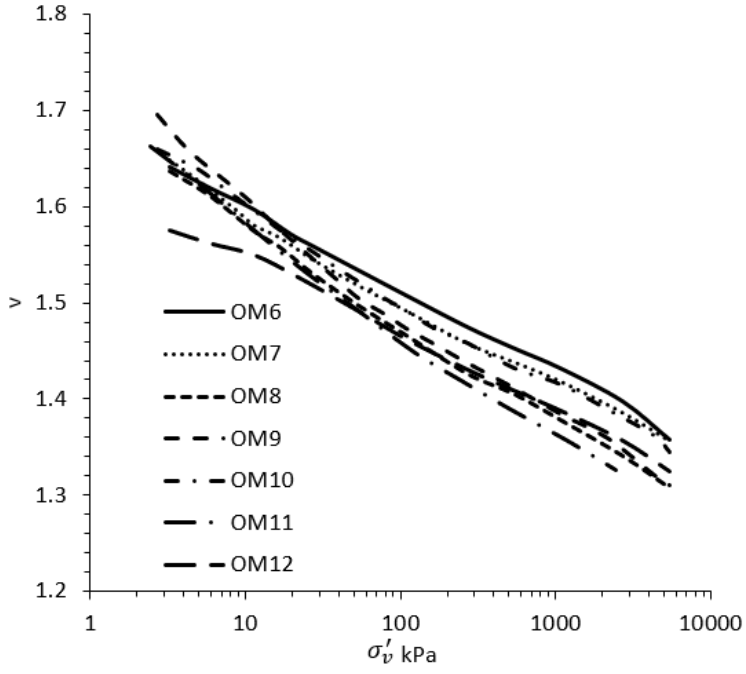

(b)

Figure 5-2 Oedometer tests for the mixture of 75% sand and 25% kaolin: (a) successful tests and (b) failed tests.

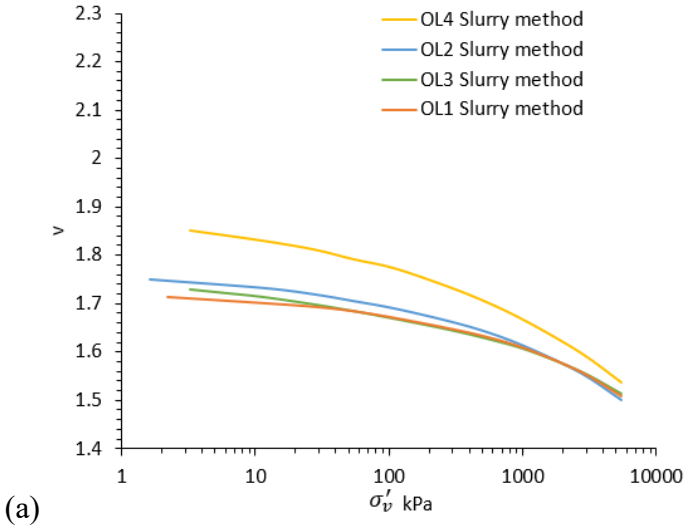

(a)

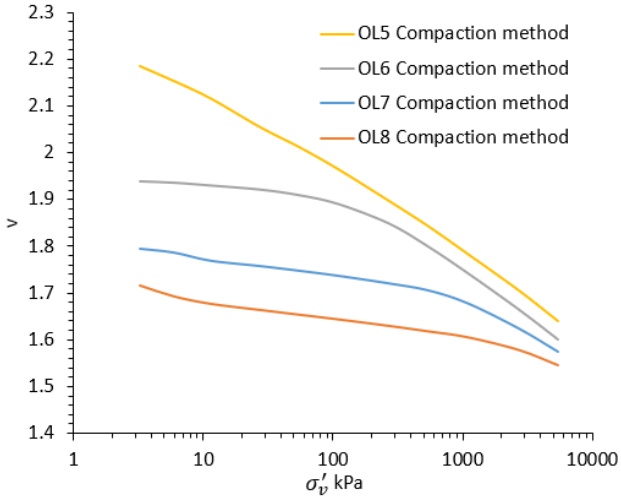

(b)

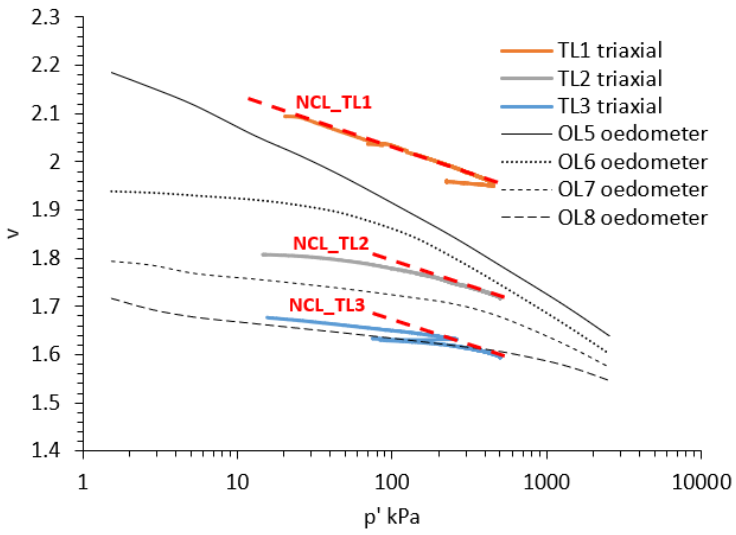

(c)

Figure 5-3 Compression behaviour of silty loess: oedometer tests on (a) slurry samples and (b) compacted samples; (c) triaxial isotropic tests on compacted samples.

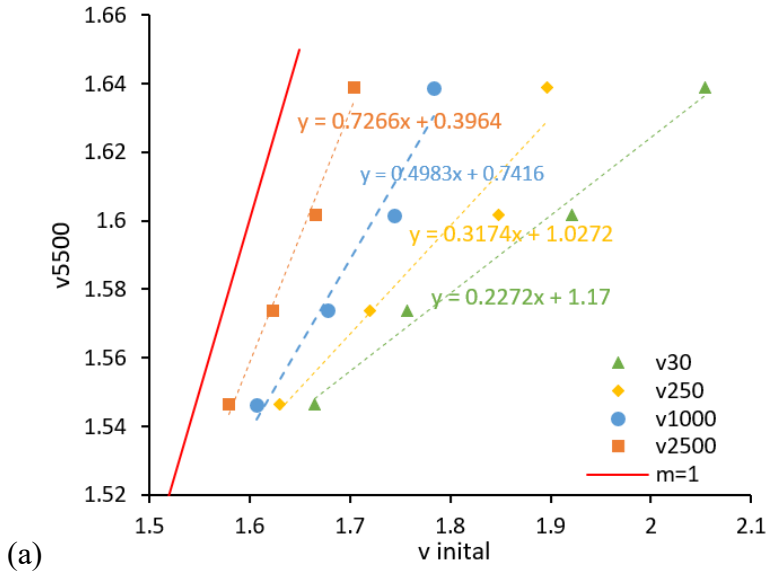

(a)

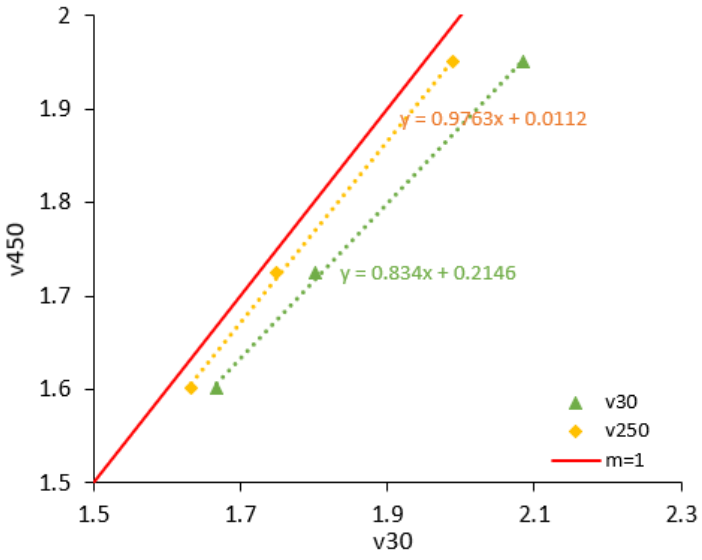

(b)

Figure 5-4 The transitional degree m value of silty loess for (a) oedometer tests and (b) triaxial tests.

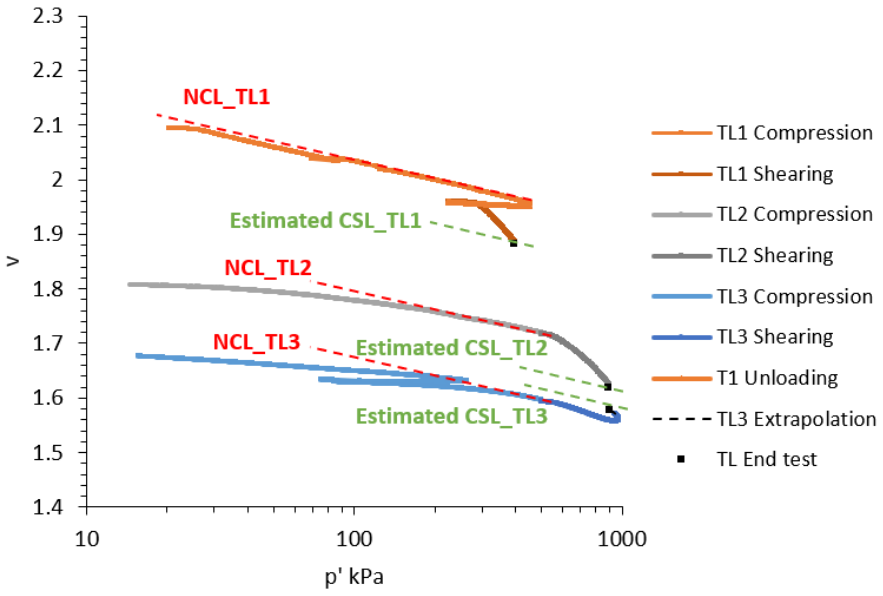
NCL_TL1
Estimated CSL_TL1
NCL_TL2
NCL_TL3
Estimated CSL_TL2
Estimated CSL_TL3
TL1 Compression
TL1 Shearing
TL2 Compression
TL2 Shearing
TL3 Compression
TL3 Shearing
T1 Unloading
TL3 Extrapolation
TL End test
v
p' kPa
2.3
2.2
2.1
2
1.9
1.8
1.7
1.6
1.5
1.4
10
100
1000

(a)

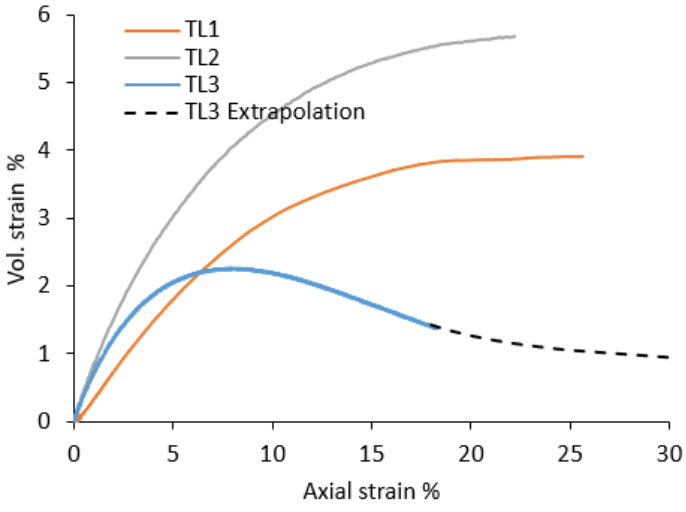
TL1
TL2
TL3
TL3 Extrapolation
Vol. strain %
Axial strain %
6
5
4
3
2
1
0
0
5
10
15
20
25
30

(b)

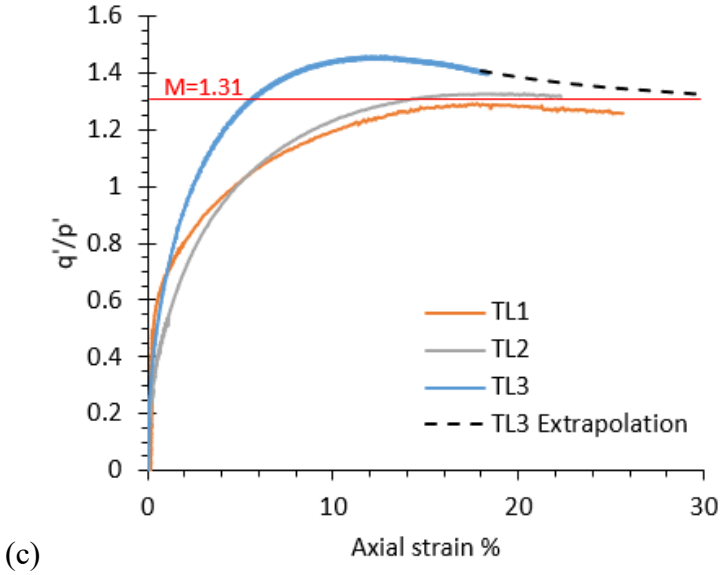

(c)

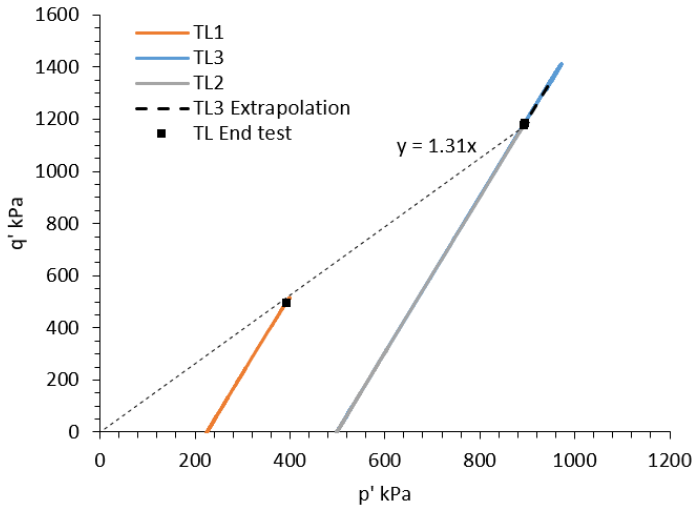

(d)

Figure 5-5 Triaxial shearing behaviour of silty loess: (a) compression line, (b) volumetric behaviour, (c) stress ratio, and (d) stress path.

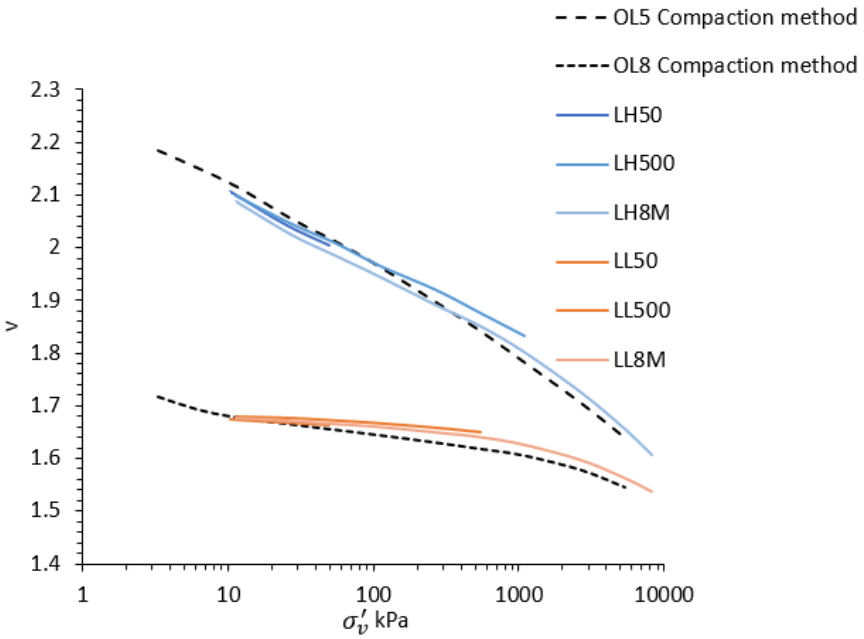

Figure 5-6 Compression behaviour of loess samples for microstructure analysis.

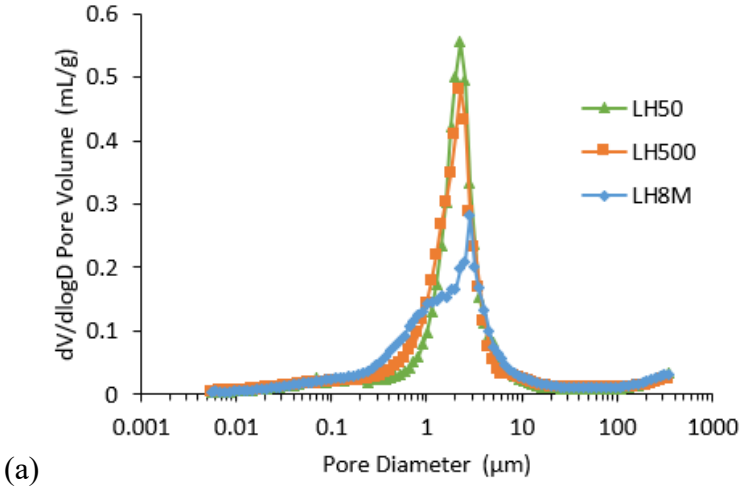

(a)

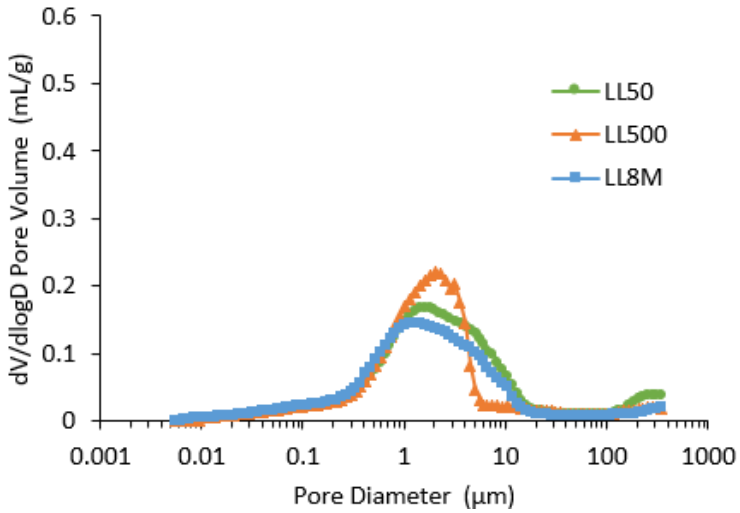

(b)

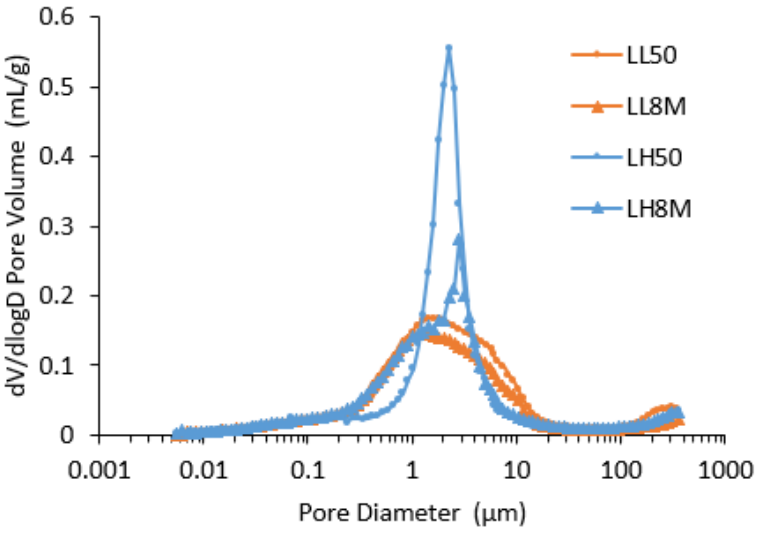

(c)

Figure 5-7 MIP results of silty loess in oedometer tests: (a) pore size distribution (PSD) of (a) loose sample LH and (b) dense sample LL under 50 kPa, 500 kPa and 8MPa vertical stress; and (c) comparison between LH and LL in 50 kPa and 8MPa.

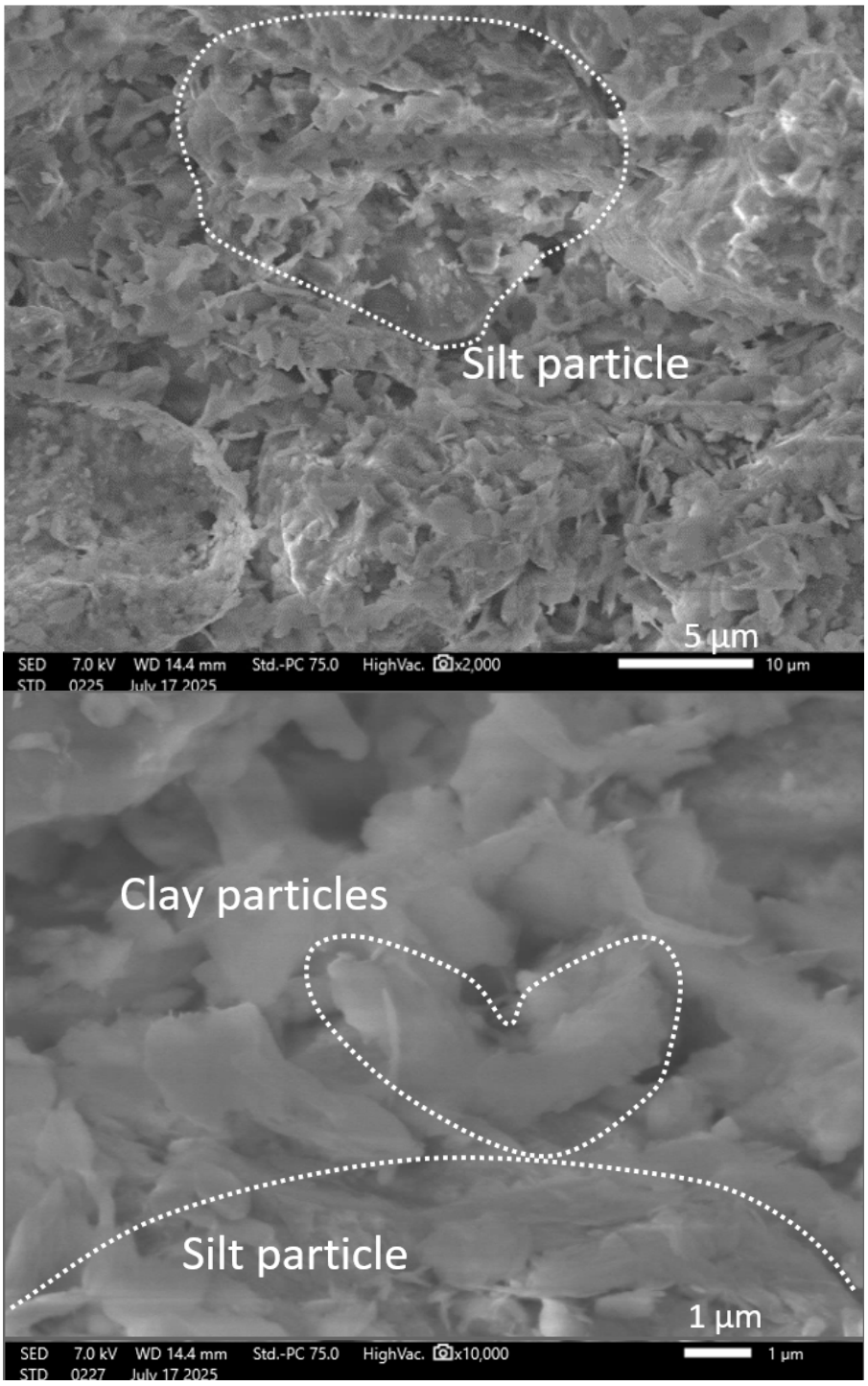
Silt particle
5 µm
SED 7.0 kV WD 14.4 mm Std.-PC 75.0 HighVac. x2,000 10 µm
STD 0225 July 17 2025
Clay particles
Silt particle
1 µm
SED 7.0 kV WD 14.4 mm Std.-PC 75.0 HighVac. x10,000 1 µm
STD 0227 July 17 2025

(a)

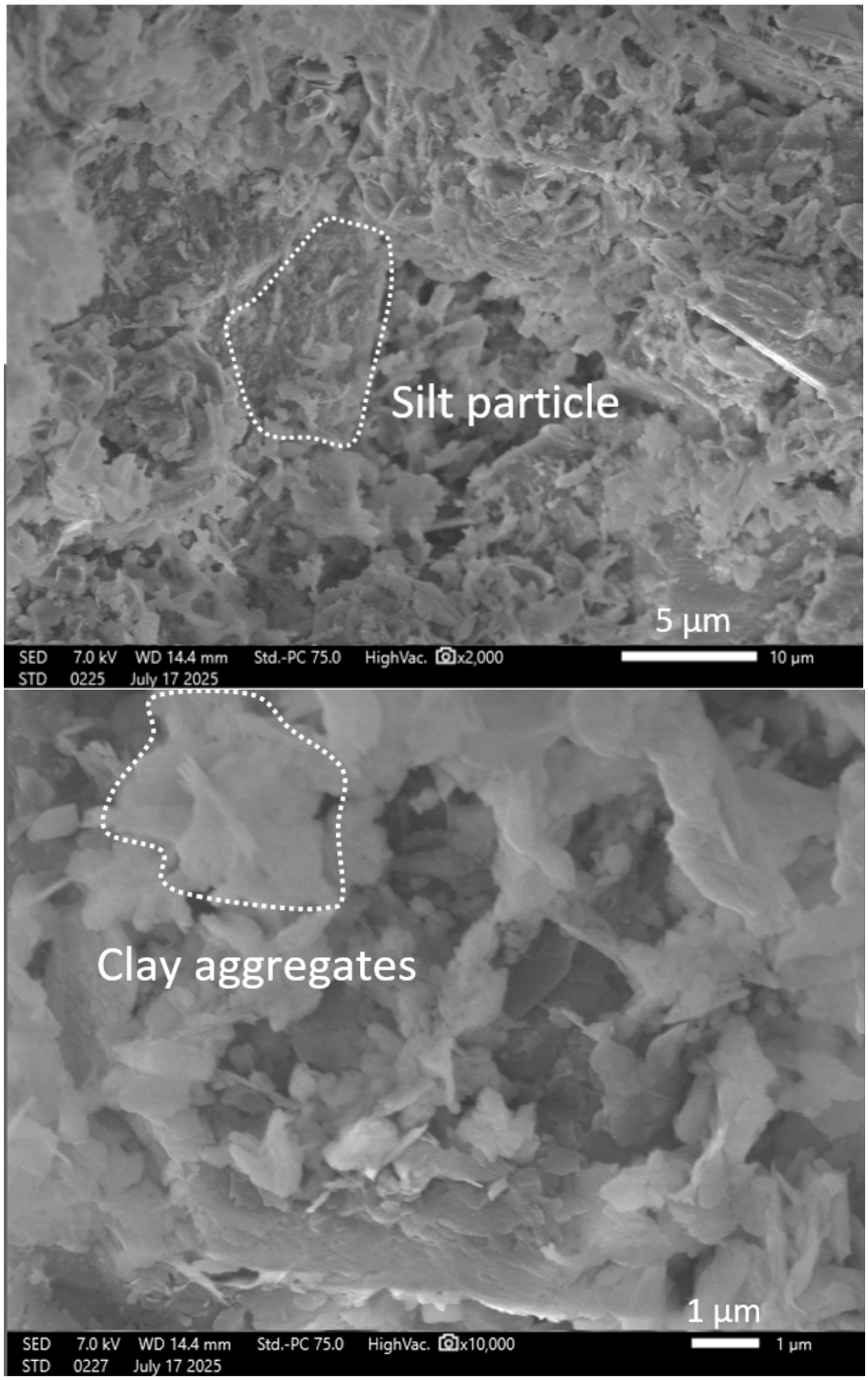
Silt particle
5 µm
SED 7.0 kV WD 14.4 mm Std.-PC 75.0 HighVac. x2,000 10 µm
STD 0225 July 17 2025
Clay aggregates
1 µm
SED 7.0 kV WD 14.4 mm Std.-PC 75.0 HighVac. x10,000 1 µm
STD 0227 July 17 2025

(b)

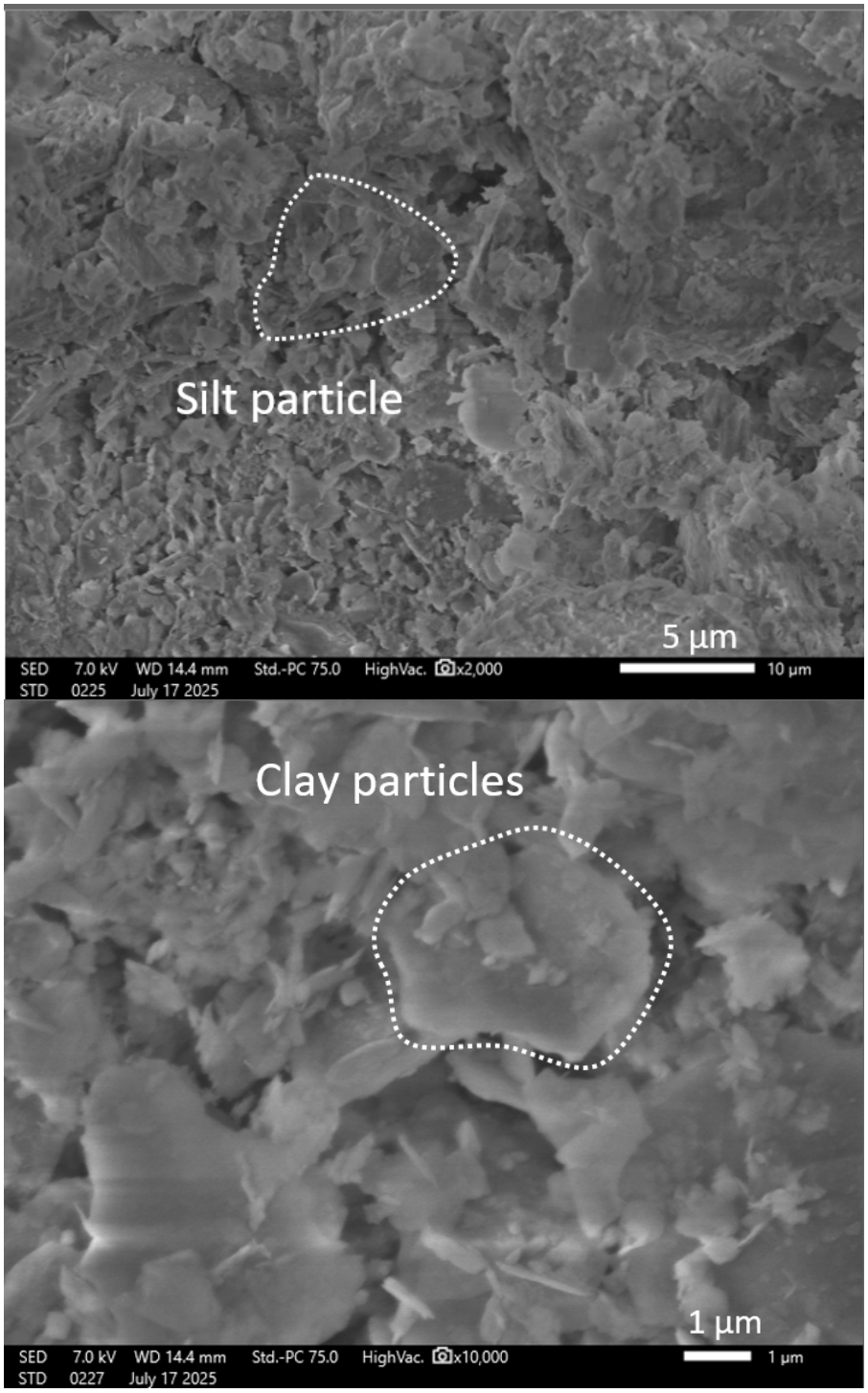
Silt particle
5 µm
SED 7.0 kV WD 14.4 mm Std.-PC 75.0 HighVac. x2,000
STD 0225 July 17 2025
10 µm
Clay particles
1 µm
SED 7.0 kV WD 14.4 mm Std.-PC 75.0 HighVac. x10,000
STD 0227 July 17 2025
1 µm

(c)

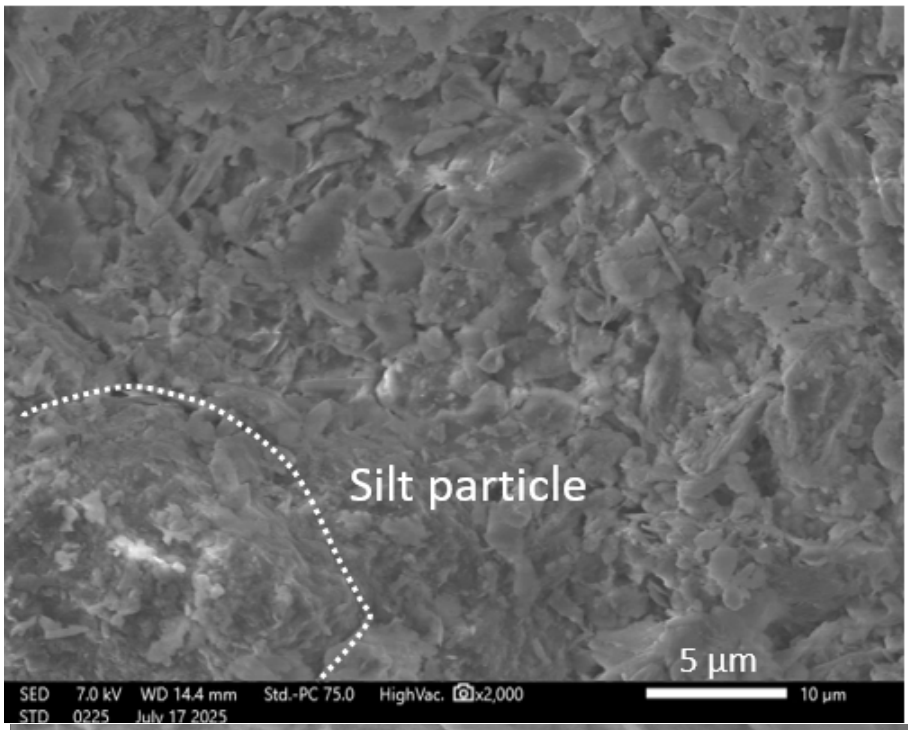

(d)

Figure 5-8 SEM results of silty loess in oedometer tests: loose sample LL (a) under 50 kPa (LL50) and (b) under 8MPa (LL8M); and dense sample LH (c) under 50 kPa (LH50) and (d) under 8MPa (LH8M) in medium and high magnifications.

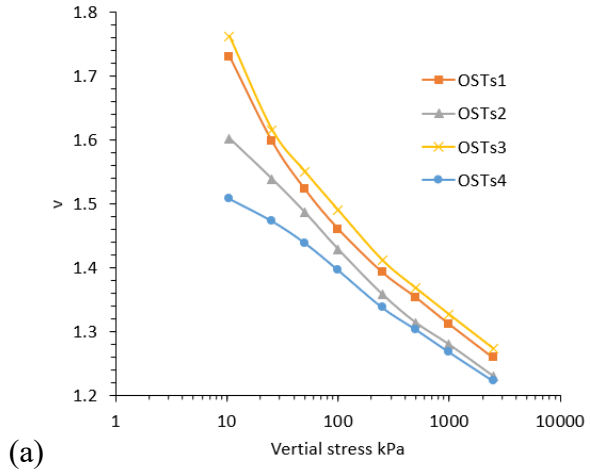

(a)

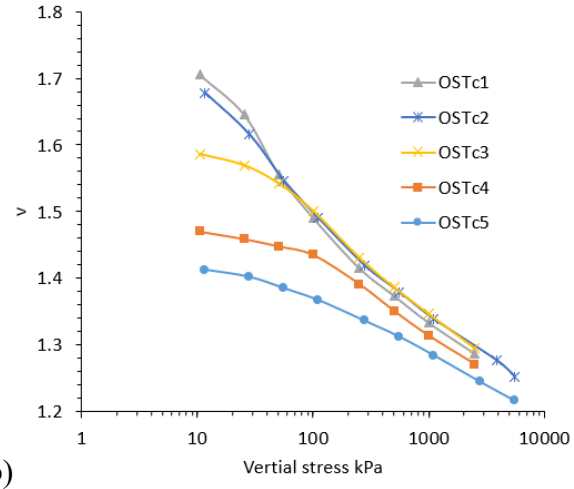

(b)

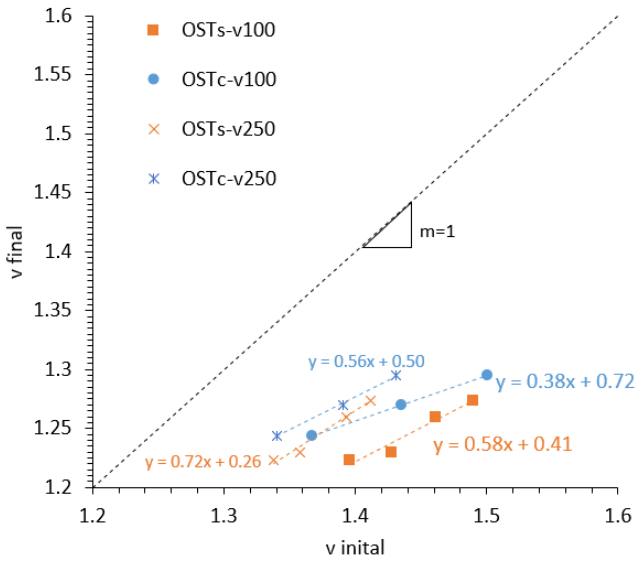

(c)

Figure 5-9 One-dimensional compression of sandy tailings on (a) slurry samples and (b) compacted samples, and (c) m values for transitional degree.

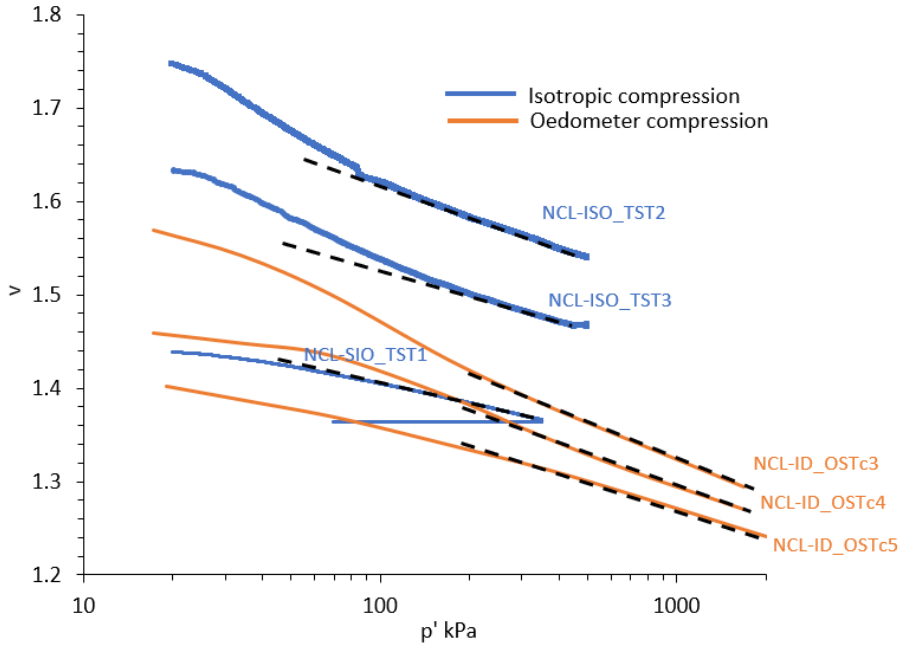
1.8
1.7
1.6
1.5
1.4
1.3
1.2
v
10
100
1000
p' kPa
Isotropic compression
Oedometer compression
NCL-ISO_TST2
NCL-ISO_TST3
NCL-SIO_TST1
NCL-ID_OSTc3
NCL-ID_OSTc4
NCL-ID_OSTc5

(a)

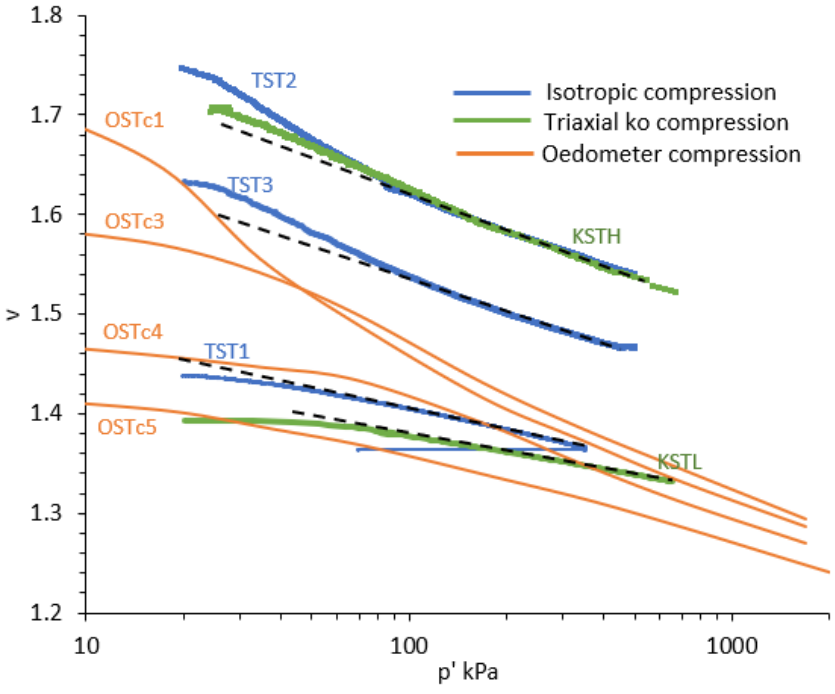
1.8
1.7
1.6
1.5
1.4
1.3
1.2
v
10
100
1000
p' kPa
TST2
OSTc1
TST3
OSTc3
KSTH
OSTc4
TST1
OSTc5
KSTL
Isotropic compression
Triaxial ko compression
Oedometer compression

(b)

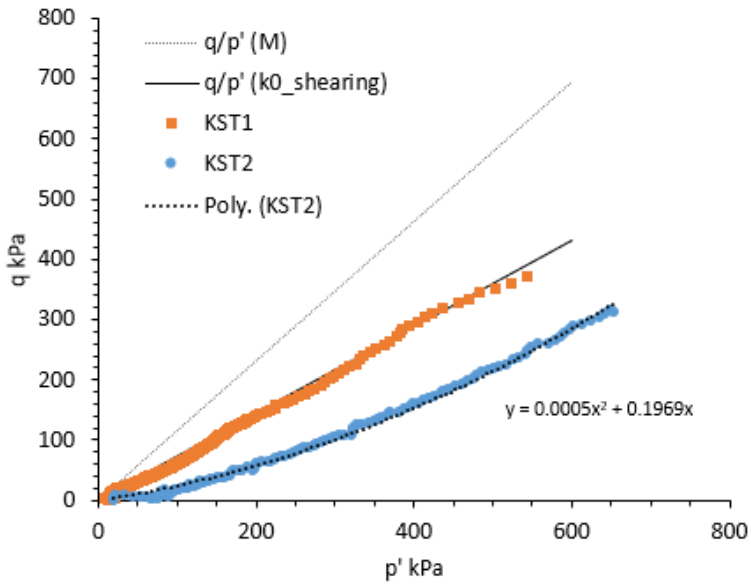

(c)

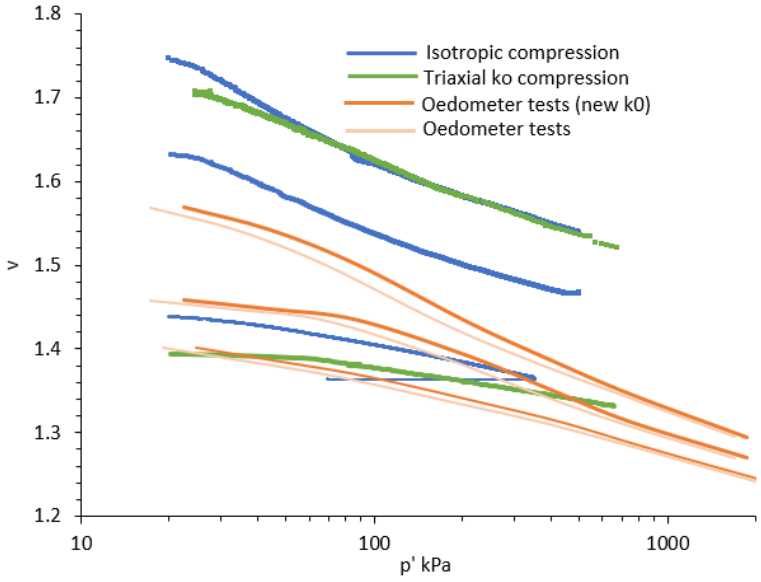

(d)

Figure 5-10 Compression behaviour of sandy tailings on compacted samples: (a) isotropic compression and (d) triaxial ko compression; (e) stress ratio of triaxial k_0 tests and (f) oedometer results based on new k_0.

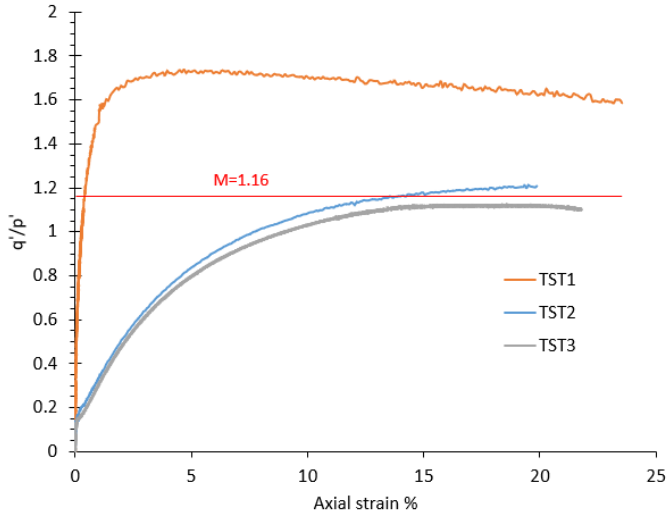
2
1.8
1.6
1.4
1.2
1
0.8
0.6
0.4
0.2
0
q'/p'
M=1.16
TST1
TST2
TST3
0
5
10
15
20
25
Axial strain %

(a)

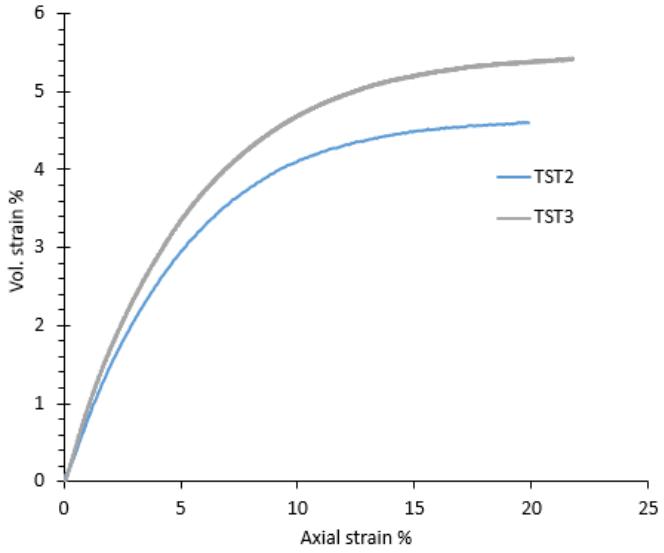
6
5
4
3
2
1
0
Vol. strain %
TST2
TST3
0
5
10
15
20
25
Axial strain %

(b)

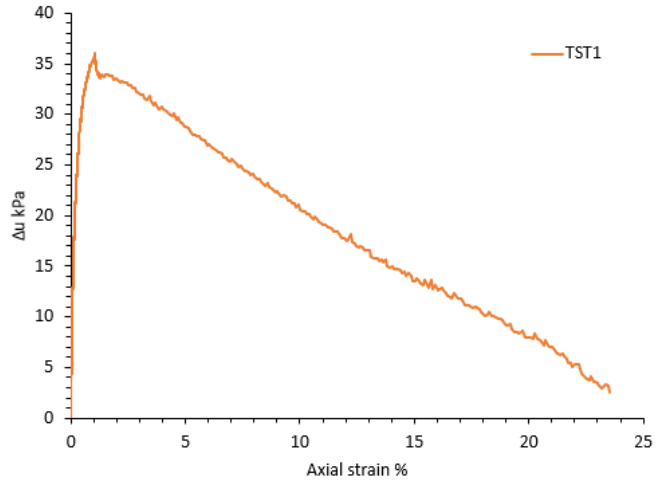
40
35
30
25
20
15
10
5
0
Δu kPa
TST1
0
5
10
15
20
25
Axial strain %

(c)

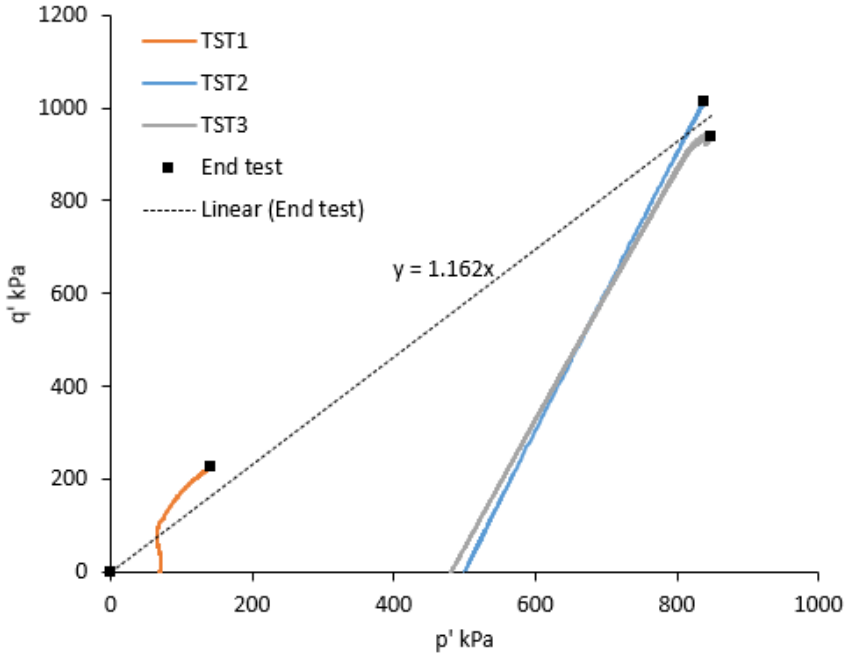

(d)

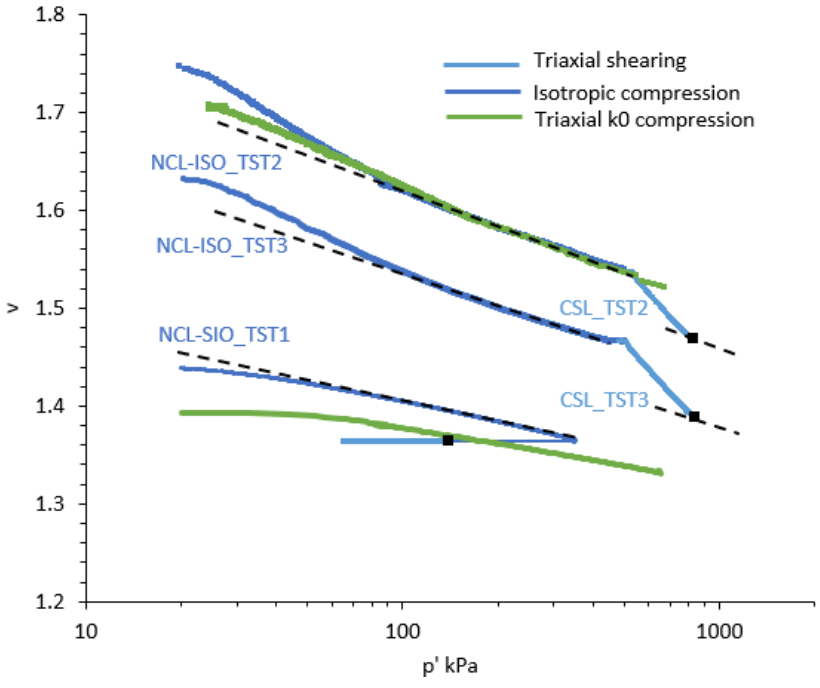

(e)

Figure 5-11 Triaxial tests on sandy tailings: (a) stress ratio, (b) volumetric behaviour, (c) excess pore water pressure, (d) shear paths and (e) shearing lines.

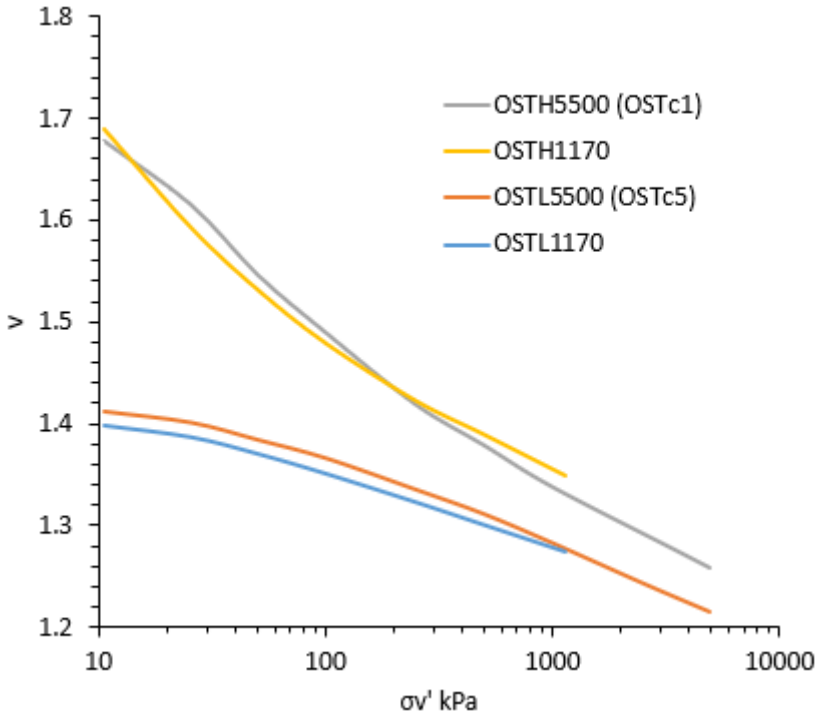

Figure 5-12 Compression behaviour of sandy tailings for microstructure analysis.

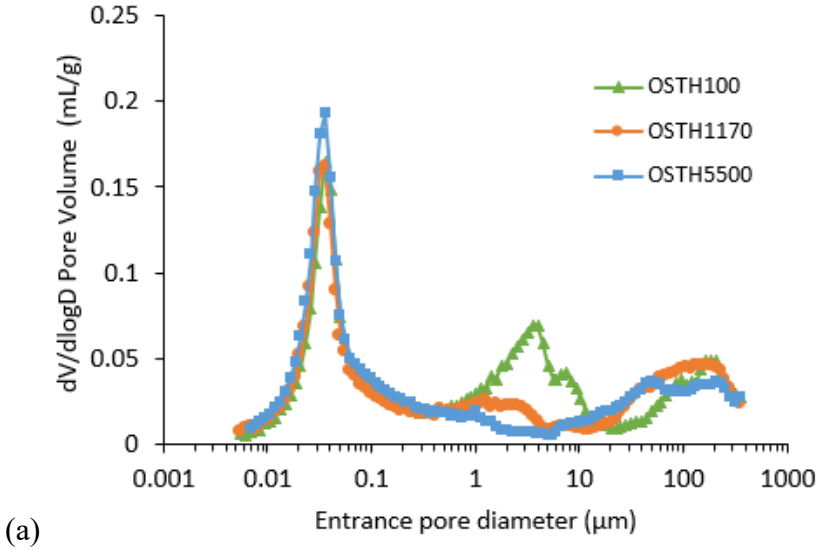

(a)

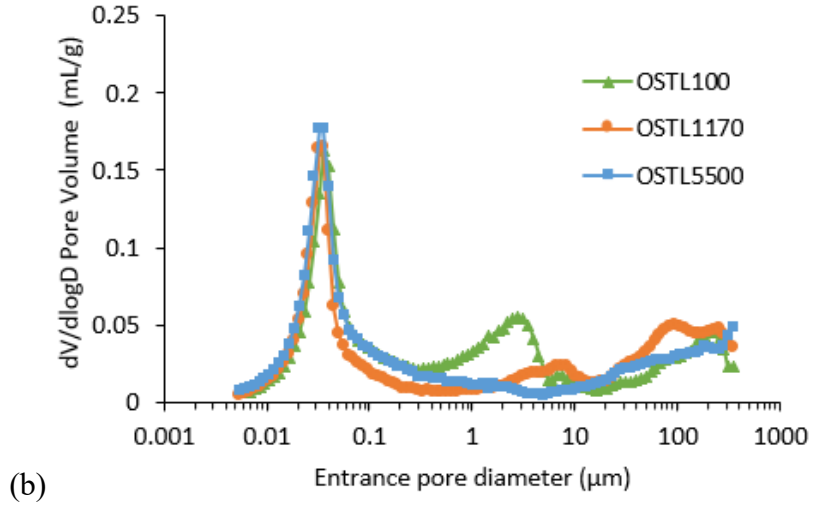

(b)

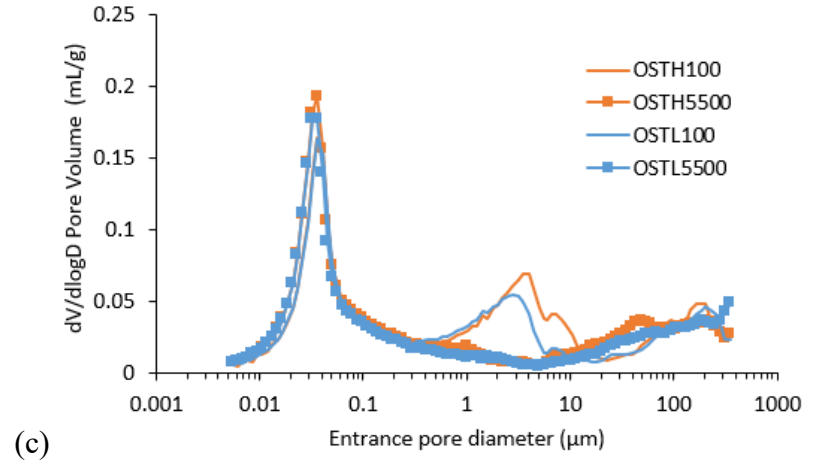

(c)

Figure 5-13 MIP results of sandy tailings in oedometer tests: (a) loose sample OSTH and (b) dense sample OSTL under vertical stress of 100 kPa, 1170 kPa and 5500 kPa; (c) comparison between OSTH and OSTL at 100 kPa and 5500 kPa.

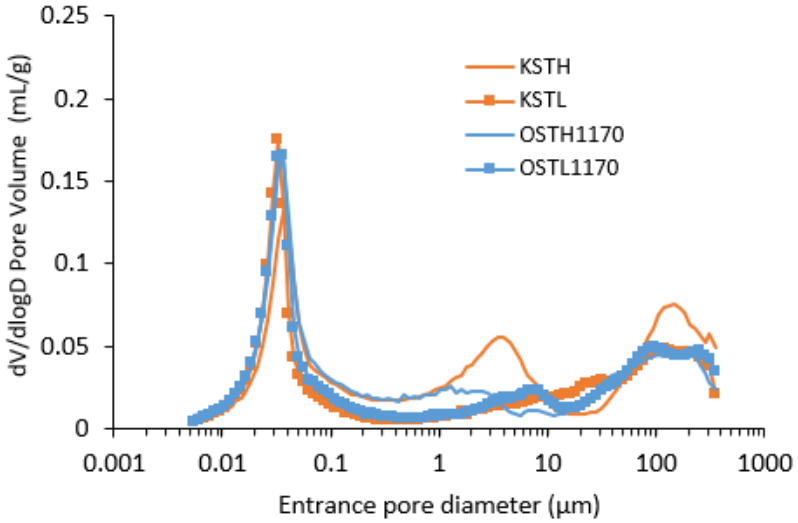

Figure 5-14: MIP tests on sandy tailings under triaxial k_0 compression, compared with sample under oedometer compression at 1170 kPa.

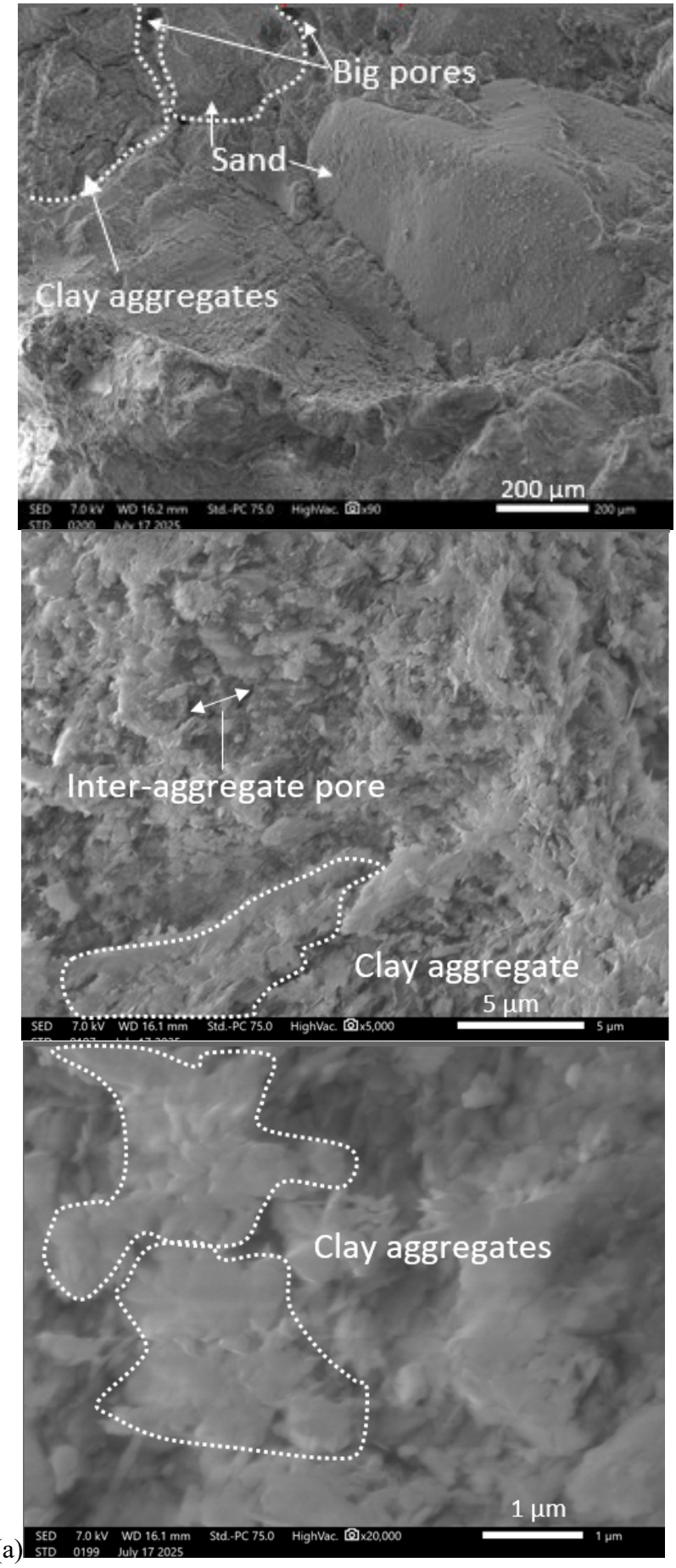
Big pores
Sand
Clay aggregates
200 µm
SED 7.0 kV WD 16.2 mm Std.-PC 75.0 HighVac. x90
Inter-aggregate pore
Clay aggregate
5 µm
SED 7.0 kV WD 16.1 mm Std.-PC 75.0 HighVac. x5,000
Clay aggregates
1 µm
SED 7.0 kV WD 16.1 mm Std.-PC 75.0 HighVac. x20,000
STD 0199 July 17 2025

(a)

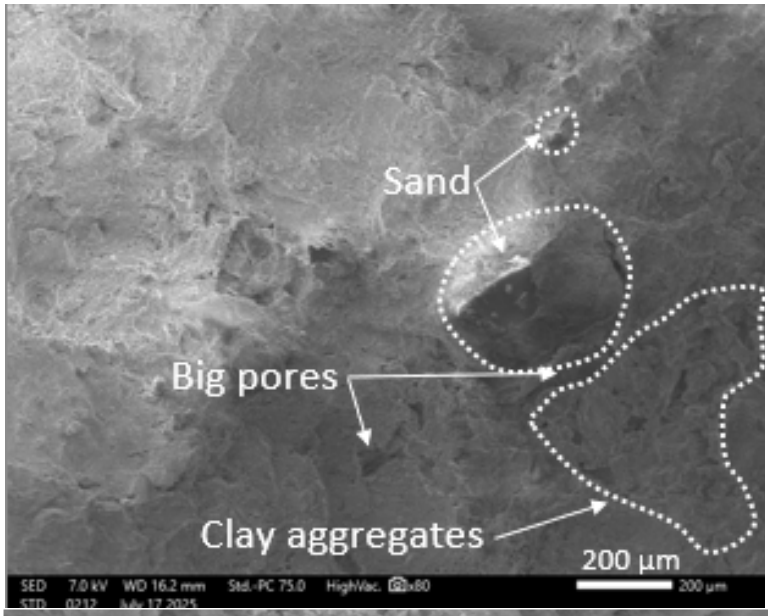
Sand
Big pores
Clay aggregates
200 µm
SED 7.0 kV WD 16.2 mm Std.-PC 75.0 HighVac. x80 200 µm


Inter-aggregate pore
Clay aggregate
5 µm
SED 7.0 kV WD 16.5 mm Std.-PC 75.0 HighVac. x5,000 5 µm
STD 0214 July 17 2025


Clay aggregates
1 µm
SED 7.0 kV WD 16.2 mm Std.-PC 75.0 HighVac. x20,000 1 µm
STD 0210 July 17 2025

(b)

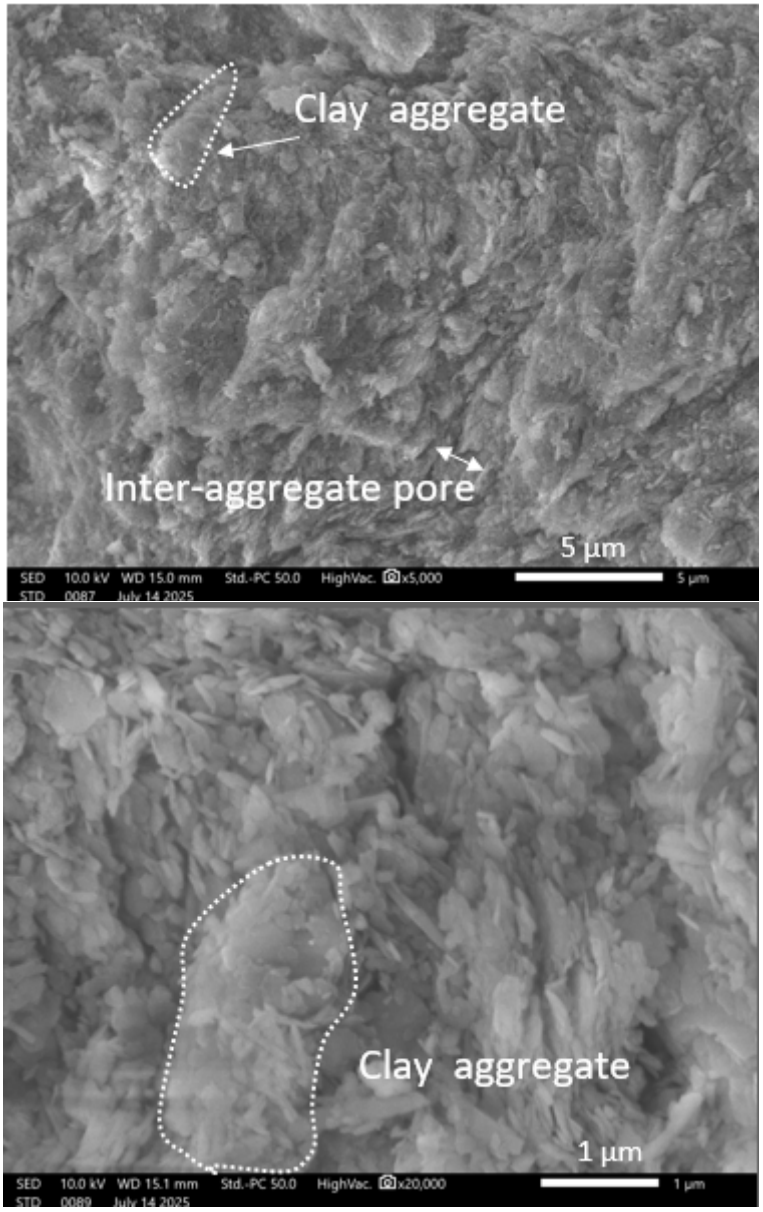
Clay aggregate
Inter-aggregate pore
5 µm
SED 10.0 kV WD 15.0 mm Std.-PC 50.0 HighVac. x5,000 5 µm
STD 0087 July 14 2025
Clay aggregate
1 µm
SED 10.0 kV WD 15.1 mm Std.-PC 50.0 HighVac. x20,000 1 µm
STD 0089 July 14 2025

(c)

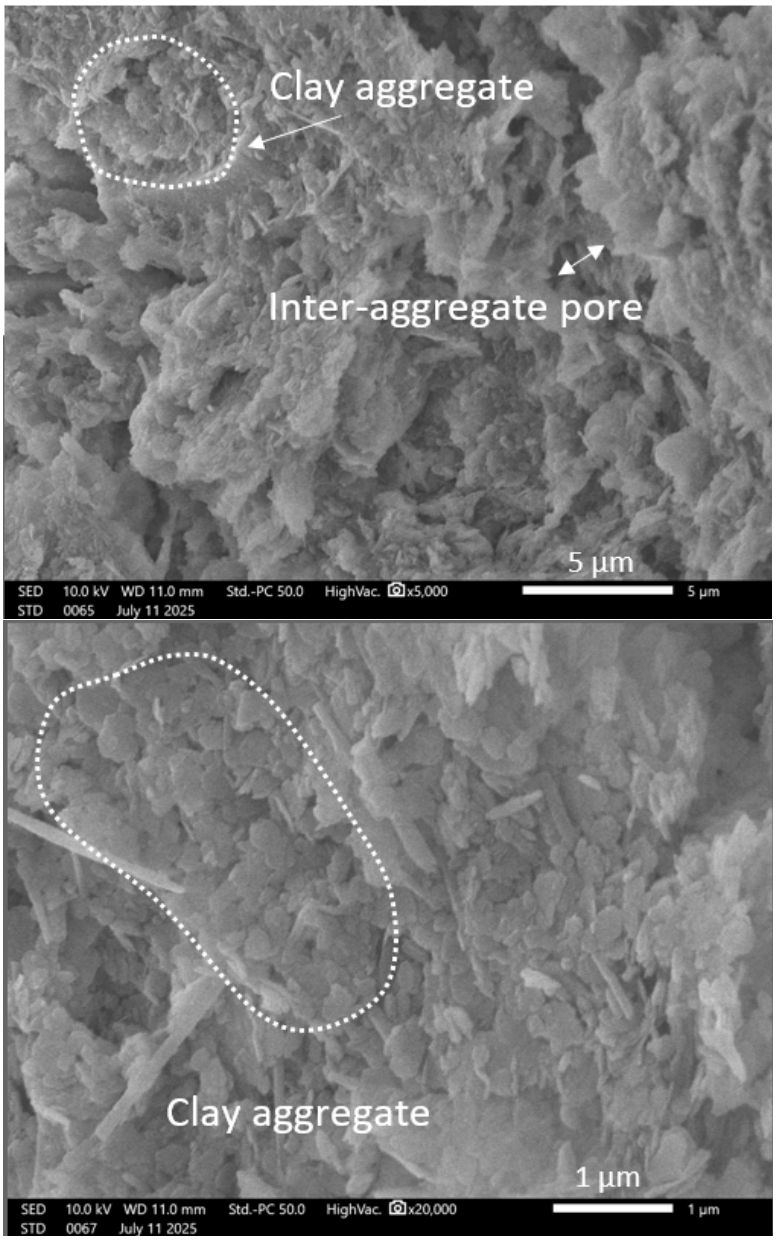
Clay aggregate
Inter-aggregate pore
5 µm
SED 10.0 kV WD 11.0 mm Std.-PC 50.0 HighVac. x5,000 5 µm
STD 0065 July 11 2025
Clay aggregate
1 µm
SED 10.0 kV WD 11.0 mm Std.-PC 50.0 HighVac. x20,000 1 µm
STD 0067 July 11 2025

(d)

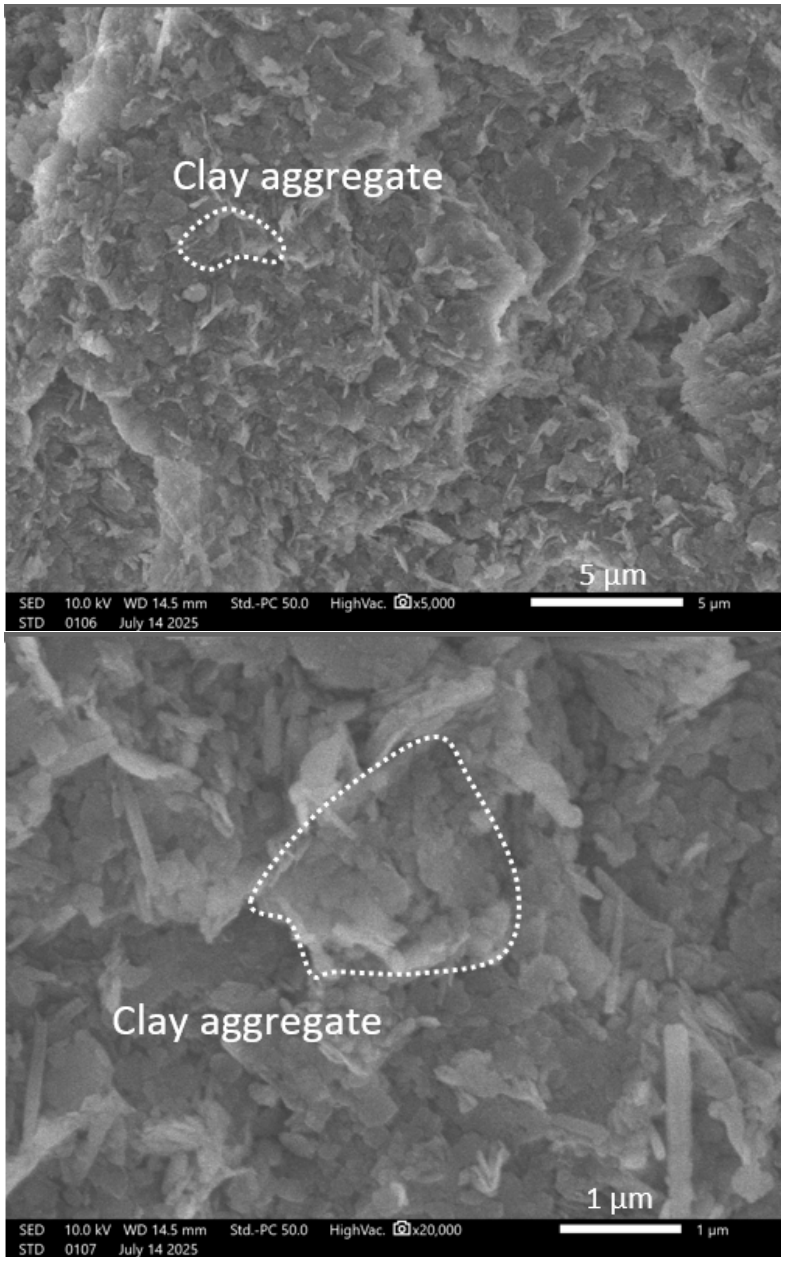
Clay aggregate
5 µm
SED 10.0 kV WD 14.5 mm Std.-PC 50.0 HighVac. x5,000 5 µm
STD 0106 July 14 2025
Clay aggregate
1 µm
SED 10.0 kV WD 14.5 mm Std.-PC 50.0 HighVac. x20,000 1 µm
STD 0107 July 14 2025

(e)

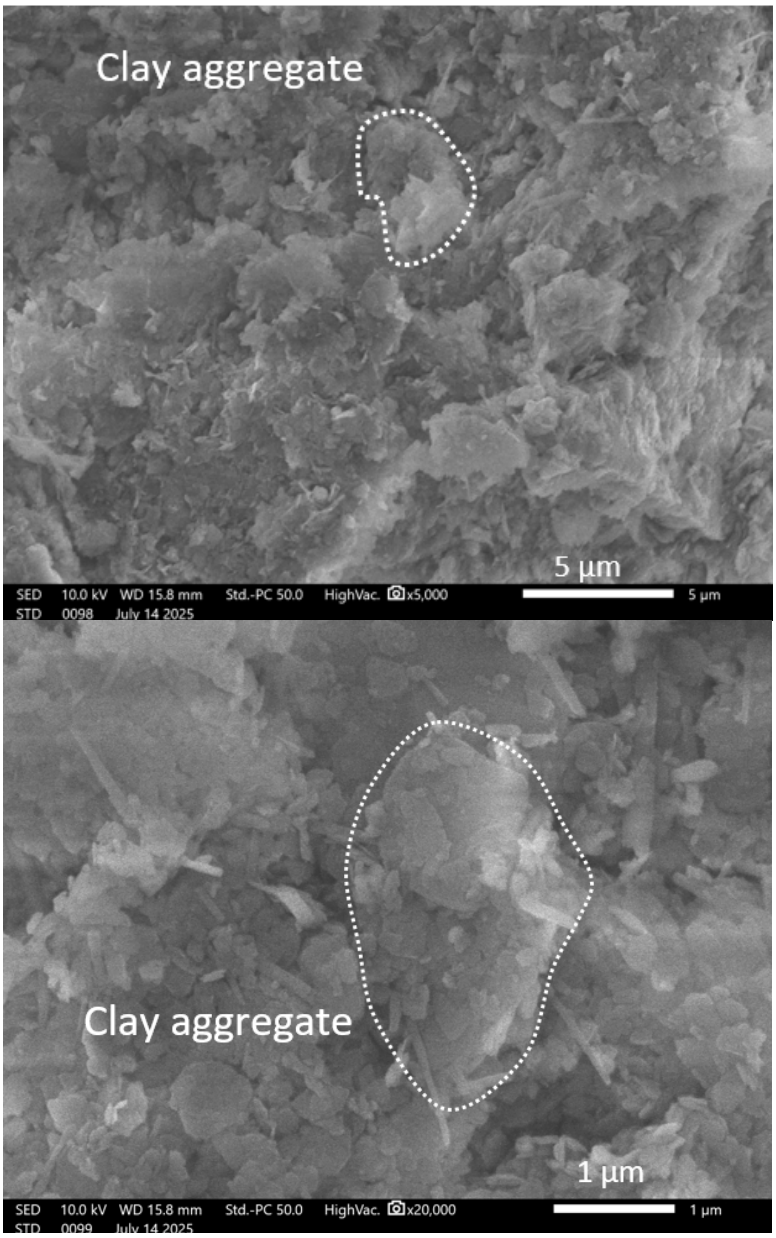
Clay aggregate
5 µm
SED 10.0 kV WD 15.8 mm Std.-PC 50.0 HighVac. x5,000 5 µm
STD 0098 July 14 2025
Clay aggregate
1 µm
SED 10.0 kV WD 15.8 mm Std.-PC 50.0 HighVac. x20,000 1 µm
STD 0099 July 14 2025

(f)

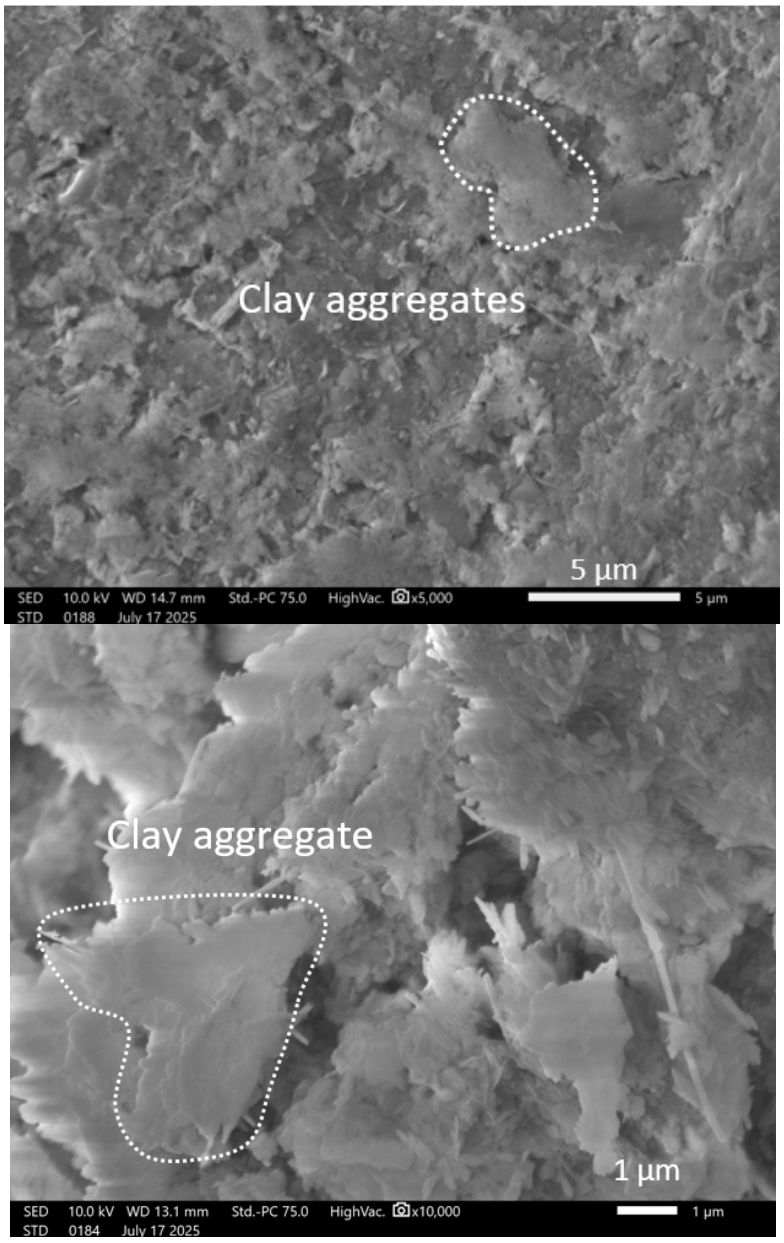
Clay aggregates
5 µm
SED 10.0 kV WD 14.7 mm Std.-PC 75.0 HighVac. x5,000 5 µm
STD 0188 July 17 2025
Clay aggregate
1 µm
SED 10.0 kV WD 13.1 mm Std.-PC 75.0 HighVac. x10,000 1 µm
STD 0184 July 17 2025

(g)

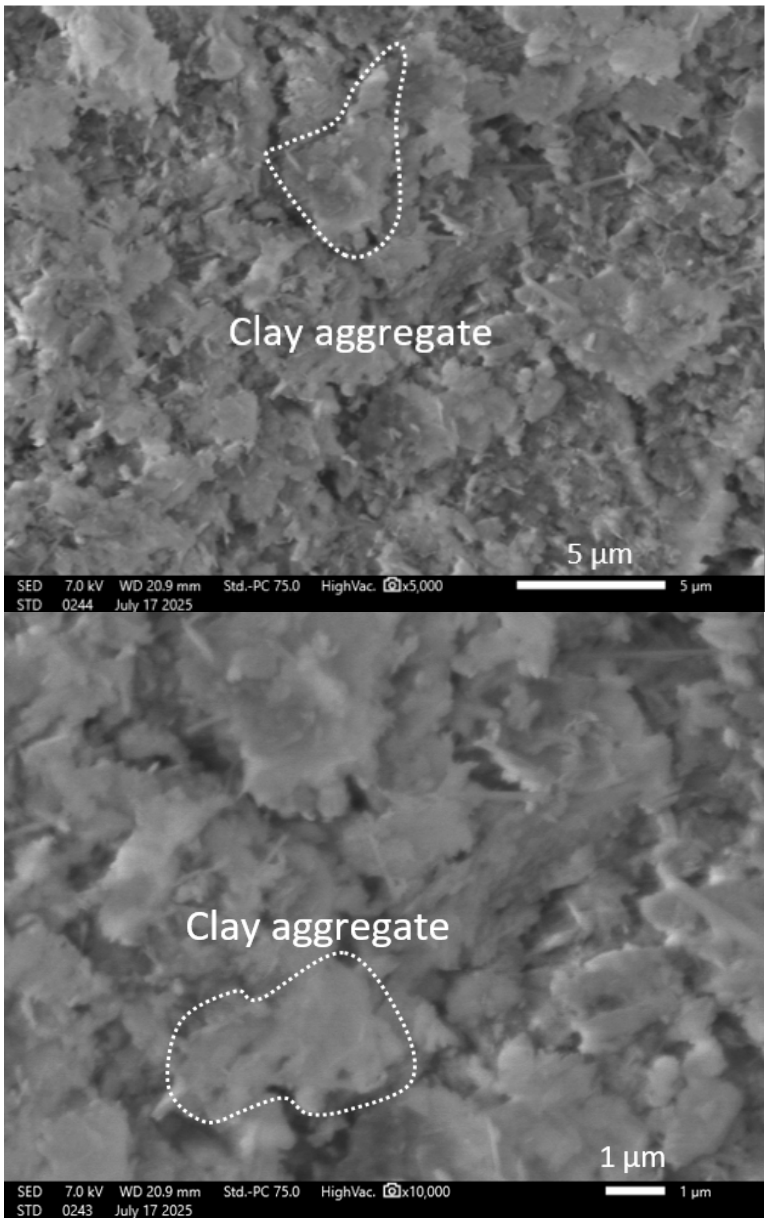

(h)

Figure 5-15 SEM images of sandy tailing in oedometer tests: (a) dense and (b) loose samples under 100 kPa in low, medium and high magnifications, (c) dense and (d) loose samples under 5500 kPa, and (e) dense and (f) loose samples under 1170 kPa in medium and high magnifications; SEM images of sandy tailings in triaxial k_0 compression tests: (g) dense and (h) loose samples in medium and high magnifications.

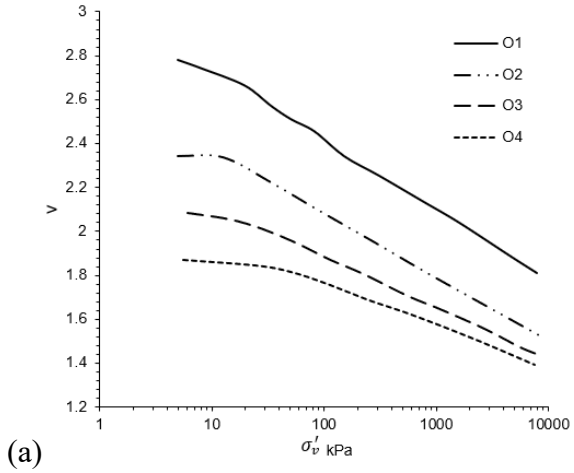

(a)

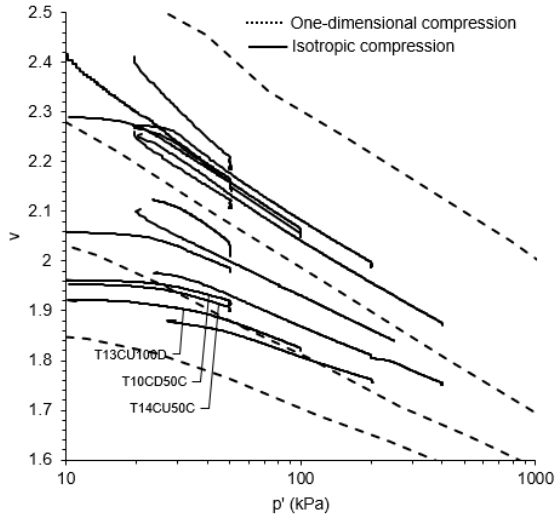

(b)

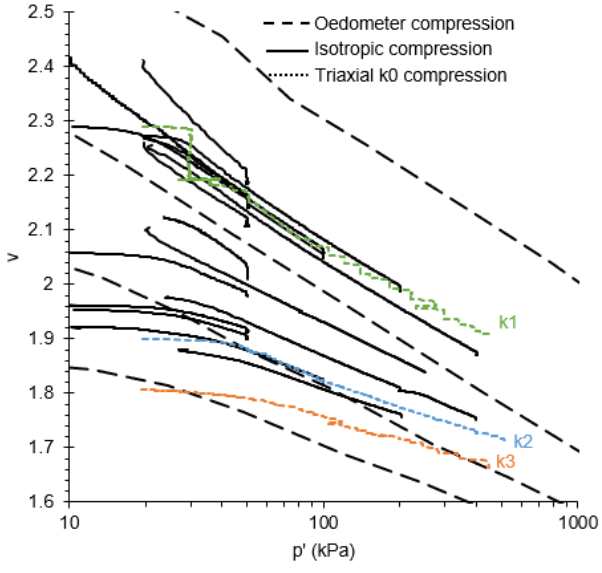

(c)

Figure 5-16 Compression curves of fine tailings for (a) oedometer tests, (b) triaxial isotropic compression tests and (c) triaxial k_0 compression tests.

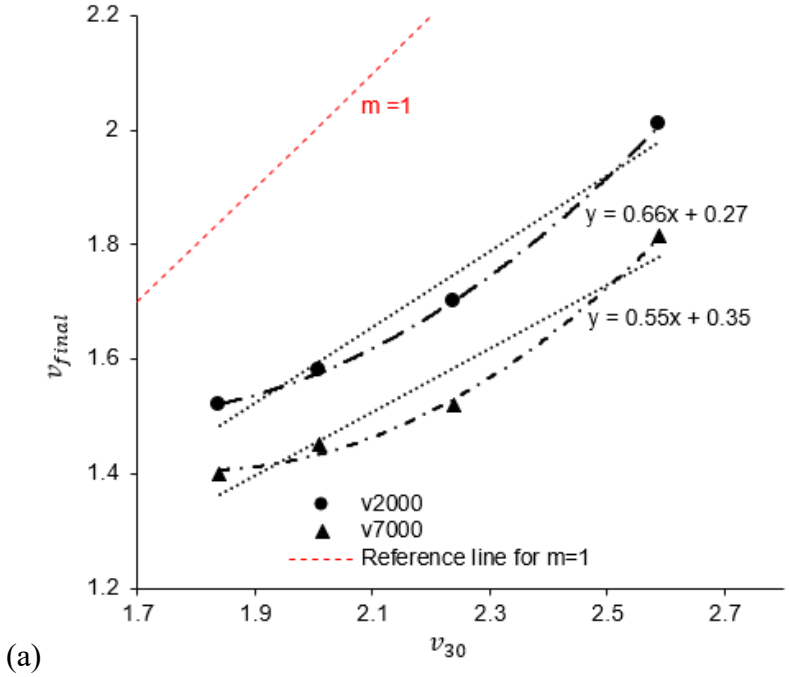

(a)

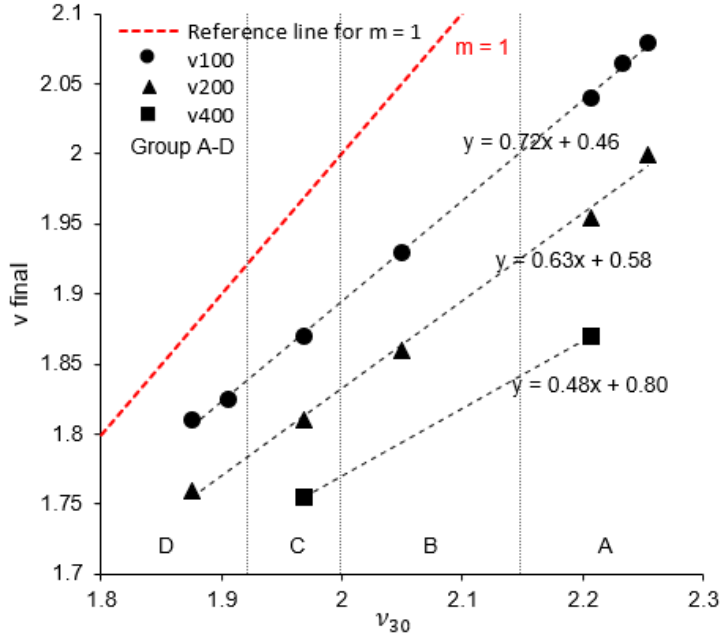

(b)

Figure 5-17 The m values for (a) one-dimensional compression and (b) isotropic compression of fine tailings.

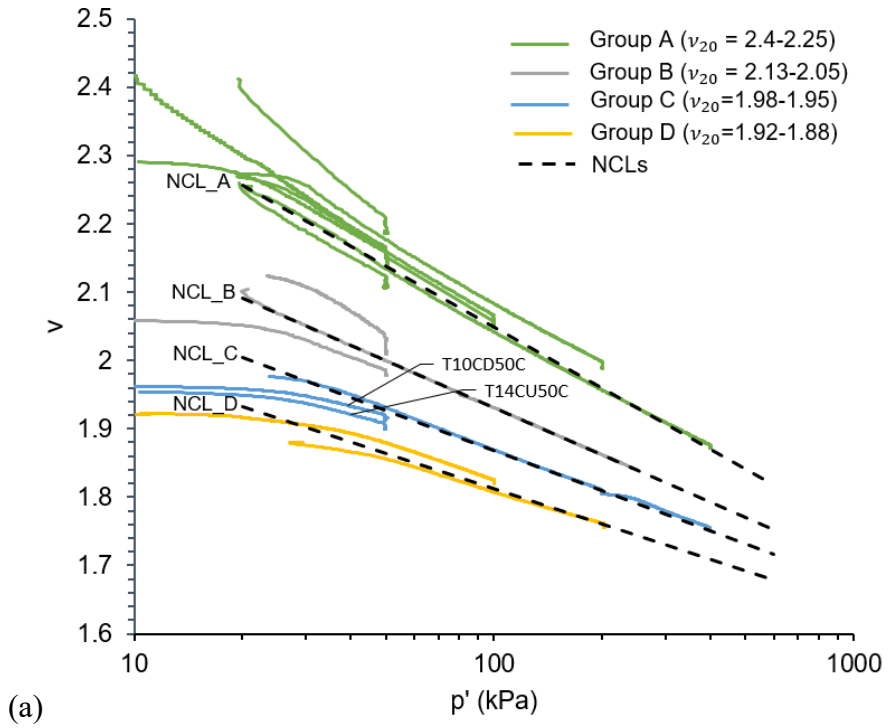

(a)

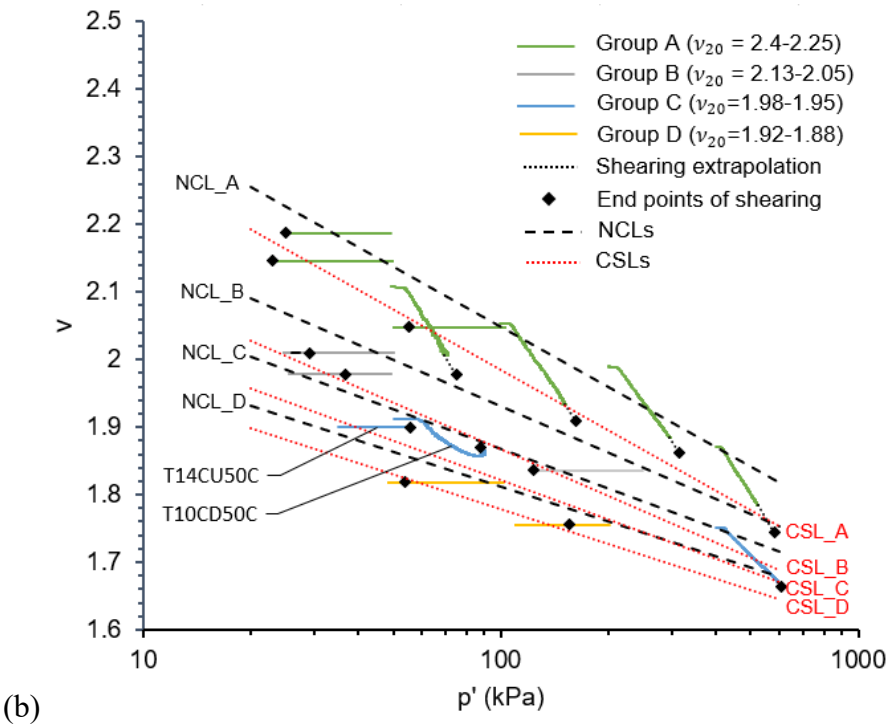

(b)

Figure 5-18 Critical states behaviour for each group: (a) isotropic compression lines and NCLs, (b) shearing paths and CSLs.

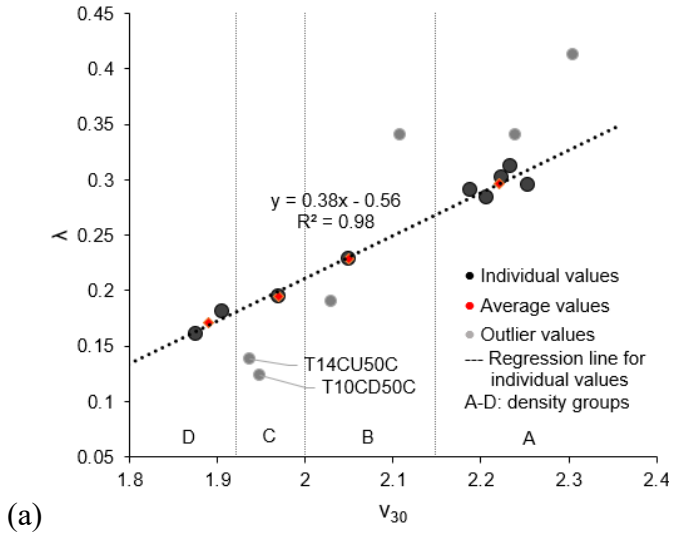

(a)

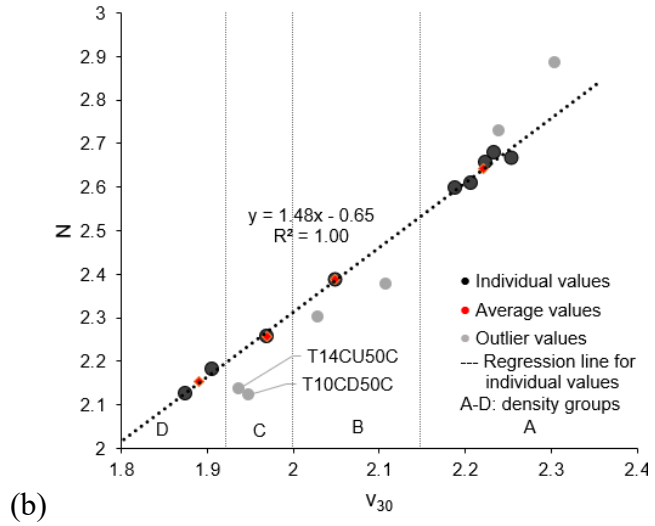

(b)

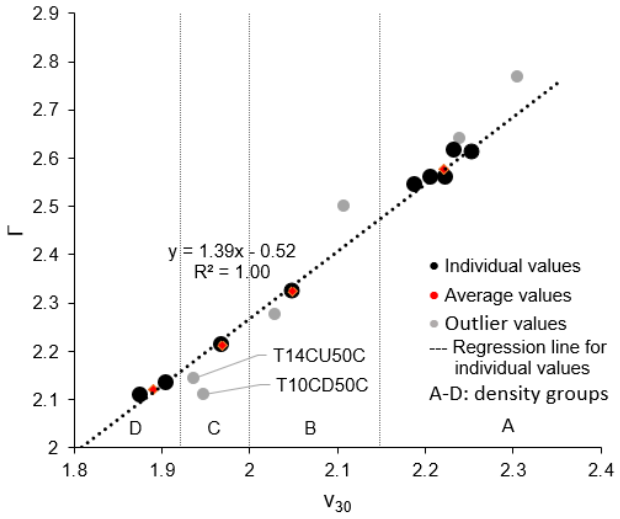

(c)

Figure 5-19 Choices of parameters of NCLs and CSLs for fine tailings: (a) gradients and (b) intercepts of NCLs and (c) intercepts of CSLs.

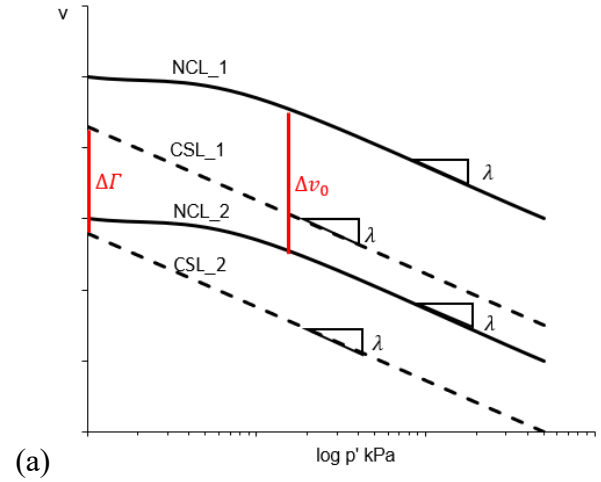

(a)

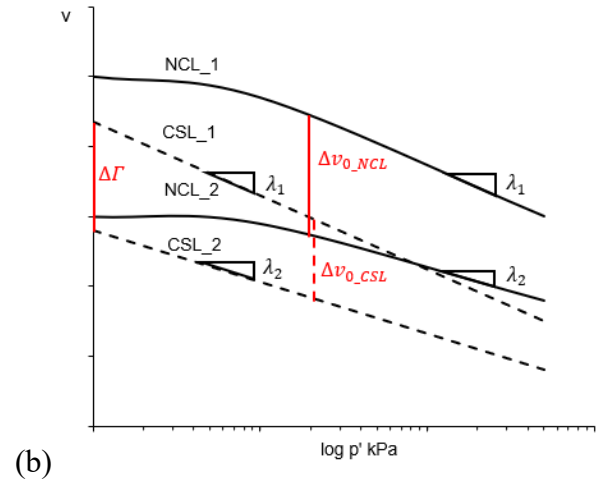

(b)

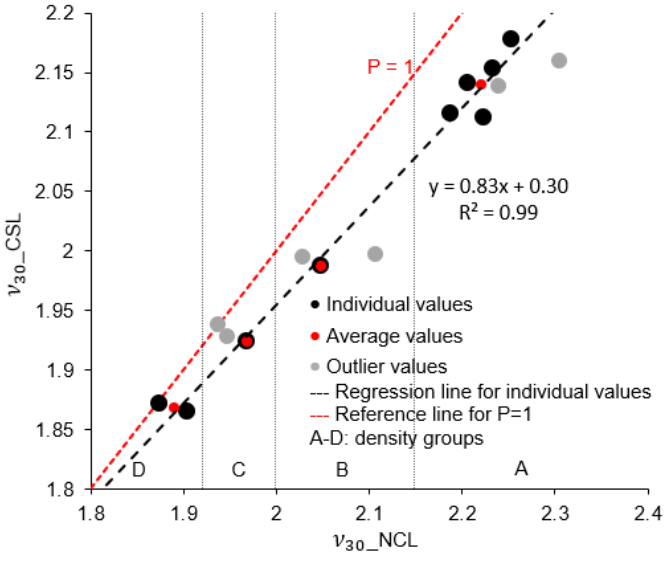

(c)

Figure 5-20 Quantification of the convergence of CSLs by P value for fine tailings: (a) schematic definition of P value based on Ponzoni et al. (2014); (b) schematic definition of modified P value; (c) calculated P value for soil tested.

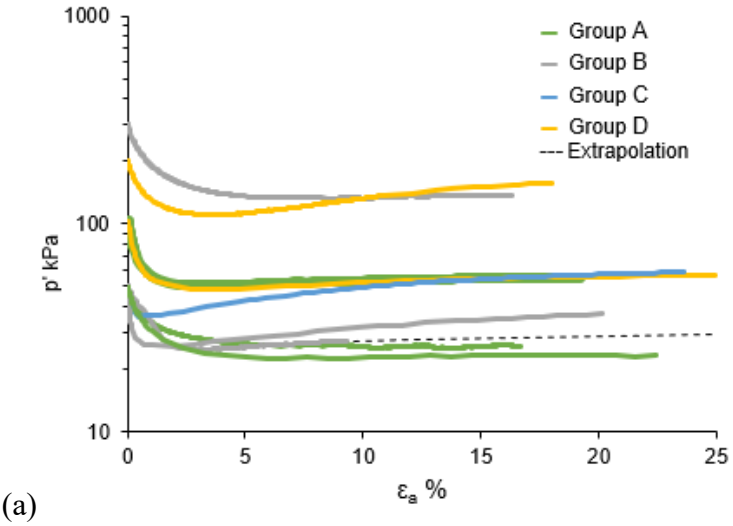

(a)

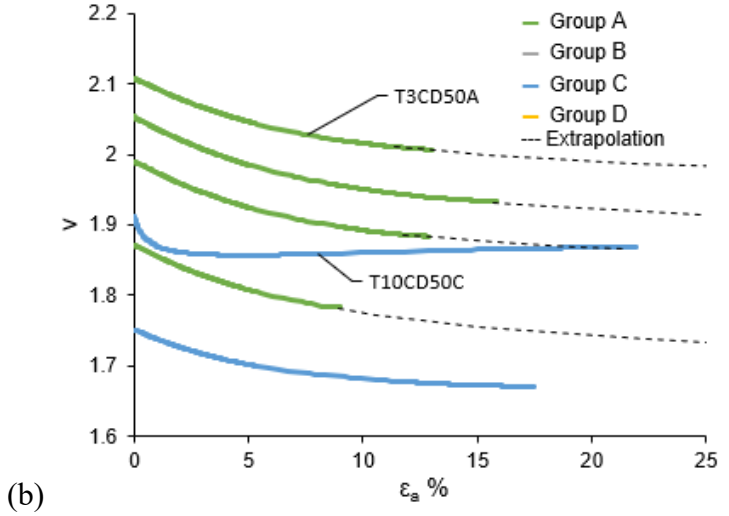

(b)

Figure 5-21 (a) non-convergence of stress states for the undrained tests on fine tailings and (b) non-convergence of specific volumes for the drained tests on fine tailings.

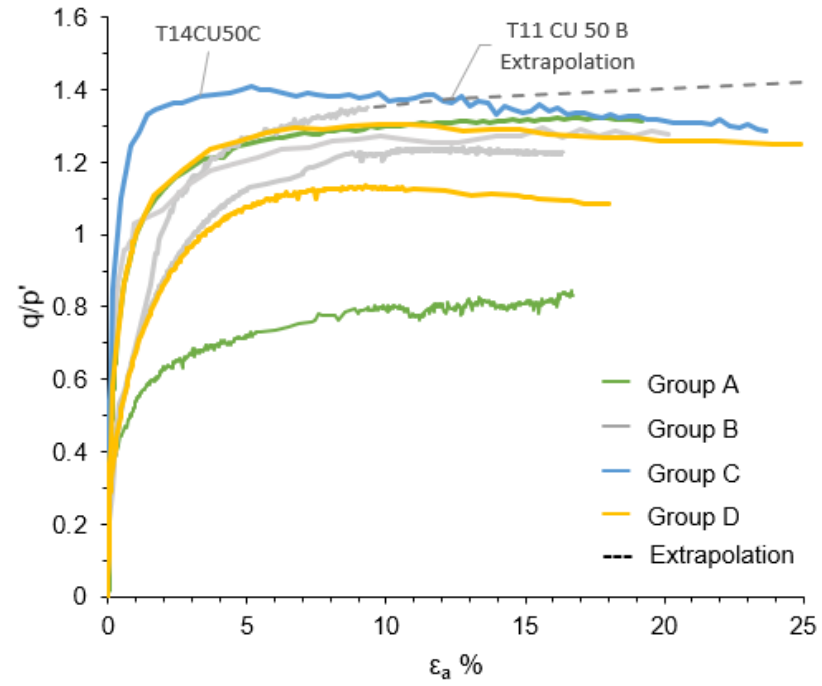
T14CU50C
T11 CU 50 B
Extrapolation
q/p'
Group A
Group B
Group C
Group D
Extrapolation
εa %

(a)

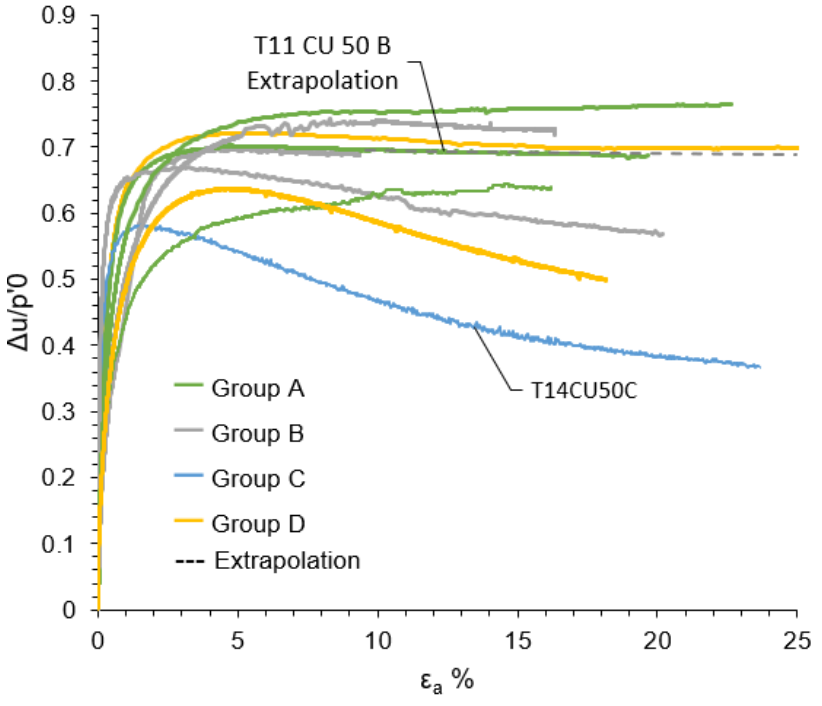
T11 CU 50 B
Extrapolation
T14CU50C
Δu/p'0
Group A
Group B
Group C
Group D
Extrapolation
εa %

(b)

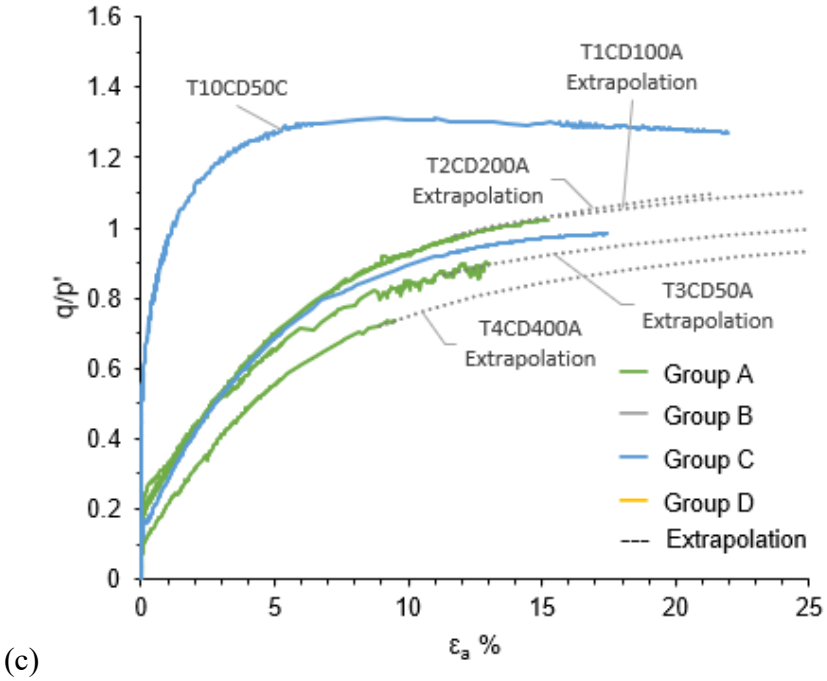

(c)

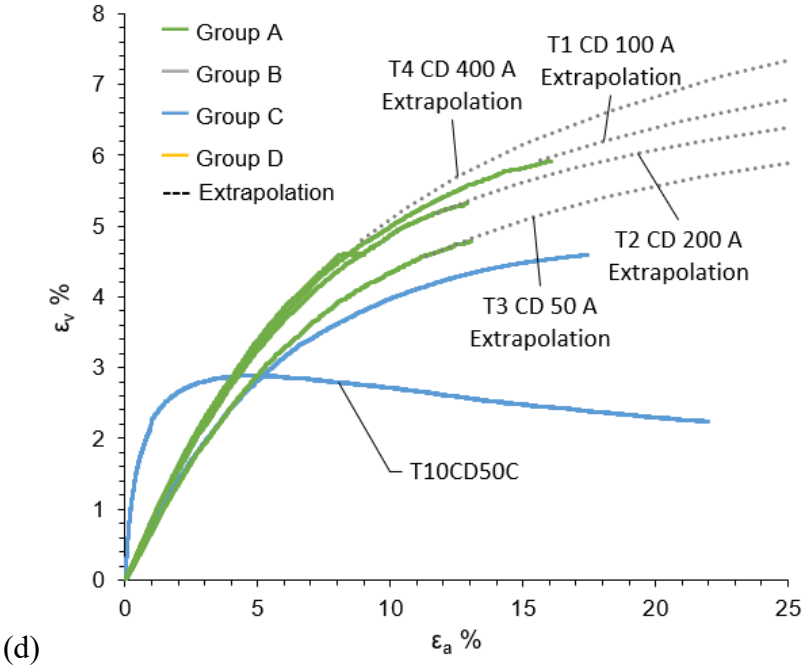

(d)

Figure 5-22 Triaxial shearing behaviour of fine tailings: (a) stress ratio and (b) normalised pore pressure change for undrained shearing tests; (c) stress ratio and (d) volume change for drained shearing tests.

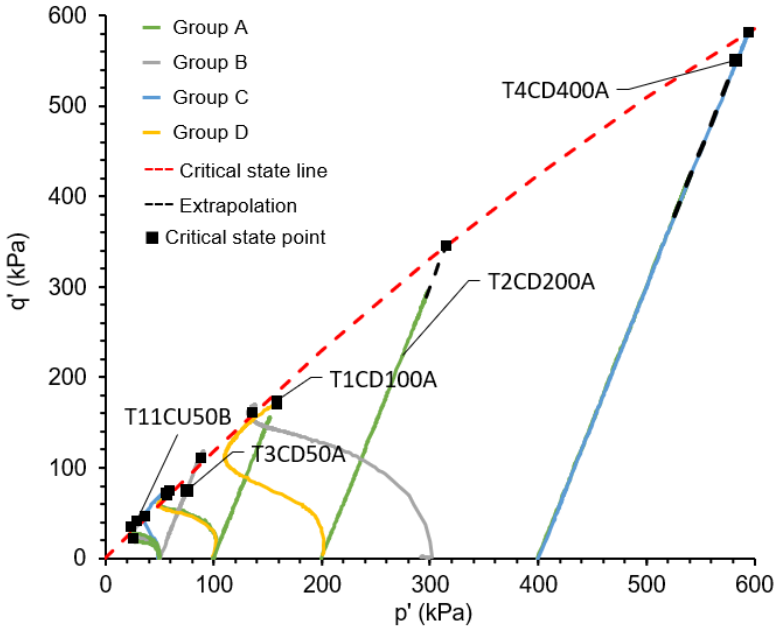

Figure 5-23 Shearing failure envelope and stress paths for fine tailings.

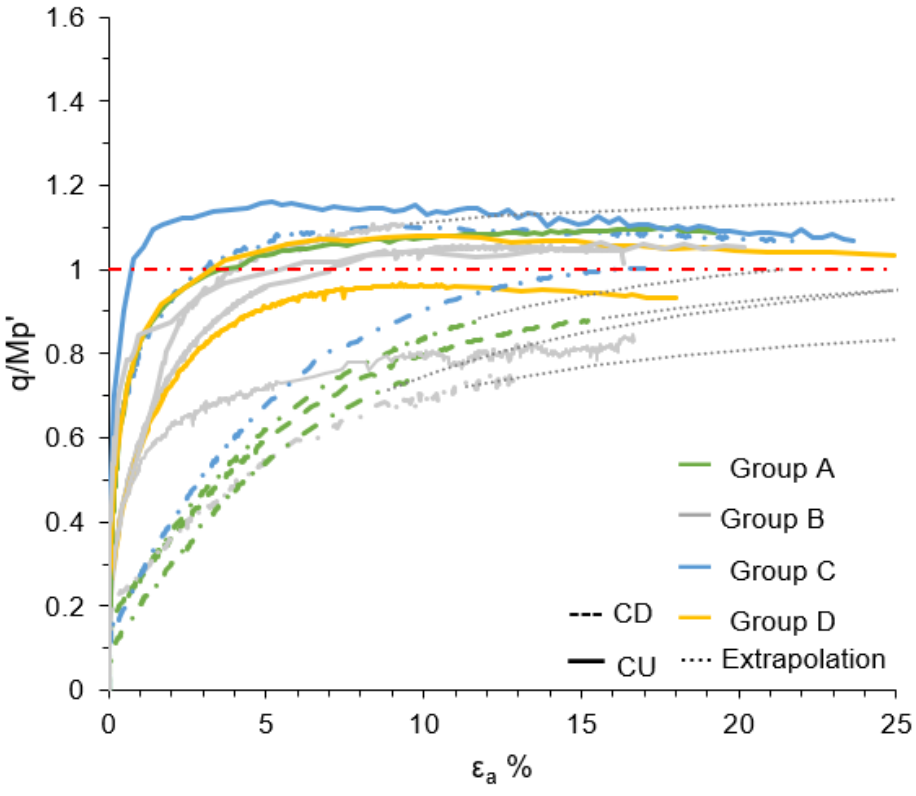

Figure 5-24 Normalised stress-strain behaviour of fine tailings.

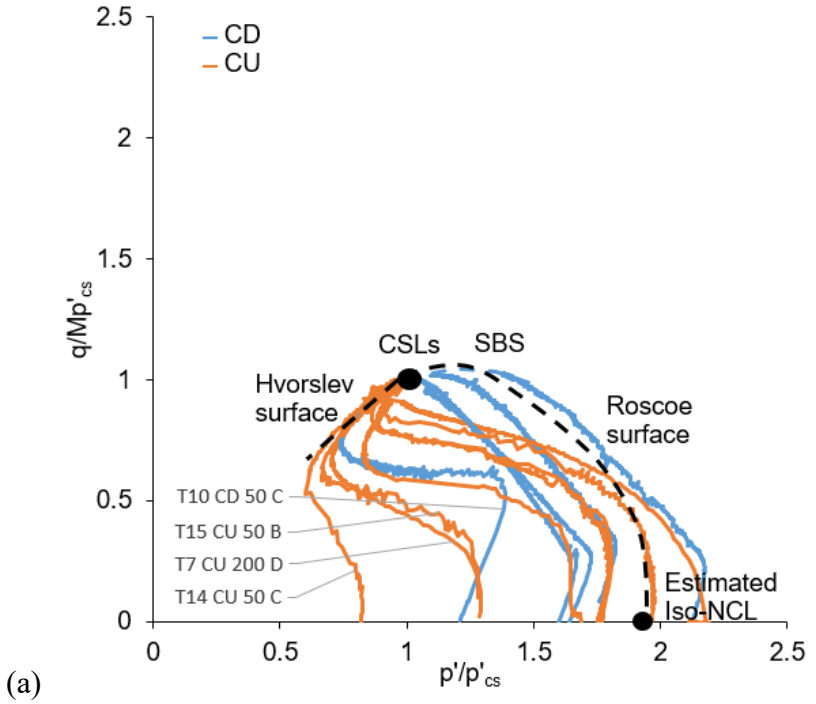

(a)

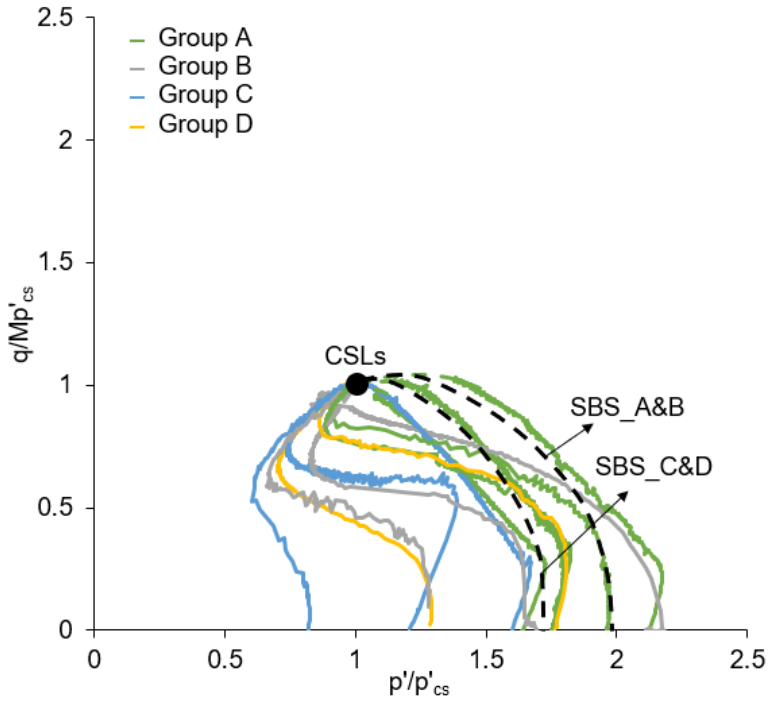

(b)

Figure 5-25 Normalised stress paths of fine tailings: (a) effect of drained and undrained shearing on state boundary surface; and (b) effect of initial density.

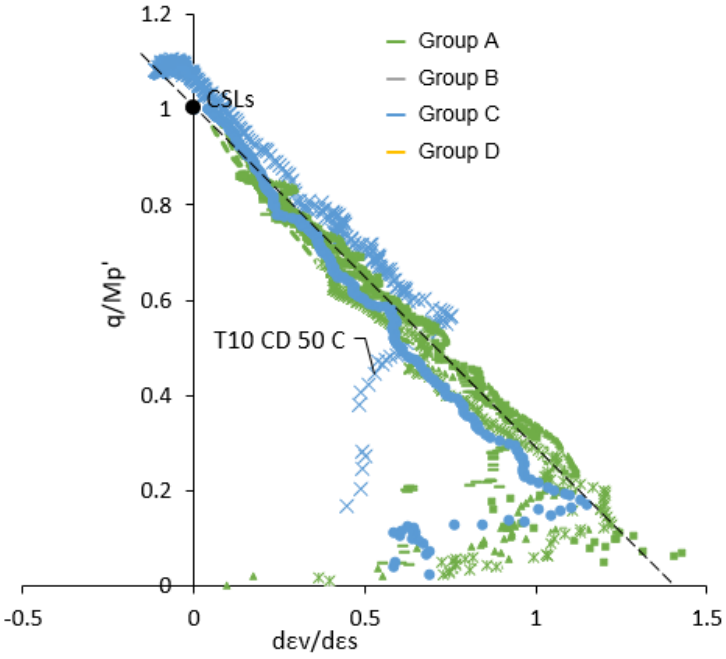

(a)

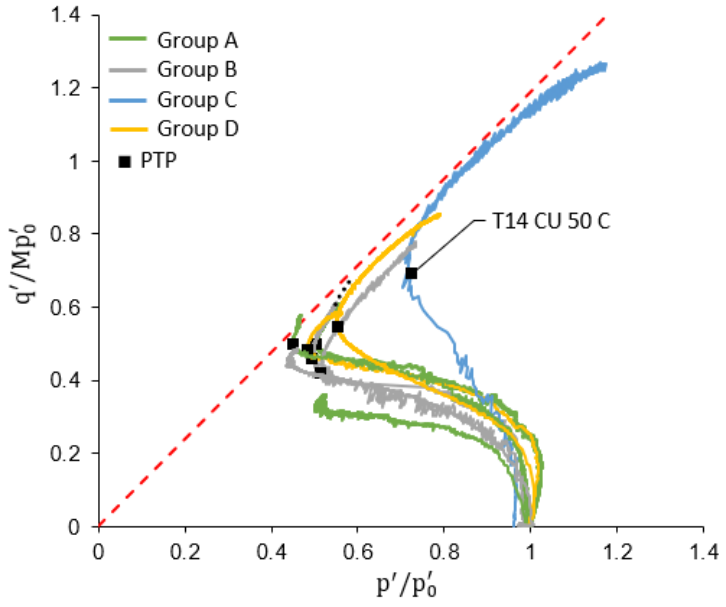

(b)

Figure 5-26 Dilatancy behaviour of fine tailings (a) for drained shearing tests and (b) for undrained shearing tests.

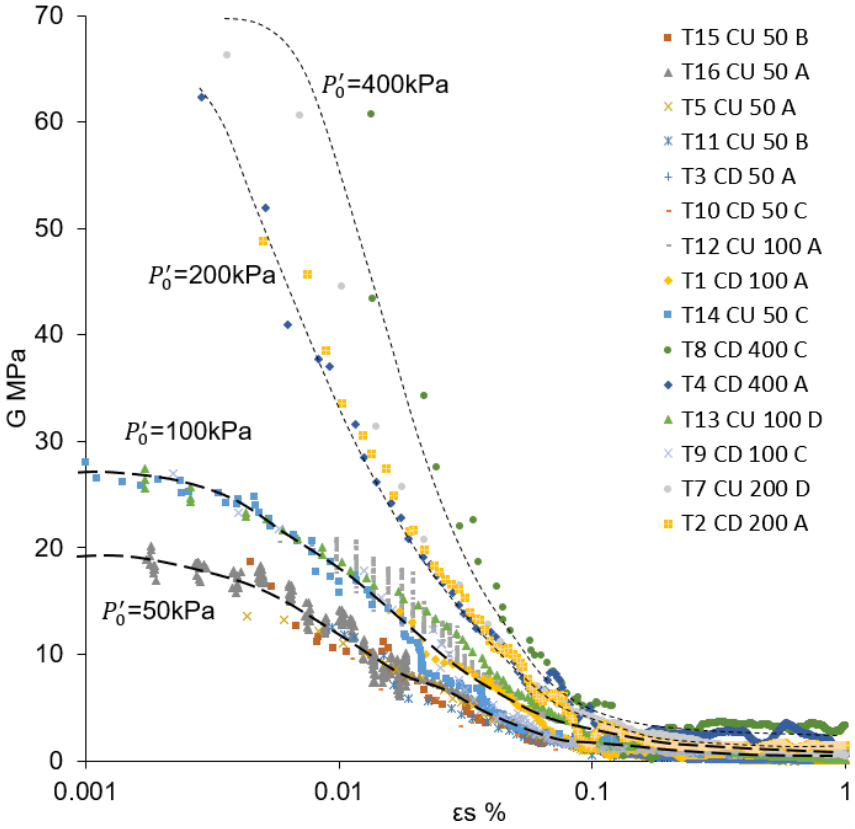

Figure 5-27 Degradation of stiffness of fine tailings for tests under various effective confining stresses.

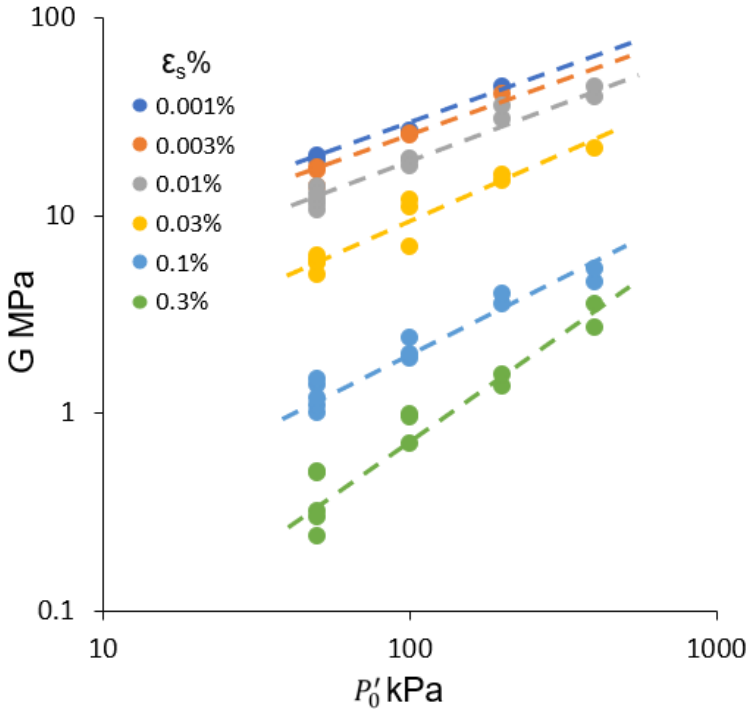

Figure 5-28 The variation of stiffness for each strain level for fine tailings.

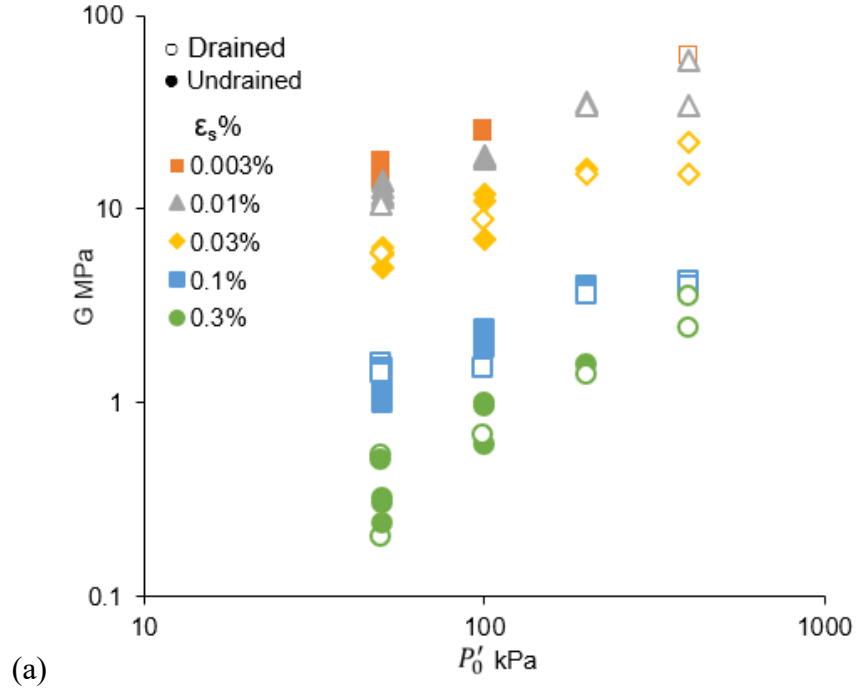

(a)

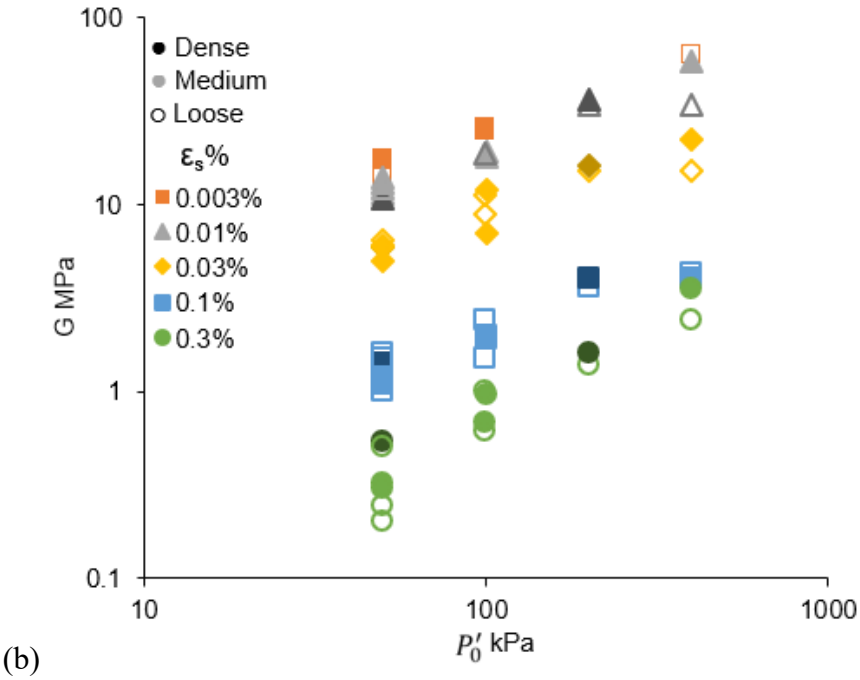

(b)

Figure 5-29 (a) comparison of stiffness between the drained and undrained tests of fine tailings; (b) effect of initial density on stiffness of fine tailings.

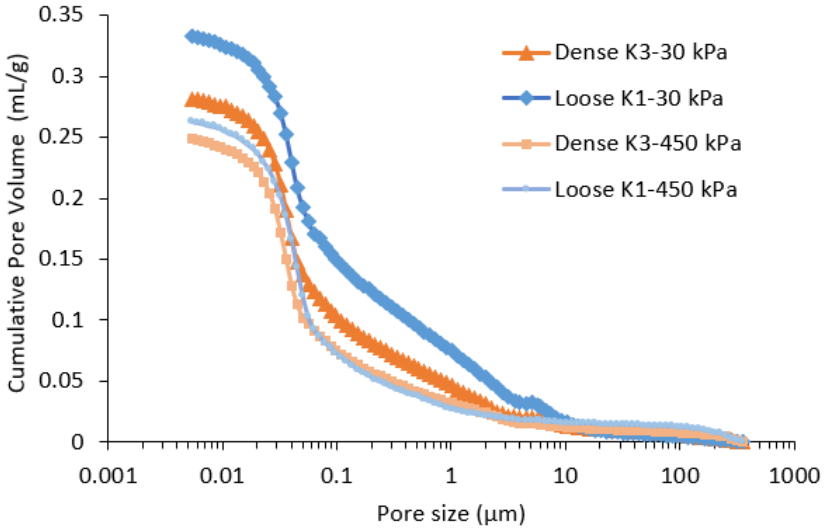

Figure 5-30 Pore size distributions for loose and dense samples of fine tailings from mercury intrusion porosimetry (MIP) tests.

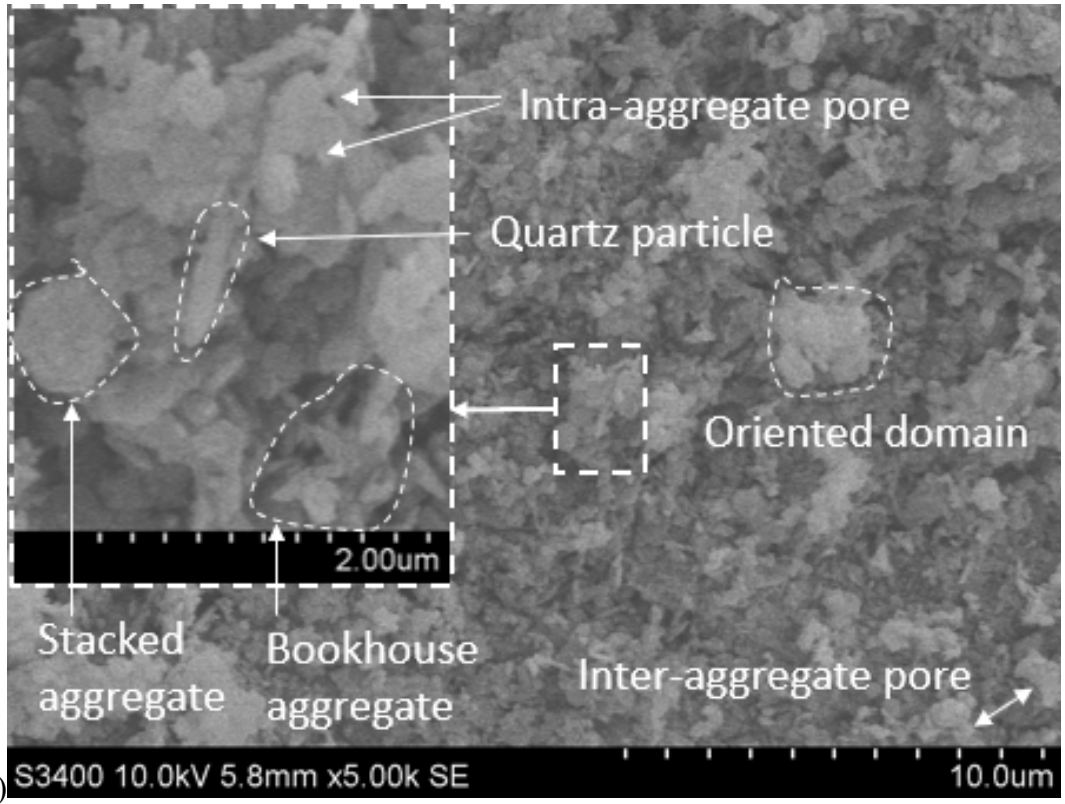
Intra-aggregate pore
Quartz particle
Oriented domain
2.00um
Stacked aggregate
Bookhouse aggregate
Inter-aggregate pore
S3400 10.0kV 5.8mm x5.00k SE
10.0um

(a)

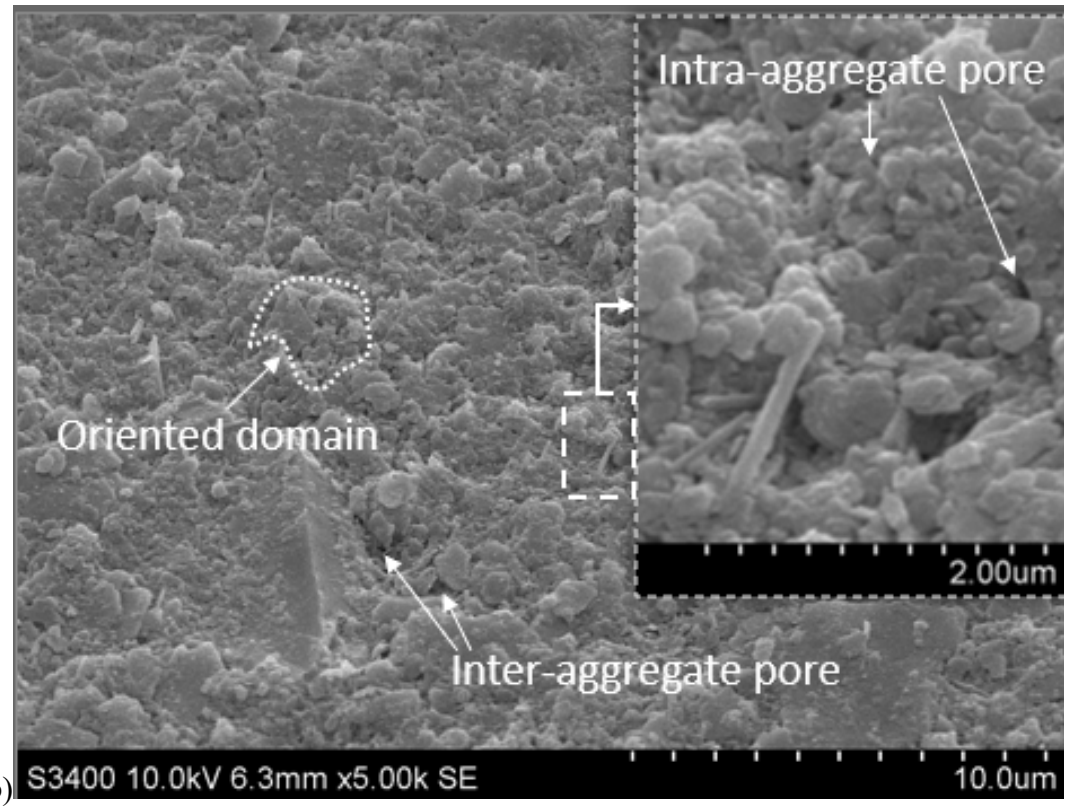
Intra-aggregate pore
Oriented domain
2.00um
Inter-aggregate pore
S3400 10.0kV 6.3mm x5.00k SE
10.0um

(b)

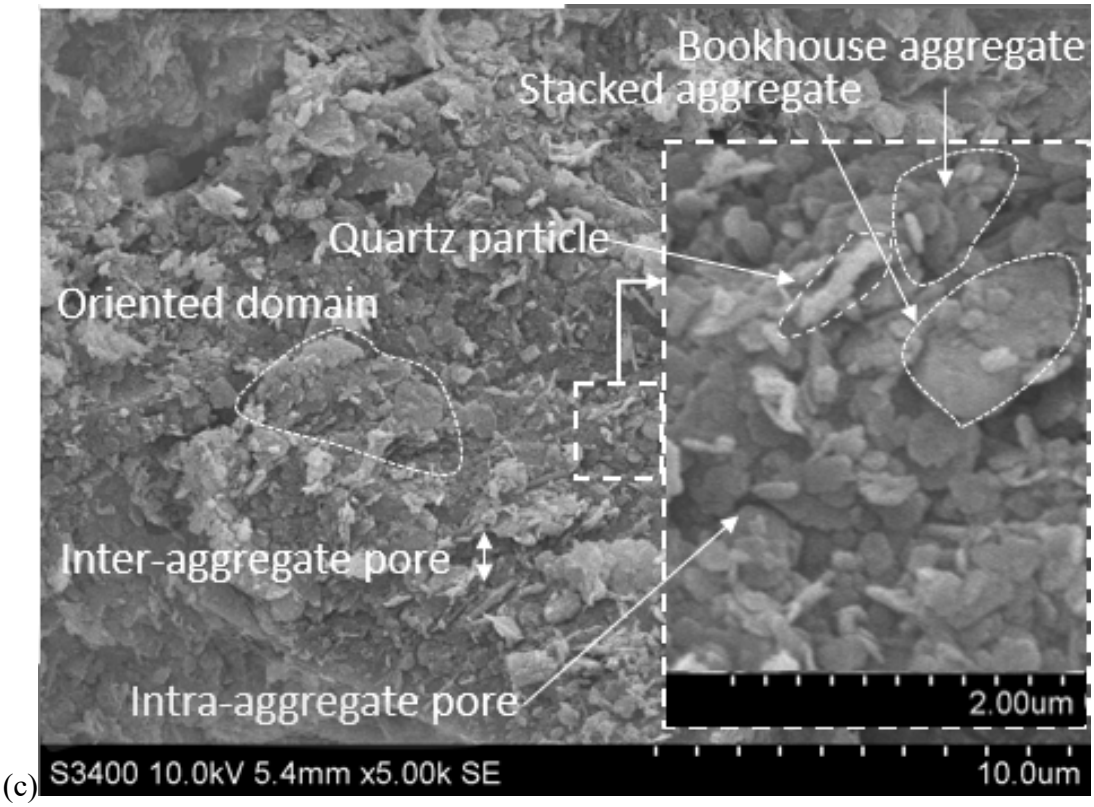

(c)

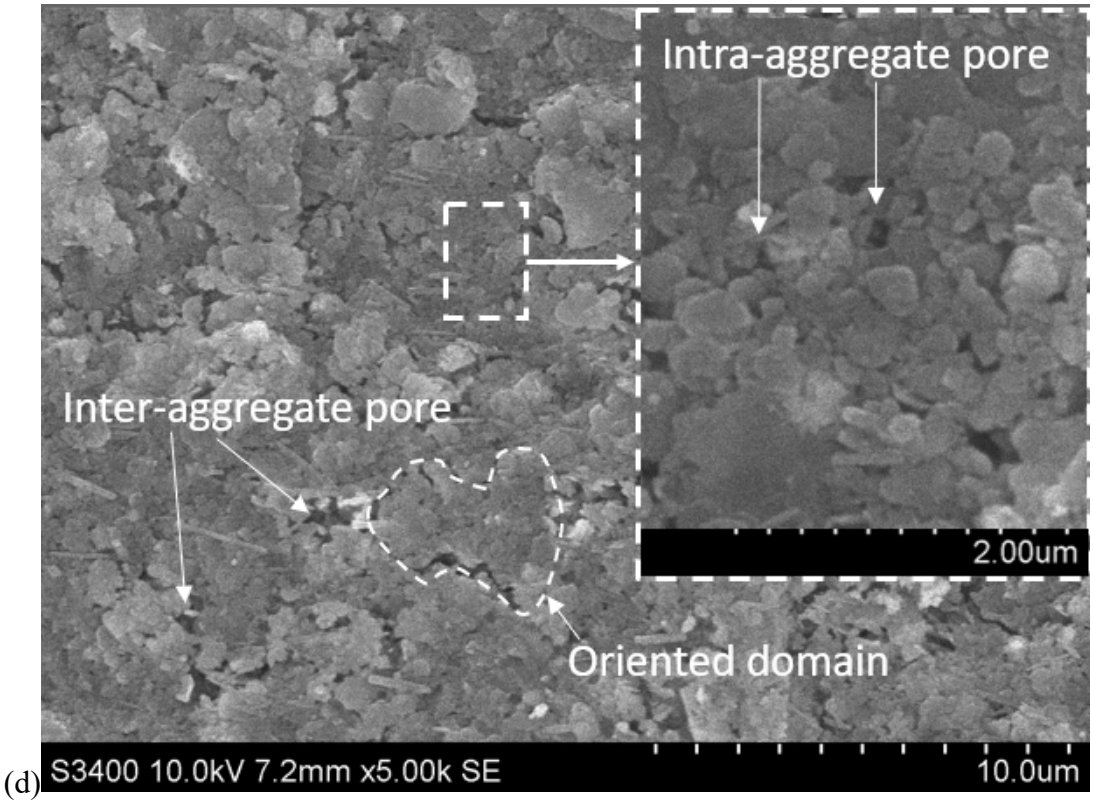

(d)

Figure 5-31 SEM images of vertically orientated samples after triaxial k_0 compression: loose sample K1compressed to (a) 30 kPa and (b) 450 kPa effective stress; dense K3 sample compressed to (c) 30 kPa and (d) 450 kPa effective stress.

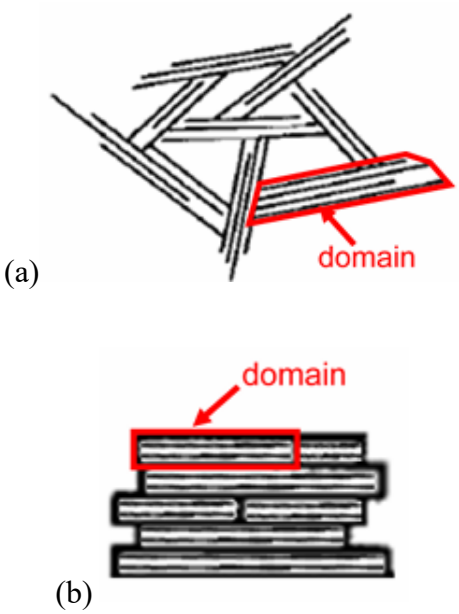

Figure 5-32 Schematic of clay structures: (a) bookhouse domains and (b) stack domains (Guglielmi et al., 2022).

CHAPTER 6 ANALYSIS OF UNSATURATED TESTS

6.1 Introduction

This chapter presents the results of unsaturated tests conducted on transitional soils to investigate their mechanical behaviour under unsaturated conditions. Following the identification of transitional behaviour in saturated soils, this chapter explores whether similar characteristics persist in the unsaturated state. The unsaturated testing programme includes filter paper tests to determine the Soil Water Retention Curves (SWRCs) in Section 6.2, which were used to guide the selection of suitable materials and sample preparation methods. Based on the SWRCs, loess and sandy tailings were selected for unsaturated triaxial tests, and fine tailings and kaolin-sand mixtures were excluded due to their high air-entry values. Unsaturated triaxial tests involved suction equilibration, constant suction isotropic compression, and constant water content shearing. The results of the unsaturated triaxial tests were analysed within the unsaturated critical state framework in Section 6.3 and Section 6.4 for loess and sandy tailings, respectively.

6.2 Filter paper results

As mentioned in Section 4.2, filter paper tests were conducted to determine the Soil Water Retention Curve (SWRC). These SWRCs were used to select soils with a wide range of suction states between the AEV and 500 kPa, corresponding to the operational range of the unsaturated triaxial equipment. The soils tested included loess, a mixture of kaolin and sand, fine tailings, and sandy tailings. Also, the outcomes of the SWRCs helped to guide the selection of appropriate sample preparation methods for the unsaturated triaxial tests. For the sample preparation, unsaturated samples with a wide range of v_i can be achieved by compressing the soil at different w_i to the same stress

level, or by compressing soil at the same w_i to different stress levels, followed by wetting or drying to a desired S_r. However, Fredlund and Rahardjo (1993) stated that both methods cannot produce identical soils with different v_i due to the impact of compaction procedures on soil structure. The SWRCs were used to assess this influence, and the results informed the final decisions on the unsaturated sample preparation for unsaturated triaxial tests. Ultimately, the SWRCs were used in the following section to estimate the water content corresponding to the specific target suction values.

6.2.1 Fine tailings

The fine tailings used in saturated tests were initially considered for the unsaturated tests. The influence of w_i on soil structure was studied. Two samples for the filter paper tests were prepared in oedometer tests using the slurry preparation method. The sample properties at different states are summarised in Table 6-1. Samples were prepared at different w_i, one higher than the liquid limit (49.9%) at around 87% and another in between the liquid limit and plastic limit (21.9%) at around 38%, so the drier sample was slightly unsaturated initially. The samples were then compressed to reach a similar final specific volume (v=1.9), corresponding to a dense sample in the saturated tests. This was achieved by applying different vertical pressures, 200kPa for the wetter sample and 50kPa for the drier one. Although the denser initial drier sample remained slightly unsaturated with a degree of saturation S_r=93%, both samples reached similar final water contents. These two samples were then continually dried to different S_r for each filter paper test, so the determined SWRCs represent the main drying curve.

This static compaction method described above is commonly used to produce dense samples but typically results in uncontrolled over-consolidation. It was found by Shipton and Coop (2015) that for a saturated transitional soil, over-consolidation from the same initial specific volume did not affect the locations of NCL and CSL, as both

were solely dependent on their initial specific volume prior to over-consolidation. In earlier saturated tests in Chapter 5, the intention of sample preparation was to prepare samples with varying v_i, making this static compaction method unsuitable for that purpose. Here, however, this method is used only to study the effect of w_i.

The results of the filter paper tests on fine tailings are presented in Figure 6-1. Approximately 16% volumetric strain occurred during desaturation, resulting in a reduction of the v from about 1.9 to 1.6 due to volume shrinkage. This highlights the difficulty of preparing unsaturated samples with a desired v using the slurry method. An alternative sample preparation method should therefore be considered to address this limitation. The results also show that the two samples with similar v, despite being prepared with very different w_i, exhibit similar changes in S_r and w during desaturation. The only notablely difference between them is a slight variation in volume change. These results suggest that the v of the sample is the dominant influencing factor for the SWRC probably, reflecting a similar soil structure. The w_i used in sample preparation has limited influence on the SWRC and only a minor effect on the extent of shrinkage during desaturation. Additionally, it is found that the air entry value (AEV) of the dense fine tailings sample is about 2000kPa, making fine tailings unsuitable for the unsaturated triaxial tests with the modified triaxial apparatus.

6.2.2 Sandy tailings

To decrease the AEV of the fine tailings, tailings sand from the same location as the fine tailings was added to produce sandy tailings. Different mixtures were tested to identify a material with a suction range suitable for unsaturated triaxial tests under the suction limit of 500kPa. The tested combinations included 75% sand with 25% fine (75ST), 60% sand with 40% fine (60ST), and 50% sand with 50% fine (50ST). After selecting the most appropriate mixture, the effect of density on the SWRC was

investigated, following the finding for the fine tailings that the v of the sample is the dominant influencing factor of the SWRC. To accelerate the filter paper tests, individual samples were used, instead of continually drying a single sample. Since all individual samples for each SWRC were prepared using the same sample preparation method, their soil structure is considered consistent.

To reduce the extent of shrinkage during desaturation, as discussed in Section 2.4.2, the compaction method described in Section 3.3.2 was used instead of the slurry method. In this method, the w_i was kept below the liquid limit, resulting in unsaturated compacted samples. For the component trial tests, the w_i was adjusted for each of the three mixtures to achieve a similar specific volume, based on the finding from the fine tailings that the v of the sample is the dominant influencing factor of the SWRC. A target specific volume of $v = 1.48$ was selected, corresponding to a loose density state in the saturated tests, with a degree of saturation around 82%. The water content value used varies from 8.44% to 12.87% across these three different mixtures, as summarised in Table 6-2. About six compacted samples were prepared for each mixture to construct the SWRC. As the samples were dried to specific S_r, the resulting SWRCs are the main drying curves.

The results of component trial tests are shown in Figure 6-2. The v of samples prepared using the compaction method during desaturation shows no clear trend. The scatter in v value is likely due to sample disturbance. This is supported by the observation that the 50ST samples with the lowest sand content show the greatest consistency in v and closely align with the v_i. In contrast, the 75ST sample with the highest sand content produced the most incoherent samples, making them more susceptible to volume disturbance. Overall, the results demonstrate better control of v using the compaction

method compared to the slurry method. The 75ST samples exhibit poor coherence, making them unsuitable for sample preparation in triaxial tests. The 50ST samples appeared to have an AEV around 100kPa, which would make them nearly saturated at the planned unsaturated tests with suction of around 100kPa. The 60ST samples show a wide range of suction state between their AEV and 500 kPa and were therefore selected for subsequent tests.

The effect of density on the SWRC for the 60ST sample was further studied. The same compaction method was used, with adjustments of the w_i to achieve a wide range of v_i, as summarised in Table 6-2. The initial S_r varied significantly among the three different densities, 83% for the dense 60ST1 sample, 43% for medium-density 60ST3 sample and 26% for loose 60ST2 sample. As a result, the 60ST1 sample follows the main drying curve of its SWRCs, while the 60ST2 sample follows the main wetting curve. The 60ST3 sample, prepared at an intermediate saturation, follows a scanning curve. The results are presented in Figure 6-3. Under limited volume change conditions, the changes in w and S_r should be proportional along the suction path, as defined by the relationship $S_r = \frac{wG_s}{e}$. However, the overall pattern of w for three samples does not appear to align with that of S_r. This discrepancy is probably because of the different SWRC branches represented by each sample. But still, the relationship between w and S_r remains consistent within each individual sample. Only the loose 60ST2 samples have a significant change of v during desaturation, likely due to its very loose initial state. In contrast, the 60ST1 and 60ST3 samples show highly consistent v values across all specimens. These indicate the sample preparation method is effective for this material. Regarding the SWRCs, they all have a workable suction range between their AEV and 500 kPa. Therefore, the 60ST samples are considered suitable for the planned unsaturated triaxial tests.

6.2.3 Loess

The loess soil used for saturated tests was considered for use in the unsaturated tests. To evaluate its suitability, two similar dense samples, L1 and L2, were prepared using the slurry method, as summarised in Table 6-3. Both samples had an initial w of approximately 36%, higher than the 29.7% liquid limit of the loess. Then slurry samples were then compressed up to 490 kPa in oedometer tests to reach a v of about 1.70, corresponding to the dense state in saturated tests, with final w around 24%. After compression, the samples were removed from the oedometer rings and dried to S_r of approximately 60% and 55%, respectively, with only minor reductions in v to about 1.67. The measured suction values from filter paper tests were about 45 kPa and 54 kPa, both well below the 500 kPa capacity of the unsaturated triaxial equipment. These results confirm that the loess soil is suitable for use in unsaturated triaxial tests.

Following the decision to adopt the compaction method, compacted loess samples were prepared to investigate the density effect. Three different densities were achieved using w_i ranging from 9.8% to 17.5%, corresponding to initial S_r between 21% to 80%, as detailed in Table 6-3. Similar to the 60ST sandy tailings, the SWRCs for the dense sample L5 and loose sample L3 represent the wetting and drying curves respectively, while the SWRC for the medium-density sample L4 corresponds to a scanning curve. The results of filter paper tests are shown in Figure 6-4. All three samples exhibit very low air entry values (AEVs), each below 10 kPa, allowing a wide suction range below 500 kPa across all densities. In addition, all samples show consistent v values during desaturation. Based on these findings, the loess was selected for further unsaturated triaxial testing.

6.2.4 Mixture of kaolin and sand

The kaolin-sand mixture used in saturated tests was evaluated for its suitability in unsaturated triaxial testing, based on the slurry sample preparation. As shown in Table 6-4, two slurry samples with the initial w of about 18.8% were compressed to 490 kPa. The final v values were about 1.39, corresponding to a dense state in saturated triaxial tests. Then samples were dried to S_r of about 57% and 79% with v values about 1.37, indicating almost no volume change during desaturation. One sample with v=1.37 had a suction of 1411 kPa at about 60% degree of saturation, and another had 117 kPa at 57% degree of saturation. These high suction values suggest a high AEV, making the mixture unsuitable for the unsaturated equipment with a capacity of 500kPa suction. Since suitable materials such as the sandy tailings and loess had already been identified, further tests on the kaolin–sand mixture were not pursued.

6.3 Unsaturated mechanical behaviour of loess

The net stress $(p - u_a)$ is initially adopted to analyse the unsaturated test data in Section 6.3.2 and Section 6.3.3, focusing on the compression and shearing behaviour within the Barcelona Basic Model (BBM) framework, as introduced in Section 2.4. As mentioned in Section 2.4.3, the choice of appropriate stress variables is crucial for describing constitutive behaviour, and different unsaturated models use different stress variables. To evaluate the influences of the selected stress variable on interpretation within the BBM, the data will be reanalysed using alternative stress variables. Additionally, to assess the suitability of the adopted model, the data will later be reinterpreted using alternative models for comparison. These analyses will be presented in Section 6.3.4.

6.3.1 Specimens and test programme

Three unsaturated triaxial tests were conducted on loess samples with two different initial densities, similar to those of the saturated sample TL1 (v_i=2.08) and sample TL3 (v_i=1.69), as described in Section 5.3. Loose samples UL1 and UL3 were prepared with a v_i of around 2.08, while dense UL2 was prepared with v_i=1.68. These compacted samples for the unsaturated tests were prepared using the same w_i as their corresponding saturated tests to achieve comparable v_i values. After sample preparation, the compacted samples were either wetted or dried to reach the estimated water contents corresponding to a suction of 100 kPa, based on the SWRC measured in Section 6.2. The specimens were then installed in the unsaturated triaxial apparatus and allowed to equilibrate at 100 kPa suction. This was followed by constant suction compression and then constant water content shearing. The sample properties, including the w, v and S_r, at different stages of tests are summarised in Table 6-5.

To verify the soil states after the suction equilibrium stage, the calculated soil properties are superimposed on the filter paper results, as shown in Figure 6-4. After suction equilibration, the values of w, S_r and v for the loose unsaturated triaxial samples UL1 and UL3 closely matched those of the loose filter paper sample L3. A similar agreement is observed between the dense unsaturated triaxial sample UL2 and the dense filter paper sample L5. This consistency confirms both the accuracy of the filter paper results and the reliability of the unsaturated triaxial testing. Additionally, the similarity in v values between the unsaturated and saturated samples demonstrates the effectiveness of the sample preparation method in achieving comparable initial densities. The close agreement in w, S_r and v between the loose samples UL1 and UL3 also indicates that the sample preparation method is repeatable and the resulting soil structure is representative.

6.3.2 Constant suction isotropic compression

Volumetric behaviour

The results of constant suction isotropic compression are shown in Figure 6-5, and the compression. As shown in Figure 6-5 (a), the loose unsaturated sample UL1 reaches its Normal Compression Line under 100 kPa suction ($NCL_{s=100}$) after yielding at around 180 kPa. The compression stopped at around 550 kPa net mean stress, due to the limited stress capacity of the triaxial system. Another loose unsaturated sample UL3 was deliberately stopped before reaching its yield point to observe potential differences in shearing behaviour compared to sample UL1. It exhibited a compression line closely aligned with that of UL1 in $v - ln(p - u_a)$ plane. The detailed percentage of total volume change for both tests is shown in Figure 6-5 (b), showing only a small difference between two tests. The consistent volumetric behaviour of UL1 and UL3 validates the reliability of the total volume change measurement.

The dense unsaturated sample UL2 does not appear to have reached its $NCL_{s=100}$, as no distinct yield point in compression line is observed in the $v - ln(p - u_a)$ plane. However, a gradual and steady volume reduction from 200 kPa to 550 kPa is already shown in the $vol\% - ln(p - u_a)$ plane, indicating that the yield point may be approaching soon. This suggests that the compression line of dense sample UL2 should not converge with the $NCL_{s=100}$ of the loose sample UL1, but instead is likely to follow its own $NCL_{s=100}$. The presence of non-unique $NCL_{s=100}$ demonstrates transitional behaviour in this unsaturated loess soil, consistent with that observed in the saturated tests.

The compression behaviour of the saturated samples is superimposed on that of the unsaturated samples with comparable initial densities in the $v - ln(p - u_a)$ plane. The

unsaturated samples exhibit significantly lower compressibility than the saturated samples. As discussed in Section 2.4, the BBM defines a unique NCL_s for each suction value in the $v - ln(p - u_a)$ plane, which shifts upward and becomes progressively flatter as suction increases. However, in this study, the $NCL_{s=100}$ of the loose sample UL1 is slightly steeper than the saturated NCL of the corresponding loose sample TL1, which differs from the BBM prediction and perhaps relates to the transitional behaviour.

Water content variations

Figure 6-5 (c) and (d) show the corresponding changes in w and S_r during unsaturated constant suction compression, both of which exhibit only slight overall variations. The w decreases in all tests as expected, since water drainage is required to maintain suction under the total volume reduction during compression. Although the loose sample UL1 experiences large volume change, the sample is so dry that a small amount of drainage is enough to maintain the suction. The S_r of loose sample UL1 increases very little as expected, which results from the minimal water loss while there was significant volume reduction. The dense sample UL2 shows an unusual decrease in S_r. It can be explained by its high initial w and limited volumetric change, which leads to a greater reduction in water volume than in total void volume and results in a reduction in S_r.

6.3.3 Constant water content shearing

Volumetric behaviour

The constant water content shearing behaviour is presented in Figure 6-6. As shown in Figure 6-6 (c) and (d), although the dense sample UL2 was stopped at 14% axial strain due to test operation error, both volumetric strain and deviator stress reached nearly stable states. Considering that the other two tests reached stabilisation at about 20%

axial strain, it is acceptable to believe UL2 almost reached the stable volumetric strain and deviator stress.

The volumetric behaviour of the saturated samples with similar initial densities is superimposed onto that of unsaturated samples in the $v - \ln(p - u_a)$ plane, as shown in Figure 6-6 (a). As concluded for transitional fine tailings in Section 5.5, the slope of the saturated Critical State Line (CSL) is expected to be similar to that of the saturated NCL, with the slopes of the NCL decreasing as initial density increases. Therefore, for the saturated loose samples, it is assumed that the slope of CSL is equivalent to that of the corresponding NCL.

As mentioned in Section 2.4, the BBM suggests that a unique Critical State Line exists for each suction value (CSL_s) in the $v - ln(p - u_a)$ plane. Toll (1990) further investigated the unsaturated critical state parameters, based on the expression for the CSL_s as $v = \Gamma_{aw} - \lambda_a \ln(p - u_a) - \lambda_w \ln(u_a - u_w)$. As reviewed in Figure 2-25, the slope of the CSL_s (λ_a) is expected to increase as the S_r decreases, indicating that the λ_a increases with increasing suction. The intercept of the CSL_s is anticipated to be lower than that of the saturated CSL, with a larger suction value leading to a greater reduction in the intercept.

Samples UL1 and UL3 reached quite similar suction values (68 kPa and 80 kPa) and very low S_r values (23% and 21%) at the end of the tests. It is therefore reasonable to plot the CSL_s for a suction of about 75 kPa ($CSL_{s=75}$) for the loose samples based on their end points in the $v - ln(p - u_a)$ plane, as shown in Figure 6-6 (a). Compared with the estimated CSL of the saturated loose sample TL1, the $CSL_{s=75}$ for the loose sample exhibits a steeper slope but a higher intercept. The difference between the

intercept from the result compared with the trend suggested by Toll (1990) may perhaps be attributed to the transitional behaviour.

For the dense sample, the unsaturated test UL2 ended with at S_r of 39% with a final suction of 56 kPa, only slightly lower than those of the two unsaturated loose samples, which reached 68 kPa and 80 kPa, respectively. In conventional unsaturated soils, critical states corresponding to the same suction align along a unique CSL_s in the $v - lnp$ plane. Accordingly, a dense unsaturated sample typically undergo significant dilation to reach this unique CSL_s defined by the loose unsaturated samples. However, the dense sample UL2 exhibited clearly compressive volumetric behaviour, as shown in Figure 6-6 (d), and its critical state point is located far from the $CSL_{s=75}$ in $v - ln(p - u_a)$ plane. This suggests that UL2 follows an individual CSL_s, indicating a clear transitional behaviour similar to that observed under the saturated state.

Although the CSL_s for the dense sample is not identified, its trend can be reasonably estimated. The critical state point of unsaturated dense sample UL2 lies very close to that of the saturated dense sample TL3, with both samples having comparable initial density. Based on the assumption that the CSL_s for unsaturated samples should have a higher slope than the saturated CSL, the intercept of CSL_s for the dense sample is also expected to be higher than that of the saturated dense CSL. This would be consistent with the trend observed for the loose sample.

Since the NCL_s and CSL_s for the unsaturated dense sample are not identified, the traditional methods such as m and P values cannot be applied to quantify the transitional degree. Instead, a direct comparison of the critical states from saturated and unsaturated tests with comparable v_i values in the $v - ln(p - u_a)$ plane provides a basic method to compare the transitional degrees under the two conditions. The unsaturated tests UL1

and UL2 exhibit critical state points closed to those of the saturated tests TL1 and TL3, respectively, which had comparable v_i. This observation suggests that the transitional degrees under unsaturated condition is similar to that under saturated states.

Stress-strain behaviour

The BBM suggests that a unique Critical State Line exists for each suction value (CSL_s) in the $q-(p-u_a)$ plane. Toll (1990) further investigated the unsaturated critical state parameters, based on the expression for the CSL_s as $q = M_a(p-u_a) + M_w(u_a-u_w)$. As reviewed in Figure 2-25, the suction related factor M_w decreases to 0 as S_r reduces, while the net stress component M_a becomes dominant and higher than that of the saturated CSL, $M_s = M$.

The stress paths of the unsaturated tests are shown in Figure 6-6 (b), compared with the failure envelope of the saturated tests. In the $q-(p-u_a)$ plane, the stress paths of all unsaturated tests are linear with a slope of 1/3, as for the saturated drained tests. The $CSL_{s=75}$ for loose samples UL1 and UL3 lies slightly above the saturated CSL, with an intercept close to 0 and a slope slightly higher than that of the saturated CSL. This observation is consistent with the trends reported by Toll (1990) for the low degrees of saturation. However, for the dense sample UL2, which has a slightly lower suction (56 kPa) and higher S_r (39%) than the two loose samples, its critical state point is located significantly above the $CSL_{s=75}$ for the loose samples.

The fact that the critical points for the unsaturated loose and dense samples do not align differs from the behaviour predicted by both the BBM and Toll (1990), which assume a unique critical state line at constant suction for conventional soil. It is not known why there is this observed difference between unsaturated loose and dense samples but it may result from the influence of initial density on transitional behaviour in unsaturated

states, while such density effects are not observed in the saturated state for this loess in the $q-(p-u_a)$ plane.

Figure 6-6 (c) shows that all three samples experience strain hardening. The dense sample UL2, compressed to 550 kPa, reaches the highest shear strength and displays the steepest stress-strain curve. In contrast, the loose sample UL3, compressed to 150 kPa, reaches the lowest shear strength with the slowest rate of increase. This suggests that both higher initial density and greater net confining stress contribute to increased strength and stiffness, highlighting clear effects of both initial density and confining stress.

Figure 6-6 (d) shows that all samples undergo compressive volumetric behaviour, resulting in a reduction in total void volume. Due to the constant water volume during shearing, S_r values increase continuously for all samples, as shown in Figure 6-6 (e). For conventional unsaturated soils, as discussed above, dense samples typically dilate during shearing, leading to an increase in total volume and a corresponding decrease in the S_r. However, this does not occur in the dense sample UL2, which mirrors the saturated condition and further confirms the presence of transitional behaviour.

Suction variations

The matric suctions for all samples are as shown in Figure 6-6 (f). As expected, all samples exhibit a reduction in suction due to the increase in S_r. However, the looser samples (UL1 and UL3) show a smaller reduction compared to the denser sample (UL2). This is because the looser samples with lower S_r values lie in the less sensitive region of the SWRCs, where suction changes less for a given increase in S_r. For the samples subjected to higher net confining stress (UL1 and UL2), the suction initially decreases but subsequently increases slightly after reaching a minimum value, especially the

dense sample UL2. In contrast, the sample under lower net confining stress (UL3) shows a continuous slight decrease in suction. The difference in suction response is likely attributable to differences in mechanical response under varying confining stresses.

State boundary surface

As mentioned in Section 2.6, the effect of structure is often assessed using state boundary surfaces (SBSs), which are the stress paths normalised by the NCL or CSL of the reconstituted soils. This normalisation method was used to study the transitional behaviour of the saturated soils in Section 5.5. A similar method is adopted here to examine the effects of suction for unsaturated behaviour on transitional soil. Normalisation for the unsaturated soils is performed relative to their corresponding CSL_s, while normalisation for the saturated soils with similar initial densities is based on their saturated CSL. After normalisation by the critical state parameters of the CSL (p_{cs}) and critical state stress ratio (M), the normalised stress paths converge to the same CSL point at (1,1), as shown in Figure 6-7.

For the saturated SBS, the normalised stress paths clearly define a Hvorslev surface from the highly over-consolidated TL3 sample and a Roscoe surface from the normally consolidated TL2 sample. The slightly over-consolidated TL1 sample fits well within the saturated SBS. The initial normalised effective stress p'/p'_{cs} of the saturated SBS is located at approximately 3.7. This value is higher than the typical value of around 2 observed in many clays, but it is consistent with values reported for loess by Xu and Coop (2017), 2.5 for a clayey loess and 3.4 for a silty loess.

The normalised unsaturated stress path of sample UL1 defines the unsaturated SBS, with an initial normalised net stress $(p-u_a)/(p-u_a)_{cs}$=6.3, reflecting the shearing

path from the $NCL_{s=100}$ to the $CSL_{s=75}$. The unsaturated UL3 sample exhibits an initial $(p-u_a)/(p-u_a)_{cs}$ less than 6.3 and a normalised stress path within the defined unsaturated SBS, because UL3 did not reach the NCL_s before shearing. Since the dense sample UL2 did not reach its NCL_s prior to shearing, the SBS for the dense sample could not be identified.

The effect of suction is highlighted by the comparison between the unsaturated and saturated SBSs. It is evident that the spacing between the unsaturated NCL and CSL is larger than that of the saturated case, reflecting the influence of suction. However, the unsaturated SBS exhibits a similar shape, including an apex, to that of the saturated SBS. This indicates that suction primarily expands the scale of the SBS without changing its shape.

6.3.4 Data reinterpretation

The choice of appropriate stress variables is crucial for accurately describing constitutive behaviour. The unsaturated soil mechanics analysis presented above was conducted using net stress, following the BBM and the modified unsaturated critical state framework. As introduced in Section 2.4, several other stress variables have been proposed for the analysis of unsaturated soil mechanics. To evaluate whether the choice of stress variable influences the critical state behaviour, the data are reinterpreted using two popular stress variables, Bishop stress (p^*) and stress with Khalili and Khabbaz's factor (p^{χ}). Additionally, the extended Mohr-Coulomb failure envelope is plotted to assess its consistency with the unsaturated critical state framework.

Bishop stress and Khalili and Khabbaz's factor

The data reinterpreted using the Bishop stress $p^*$are shown in Figure 6-8 (a) and (c) for volumetric behaviour and critical state shear stress ratio, respectively. The calculation

of p^* follows Equation 6-1, where S_r is used as the weighting factor for suction. As shown in Figure 6-6 (e) and (f), the S_r and suction at critical state for the unsaturated loose and dense samples are about 20% or 40% and 60 kPa or 80 kPa, respectively. Accordingly, the suction contribution to p^* is about 25 kPa for the loose sample and 16 kPa for dense samples. Given that the net stress levels reach up to about 1000 kPa, the suction contribution to p^* is relatively small. As a result, the location and shape of the NCL and CSL in the $v - ln\, p^*$ plane as well as the location of the critical state stress ratio in the $q - p^*$ plane are very similar to those based on net stress ($p - u_a$) shown in Figure 6-6 (a) and (b).

The calculation for the effective stress based on the Khalili and Khabbaz's factor (χ) is based on Equation 6-2, where S_e is the air entry value. The corresponding volumetric behaviour and critical state shear stress ratio are presented in Figure 6-8 (b) and (c). As shown in Figure 6-4 (a), the air entry values for all loess samples are about 5-10 kPa, resulting in χ values of about 0.19-0.28. Consequently, a suction of 100 kPa contributes about 25 kPa to p^{χ}, which is a relatively small portion compared to the net stress reached at around 1000kPa. Therefore, similar to the case with Bishop's stress, the influence of the χ factor on the data analysis is minimal compared to that of the net stress.

$$p^* = (p - u_a) + S_r(u_a - u_w) \qquad \text{Equation 6-1}$$

$$p^{\chi} = (p - u_a) + \chi(u_a - u_w)$$

$$\text{where } \chi = \begin{cases} 1, & for\ s \le S_e \\ (s_e/s)^{\gamma}, & for\ s \ge S_e, and\ \gamma = 0.55 \end{cases} \qquad \text{Equation 6-2}$$

The main difference in the mechanical behaviour is observed primarily at the starting points of the compression lines in the $v - \ln(p - u_a)$ plane. The similarity in the position and shape of NCL and CSL lines based on Bishop stress and χ factor compared to those based on net stress results from the small contribution of suction under high net stress conditions, regardless of the expression of the weighting factor. High net stress conditions were necessary to examine the convergence of NCLs and CSLs to study the transitional behaviour. This indicates that the choice of effective stress has minimal influence on the description of the unsaturated critical state framework at high stress level and low suction condition.

Extended Mohr-Coulomb failure envelope

The equation for the extended Mohr-Coulomb failure envelope (FE) is $\tau = c' + (\sigma - u_a)\tan\varphi^a + (u_a - u_w)\tan\varphi^b$, and the corresponding plot for this study is shown in Figure 6-8 (d). The FE for the saturated tests exhibits an intercept of $c' = 0$ and a friction angle associated with the net normal stress of $\varphi^a = \varphi' = 32.4°$. This is very close to the FE of loose unsaturated samples under a suction of 75kPa, which has a similar $\varphi^a = \varphi'$ value and friction angle related to matric suction $\varphi^b = 10.6°$. Assuming the same φ^a value as the saturated case, following Fredlund et al. (1978) and Toll (2000), the FE for the dense sample under 75kPa has $\varphi^b = 45.6°$, which is much larger compared to the loose unsaturated samples. The relationships between these FE in the Mohr-Coulomb model are very consistent with the CSL observed in the critical state framework shown in Figure 6-6 (b). This confirms the conclusion regarding the density effect on CSLs for unsaturated transitional loess, which is not observed in the saturated state.

6.3.5 Microstructure

One loose and one dense unsaturated samples, UL1 and UL2, were preserved after constant suction compression and constant water content shearing, ending with suction values of 68 kPa and 56 kPa, respectively. For conventional soils, unsaturated soils are expected to follow a unique CSL for each suction value. However, for this transitional loess as shown in Figure 6-6 (a), the critical states of UL1 and UL2 samples exhibit similar net stress but different v under comparable suction values, indicating non-unique CSLs for them. The microstructural differences responsible for the non-convergent volumetric behaviour between UL1 and UL2 samples are further investigated through MIP and SEM tests. Unfortunately, the microstructural differences between saturated and unsaturated samples cannot be directly compared using the existing data. This is because the unsaturated samples experienced shearing stages but the saturated samples only experienced compression.

MIP tests

The pore size distributions (PSDs) from the MIP tests are shown in Figure 6-9. Four dominant pore sizes can be observed from the peak values in the differential PSDs. The system transition from low to high pressure coincides with the position of peak 2. This transfer typically causes a temporary lag in mercury intrusion, resulting in an artificial dip between peak 2 and peak 3, although the cumulative intrusion volume remains accurate. Therefore, it is highly likely that the peak 3 should connect more smoothly to peak 2 without the artificial dip in between.

The cumulative PSDs show that the loose sample UL1 exhibits a higher total mercury intrusion compared to dense sample UL2 across all pore size ranges, indicating a more open structure. This also means a greater v for UL1, which is consistent with the measurements. The corresponding differential PSD reveals that both samples exhibit a

multi-modal pore structure, with dominant pore sizes at 200μm, 6μm, 3μm and 0.2μm. The difference between the two samples is pronounced in each peak, especially at peak 2. Given the well-distributed silty particle size, the dominant pores at 200μm, 6μm and 3μm, and 0.2μm are likely to reflect large inter-aggregate pores, medium and small inter-aggregate pores, and intra-aggregate pores, respectively, which will be further clarified and discussed with the SEM tests. The main differences between the two samples are that the loose sample UL1 contains more inter-aggregate pores at 200μm and 6μm and the smaller intra-aggregate pores at 0.2μm.

The higher pore volume retained by the loose UL1 sample confirms the persistence of structural differences even after compression and shearing. This supports the non-convergent volumetric behaviour observed in the mechanical response. It suggests that the transitional behaviour is likely linked to the incomplete breakdown of the original microstructure, particularly in pores around 6μm.

SEM tests

SEM images on the loose (UL1) and dense (UL2) unsaturated samples are shown in Figure 6-10. The silt particles in both samples appear closely packed with some inter-particle pores, particularly in the loose sample. Clay aggregates are observed coating the silt grains in both samples, but their structures differ significantly between the two samples. In the dense sample UL2, the clay aggregates appear more compacted and aligned, but the loose sample UL1 shows clay aggregates arranged more randomly and loosely. These microstructural differences directly correspond to the observations from the MIP tests. UL1 retained higher volumes of inter-aggregate pores, particularly at 6 μm. The preservation of these structural differences explains the non-convergent volumetric behaviour observed in the mechanical tests.

6.4 Unsaturated mechanical behaviour of sandy tailings

6.4.1 Specimens and test programme

Three unsaturated triaxial tests were conducted on sandy tailings with three different initial densities, corresponding to the three saturated samples introduced in Section 5.4. The unsaturated tests consisted of three main stages, including suction equilibration, constant suction isotropic compression, and constant water content shearing. Detailed sample properties, including the w, v and S_r, at different stages are summarised in Table 6-6.

The unsaturated samples were prepared using the same compaction method with the same w_i as their respective saturated samples in order to reach comparable v_i values. After compaction, the samples were either wetted or dried to reach the estimated water contents corresponding to a suction of 100 kPa, based on the SWRC measured in Section 6.2. Following suction equilibration at 100 kPa, the loose sample UST3, medium-dense sample UST1 and dense sample UST2 reached v_i values of around 1.78, 1.64 and 1.37. Due to these differences in v_i, their S_r varied significantly, ranging from 31.2% to 70.3%.

To validate the sample conditions after suction equilibrium, the soil properties were compared with the filter paper results, as shown in Figure 6-3. As with the loess samples, the measured values of w, S_r and v for the unsaturated sandy tailings closely match those of the filter paper samples. Notably, the dense sample UST2 was deliberately prepared slightly denser than the dense filter paper sample to expand the range of v_i for studying transitional behaviour, which resulted in a slightly higher S_r as expected. This overall agreement supports the accuracy of the filter paper results and confirms the reliability of the unsaturated triaxial testing.

6.4.2 Constant suction isotropic compression

Volumetric behaviour

The constant suction isotropic compression tests were conducted up to 550 kPa again, limited by the pressure capacity of the triaxial system. The results are presented in Figure 6-11. Net stress ($p - u_a$) was adopted for analysing the unsaturated tests, in accordance with the Barcelona Basic Model (BBM). For reference, the compression curves from saturated tests with comparable initial densities are superimposed in Figure 6-11 (a). These saturated tests were isotropically compressed to about 550 kPa, except for the dense sample TST1, which was unloaded after being compressed to that stress level. A clear transitional behaviour is observed through their individual saturated NCLs.

To evaluate transitional behaviour in the unsaturated state, the Normal Compression Lines at a constant suction of 100 kPa ($NCL_{s=100}$) are compared across different initial densities. As shown in Figure 6-11 (a), the loose and medium-dense unsaturated samples UST3 and UST1 reach their individual $NCL_{s=100}$ after yielding at around 100 kPa and 150 kPa, respectively. According to the BBM, a single unique NCL_s should exist at a given suction level in the $v - ln(p - u_a)$ plane. However, the presence of separate $NCL_{s=100}$ for unsaturated samples UST3 and UST1 demonstrates transitional behaviour in the unsaturated state, consistent with observations from the saturated tests.

The slopes of the $NCL_{s=100}$ for both UST3 and UST1 are steeper than those of the NCLs for their corresponding saturated samples (TST2 and TST3), similar to the behaviour observed in unsaturated loess, as shown in Figure 6-11 (a). This contradicts the BBM framework, which may be attributed to transitional behaviour. The slopes of

these two $NCL_{s=100}$ are similar, just as their corresponding saturated NCLs. The spacing between the parallel $NCL_{s=100}$ is smaller than that of the parallel saturated NCLs. This indicates that the degree of the transitional behaviour during compression under unsaturated conditions is smaller than that in the saturated state. Due to the steeper slope, the $NCL_{s=100}$ of loose sample UST3 slightly crosses the saturated NCL of the loose sample TST2. Therefore, the transitional behaviour observed in their saturated states is still retained in both silty loess and sandy tailings during constant suction isotropic compression.

The dense unsaturated sample UST2 does not exhibit a clear yield point and therefore may not have reached its $NCL_{s=100}$. Nevertheless, its compression curve shows a gradual and steady decrease in volume, as shown in Figure 6-11 (b), suggesting that the yield point may be approaching, similar to the behaviour observed in the unsaturated dense loess sample. This implies that the compression curve of UST2 is unlikely to converge with the $NCL_{s=100}$ of the medium-dense sample UST1, and is instead likely to follow a separate $NCL_{s=100}$, again consistent with transitional soil behaviour.

Water content variations

The changes in w and S_r during constant suction compression are illustrated in Figure 6-11 (c) and (d). In the dense sample UST2, only slight drainage was required to maintain the constant suction due to minimal volume reduction. This led to a slight net decrease in S_r. In contrast, the loose and medium-dense samples UST1 and UST3, which started in drier conditions and experienced more substantial volume compression, absorbed water to maintain constant suction. This water absorption resulted in an increase in their S_r values.

6.4.3 Constant water content shearing

Suction variations

The constant water content shearing behaviour is presented in Figure 6-12. All three unsaturated samples practically reached critical states, as evidenced by reaching the near stabilisation of both stress and volumetric responses in Figure 6-12 (c) and (d). All samples experienced comparable volumetric compression, which led to a decrease in S_r under constant water content conditions. As shown in Figure 6-12 (e) and (f), the loose sample UST3 ended with the highest suction value (130 kPa) and the lowest S_r (83%). The increase in S_r pushed the sample state leftward on the SWRC, resulting in an increase in suction. In contrast, the medium-dense and dense samples UST1 and UST2 reached quite similar final suction values (49 kPa and 32 kPa) and were nearly saturated at the end of shearing (99% and 97%). Their soil states were likely on the portion of the SWRC where small increases in saturation lead to a rapid reduction in suction.

Volumetric behaviour

According to the BBM, a unique CSL_s for each suction value should exist in the $v - ln(p - u_a)$ plane. However, this is not observed in these three tests. As shown in Figure 6-12 (a), medium-dense and dense samples UST1 and UST2 exhibit distinctly different critical state points, despite having quite similar final suction values (49 kPa and 32 kPa). Since their critical states are far apart, these two critical states are likely to lie on separate CSL_s, indicating transitional behaviour. Meanwhile, the loose and medium-dense samples UST3 and UST1 reached their critical states at significantly different suction values (131 kPa and 49 kPa), but their critical points are located closely. Based on the critical state point at 49 kPa for the medium-dense sample UST1, the critical state point at 131 kPa should be located further upward, and therefore

separate from the critical state point at 131 kPa of the loose sample UST3. This again suggests the presence of non-unique CSL_s for loose and medium-dense samples UST3 and UST1, reinforcing the evidence for the transitional behaviour. Compared with the corresponding saturated tests, the unsaturated samples exhibit significantly greater volume reduction at critical states during shearing, suggesting a smaller degree of transitional behaviour. For the silty loess, as shown in Figure 6-6 (a), due to the over-consolidation of the saturated test, the saturated and unsaturated tests cannot be directly compared, unlike the sandy tailings.

Stress-strain behaviour

In the $q-(p-u_a)$ plane, the critical state points of the unsaturated tests are clearly located above the saturated failure envelope. The BBM suggests that a unique CSL_s exists for each suction value in the $q-(p-u_a)$ plane and that it shifts upward with increasing suction. However, the dense sample UST2 with the lowest suction of 32 kPa lies between medium-dense and loose samples UST3 and UST1, which have higher suctions (131 kPa and 49 kPa). This contradicts the BBM prediction and instead indicates a clear density effect on the location of CSL_s in the $q-(p-u_a)$ plane. This finding is consistent with similar results obtained from the unsaturated tests on the silty loess.

Data reinterpretation

The selection of an appropriate stress variable is crucial for accurately describing the constitutive behaviour. Two widely used stress variables, Bishop stress (p^*) and stress incorporating the Khalili and Khabbaz's factor (p^{χ}), were evaluated for their impact on the critical state behaviour. These two stresses were calculated based on Equation 6-1 and Equation 6-2. Compared with the net stress $(p-u_a)$, as shown in Figure 6-13, the additional contribution from suction on p^* and p^{χ} are limited to maximum values of

about 100 kPa and the 65 kPa, respectively. Given that the net stress reached up to about 1000 kPa, the influence of stress variable choice is minimal. This conclusion is consistent with findings from the unsaturated loess tests and supports the net stress approach for interpreting critical state behaviour in this study.

6.4.4 Microstructure

In conventional soils, unsaturated samples are expected to follow a unique CSL_s for each suction value. However, samples UST1 and UST2 did not converge to the same critical state point, despite having similar final suction values. This indicates distinct volume states and suggests the presence of transitional behaviour. To explore the potential causes for it, MIP and SEM tests were conducted on all three unsaturated samples preserved after shearing.

MIP tests

As shown in Figure 6-14, all three samples exhibit a sharp, dominant peak near 0.03 μm, corresponding to intra-aggregate pores. The alignment of this peak suggests that the smallest pore structures remained relatively consistent across different densities and mechanical histories. However, notable differences are observed in the larger pore range, particularly around 10 μm. Sample UST2 shows a lower overall pore volume compared to UST1 and UST3, mainly resulting from the difference in this larger pore range around 10μm. This reflects a denser microstructure, which aligns with its lower specific volume. Therefore, the non-convergence in volume state between UST1 and UST2 can be attributed to persistent microstructural differences, particularly in pores around 10μm, that were not erased through compression and shearing.

SEM tests

Structural differences among the three unsaturated samples were further examined using SEM, as shown in Figure 6-15. The dense sample UST2 exhibits the most compact and aligned clay aggregates with few intra-aggregate pores. The loose sample UST3 shows the most open clay fabric. The medium-density sample UST1 has clay aggregates that are similarly loose as in UST3, but its inter-aggregate structure appears slightly more compact. These microstructural observations align well with the MIP results. Samples UST1 and UST3 share similar PSDs, with higher pore volumes around 10 μm, indicating the presence of larger inter-aggregate pores. UST2, on the other hand, shows significantly lower pore volume in this range, reflecting a denser structure. The persistence of these structural differences explains why UST1 and UST2, despite having similar final suction values and net stress, did not converge to the same void ratio. These results support the presence of transitional behaviour, where initial density and microstructural conditions continue to influence the critical state. The SEM findings thus reinforce the conclusion that transitional behaviour in this sandy tailings is closely linked to the incomplete breakdown of the original fabric, particularly in inter-aggregate pore ranges.

6.5 Conclusions for unsaturated tests

Unsaturated triaxial tests were successfully conducted on transitional loess and sandy tailings to characterise their mechanical behaviour under unsaturated conditions and to assess the persistence of transitional behaviour identified in saturated states. The main findings are as follows:

- Transitional behaviour was clearly observed in both the unsaturated loess and sandy tailings, as evidenced by the presence of non-unique Normal Compression

Lines (NCLs) and Critical State Lines (CSLs) among samples with similar suctions.

- The slopes of the unsaturated NCLs are steeper than those of the corresponding saturated NCLs in the $v - ln(p - u_a)$ plane for both loess and sandy tailings. In the case of loess, the unsaturated NCL slightly crosses the saturated NCL. The steeper slope of unsaturated NCL and the crossing of the saturated and the unsaturated NCLs contradict the BBM framework, which may be attributed to transitional behaviour.
- The degree of transitional behaviour could not be quantified due to an insufficient number of tests to establish a family of NCLs. However, the degree of transitional behaviour during constant suction compression appears to be smaller than that in the saturated state, as indicated by the narrower spacing between unsaturated NCLs compared to the saturated NCLs.
- Unsaturated CSLs of loess were found to have steeper slopes than their saturated counterparts in the $v - ln(p - u_a)$ plane.
- The degree of transitional behaviour could not be quantified due to an insufficient number of tests to establish a family of CSLs. However, the degree of transitional behaviour during shearing is smaller under unsaturated conditions than under saturated conditions, which results from greater volume reduction for unsaturated sandy tailings.
- An effect of initial density was observed in the $q - (p - u_a)$ stress plane for both loess and sandy tailings, which was not present in their saturated states.
- The choice of stress variable (net stress, Bishop stress, or χ-based stress) had a limited influence on the interpretation of critical state behaviour in both materials. This was because the 100 kPa suction contributed little to the effective stress

compared with around 1000 kPa net stress at critical state, especially on the logarithmic stress scale used to define the NCL and CSL.

The unsaturated mechanical behaviour of loess and sandy tailings provides clear evidence of transitional behaviour, consistent with that observed under saturated states. These findings demonstrate that transitional behaviour in the saturated states persists under unsaturated conditions. This should be considered in critical state modelling and practical engineering assessments of unsaturated soils.

For engineering practice, particularly in the design and maintenance of tailings dams, the increasingly popular dry stacking method for tailings dams, which uses unsaturated tailings, is often assumed to offer greater safety and stability than the conventional upstream method, which uses saturated tailings. It is true that the CSLs for unsaturated tailings are lower than those in the saturated state, suggesting higher shear resistance. However, unsaturated tailings may undergo less volume reduction during construction, which can affect the storage efficiency. Moreover, loose unsaturated soils can become highly unstable if re-saturated by rainfall or additional loading.

Table 6-1 Samples of fine tailings in filter paper tests.

Sample	Slurry		Slurry sample		
	w_i%	Compressed pressure kPa	v	w%	S_r
FT1	87.22	200	1.91	34.49	1.02
FT2	37.87	50	1.89	31.11	0.93

Table 6-2 Samples of sandy tailings for filter paper tests.

Tests	Component	Sample	Compacted sample		
			$\bar{v}$	$\bar{w}$%	$\bar{S_r}$
Component trial	75% sand + 25% fine	75ST	1.54	8.44	0.76
	60% sand + 40% fine	60ST	1.45	10.65	0.83
	50% sand + 50% fine	50ST	1.47	12.87	0.87
Density effect	60% sand + 40% fine	60ST1	1.45	10.78	0.83
	60% sand + 40% fine	60ST3	1.66	10.65	0.43
	60% sand + 40% fine	60ST2	1.91	9.24	0.26

Table 6-3 Samples of loess for filter paper tests.

Sample	Slurry		Slurry sample			Tested sample			
	w_i%	Compressed pressure kPa	v	w%	S_r	v	w%	S_r	Suction kPa
L1	36.54	490	1.71	25.59	0.98	1.68	14.73	0.59	44.84
L2	35.82	490	1.69	23.55	0.94	1.66	13.46	0.55	53.93
Sample			Compacted sample						
			$\bar{v}$	$\bar{w}$%	$\bar{S_r}$				
L3			2.136	9.76	0.21				
L4			1.874	15.16	0.45				
L5			1.755	17.53	0.80				

Table 6-4 Samples of mixture of 25% kaolin and 75% sand for filter paper tests.

Sample	Slurry		Slurry sample			Tested sample			
	w_i%	Compressed pressure kPa	v	w%	S_r	v	w%	S_r	Suction kPa
KS1	18.78	490	1.41	12.07	0.77	1.40	8.59	0.57	1411.43
KS2	18.82	490	1.37	11.61	0.83	1.36	10.75	0.79	117.42

Table 6-5 Sample properties at different stages of unsaturated triaxial tests of loess.

Sample		**UL1**	**UL2**	**UL3**
Sample preparation	$w\%$	9.3	20.0	9.3
Initial sample	$w\%$	6.9	9.9	6.8
	v	2.084	1.683	2.077
	$S_r\%$	17.1	38.6	16.9
After equilibration	$w\%$	7.6	10.4	8.2
	v	2.103	1.687	2.105
	$S_r\%$	17.1	38.1	20.4
After compression	$w\%$	6.8	8.9	7.8
	v	2.007	1.672	2.095
	$S_r\%$	16.4	33.2	19.6
After Shearing	$w\%$	6.8	8.9	7.8
	v	1.753	1.586	1.891
	$S_r\%$	23.3	39.0	22.7

Table 6-6 Sample properties at different stages of unsaturated triaxial tests of sandy tailings.

Sample		**UST1**	**UST2**	**UST3**
Sample preparation	$w\%$	11.3	13.6	9.4
Initial sample	$w\%$	10.3	8.9	7.9
	v	1.635	1.366	1.773
	$S_r\%$	45.2	53.6	27.2
After equilibration	$w\%$	9.33	11.7	9.0
	v	1.635	1.366	1.775
	$S_r\%$	40.9	70.3	31.2
After compression	$w\%$	10.5	10.4	9.5
	v	1.467	1.340	1.523
	$S_r\%$	63.3	66.2	48.9
After Shearing	$w\%$	10.5	10.4	9.5
	v	1.304	1.215	1.312
	$S_r\%$	99.2	96.9	82.6

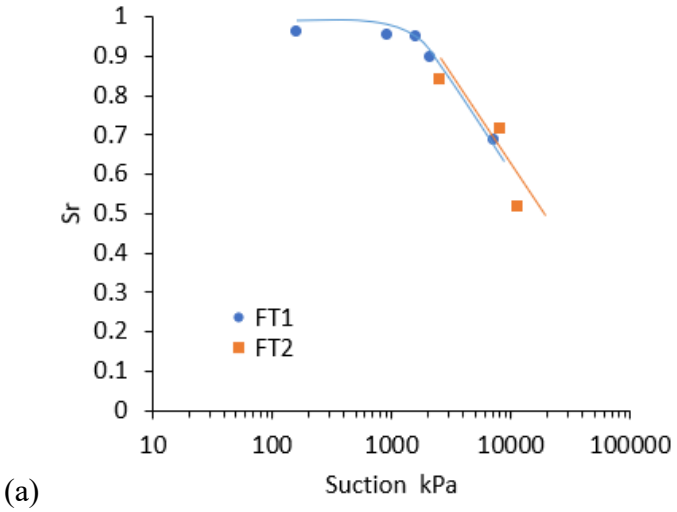

(a)

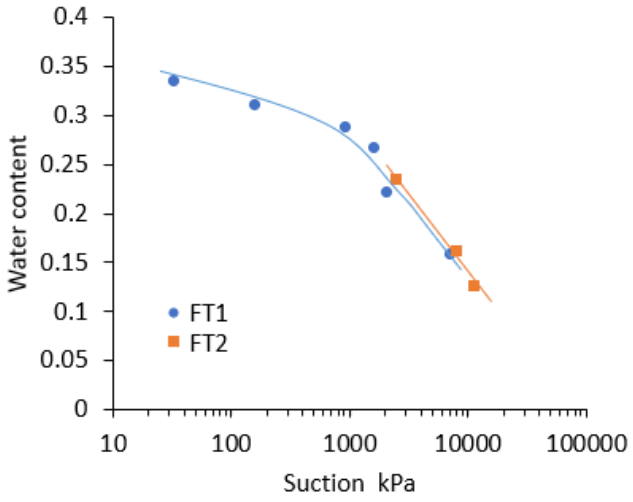

(b)

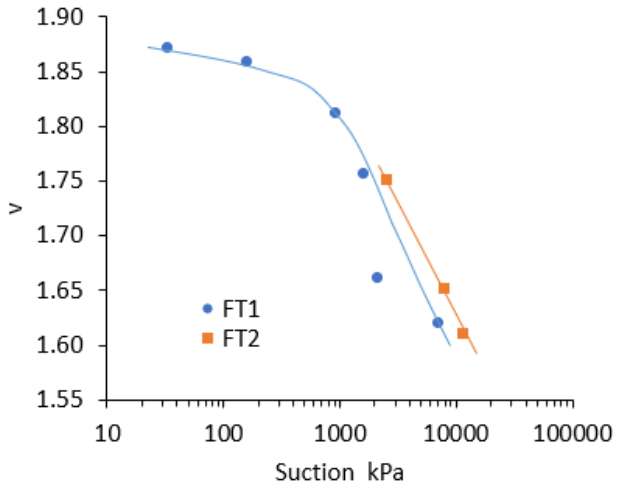

(c)

Figure 6-1 Results of filter paper tests of the fine tailings for two samples prepared at different initial water contents, wetter sample FT1 and drier sample FT2.

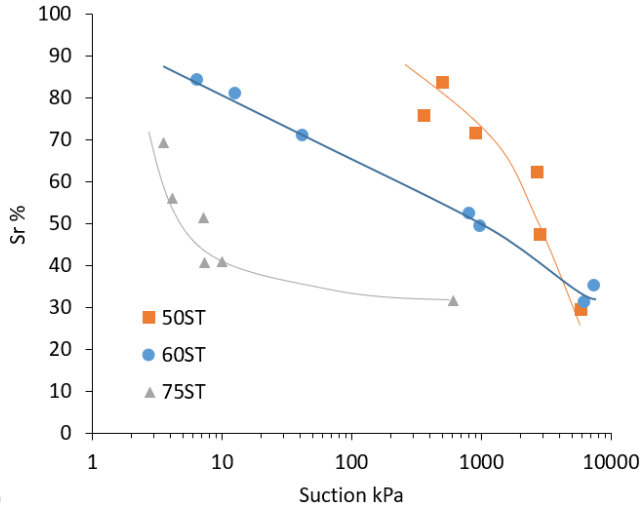

(a)

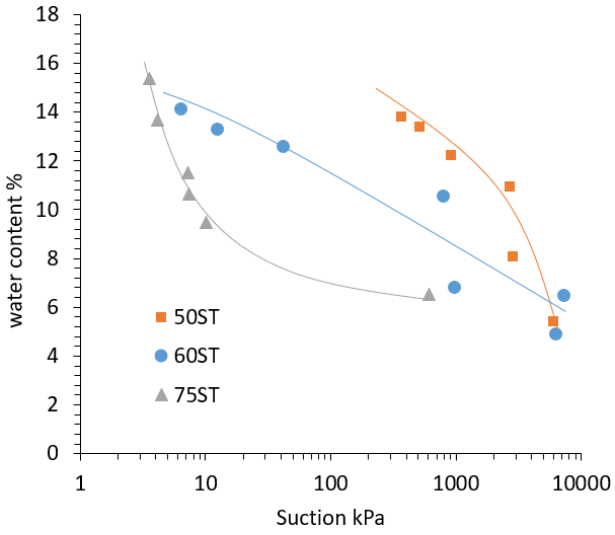

(b)

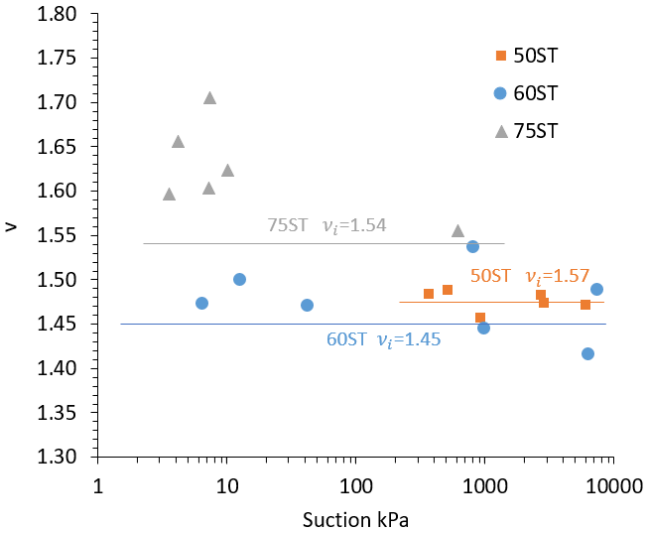

(c)

Figure 6-2 Results of filter paper tests on sandy tailings with 50% sand (50ST), 60% sand (60ST), and 75% sand (75ST) for component trial tests.

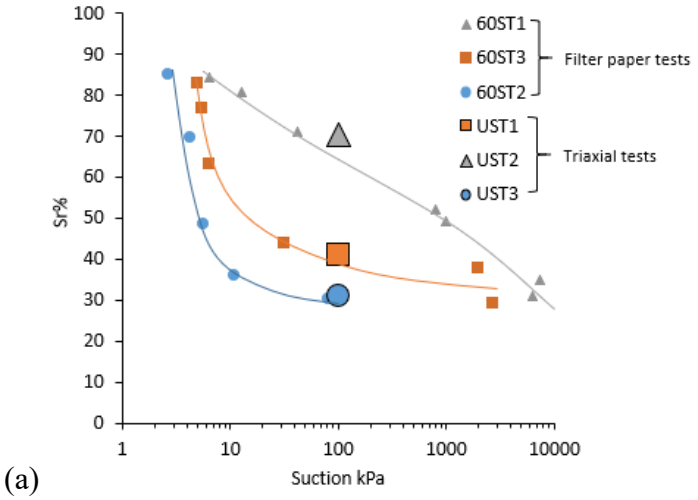

(a)

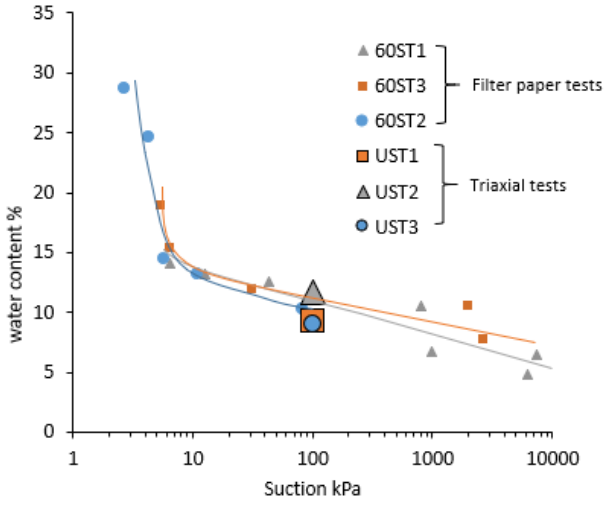

(b)

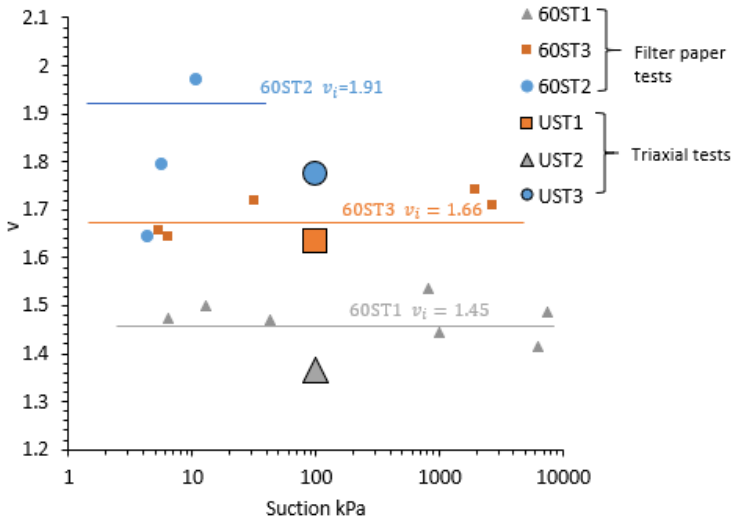

(c)

Figure 6-3 Results of filter paper tests of the sandy tailings with 60% sand (60ST) for density effect tests, including loose sample 60ST2, medium-density sample 60ST3, and dense sample 60ST1.

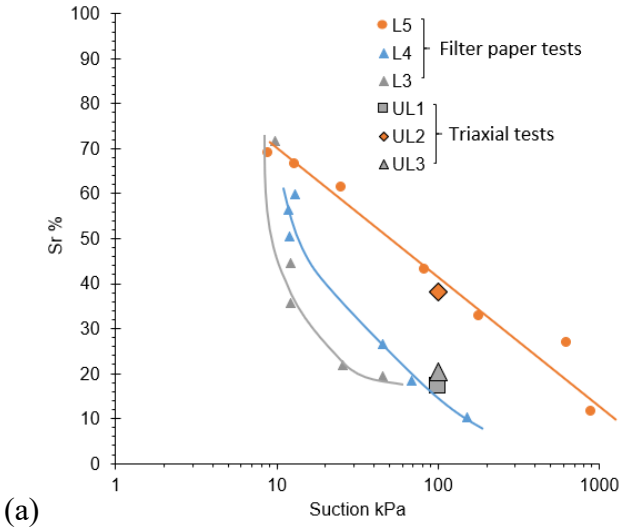

(a)

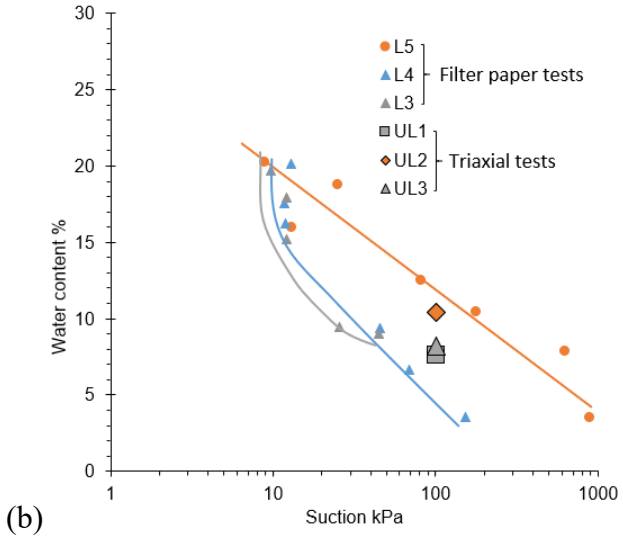

(b)

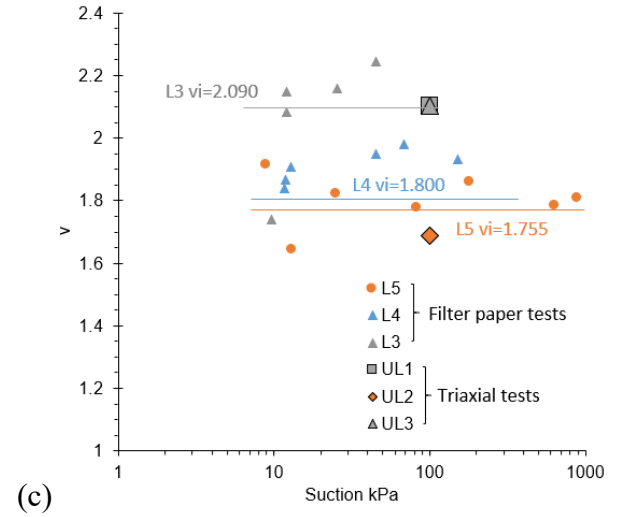

(c)

Figure 6-4 Results of filter paper tests on loess.

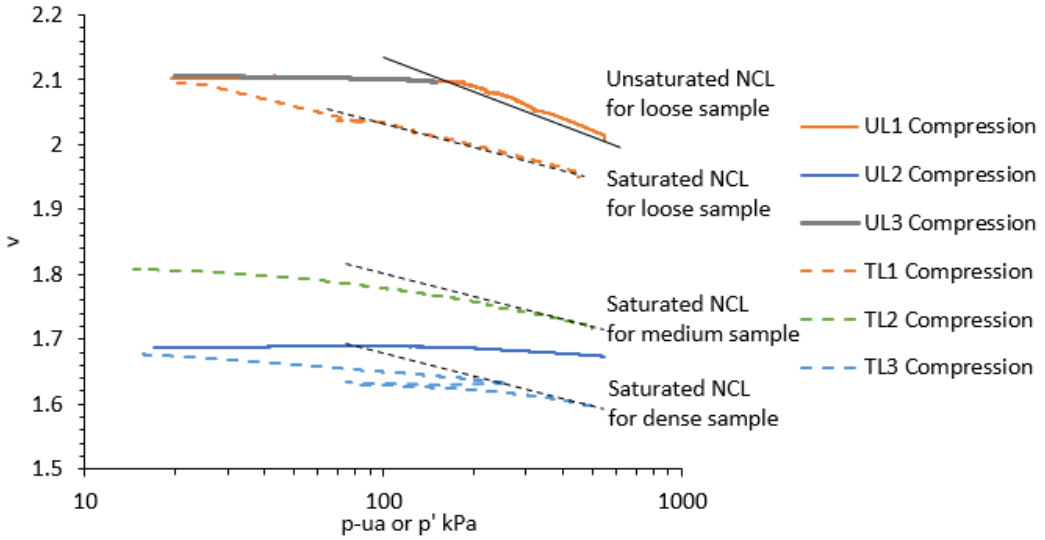
2.2
2.1
2
1.9
1.8
1.7
1.6
1.5
v
10
100
1000
p-ua or p' kPa
Unsaturated NCL
for loose sample
Saturated NCL
for loose sample
Saturated NCL
for medium sample
Saturated NCL
for dense sample
UL1 Compression
UL2 Compression
UL3 Compression
TL1 Compression
TL2 Compression
TL3 Compression

(a)

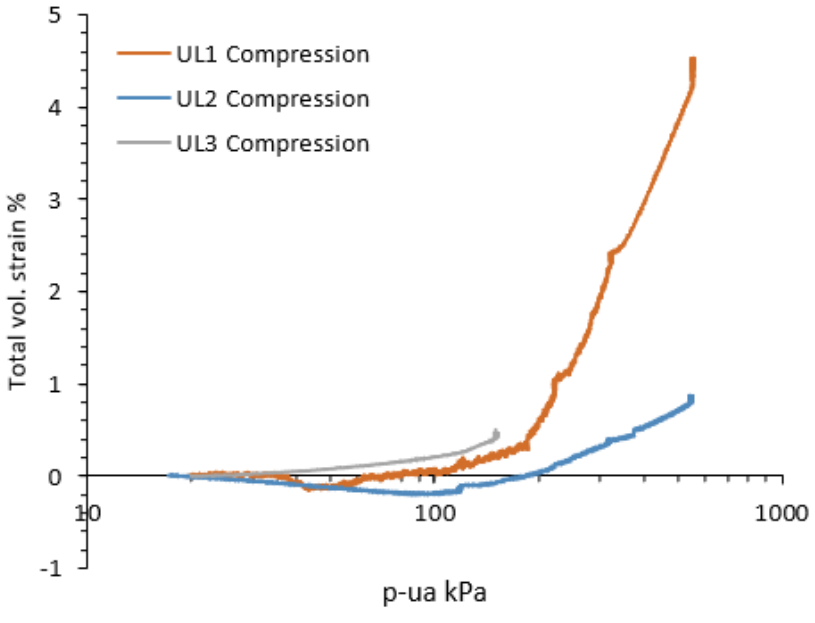
5
4
3
2
1
0
-1
Total vol. strain %
10
100
1000
p-ua kPa
UL1 Compression
UL2 Compression
UL3 Compression

(b)

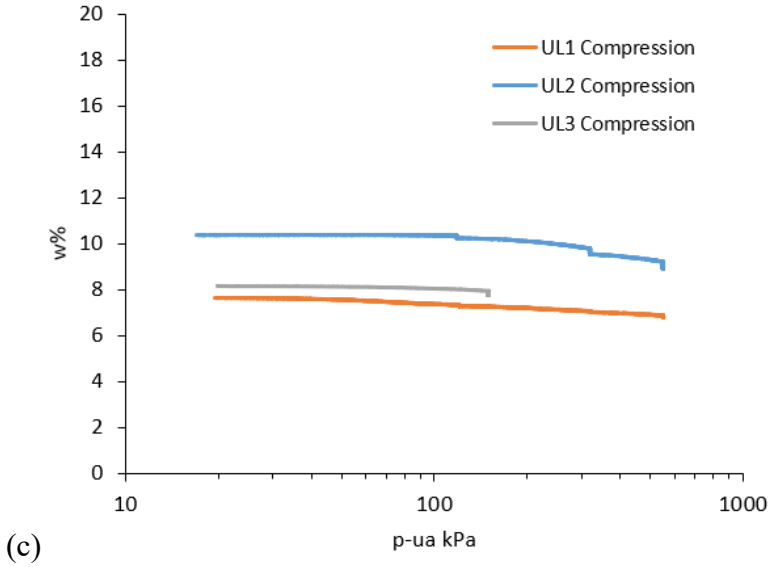

(c)

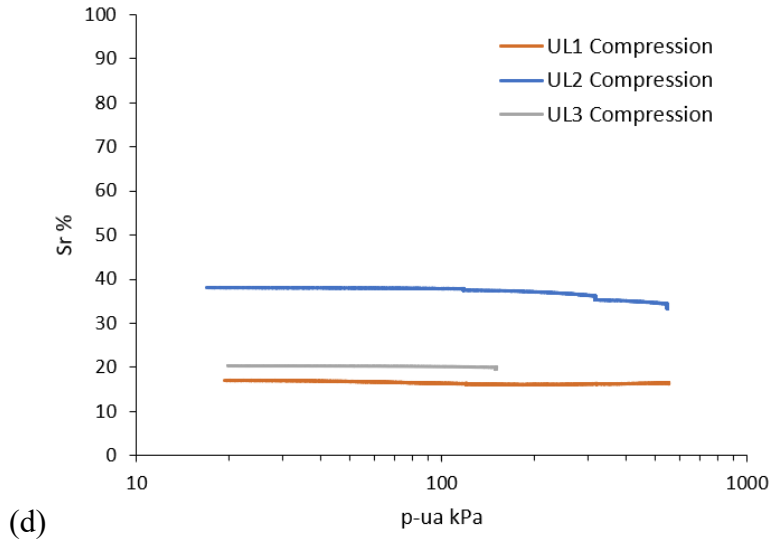

(d)

Figure 6-5 Unsaturated isotropic compression behaviour of loess under constant 100 kPa suction: (a) compression lines, (b) volumetric behaviour, (c) water content variation, (d) degree of saturation variation.

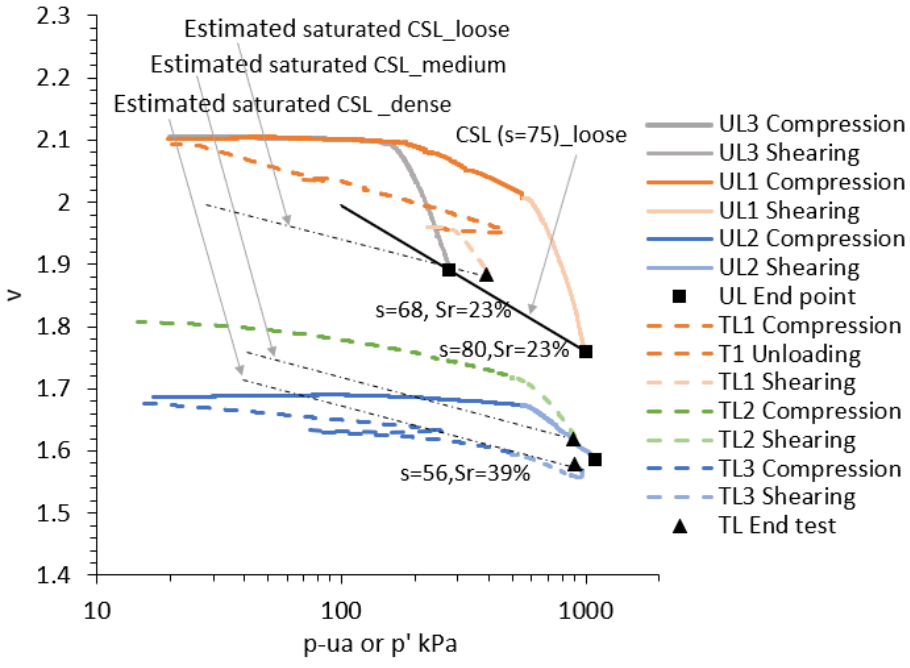
Estimated saturated CSL_loose
Estimated saturated CSL_medium
Estimated saturated CSL _dense
CSL (s=75)_loose
s=68, Sr=23%
s=80,Sr=23%
s=56,Sr=39%
v
p-ua or p' kPa
UL3 Compression
UL3 Shearing
UL1 Compression
UL1 Shearing
UL2 Compression
UL2 Shearing
UL End point
TL1 Compression
T1 Unloading
TL1 Shearing
TL2 Compression
TL2 Shearing
TL3 Compression
TL3 Shearing
TL End test

(a)

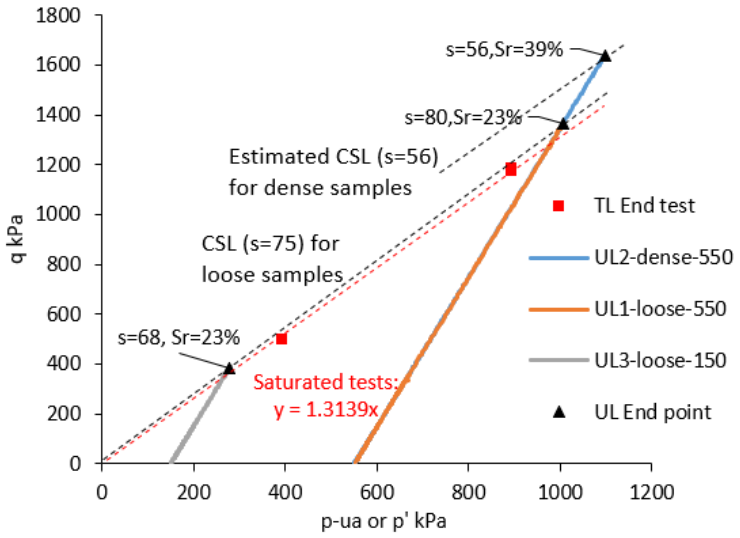
s=56,Sr=39%
s=80,Sr=23%
Estimated CSL (s=56)
for dense samples
CSL (s=75) for
loose samples
s=68, Sr=23%
Saturated tests:
y = 1.3139x
q kPa
p-ua or p' kPa
TL End test
UL2-dense-550
UL1-loose-550
UL3-loose-150
UL End point

(b)

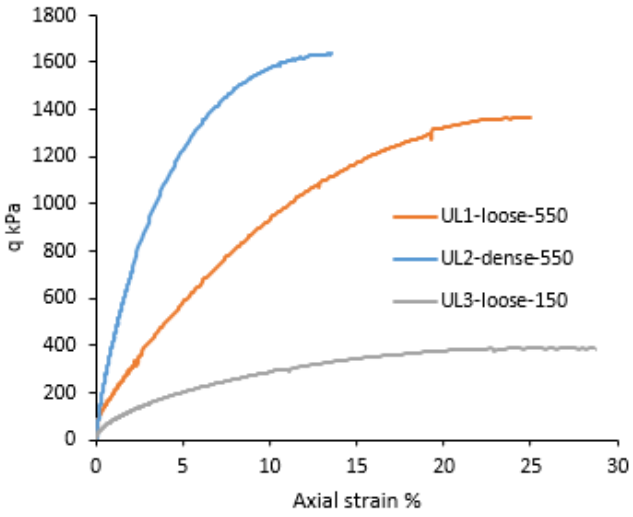
q kPa
Axial strain %
UL1-loose-550
UL2-dense-550
UL3-loose-150

(c)

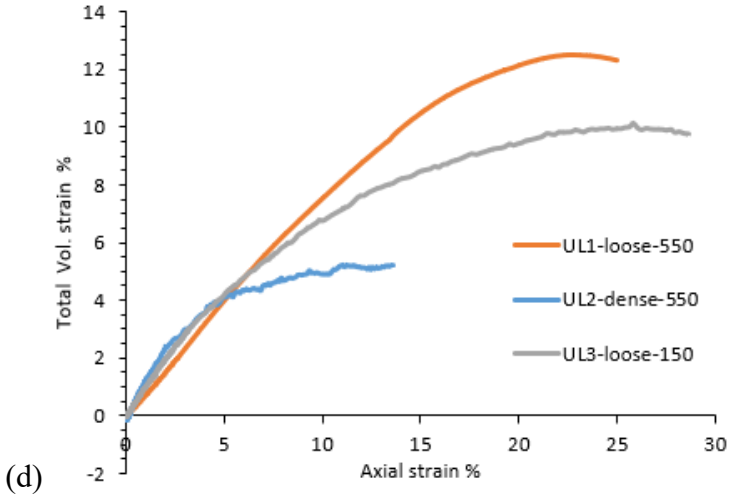

(d)

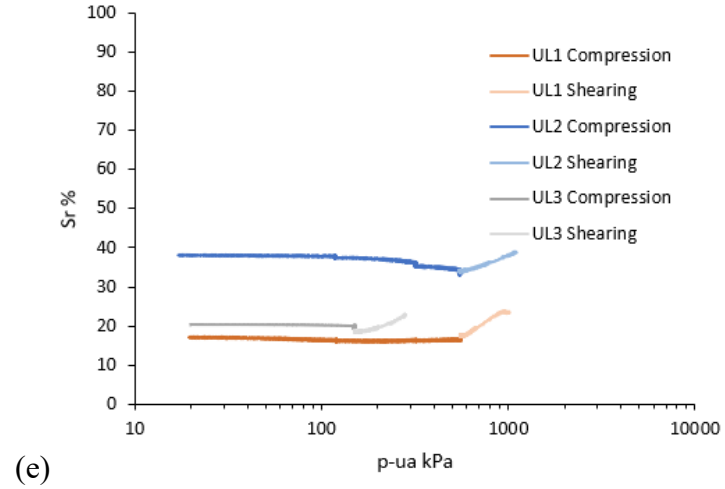

(e)

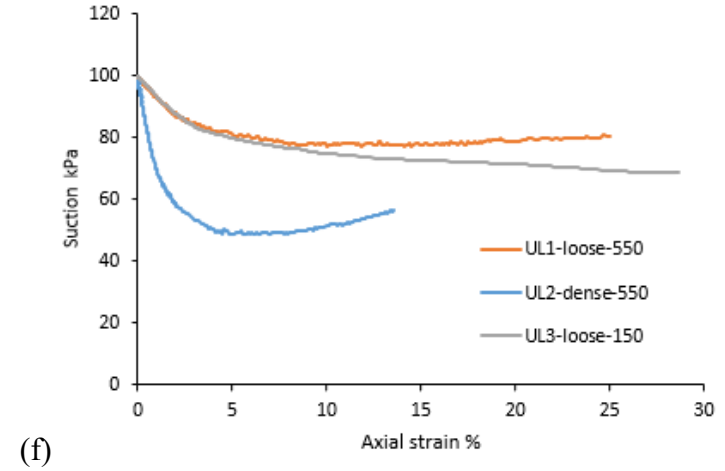

(f)

Figure 6-6 Unsaturated mechanical behaviour of loess during constant water content shearing.

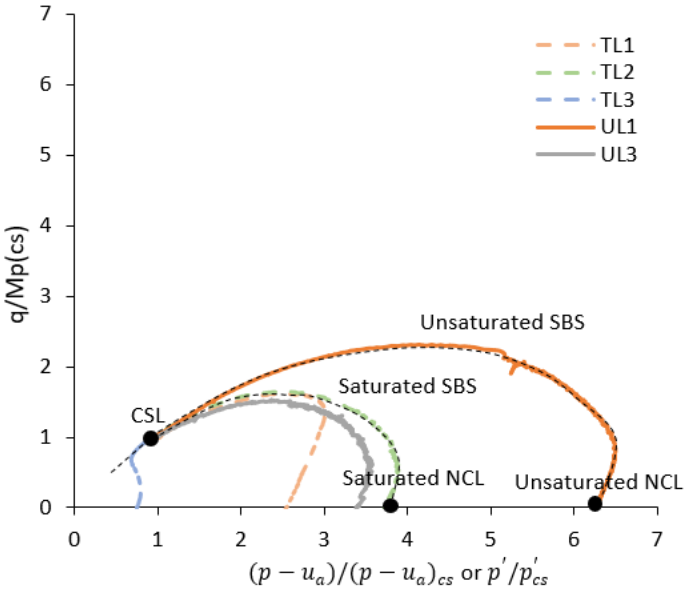

Figure 6-7: Normalised stress paths of saturated and unsaturated loess samples.

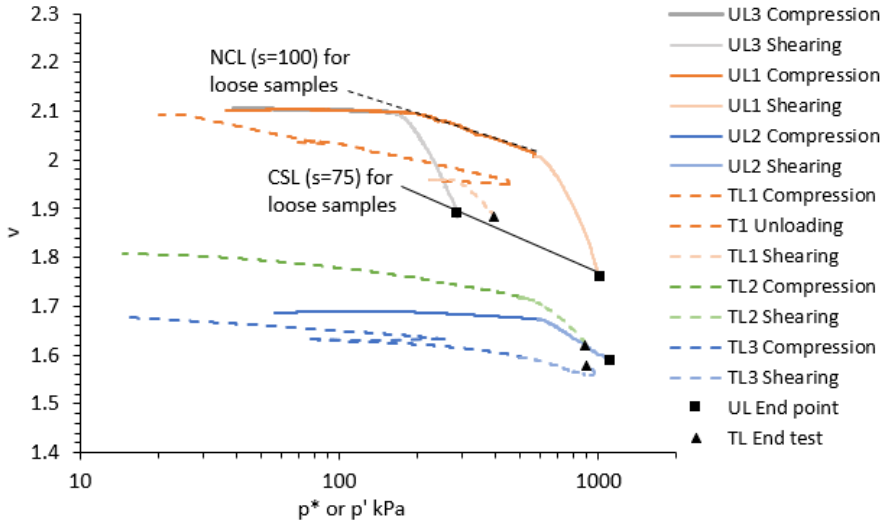

(a)

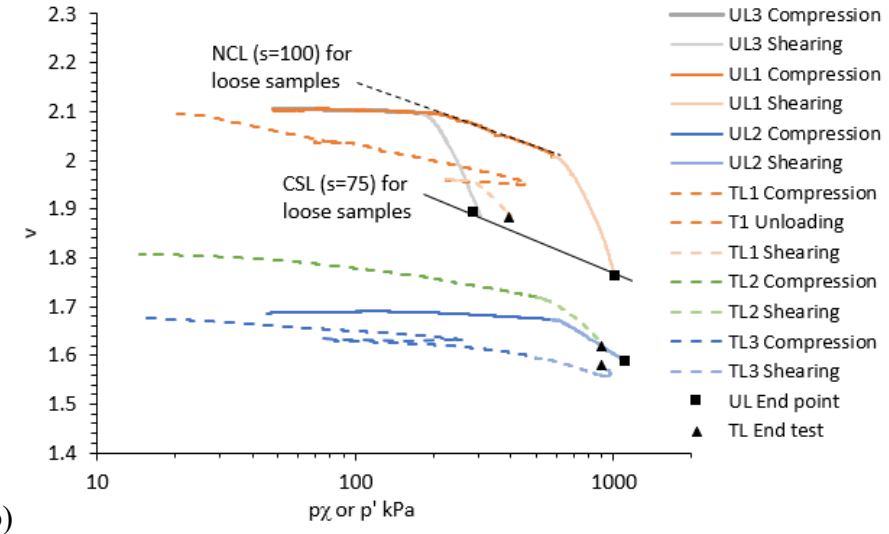

(b)

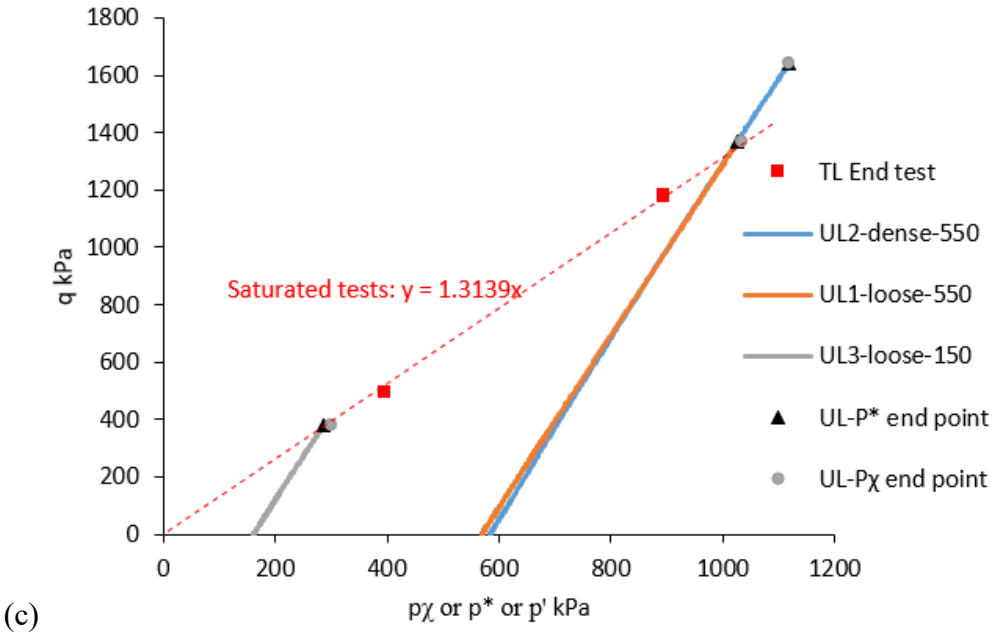

(c)

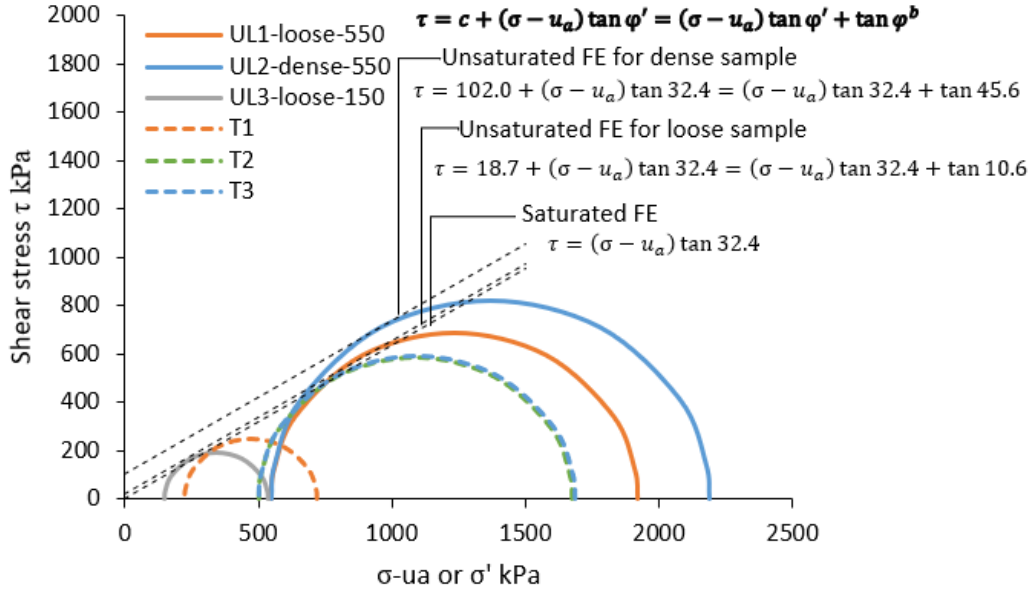

(d)

Figure 6-8 Data reinterpretation for the unsaturated loess: volumetric behaviour based on (a) Bishop factor and (b) Khalili and Khabbaz factor, (c) stress paths based on two stress factors; (d) Extended Mohr-Coulomb failure envelope.

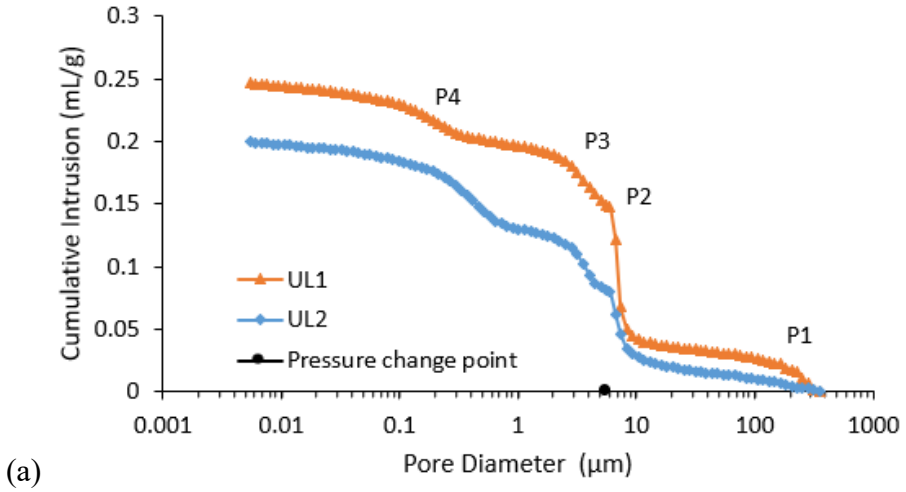

(a)

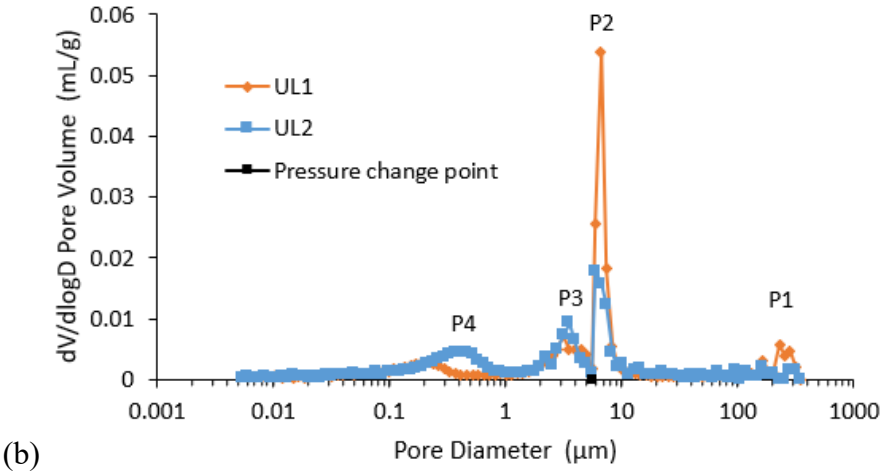

(b)

Figure 6-9 MIP results for the unsaturated loess samples: (a) cumulative pore size distributions and (b) differential pore size distributions.

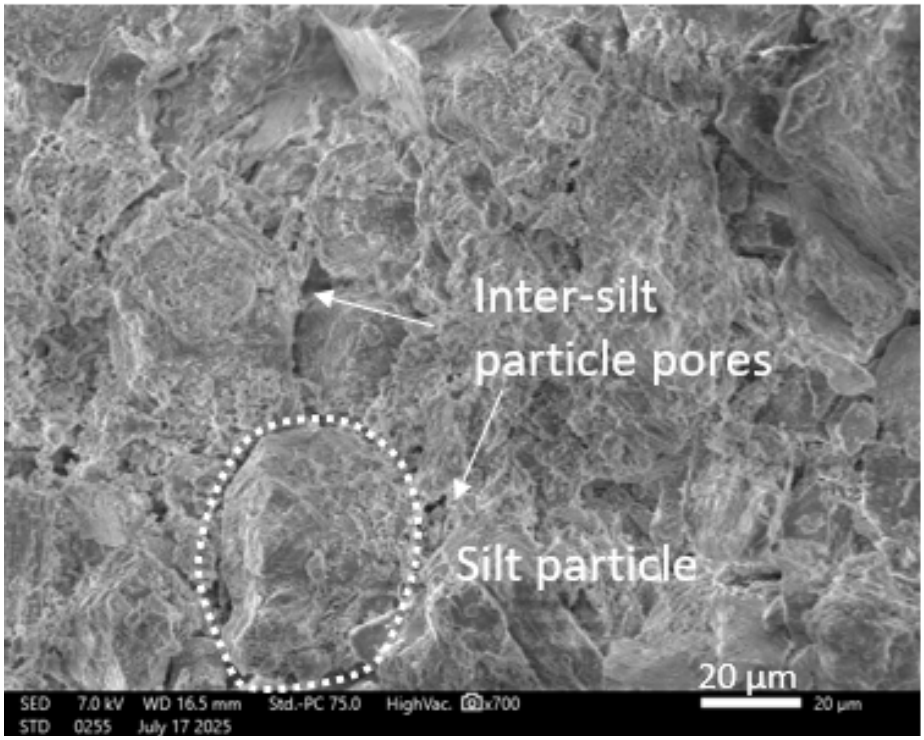
Inter-silt
particle pores
Silt particle
20 µm
SED 7.0 kV WD 16.5 mm Std.-PC 75.0 HighVac. x700
STD 0255 July 17 2025
20 µm

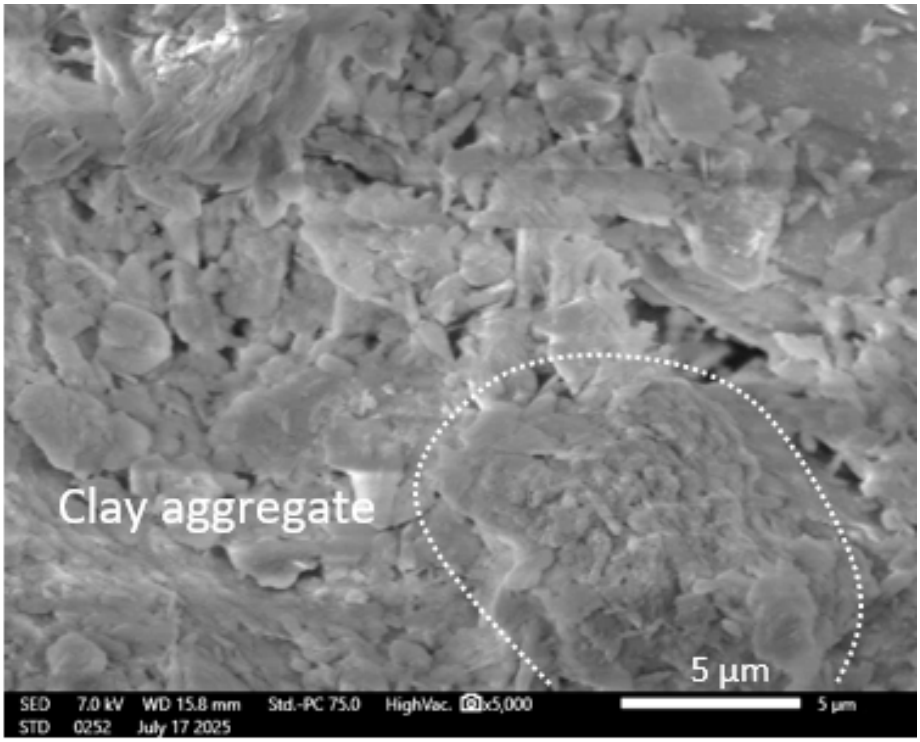
Clay aggregate
5 µm
SED 7.0 kV WD 15.8 mm Std.-PC 75.0 HighVac. x5,000
STD 0252 July 17 2025
5 µm

(a)

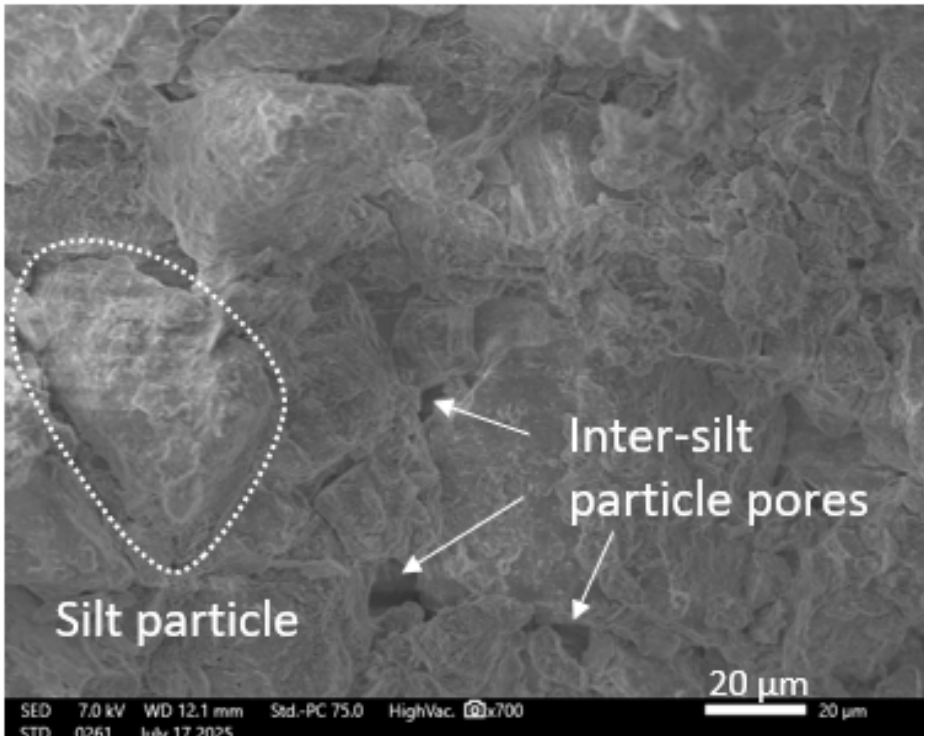

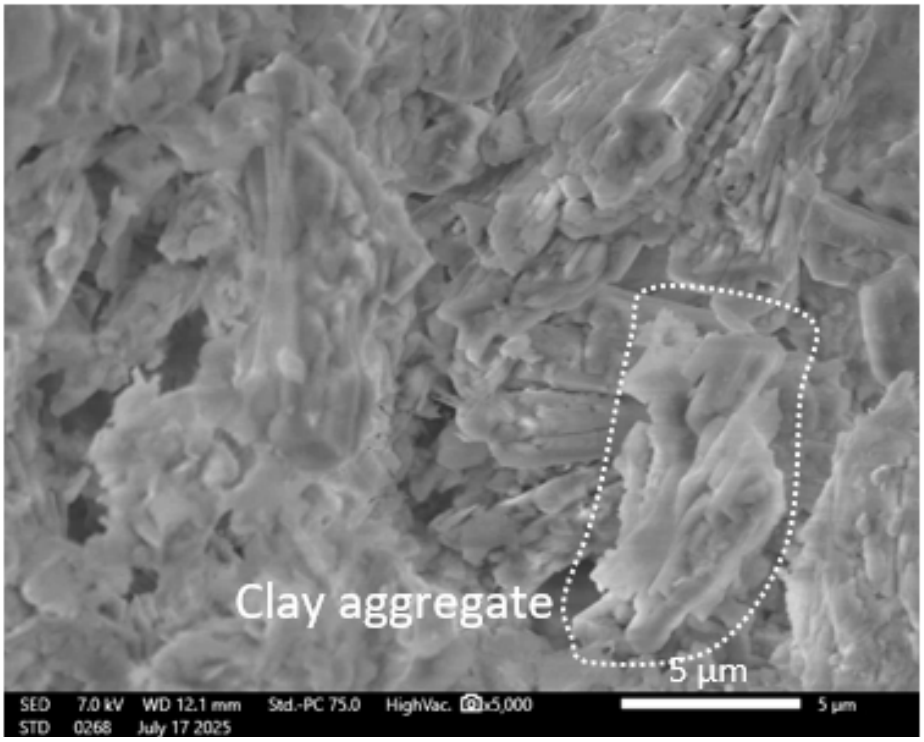

(b)

Figure 6-10 SEM test results of unsaturated silty loess: (a) dense sample UL2 and (b) loose sample UL1.

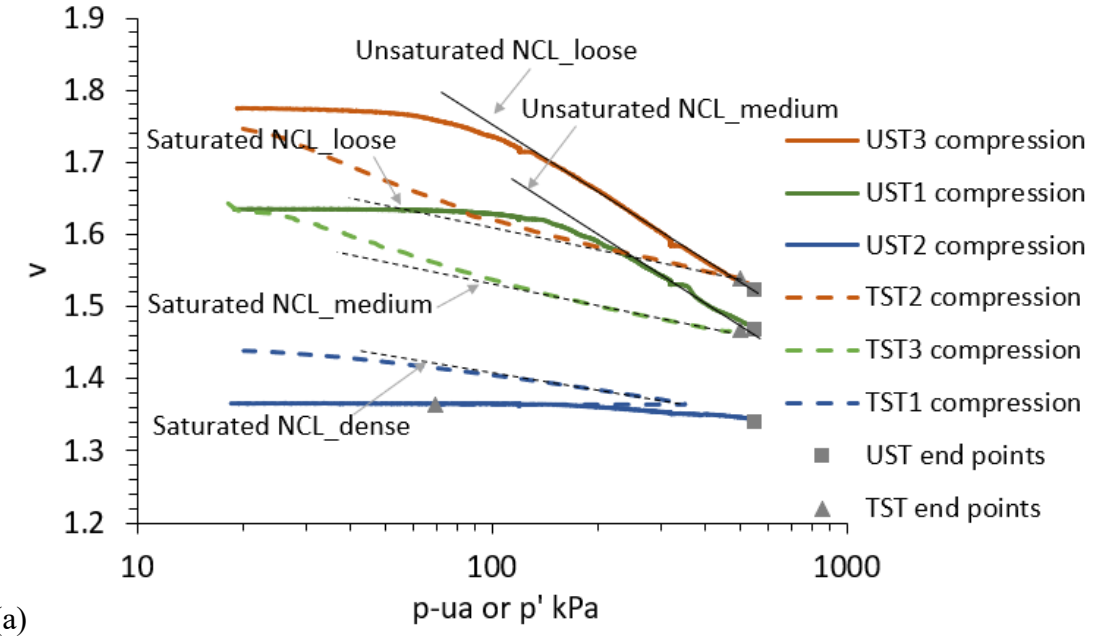
Unsaturated NCL_loose
Unsaturated NCL_medium
Saturated NCL_loose
Saturated NCL_medium
Saturated NCL_dense
UST3 compression
UST1 compression
UST2 compression
TST2 compression
TST3 compression
TST1 compression
UST end points
TST end points
v
p-ua or p' kPa

(a)

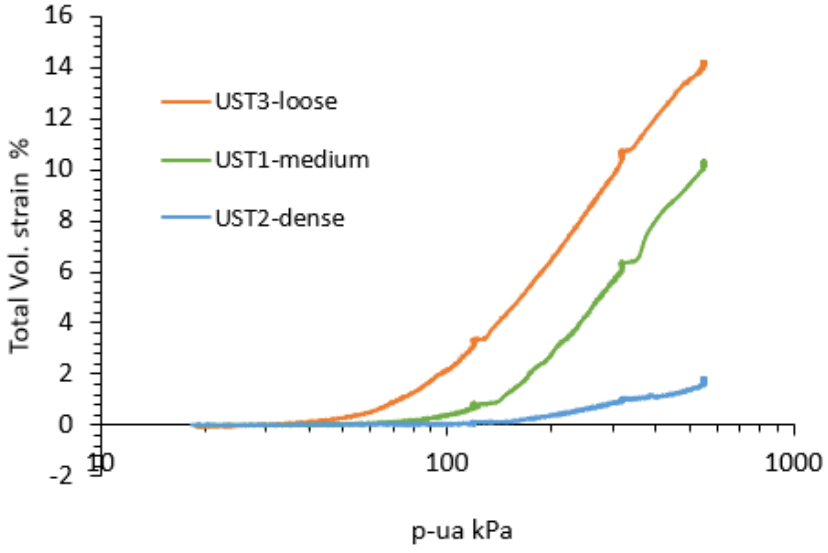
UST3-loose
UST1-medium
UST2-dense
Total Vol. strain %
p-ua kPa

(b)

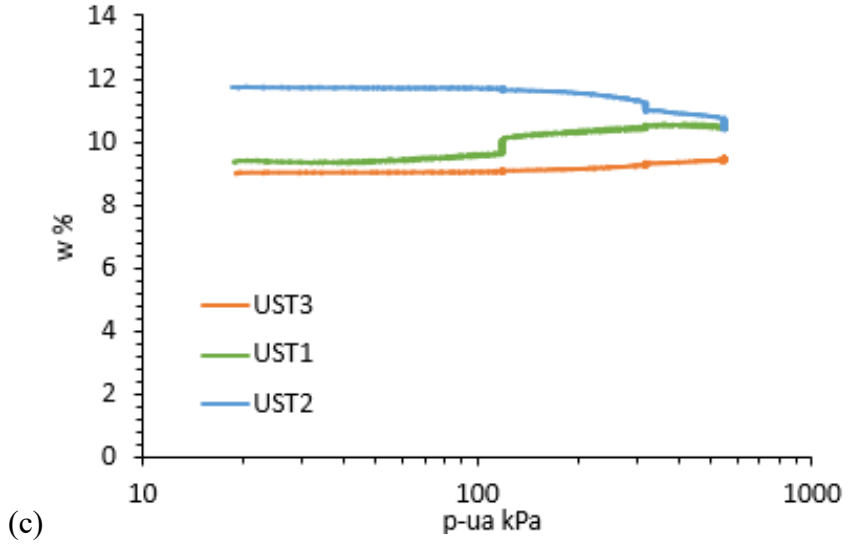

(c)

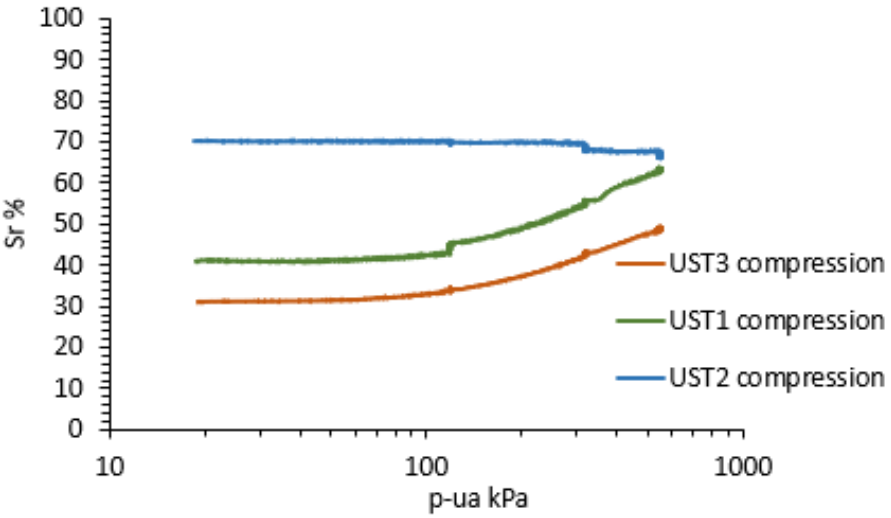

(d)

Figure 6-11 Unsaturated mechanical behaviour of sandy tailings during constant 100 kPa suction isotropic compression: (a) compression lines, (b) volumetric behaviour, (c) water content variation, and (d) degree of saturation variation.

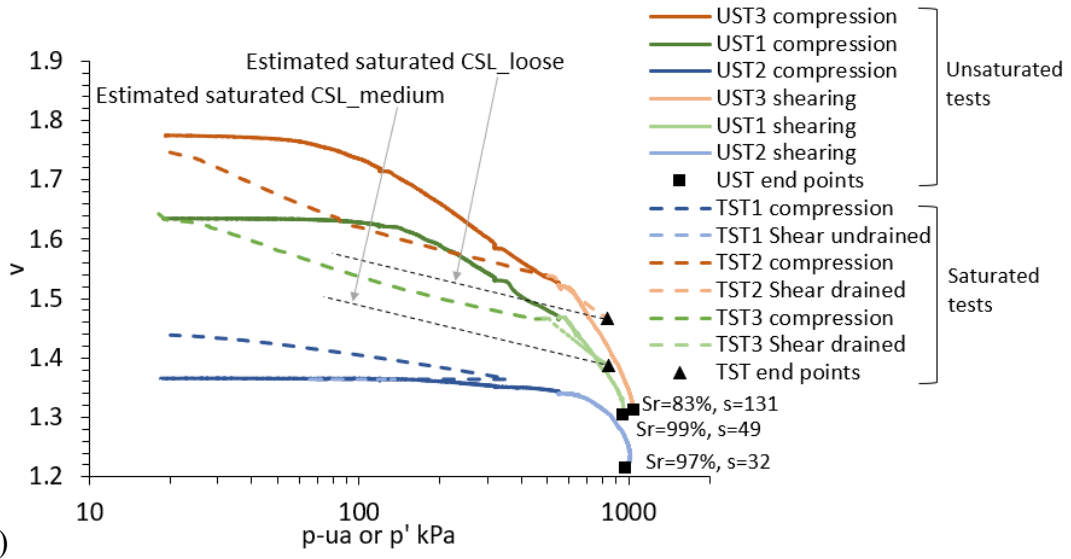
Estimated saturated CSL_loose
Estimated saturated CSL_medium
UST3 compression
UST1 compression
UST2 compression
UST3 shearing
UST1 shearing
UST2 shearing
UST end points
Unsaturated tests
TST1 compression
TST1 Shear undrained
TST2 compression
TST2 Shear drained
TST3 compression
TST3 Shear drained
TST end points
Saturated tests
Sr=83%, s=131
Sr=99%, s=49
Sr=97%, s=32
v
p-ua or p' kPa

(a)

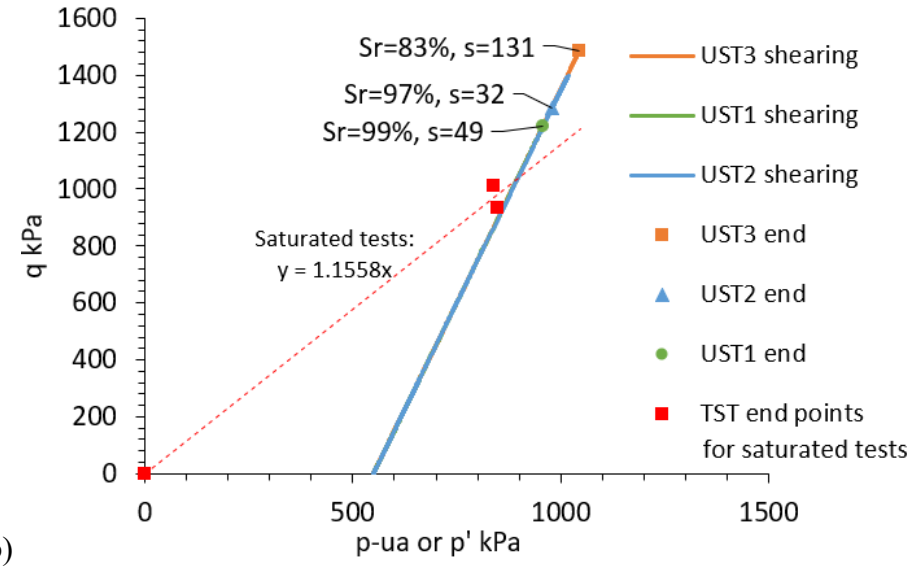
Sr=83%, s=131
Sr=97%, s=32
Sr=99%, s=49
Saturated tests:
y = 1.1558x
UST3 shearing
UST1 shearing
UST2 shearing
UST3 end
UST2 end
UST1 end
TST end points for saturated tests
q kPa
p-ua or p' kPa

(b)

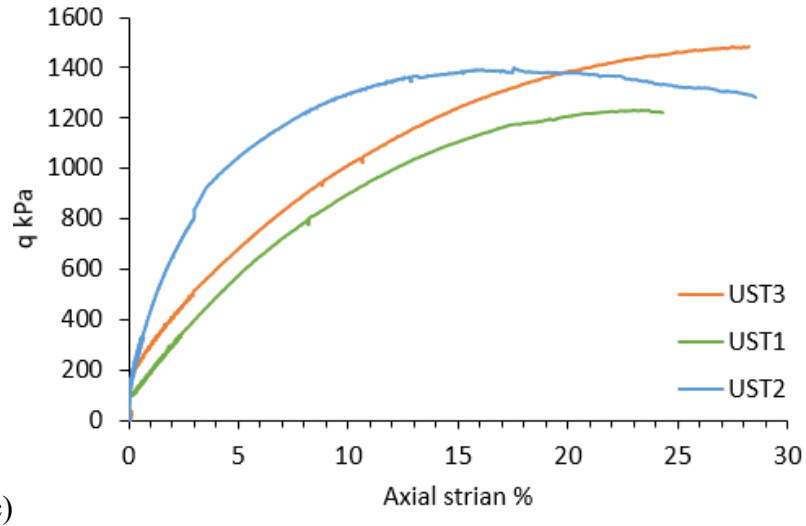
UST3
UST1
UST2
q kPa
Axial strian %

(c)

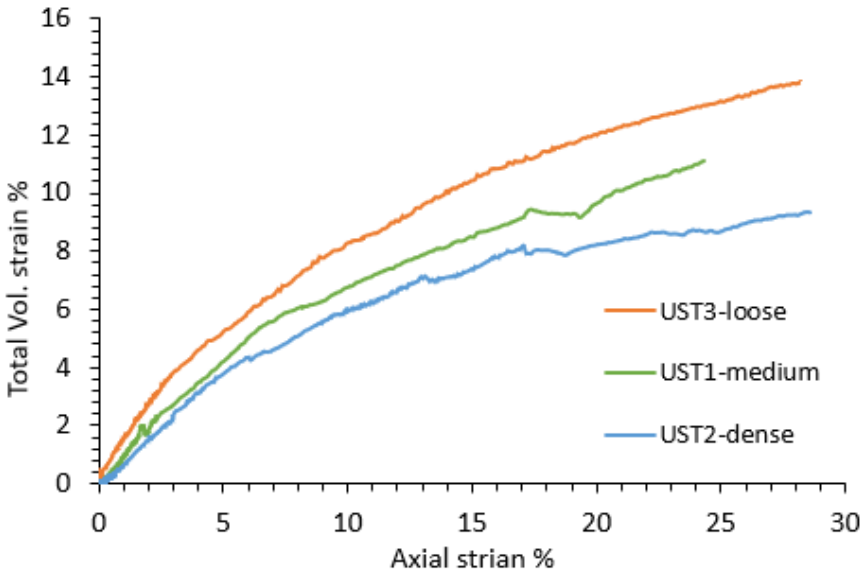

(d)

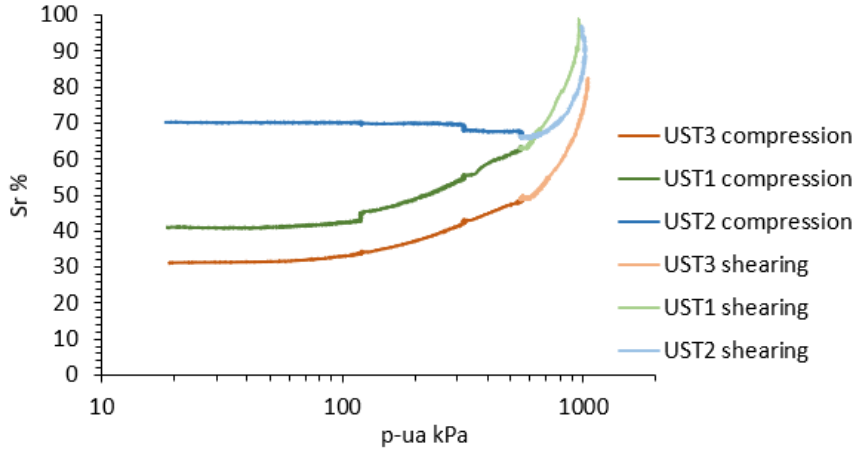

(e)

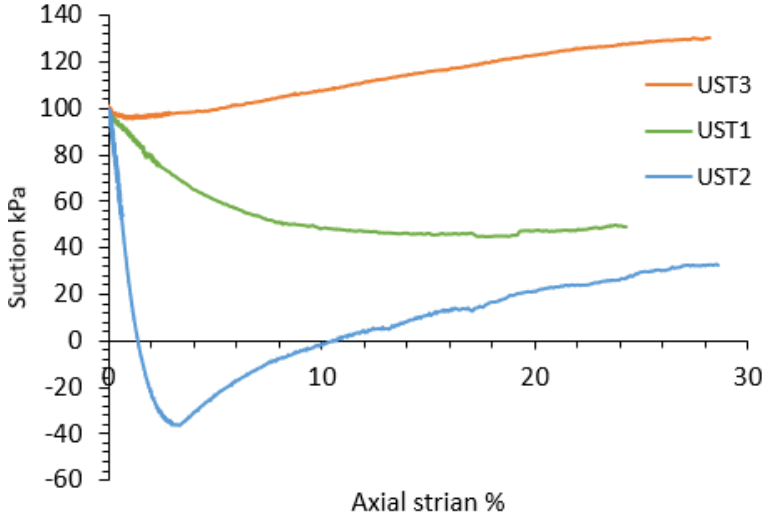

(f)

Figure 6-12 Unsaturated mechanical behaviour of sandy tailings during constant water content shearing.

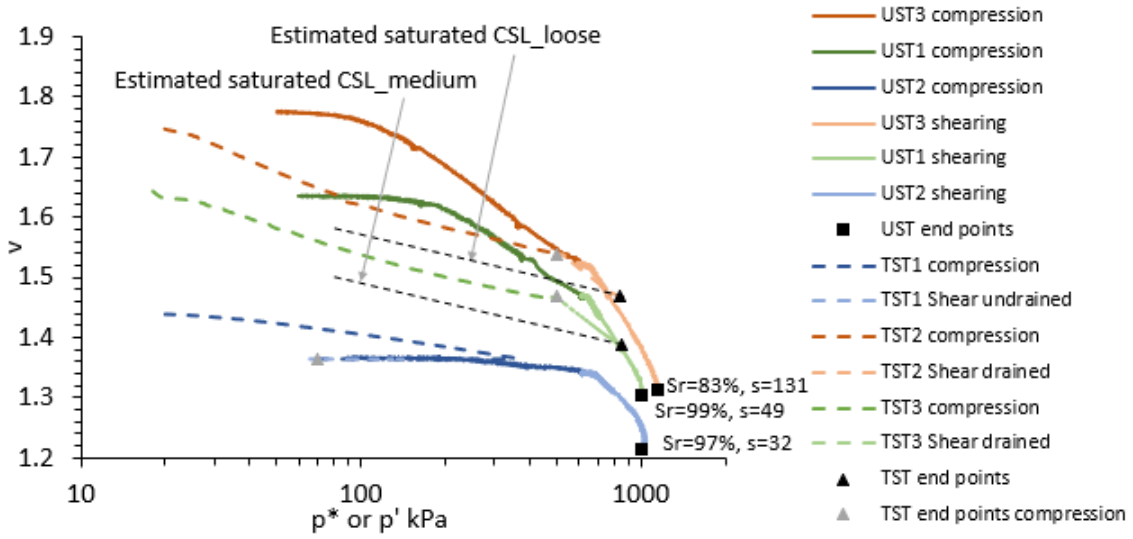
Estimated saturated CSL_loose
Estimated saturated CSL_medium
v
p* or p' kPa
Sr=83%, s=131
Sr=99%, s=49
Sr=97%, s=32
UST3 compression
UST1 compression
UST2 compression
UST3 shearing
UST1 shearing
UST2 shearing
UST end points
TST1 compression
TST1 Shear undrained
TST2 compression
TST2 Shear drained
TST3 compression
TST3 Shear drained
TST end points
TST end points compression

(a)

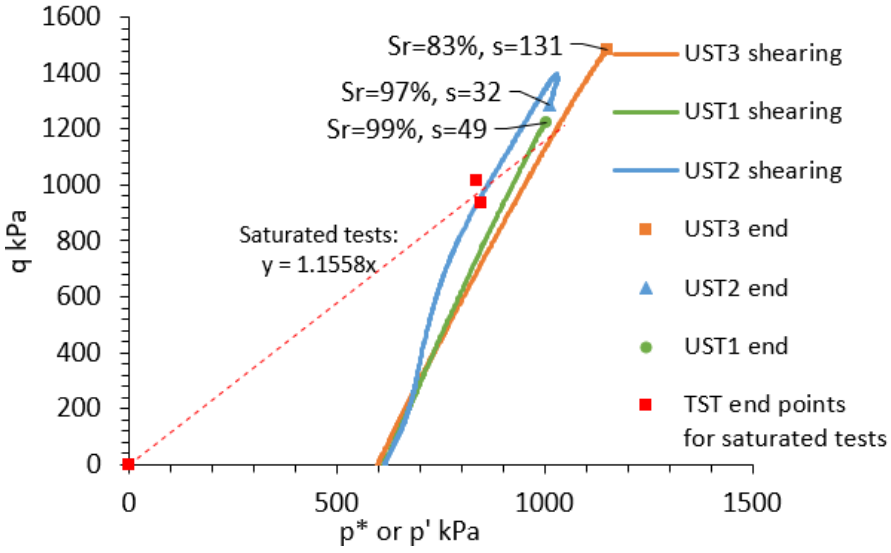
q kPa
p* or p' kPa
Sr=83%, s=131
Sr=97%, s=32
Sr=99%, s=49
Saturated tests:
y = 1.1558x
UST3 shearing
UST1 shearing
UST2 shearing
UST3 end
UST2 end
UST1 end
TST end points
for saturated tests

(b)

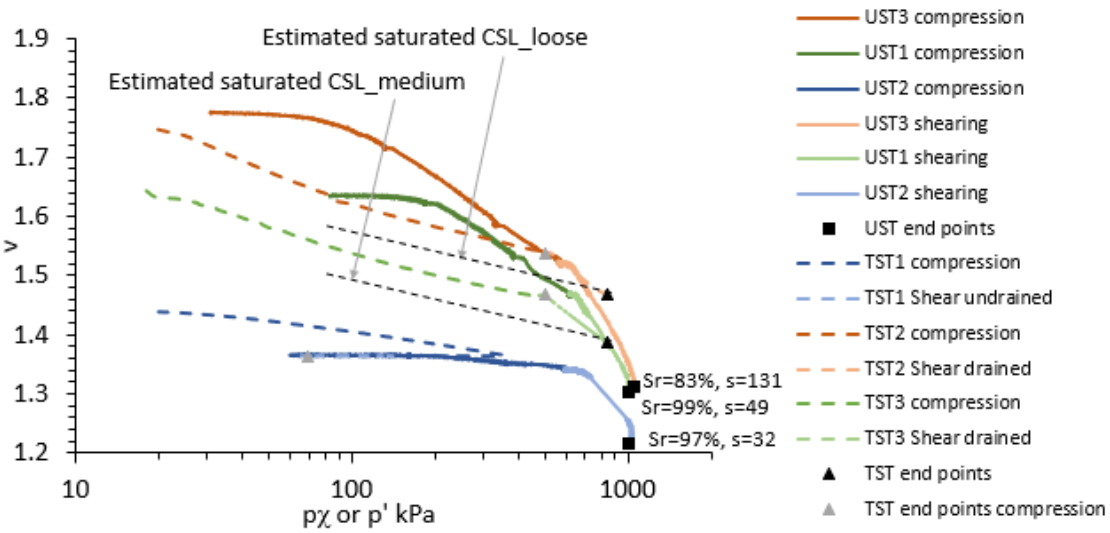

(c)

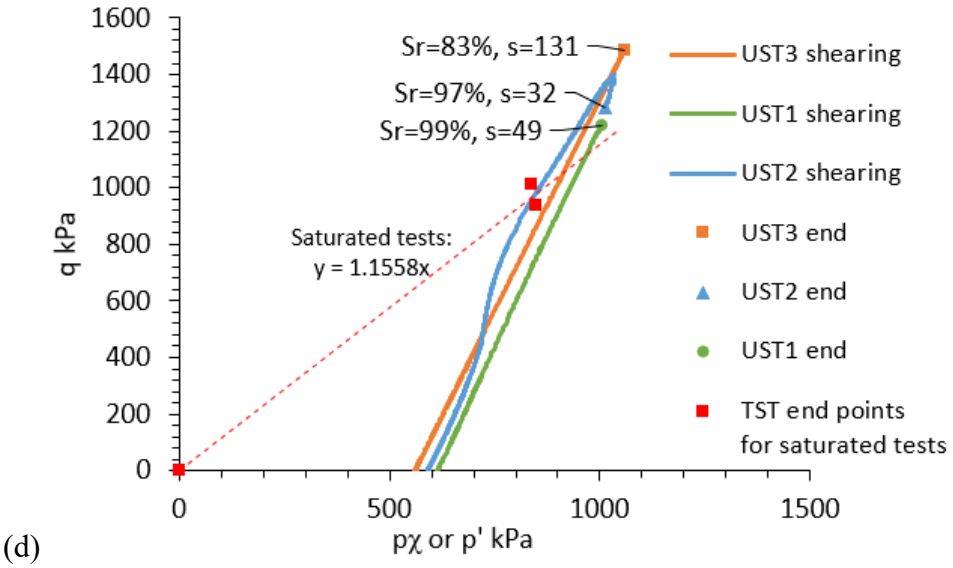

(d)

Figure 6-13 Data reinterpretation for the unsaturated sandy tailings: (a) volumetric behaviour and (b) stress path based on Bishop factor, and (c) volumetric behaviour and (d) stress path based on Khalili and Khabbaz factor.

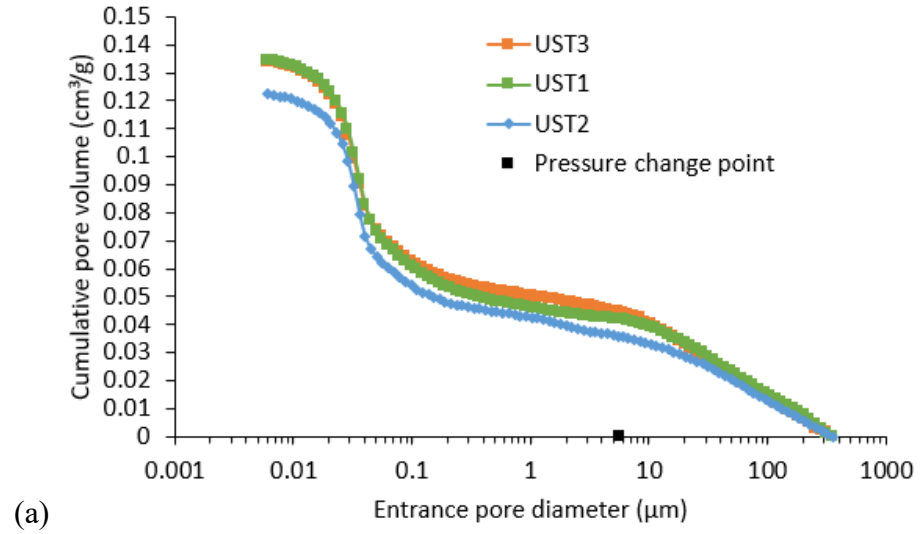

(a)

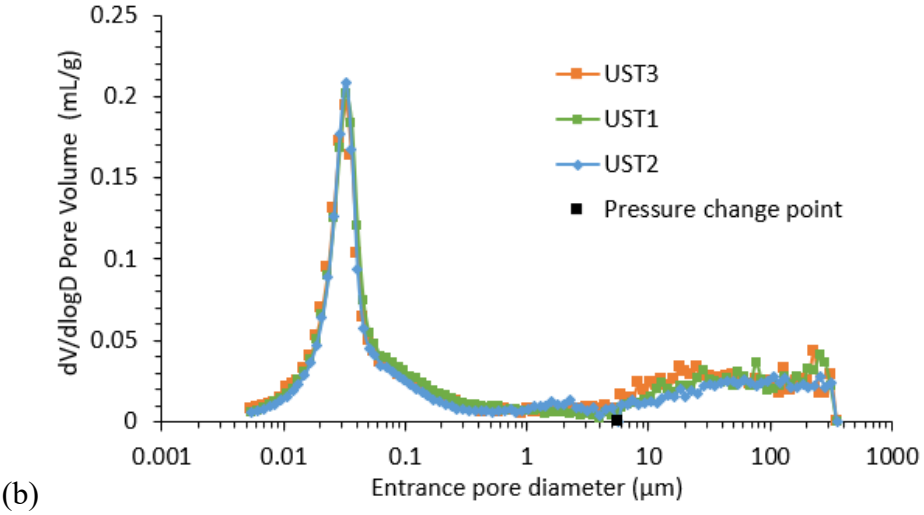

(b)

Figure 6-14 MIP results for the unsaturated sandy tailings: (a) cumulative pore size distributions and (b) differential pore size distributions.

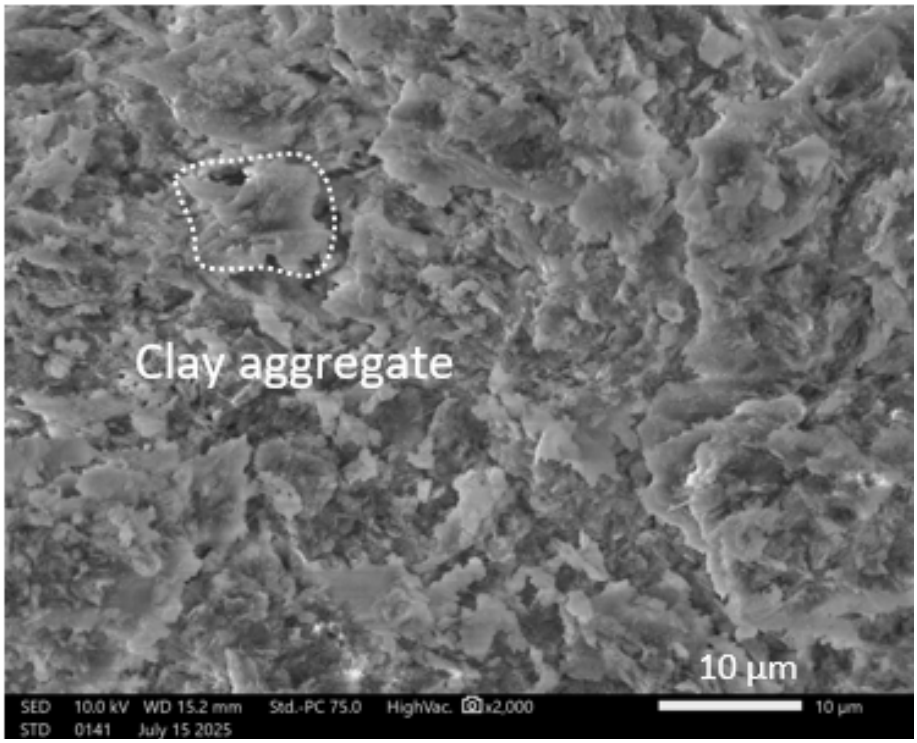
Clay aggregate
10 µm
SED 10.0 kV WD 15.2 mm Std.-PC 75.0 HighVac. x2,000 10 µm
STD 0141 July 15 2025

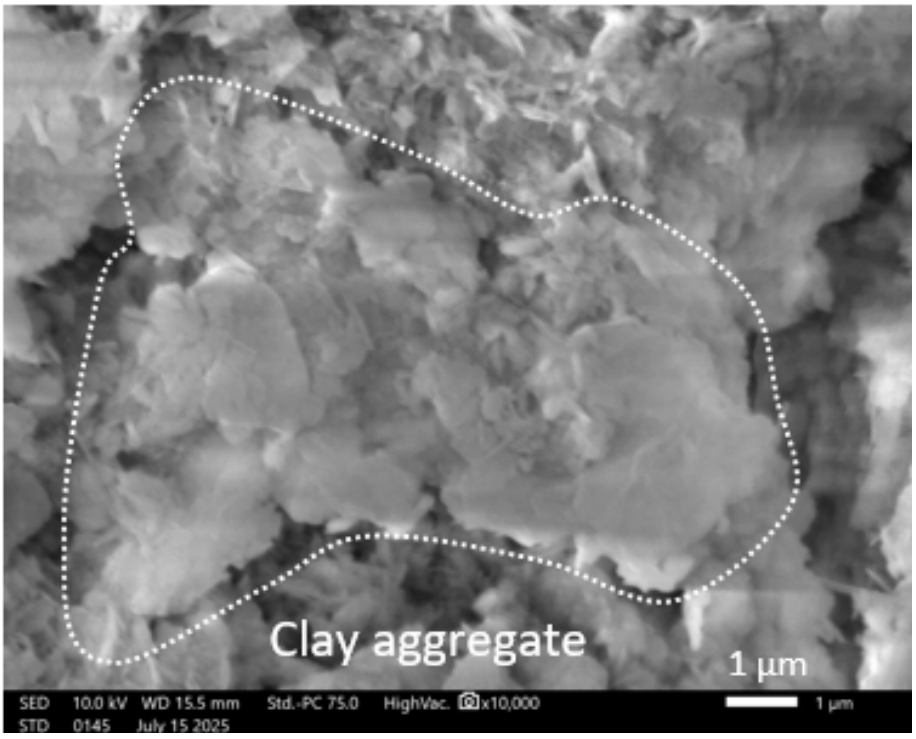
Clay aggregate
1 µm
SED 10.0 kV WD 15.5 mm Std.-PC 75.0 HighVac. x10,000 1 µm
STD 0145 July 15 2025

(a)

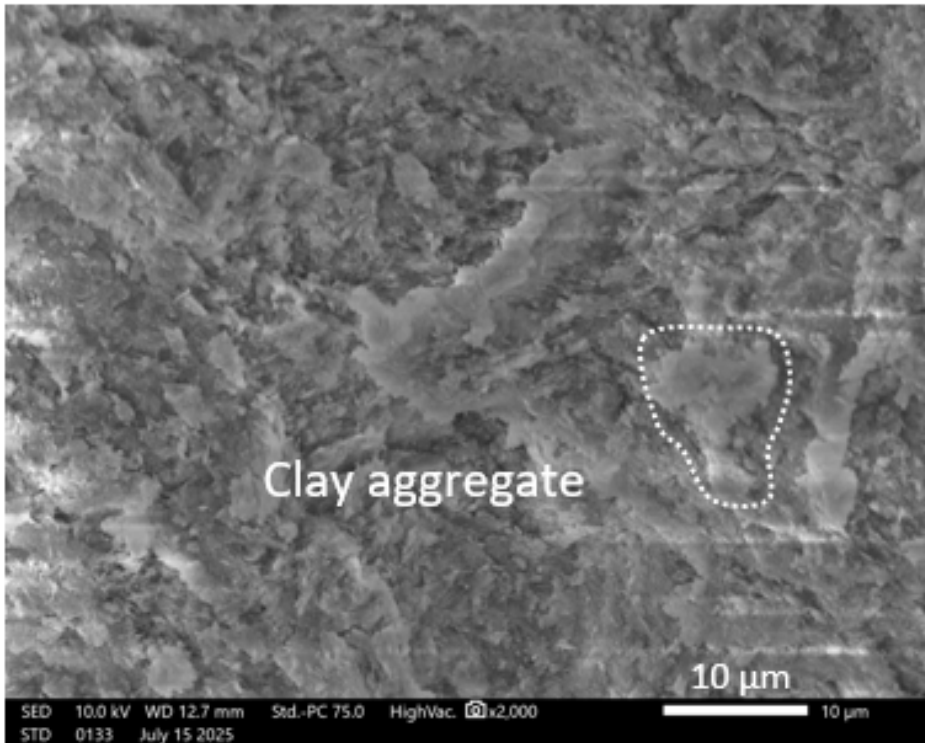
Clay aggregate
10 µm
SED 10.0 kV WD 12.7 mm Std.-PC 75.0 HighVac. x2,000 10 µm
STD 0133 July 15 2025

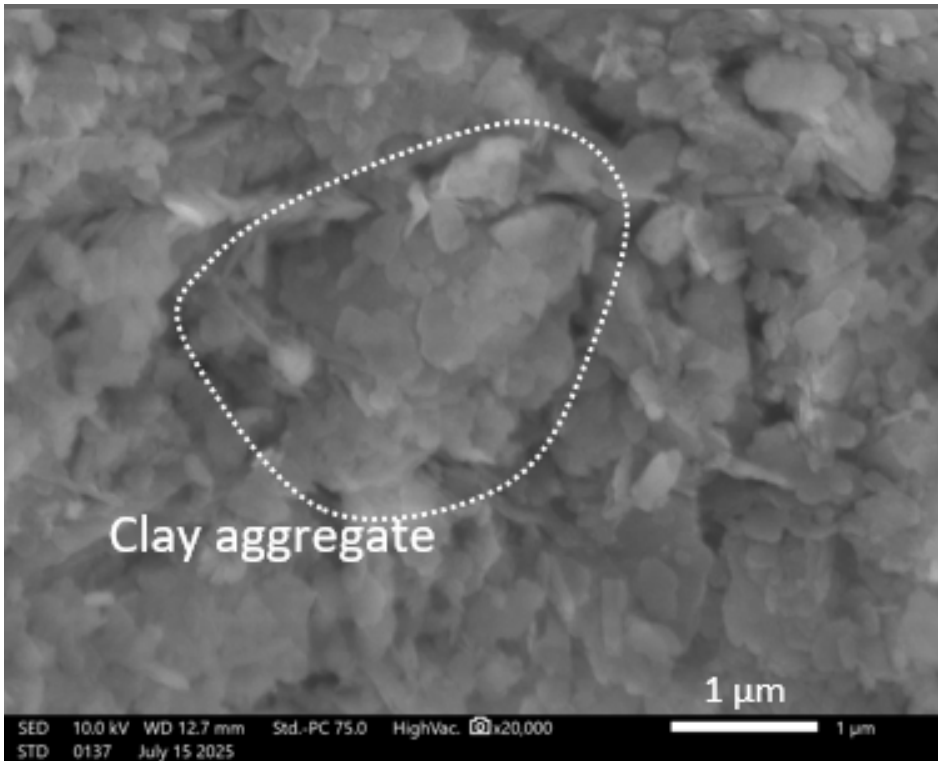
Clay aggregate
1 µm
SED 10.0 kV WD 12.7 mm Std.-PC 75.0 HighVac. x20,000 1 µm
STD 0137 July 15 2025

(b)

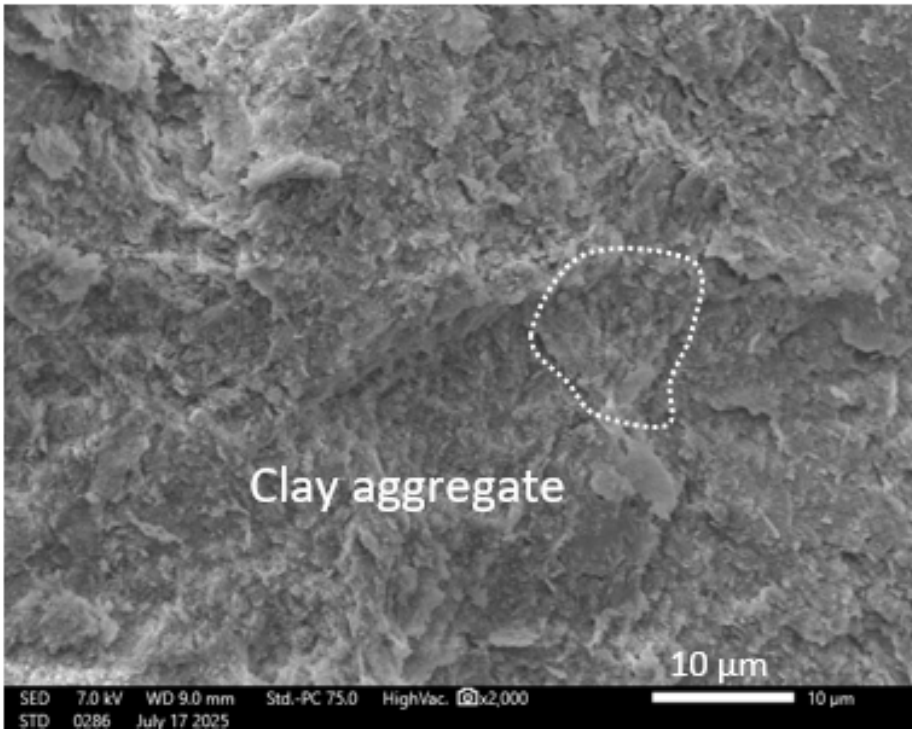

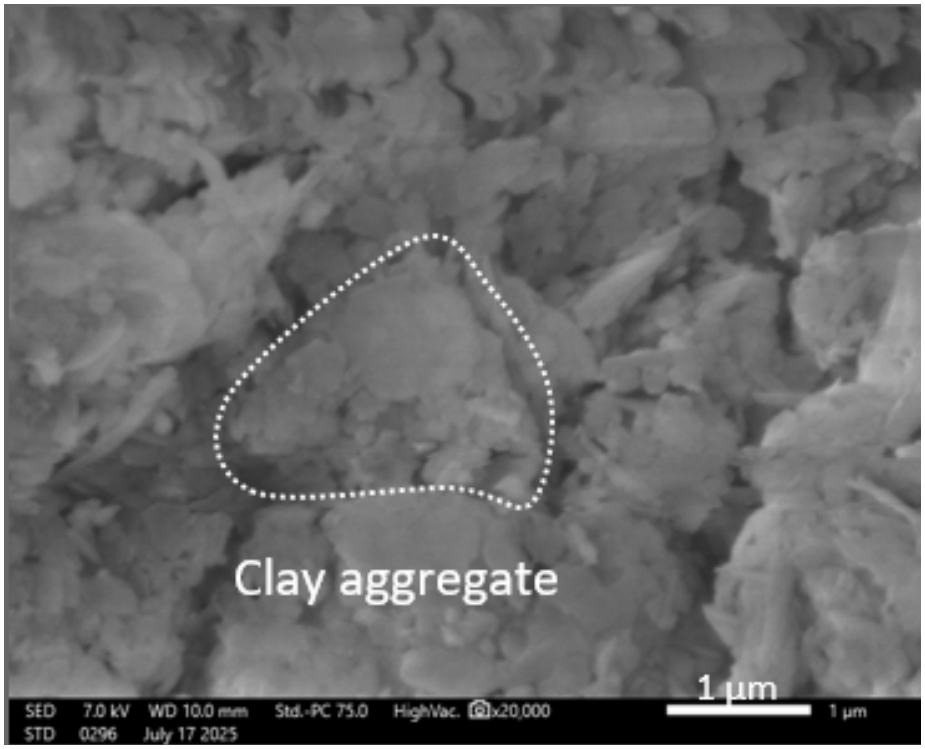

(c)

Figure 6-15 SEM test results of unsaturated sandy tailings: (a) dense sample UST2, (b) medium-dense sample UST1, and (c) loose sample UST3.

CHAPTER 7 CONCLUSIONS

7.1 Introduction

This chapter summarises main findings of this study and highlights the contributions made toward understanding transitional soil behaviour under both saturated and unsaturated conditions. The research aimed to investigate the characteristics of transitional behaviour under saturated conditions across a range of soils and the influence of suction on this behaviour in unsaturated states. This chapter is organised into four sections. Section 7.2 summarises the main works in this study, including the study scope, materials tested, and the testing programmes with their main purposes. Section 7.3 outlines the key contributions of the study in relation to previous work and some practical implications of the findings. Finally, Section 7.4 presents recommendations for future research.

7.2 Research summary

This study investigated the transitional behaviour of soils under both saturated and unsaturated conditions through a series of laboratory experiments. Four soils were selected, including fine tailings, sandy tailings, silty loess, and a kaolin–sand mixture. These materials represent a range of particle size distributions, gradings, and mineralogies, and were tested over wide ranges of initial specific volume to assess the transitional behaviour. Selected saturated and unsaturated samples were preserved for Mercury Intrusion Porosimetry (MIP) and Scanning Electron Microscopy (SEM) to support interpretation of the mechanical behaviour.

In the saturated programme, oedometer tests and triaxial tests were carried out to study the mechanical behaviour. These tests were used to identify the development of non-unique Normal Compression Lines (NCLs) and Critical State Lines (CSLs) in each soil.

The presence of transitional behaviour was confirmed in all four materials. Fine tailings showed the most prominent transitional characteristics and were selected for further investigation. Additional analyses on fine tailings included the quantification of NCL and CSL parameters, assessment of small-strain stiffness using local LVDTs, evaluation of compression and dilatancy behaviour, and examination of the state boundary surface.

For unsaturated testing, an unsaturated triaxial apparatus was developed based on modifications to an existing saturated system using the axis translation technique. The new system incorporated new pedestal with a 5-bar air-entry porous stone, pore air pressure system, and a total volume measurement setup combining local LVDT displacement transducers and cell volume gauge. Calibration was conducted carefully to ensure accurate measurement under unsaturated conditions. Filter paper tests were used to determine Soil Water Retention Curves (SWRCs) and to support the selection of appropriate suction levels and sample preparation methods. Unsaturated triaxial tests were conducted on sandy tailings and silty loess under constant suction compression and constant water content shearing. Transitional behaviour was clearly observed in both soils, and the influence of suction on the convergence of NCLs and CSLs was analysed.

7.3 Research contributions

This research provides new insights into transitional soil behaviour based on experimental findings from both saturated and unsaturated conditions.

Transitional behaviour in saturated states

In the saturated testing programme, transitional behaviour was identified in four types of reconstituted soils, namely fine tailings, sandy tailings, silty loess, and a kaolin–sand

mixture. All materials exhibited non-unique Normal Compression Lines (NCLs) and Critical State Lines (CSLs). Among them, fine tailings showed the most pronounced transitional features and were therefore selected for further investigation on the transitional behaviour in the saturated state. The key findings are summarised below:

- Triaxial k_0 compression tests provided more consistent results than oedometer one-dimensional compression tests, probably due to the advantage of zero sidewall friction.
- Transitional behaviour was identified through non-unique NCLs and CSLs, and quantified using the m and P parameters. A modified formulation for the P value was proposed to handle cases where the NCL or CSL has a different gradient for different initial density groups.
- The intercepts and gradients of NCLs and CSLs were found to vary linearly with initial density. As the initial specific volume for the samples decreases, the slopes of the NCLs or CSLs decrease and the spacings between the NCLs and CSLs decrease. These contrast with earlier assumptions that the slopes of NCLs and CSLs remained constant.
- Apart from these above, the influence of initial density is slight, since samples with any initial density predominantly have compressive and strain-hardening behaviour. The initial density has no effect on dilatancy behaviour and stiffness.
- Microstructural observations from SEM and pore size distributions from MIP tests indicated that transitional features are linked to persistent differences in pore structures below 0.04 μm.
- There have been very few comprehensive investigations into the transitional behaviour of soil, although some features have been seen in transitional behaviour of other soils but not previously observed for tailings. In this study,

the State Boundary Surface (SBS), small strain stiffness, and stress-dilatancy behaviour of tailings were investigated for the first time.

For engineering practice, the study highlighted that hydraulically deposited tailings with a varied initial density can have transitional responses. Neglecting transitional behaviour can result in missing the NCLs and CSLs associated with different initial densities, especially for dense soils. This may lead to underestimating the compressibility and liquefaction potential of dense states. Therefore, ignoring transitional behaviour could introduce serious risks during both construction and maintenance of tailings dam.

Transitional behaviour in unsaturated states

Unsaturated triaxial tests were conducted on silty loess and sandy tailings to investigate whether transitional behaviour identified in saturated conditions persists under partial saturation. The unsaturated soil mechanics analysis was conducted using net stress, following the Barcelona Basic Model (BBM) and the modified unsaturated critical state framework. The key findings are summarised below:

- The results clearly demonstrated transitional features in both materials, as shown by the presence of non-unique Normal Compression Lines (NCLs) and Critical State Lines (CSLs) for samples with different initial densities but similar suction. These findings confirm that transitional behaviour is not confined to saturated conditions and can persist under unsaturated states.
- The degree of transitional behaviour could not be quantified due to an insufficient number of tests to establish a family of NCLs. The degrees of transitional behaviour during both constant suction compression and shearing appear to be smaller than those in the saturated state. This was observed by the

narrower spacing between unsaturated NCLs compared to the saturated NCLs in loess and greater volume reduction under critical states for unsaturated state than saturated state in sandy tailings.

- The slopes of the unsaturated NCLs and CSLs are steeper than those of the corresponding saturated condition in the $v - ln(p - u_a)$ plane for both loess and sandy tailings. The unsaturated NCL slightly crosses the saturated NCL in the loess studied. The steeper slope of the unsaturated NCL and the crossing of the saturated and unsaturated NCLs contradict the BBM framework, which may be attributed to transitional behaviour.
- The influence of initial density was observed in the $q - (p - u_a)$ plane for both materials, confirming that the critical state response is affected by the initial density under unsaturated conditions, which did not happen in saturated states.
- The choice of stress variable (net stress, Bishop stress, or Khalili and Khabbaz's factor based stress) had a limited influence on the interpretation of critical state behaviour in both materials. This was because the 100 kPa suction contributed little to the effective stress compared with around 1000 kPa net stress at critical state, especially on the logarithmic stress scale used to define the NCL and CSL. Higher suctions were not investigated, as 100 kPa was sufficient to demonstrate the effects of unsaturation on soil mechanical behaviour. The focus on high stress levels is required in order to obtain the critical states at the higher stress range, which is necessary for investigating transitional behaviour.

These findings have important implications for dry stacking tailings dams. In such systems, where tailings are placed in an unsaturated state, the expected volumetric reduction during compression may not occur, especially for loose soils, due to the presence of non-unique NCLs. This reduced compressibility could lead to a less

efficient use of space, affecting the economic performance of the dam. More critically, the initially loose tailings compacted under loads less than yielding stress may still remain in a very loose state. Once the yield stress is reached due to subsequent construction on top, the loose tailings may experience significant volumetric changes but may still stay loose due to small compressibility. When re-saturated by rainfall, they could undergo sudden volumetric changes. This poses a significant risk to both the stability and the long-term safety of the structure. Therefore, the transitional behaviour in unsaturated states must be considered in practical geotechnical applications.

7.4 Recommendations for future research

The first suggested direction for future research is to further characterise the transitional behaviour of unsaturated soils. Although clear transitional behaviour was observed in the unsaturated tests for both sandy tailings and silty loess, further testing is required to enable more detailed characteristics of transitional behaviour under unsaturated states. Studying transitional behaviour requires at least three initial density groups, loose, medium density and dense. For each suction level, two unsaturated samples per density group are required to establish the Normal Compression Line (NCL_s) and the Critical State Line (CSL_s) at that suction value. These results can be used to characterise the location and parameters of the NCL_s and CSL_s. However, due to time constraints, these additional tests for both sandy tailings and silty loess could not be completed within the duration of this PhD.

The second recommended direction for future research is to quantify the microstructure associated with transitional behaviour. The non-convergent volumetric state in transitional soils indicates the presence of a stable or robust fabric that cannot be easily destructured through conventional loading (Coop, 2015). At present, microstructural

analyses of transitional soils are primarily qualitative, focusing on pore structure Mercury Intrusion Porosimetry (MIP) tests and particle arrangement through Scanning Electron Microscopy (SEM) tests. These methods reveal persistent microstructural differences between loose and dense samples after mechanical testing, which may represent the robust fabric responsible for transitional behaviour. A further study would be to develop approaches to directly quantify this fabric from qualitative results and to establish parameters or models that link microstructural characteristics to mechanical behaviour.

The final suggested direction for future research is a comprehensive investigation into the transitional behaviour of a wide range of tailings soils. Soils with mixed mineralogy and/or mixed grading are more likely to have transitional behaviour (Shipton & Coop, 2015), for example, the tailings soils examined in this study. However, since there is no definitive indicator to predict transitional behaviour and small changes in soil components can change this behaviour, there appears to be no simple method to predict the transitional soils (Shipton & Coop, 2015). A broad and systematic study may help establish a definitive indicator for predicting transitional behaviour.

REFERENCES

Ackerley, S., Standing, J., & Hosseini Kamal, R. (2016). A system for measuring local radial strains in triaxial apparatus. *Géotechnique*, *66*(6), 515-522.

Alonso, E. E. (1987). Special problem soils, General Report. In *Proc. 9th European Conf. SMFE*, 3, 1087-1146.

Alonso, E. E., Gens, A., & Hight, D. W. (1987, August). General report. Special problem soils. In *Proceedings of the 9th European Conference on soil mechanics and foundation engineering, Dublin* (Vol. 3, pp. 1087-1146).

Alonso, E. E., Gens, A., & Josa, A. (1990). A constitutive model for partially saturated soils. *Géotechnique*, *40*(3), 405-430.

Altuhafi, F. N., & COOP, M. R. (2011). Changes to particle characteristics associated with the compression of sands. *Géotechnique*, *61*(6), 459-471.

Altuhafi, F., Baudet, B. A., & Sammonds, P. (2010). The mechanics of subglacial sediment: an example of new "transitional" behaviour. *Canadian Geotechnical Journal*, *47*(7), 775-790.

ASTM. *ASTM D5298-16 Standard Test Method for Measurement of Soil Potential (Suction) Using Filter Paper*.

Azcue, J. M. (Ed.). (2012). *Environmental impacts of mining activities: emphasis on mitigation and remedial measures*. Springer Science & Business Media.

Barbour, S. L. (1998). Nineteenth Canadian Geotechnical Colloquium: The soil-water characteristic curve: a historical perspective. *Canadian Geotechnical Journal*, *35*(5), 873-894.

Baudet, B., & Stallebrass, S. (2004). A constitutive model for structured clays. *Géotechnique*, *54*(4), 269-278.

Bishop, A. W. (1959). The principle of effective stress. *Teknisk ukeblad*, *39*, 859-863.

Bishop, A. W. (1961). The experimental study of partly saturated soil in the triaxial apparatus. In *Proc. 5th International Conference on Soil Mechanics and Foundation Engineering, Paris, 1961* (Vol. 1, pp. 13-21).

Bocking, K. A., & Fredlund, D. G. (1980). Limitations of the axis translation technique. In *Expansive Soils* (pp. 117-135). ASCE.

Bolzon, G., Schrefler, B. A., & Zienkiewicz, O. C. (1996). Elastoplastic soil constitutive laws generalized to partially saturated states. *Géotechnique*, *46*(2), 279-289.

Brooks, R. H., & Corey, A. T. (1963). Hydraulic properties of porous media and their relationship to drainage design. *Am Soc Agric Eng Trans*, *7*(1), 26–28.

Burland, J. B. (1965). Some aspects of the mechanical behaviour of party saturated soils. *Moisture equilibria and moisture changes in soils beneath covered areas*, 270-278.

Burland, J. B. (1990). On the compressibility and shear strength of natural clays. *Géotechnique*, *40*(3), 329-378.

Burland, J. B., & Ridley, A. M. (1996, May). The importance of suction in soil mechanics. In *Proceedings of 12th south-east Asian conference on soil mechanics and foundation engineering, Kuala Lumpur* (Vol. 2, pp. 27-49).

Burland, J. B., & Symes, M. J. P. R. (1982). A simple axial displacement gauge for use in the triaxial apparatus. *Geotechnique*, *32*(1), 62-65.

Cai, J., & Dong, B. Y. (2011). Micro-structure study on collapsibility loess with SEM method. In *Applied Mechanics and Materials* (Vol. 52, pp. 1279-1283). Trans Tech Publications Ltd.

Cartwright, A. (2022). *Investigating cyclic liquefaction in transitional tailings* (Doctoral dissertation, UCL (University College London)).

Carrera, A., Coop, M. R., & Lancellotta, R. (2011). Influence of grading on the mechanical behaviour of Stava tailings. *Géotechnique*, *61*(11), 935-946.

Cartwright, A., Coop, M., Wei, L., & Fourie, A. (2025). Cyclic liquefaction in transitional and non-transitional tailings. *Géotechnique*, *75*(4), 446-458.

Chandler, R. J., & Gutierrez, C. I. (1986). The filter-paper method of suction measurement. *Géotechnique*, *36*(2), 265-268.

Coleman, J. D. (1962). Stress strain relations for partly saturated soil. *Correspondence to Geotechnique*, *12*(4), 348-350.

Colmenares Montanez, J. E. (2002). *Suction and volume changes of compacted sand-bentonite mixtures* (Doctoral dissertation, Imperial College London (University of London)).

Coop, M. (2015). Limitations of a critical state framework applied to the behaviour of natural and "transitional" soils. In *Deformation characteristics of Geomaterials* (pp. 115-155). IOS Press.

Coop, M. R., & Cotecchia, F. (1995). The compression of sediments at the archaeological site of Sibari. In *Proceedings of 11th European Conference on Soil Mechanics and Foundation Engineering, Copenhagen*, 8, 19-26.

Coop, M. R., & Lee, I. K. (1993). The behaviour of granular soils at elevated stresses. In *Predictive soil mechanics: Proceedings of the Wroth Memorial Symposium held at St Catherine's College, Oxford, 27-29 July 1992* (pp. 186-198). Thomas Telford Publishing.

Coop, M. R., Atkinson, J. H., & Taylor, R. N. (1995). Strength and stiffness of structured and unstructured soils. In *Proceedings of the 11th European Conference on Soil Mechanics and Foundation Engineering, Danish Geotechnical Society, Bulletin*, 11, 55-62.

Cotecchia, F., & Chandler, R. J. (2000). A general framework for the mechanical behaviour of clays. *Géotechnique*, *50*(4), 431-447.

Cuccovillo, T., & Coop, M. R. (1997). The measurement of local axial strains in triaxial tests using LVDTs. *Géotechnique*, *47*(1), 167-171.

Cui, Y. J., & Délage, P. (1996). Yielding and plastic behaviour of an unsaturated compacted silt. *Géotechnique*, *46*(2), 291-311.

Cunningham, M. R. (2000). *The mechanical behaviour of a reconstituted, unsaturated soil* (Doctoral dissertation, Imperial College London (University of London)).

Délage, P. (1987). Unnouvel appareil triaxial pour les sols non satures. In *9th Eur. Conf. of Soil Mechanics* (pp. 26-28).

Délage, P., & Cui, Y. J. (2008). An evaluation of the osmotic method of controlling suction. *Geomechanics and Geoengineering: An International Journal*, *3*(1), 1-11.

Délage, P., & Graham, J. (1995). Understanding the behaviour of unsaturated soils requires reliable conceptual models: state of the art report. *Unsaturated soils. Edited by EE Alonso and P. Délage. Balkema, Rotterdam*, *3*, 1223-1256.

Délage, P., & Pellerin, F. M. (1984). Influence de la lyophilisation sur la structure d'une argile sensible du Québec. *Clay minerals*, *19*(2), 151-160.

Estabragh, A. R., Javadi, A. A., & Boot, J. C. (2004). Effect of compaction pressure on consolidation behaviour of unsaturated silty soil. *Canadian Geotechnical Journal*, *41*(3), 540-550.

Fearon, R. E., & Coop, M. R. (2000). Reconstitution: what makes an appropriate reference material?. *Géotechnique*, *50*(4), 471-477.

Ferreira, P. M. V., & Bica, A. V. D. (2006). Problems in identifying the effects of structure and critical state in a soil with a transitional behaviour. *Géotechnique*, *56*(7), 445-454.

Fredlund, D. G. (1975). A diffused air volume indicator for unsaturated soils. *Canadian Geotechnical Journal*, *12*(4), 533-539.

Fredlund, D. G., & Morgenstern, N. R. (1977). Stress state variables for unsaturated soils. *Journal of the geotechnical engineering division*, *103*(5), 447-466.

Fredlund, D. G., & Rahardjo, H. (1993). *Soil mechanics for unsaturated soils*. John Wiley & Sons.

Fredlund, D. G., Morgenstern, N. R., & Widger, R. A. (1978). The shear strength of unsaturated soils. *Canadian geotechnical journal*, *15*(3), 313-321.

Fredlund, D. G., Rahardjo, H., & Gan, J. K. M. (1987, December). Non-linearity of strength envelope for unsaturated soils. In *Proceedings of the 6th international conference on expansive soils, New Delhi, India* (Vol. 1, pp. 49-54).

Gan, J. K., & Fredlund, D. G. (1996). Shear strength characteristics of two saprolitic soils. *Canadian Geotechnical Journal*, *33*(4), 595-609.

Germaine, J. T., & Ladd, C. C. (1988). State-of-the-art paper: Triaxial testing of saturated cohesive soils. In *Advanced triaxial testing of soil and rock*. ASTM International.

Guglielmi, S., Cotecchia, F., Cafaro, F., & Gens, A. (2022). Analysis of the micro to macro response of clays to compression. *Géotechnique*, *74*(2), 134-154.

Hilf, J. W. (1956). *An investigation of pore-water pressure in compacted cohesive soils*. University of Colorado at Boulder.

Javadi, A. A., & Snee, C. P. (2001). The effect of air flow on the shear strength of soil in compressed-air tunneling. *Canadian geotechnical journal*, *38*(6), 1187-1200.

Jennings, J. E. B., & Burland, J. B. (1962). Limitations to the use of effective stresses in partly saturated soils. *Géotechnique*, *12*(2), 125-144.

Jiang, M., Hu, H., Peng, J., & Leroueil, S. (2011). Experimental study of two saturated natural soils and their saturated remoulded soils under three consolidated undrained stress paths. *Frontiers of Architecture and Civil Engineering in China*, *5*(2), 225-238.

Jiang, M., Shen, Z., Adachi, T., & Hongo, T. (1999). Microscopic analysis on artificially prepared structured collapsible loess. In *Chinese Journal of Geotechnical Engineering-Chinese Edition*, *21*(4), 486-491.

Jiang, M., Zhang, F., Hu, H., Cui, Y., & Peng, J. (2014). Structural characterization of natural loess and remolded loess under triaxial tests. *Engineering Geology*, *181*, 249-260.

Jommi, C. (2000). Remarks on the constitutive modelling of unsaturated soils. In *Experimental evidence and theoretical approaches in unsaturated soils* (pp. 147-162). CRC Press.

Jotisankasa, A. (2005). *Collapse behaviour of a compacted silty clay* (Doctoral dissertation, University of London).

Jovičić, V., & Coop, M. R. (1997). Stiffness of coarse-grained soils at small strains. *Géotechnique*, *47*(3), 545-561.

Karube, D. (1988). New concept of effective stress in unsaturated soil and its proving test. In *Advanced triaxial testing of soil and rock*. ASTM International.

Kassiff, G., & Shalom, A. B. (1971). Experimental relationship between swell pressure and suction. *Géotechnique*, *21*(3), 245-255.

Khalili, N., & Khabbaz, M. H. (1998). A unique relationship for χ for the determination of the shear strength of unsaturated soils. *Geotechnique*, *48*(5), 681-687.

Klotz, E. U., & Coop, M. R. (2002). On the identification of critical state lines for sands. *Geotechnical Testing Journal*, *25*(3), 289-302.

Ladd, R. (1978). Preparing test specimens using undercompaction. *Geotechnical Testing Journal, 1*(1), 16-23.

Li, W., & Coop, M. R. (2019). Mechanical behaviour of Panzhihua iron tailings. *Canadian Geotechnical Journal*, *56*(3), 420-435.

Li, W., Coop, M. R., Senetakis, K., & Schnaid, F. (2018). The mechanics of a silt-sized gold tailing. *Engineering Geology*, *241*, 97-108.

Liu, T. S. (1985). *Loess and environment*. Beijing, China: China Ocean Press.

Lourenço, S., Gallipoli, D., Toll, D., Augarde, C., & Evans, F. (2011). A new procedure for the determination of soil-water retention curves by continuous drying using high-suction tensiometers. *Canadian Geotechnical Journal*, *48*(2), 327-335.

Martins, F. B., Bressani, L. A., Coop, M. R., & Bica, A. V. D. (2001). Some aspects of the compressibility behaviour of a clayey sand. *Canadian Geotechnical Journal*, *38*(6), 1177-1186.

Mmbando, E., Fourie, A., & Reid, D. (2023). Mechanics of an Iron Ore Tailings Exhibiting Transitional Behaviour. *Geotechnical and Geological Engineering*, 1-10.

Murray, E. J. (2002). An equation of state for unsaturated soils. *Canadian Geotechnical Journal*, *39*(1), 125-140.

Nocilla, A., & Coop, M. R. (2008). The behaviour of sub-soils from the Po river embankments: an example of transitional behaviour in natural soils. *Italian Geotechnical Journal*, *42*(1), 49-58.

Nocilla, A., Coop, M., & Colleselli, F. (2006). The mechanics of an Italian silt: an example of 'transitional'behaviour. *Géotechnique*, *56*(4), 261-271.

Okewale, I. A., & Coop, M. R. (2020). A study of completely decomposed volcanic rock with a transitional mode of behaviour. *Bulletin of Engineering Geology and the Environment*, *79*(8), 4035-4050.

Piciullo, L., Storrøsten, E. B., Liu, Z., Nadim, F., & Lacasse, S. (2022). A new look at the statistics of tailings dam failures. *Engineering Geology*, *303*, 106657.

Polidori, E. (2007). Relationship between the Atterberg limits and clay content. *Soils and foundations*, *47*(5), 887-896.

Ponzoni, E., Nocilla, A., Coop, M. R., & Colleselli, F. (2014). Identification and quantification of transitional modes of behaviour in sediments of Venice lagoon. *Géotechnique*, *64*(9), 694-708.

Ridley, A. M., & Burland, J. B. (1999). Use of the tensile strength of water for the direct measurement of high soil suction: discussion. *Canadian Geotechnical Journal*, *36*(1), 178-180.

Ridley, A. M., & Wray, W. K. (1996). Suction measurement—theory and practice. A state-of-the-art review. In *Unsaturated soils: Proc. 1st Int. Conf. Unsaturated Soils, Paris,* Alonso & Délage, (eds)*,* 1293-1322.

Rocchi, I., & Coop, M. R. (2014). Experimental Accuracy of the Initial Specific Volume. *Geotechnical Testing Journal*, *37*(1).

Rogers, C. D. F., Dijkstra, T. A., & Smalley, I. J. (1994). Hydroconsolidation and subsidence of loess: studies from China, Russia, North America and Europe: in memory of Jan Sajgalik. *Engineering Geology*, *37*(2), 83-113.

Schofield, A. N., & Wroth, P. (1968). *Critical state soil mechanics* (Vol. 310). London: McGraw-hill.

Shipton, B. J. I., Coop, M. R., & Nocilla, A. (2017). Particle breakage in transitional soils. In *Geomechanics and geotechnics of particulate media* (pp. 143-147). CRC Press.

Shipton, B., & Coop, M. R. (2012). On the compression behaviour of reconstituted soils. *Soils and Foundations*, *52*(4), 668-681.

Shipton, B., & Coop, M. R. (2015). Transitional behaviour in sands with plastic and non-plastic fines. *Soils and Foundations*, *55*(1), 1-16.

Sivakumar, V. (1993). *A critical state framework for unsaturated soil* (Doctoral dissertation, University of Sheffield).

Todisco, M. C., & Coop, M. R. (2019). Quantifying “transitional” soil behaviour. *Soils and Foundations*, *59*(6), 2070-2082.

Todisco, M. C., Coop, M. R., & Pereira, J. M. (2018). Fabric characterisation in transitional soils. *Granular Matter*, *20*(2), 20.

Toker, N. K., Germaine, J., Sjoblom, K., & Culligan, P. (2004). A new technique for rapid measurement of continuous soil moisture characteristic curves. Géotechnique, 54(3), 179-186.

Toll, D. G. (1990). A framework for unsaturated soil behaviour. *Géotechnique*, *40*(1), 31-44.

Toll, D. G. (2000). The influence of fabric on the shear behaviour of unsaturated compacted soils. In *Advances in unsaturated geotechnics* (pp. 222-234).

Toll, D. G., & Ong, B. H. (2003). Critical-state parameters for an unsaturated residual sandy clay. *Géotechnique*, *53*(1), 93-103.

Vanapalli, S. K., Fredlund, D. G., & Pufahl, D. E. (1999). The influence of soil structure and stress history on the soil–water characteristics of a compacted till. *Géotechnique*, *49*(2), 143-159.

Vanapalli, S. K., Fredlund, D. G., Pufahl, D. E., & Clifton, A. W. (1996). Model for the prediction of shear strength with respect to soil suction. *Canadian geotechnical journal*, *33*(3), 379-392.

Viggiani, G., & Atkinson, J. H. (1995). Interpretation of bender element tests. *Geotechnique*, *45*(1), 149-154.

Wheeler, S. J., & Sivakumar, V. (1995). An elasto-plastic critical state framework for unsaturated soil. *Géotechnique*, *45*(1), 35-53.

Xiao, Y., Coop, M. R., Liu, H., Liu, H., & Jiang, J. (2016). Transitional behaviors in well-graded coarse granular soils. *Journal of Geotechnical and Geoenvironmental Engineering*, *142*(12), 06016018.

Xu, L., & Coop, M. R. (2016). Influence of structure on the behaviour of a saturated clayey loess. *Canadian Geotechnical Journal*, *53*(6), 1026-1037.

Xu, L., & Coop, M. R. (2017). The mechanics of a saturated silty loess with a transitional mode. *Géotechnique*, *67*(7), 581-596.

Xu, L., Coop, M. R., Zhang, M., & Wang, G. (2018). The mechanics of a saturated silty loess and implications for landslides. *Engineering Geology*, *236*, 29-42.

Xu, L., Gao, C., Lan, T., Lei, J., & Zuo, L. (2020). Influence of grading on the compressibility of saturated loess soils. *Géotechnique Letters*, *10*(2), 198-204.